Dust in Early-Type Galaxies using Herschel-ATLAS and GAMA data

Nicola Kristina Agius

A thesis submitted in partial fulfilment
of the requirements for the degree of
Doctor of Philosophy

Jeremiah Horrocks Institute for Mathematics, Physics and Astronomy
University of Central Lancashire

April 2014

Declaration

The work presented in this thesis was carried out at the Jeremiah Horrocks Institute for Mathematics, Physics and Astronomy, University of Central Lancashire.

I declare that while registered as a candidate for the research degree, I have not been a registered candidate or enrolled student for another award of the University or other academic or professional institution.

I declare that no material contained in the thesis has been used in any other submission for an academic award. Data and models used in this thesis that are not my own are clearly cited in the text.

Abstract

This work investigates the properties of Early-Type Galaxies (ETGs; elliptical and lenticulars) containing thermal dust emission, with aims of linking the formation and evolution of these galaxies with their current dust properties.

Three different proxies for morphology are considered for selecting ETGs, and these are tested against three sets of visually classified galaxies. We find that classifying ETGs as those galaxies in the optical Red Sequence results in samples with $\gtrsim$35% contamination by late-types, and $\lesssim$82% completeness. Concentration and Sérsic index proxies result in slightly improved contamination levels of $\gtrsim$30% and $\sim$60-70% completeness. These results lead to the conclusion that morphological proxies cannot be used to create fully robust samples of ETGs. Therefore, we choose to use visual inspection to identify ETGs at low redshifts.

Two large, nearby ($0.013 \leq z \leq 0.06$) samples of ETGs are created: a visually classified sample of 220 ETGs, formed from the Galaxy and Mass Assembly (GAMA) database with FIR/sub-mm detections from *Herschel*-ATLAS; and a visually classified sample of 551 ETGs which are undetected with *Herschel*-ATLAS. These samples are scrutinised to determine characteristics of sub-mm detected versus undetected ETGs. Lower concentration and Sérsic indices are found in the sub-mm detected sample - a result which may be linked to the presence of dust in the

former. Optical and UV-optical colours are also shown to be much bluer, indicating that the dust is linked with recent star formation. Surface densities and groups data from the GAMA database reveal that dusty ETGs inhabit sparser environments than non-dusty ETGs in the nearby universe. Modified Planck functions are fit to the H-ATLAS detected PACS and SPIRE fluxes for ETGs with sub-mm flux densities of $\geq 3\sigma$ in the 350μm SPIRE band, giving a resultant mean cold dust temperature of T_d=22.1 K, with a range of 9-30 K and a mean dust mass of 1.8×10^7 $M_\odot$, with a range of $(0.08\text{-}35.0)\times10^7$ $M_\odot$. Dust-to-stellar mass ratios are shown to increase with decreasing stellar mass and bluer colours. These results indicate that there is a population of ETGs which exhibits larger dust masses, lower Sérsic index and bluer colours than the more well-known, massive, red population of ellipticals.

Follow-on work contrasts results from our sub-mm detected ETG sample with a nearby *Herschel* ETG study - the HeViCS Virgo cluster study described in di Serego Alighieri et al. (2013). This comparison reveals strong differences between H-ATLAS and Virgo HeViCS ETGs in both dust mass and dust-to-stellar mass ratio. From nearest neighbour environment densities we find that H-ATLAS ETGs occupy sparser regions ($\lesssim$0.1-10 galaxies/Mpc) of the local Universe, whereas HeViCS ETGs occupy dense regions ($\sim$25-500 galaxies/Mpc). Spectral energy distributions (SEDs) are fit to the ETG panchromatic data using MAGPHYS (da Cunha et al. 2008), and reveal strong anti-correlations between dust-to-stellar mass ratio and stellar mass for both samples. A correlation between dust-to-stellar mass ratio and environmental density is found, where H-ATLAS ETGs occupy low density regions and HeViCS ETGs occupy high density regions. Differences in specific star formation rate (sSFR) and stellar mass are also found. HeViCS ETGs exhibit

sSFRs consistent with those of the most massive H-ATLAS ETGs. These trends indicate that H-ATLAS ETGs have more extended star formation histories and younger stellar populations than HeViCS ETGs.

The final project in this thesis investigates the presence of dust in small samples of GAMA and Virgo cluster ETGs. We develop a new technique using both a radiative transfer model and template SED fitting to calculate radiation field energy densities and to find the typical extent of a galaxy's dust disk. Dust extents were found to be between 0.12 and 0.2 of galactic effective radius for two of three Virgo galaxies tested. Either of the following scenarios could be true: the dust resides in an optically thin disk heated predominantly by the old stellar population in the spheroidal component, with a small excess contribution at 22μm coming from circumstellar dust, or the dust could be heated by diffuse UV and optical radiation fields, and with a very low star formation rate. The third Virgo galaxy can be accounted for by a marginally optically thin solution with diffuse dust heated by both optical and UV photons. In the case of the GAMA ETGs, an optically thin solution can be found for two ETGs of the four tested, and only if substantial contribution to the dust heating from star formation is allowed. These two ETGs are found to have dust disk extents of $\sim$0.5-0.6 effective radius - roughly a factor of three larger than those found for the Virgo ETGs.

Origins of a dust disk are discussed. Given the difference in total dust mass and dust disk extent between the Virgo and GAMA ETGs, it seems likely that dust in GAMA ETGs is acquired through interactions and mergers, whereas dust originating from the old stellar population is more likely for Virgo ETGs.

Contents

List of Tables

List of Figures

Acknowledgements

The completion of this thesis would not have been possible without the help of my supervisors: Dr Anne Sansom, Dr Cristina Popescu and Dr Giovanni Natale. I would like to express my gratitude towards Anne for introducing me to the study of early-type galaxies and her guidance throughout my postgraduate years; to Cristina for teaching me to love dust, and to Giovanni for his paternal concern for my welfare. Additionally I would like to express my appreciation towards members of both GAMA and H-ATLAS consortia for inviting me in, collaborating with me, and pushing me towards every success. This work belongs to them as much as to me.

The University of Central Lancashire, its staff members and students have been a good home to me for the past three years. I'd like to thank Danielle and Daniel, for spending many a Friday pub cheering me up about work and reminiscing about Saint Andrews. Further thanks to Brad, for providing advice, wisdom and some fantastic wine. My greatest appreciation goes to Caroline, for the coffee breaks, holidays, wine and strongbow, and for being there when I needed it.

A special thanks goes to my family, whose support has been invaluable to me. Sandra and Ric, for constantly being there for me, offering me advice and support. Mark, for his occasional supply of good whiskey and for always keeping me grounded. Becky and Bettina, for keeping me in fashion and on the ball with

the latest entertainment. Oli and Sebi, my gorgeous cousins and godchildren, for making me laugh and want to go home. To the rest of my family, for their constant interest, help and appreciation. I could not have written this thesis without knowing all of them were behind me every step of the way.

Above all others, I am most grateful for Mike, my partner in crime and all else. He has stood by me, showed the uttermost patience and love towards me, even at my very worst. He has helped with every problem, commiserated and celebrated, and never stopped holding my hand. The future is a bright place for us.

Finally, I would like to dedicate this thesis to my brother, Marc. He has been my constant companion, and he will forever live in my memory.

Chapter 1

Introduction

It's a dangerous business, Frodo, going out your door.
You step into the road, and if you don't keep your feet,
there's no knowing where you might be swept off to.

J.R.R. Tolkien, The Fellowship of the Ring

The phrase *smoking gun* was coined by fictional detective Sherlock Holmes and has since been used to describe conclusive evidence of a crime. In this thesis we will extend this term to the study of early-type galaxies (ETGs), using their dust properties as the theoretical *smoking gun* to trace their evolution and formation history. This is made possible by the advent of new, highly sensitive data from the *Herschel Space Observatory*, as well as panchromatic data available from a host of combined surveys. Diffuse dust has been chosen as the conduit for exploring these galaxies' histories because of its direct link with cold gas in the interstellar medium; this in turn is linked to the star formation history of a galaxy.

There are several aims to this study which will be addressed throughout the thesis. A primary aim is to choose a selection method for ETGs, to create an uncontaminated, complete and statistically significant sample of sub-mm detected ETGs. Following the completion of such a sample, a study of the multi-wavelength properties of the galaxies will be run, including an analysis of the dust properties; this will allow some diagnosis of where these ETGs fit into the evolutionary sequence as it is currently known and understood. The sub-mm detected ETGs will also be compared to a host of control samples: undetected ETGs chosen with the same selection method, and detected ETGs from other nearby studies.

In order to address the main motivation behind this study (i.e. how ETGs form and evolve) we will run a study on a pilot sample of ETGs, whereby a combination of radiative transfer simulations and spectral energy distribution fits to observed data will be used to gain understanding of the physical distribution of dust grains in these ETGs. This will lead to some understanding of the manner in which dust is heated to emission. Furthermore, statements about the origin of these dust grains (internal accumulation from stellar mass loss (Goudfrooij & de Jong 1995) or external injection via accretion from galaxy interactions (Temi et al. 2007; Kaviraj et al. 2009; Shapiro et al. 2010)) may be made, enhancing our understanding about the timescales on which ETGs form and produce stars. All of this work should be of use to future work on constraining simulations that include interstellar media and dust properties of populations of galaxies.

This first chapter is an introduction to our knowledge of ETGs, beginning with a description of their structural properties (including shape, kinematics, radio and x-ray properties) in Section 1.1. A discussion on the different types of ETGs and their position in colour-magnitude space is also given here. Next ETG formation and evolution is examined in a description of hierarchical merging, downsizing and the influence of environment in Section 1.1.2. The task of sample selection is

discussed in Section 1.1.3 - focus is laid primarily on what has been done in the past to select ETGs and what methods we will be looking at utilising.

Section 1.2 of the introduction takes an in depth look at diffuse dust in ETGs, including the dust grain composition, the physical effects of dust, and dust grain production and destruction. Sections 1.3 and 1.4 describe the *Herschel*-ATLAS and Galaxy and Mass Assembly (GAMA) consortia respectively, giving information on their motivations, instruments, data and results thus far. Finally Section 1.5 gives a summary of the thesis layout.

1.1 Early-Type Galaxies

1.1.1 Morphological and Observed Properties

Hubble Sequence

The original classification by Hubble laid out a solid foundation for groupings of galaxies (Hubble 1936). This Hubble Tuning Fork describes three main classes of galaxy: the Ellipticals (E), Spirals (S) and Barred Spirals (SB), separated by an intermediary lenticular (S0) type. This linear system does not directly relate to, or identify, the formation or evolution of such galactic systems but has been used in the past as a tool to identify differences in the structure and components of galaxies.

Early-type galaxies (ETGs) are generally considered to be comprised of E and S0 galaxies (e.g. Baldry et al. 2004), a homogeneous class within the Hubble sequence (e.g. D'Onofrio et al. 2011). These are shown in Fig. 1.1 in the handle of the Hubble Tuning Fork, with S0s forming a transition sequence between Es and spiral galaxies. They are generally found to be an old, passive (low levels of star formation), high central surface brightness subset and cover a wide range of luminosities (Baade & Gaposchkin 1963); in contrast late-type galaxies (LTGs) are

viewed as a young, blue, star forming, intermediate surface brightness grouping of spiral (S and SB) and irregular (Irr) galaxies (e.g. Trager et al. 2000; Driver et al. 2006). Although it is well agreed that galaxies express diversity in all aspects (including but not limited to luminosity, size, colour, star formation rate (SFR), metallicity, gas and dust contents), E and S0 galaxies are generally considered to be highly concentrated and smooth systems. Ellipticals are purely spheroidal whilst S0s are spheroidal galaxies with a disk, yet both are lacking in spiral structure (Hubble 1936; Driver et al. 2006). In the Hubble sequence Es are classed from left (E0) to right (E7) according to their ellipticity, which is defined as

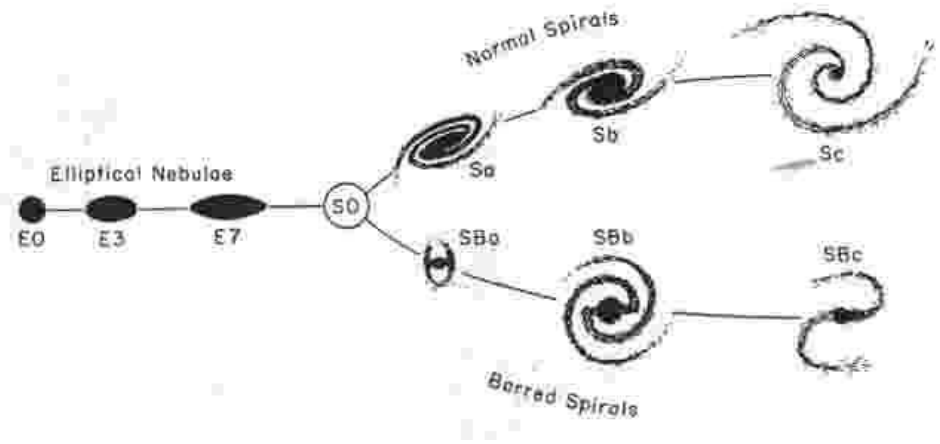

Figure 1.1: Hubble (1936) - Original Tuning Fork diagram demonstrating the smooth flow from left to right of ellipticals to lenticulars and branching out into spirals and barred spirals.

$$\epsilon = 1 - \frac{b}{a}, \tag{1.1}$$

where a and b are the apparent major and minor axes of the elliptical respectively. The ellipticity is multiplied by ten to give the type of elliptical (where E0s are completely spheroidal and E7s are the most elongated).

General properties of this galactic class include a tendency towards redder

colours, little or no recent star formation, and mass and light distributions which decline smoothly over large radial ranges (Driver et al. 2006; Kormendy et al. 2009). They can be flattened by rotation (Illingworth 1977) or due to velocity anisotropies (Binney 1976). Their luminosity profiles are believed to follow the de Vaucouleurs $\log(I(r)) \sim r^{1/4}$ law (D'Onofrio et al. 2011) or exhibit similar high Sérsic indices (Kormendy et al. 2009). These are discussed and clarified further in Chapter 2.

It can be exceptionally difficult to distinguish between Es and S0s, especially when viewed face-on (van den Bergh 2009), hence the combined ETG group will be referred to for the majority of this thesis.

van den Bergh (1976) proposed that lenticular galaxies form a parallel sequence to spiral galaxies, instead of acting as the hypothetical transition class between ellipticals and spirals. If Hubble's transition theory was accurate, S0s would be expected to have large bulge fractions; this is not always the case. After a process of examining $\gtrsim$200 kinematically sampled ETGs, the ATLAS^{3D} survey proposed their own formulation of the tuning fork which looks more like a comb (see Fig. 1.2). Morphology is not the only property which varies smoothly along the sequence; other galaxy properties such as kinematics and bulge fractions also vary from one side to the other. Galactic luminosity decreases on average from left to right, and colours on average become bluer from bottom to top.

Elliptical galaxies can be distinguished according to their intrinsic brightness: bright Es have velocity dispersions which are slightly anisotropic with box-shaped isophotes. The stars orbit within a well-defined family in triaxial systems (Bender et al. 1989; Emsellem et al. 2011). These ellipticals are also slow rotators (Emsellem et al. 2011), indicating that the spheroidal structure is supported by the orbital pressure of the stellar motion (Kormendy & Bender 1996; Naab et al. 1999; Emsellem et al. 2007). This subset are generally radio-loud (Bender et al.

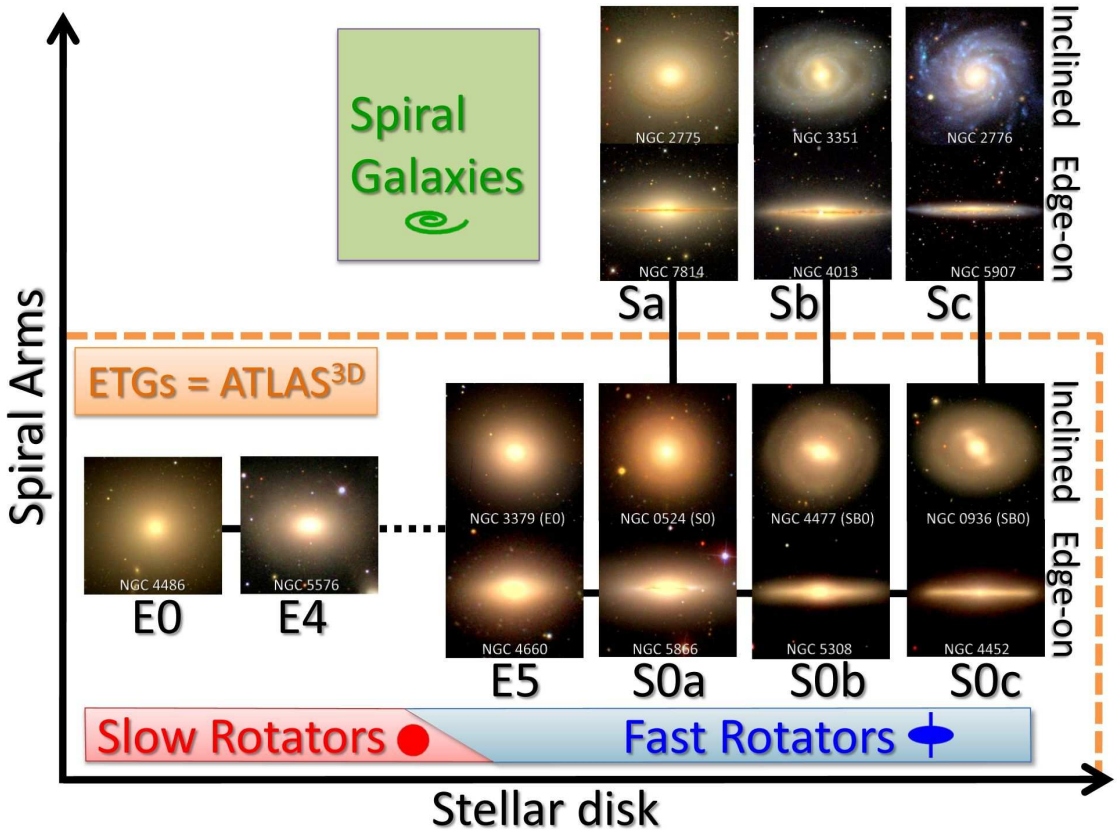

Figure 1.2: Cappellari et al. (2011b) show the morphology of nearby galaxies in their ATLAS^{3D} parent sample forming a new 'tuning fork'. Ellipticals with disky isophotes fall into the fast rotator class with lenticulars, whereas boxy ellipticals are found to be slow rotators. The fast-rotators are thought to form a parallel sequence to spiral galaxies, as predicted for lenticulars by van den Bergh (1976). The black solid lines connecting the images indicate an empirical continuity, while the dashed line suggests a possible dichotomy.

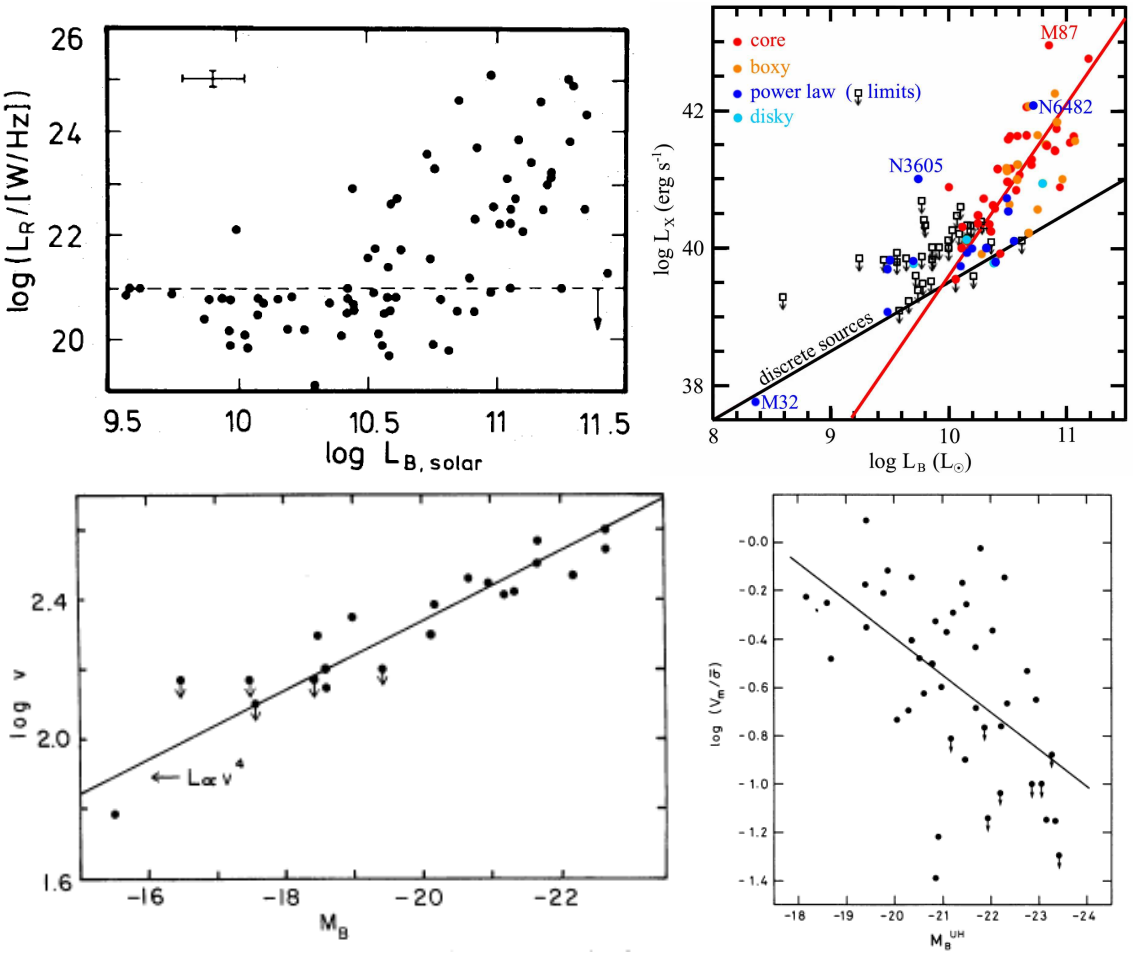

Figure 1.3: Top-left. Bender et al. (1989) - 1.4 GHz (radio) luminosity vs. total blue band luminosity for a sample of nearby massive elliptical galaxies. Top-right. Kormendy et al. (2009) - Total observed X-ray emission versus galaxy B-band luminosity. Bottom-left. Faber & Jackson (1976) - Line-of-sight velocity dispersions versus absolute magnitude. Bottom-right. Davies et al. (1983) - The normalized ratio of maximum rotation velocity over average velocity dispersion (V_m/σ) is plotted against B-band absolute magnitude for a sample of ellipticals.

1987), surrounded by gaseous X-ray halos (Naab et al. 1999; Ellis & O'Sullivan 2006) and often have large amounts of minor-axis rotation (Kormendy & Bender 1996). Faint Es are conversely mostly oblate due to the majority of stars rotating anisotropically and quickly in a fixed plane (equatorial plane) (Bender et al. 1987). Their structure is rotationally supported which results in disky isophotes (Bender et al. 1994). These ellipticals are radio-quiet and have no X-ray emission (Kormendy & Bender 1996; Naab et al. 1999); this latter set has more in common with lenticular galaxies (Cappellari et al. 2011b). The differences in the properties of these ellipticals are highlighted in the panels in Fig. 1.3, where two groupings of ellipticals stand out clearly in radio- and X-ray-luminosity space (top two plots). Such a bimodality is not evident in the lower plots of velocity dispersion or relative rotation velocity, but these figures indicate that brighter ellipticals have larger velocity dispersion yet slower rotation than fainter ellipticals.

Colour-Magnitude Relation

The link between the overall colour of a galaxy and its luminosity was first established by Baum (1959), and confirmed by Sandage (1972). Initial studies were focussed on the local Universe, resulting in the development of a colour-magnitude relation (CMR) for Virgo and Coma Cluster ellipticals (Stebbins & Whitford 1952; de Vaucouleurs 1961a; Faber 1973; Visvanathan & Sandage 1977). These works all conclusively discovered that elliptical galaxies typically occupy the red region (or so-called 'Red Sequence'; RS) of colour-magnitude space, whereas spiral galaxies mostly dominate the blue region ('Blue Cloud'; BC). More recent work confirms this, with surveys finding $\sim$85% of RS galaxies appear to be ETGs (Bell et al. 2004). The intermediate region of the CM diagram is called the Green Valley (GV) - this is populated by a range of galaxy morphologies.

The CMR sparked such interest because it could be interpreted as a sequence

of increasing metallicity (becoming redder) with increasing luminosity (brighter magnitudes; e.g. Faber 1973; Worthey et al. 1994; Kodama & Arimoto 1997; Kodama et al. 1999); however it is also acknowledged that age could at least in part drive the relation (e.g. Ferreras et al. 1999; Terlevich et al. 1999). Both high metallicities and older ages are frequently associated with ETGs, hence their occupation of the RS (D'Onofrio et al. 2011). It should be noted that colours can also be affected by the presence of dust (e.g. Gallazzi et al. 2006) or an AGN.

An example of the optical CMR is shown in Fig. 1.4. Note the distribution of ETGs (selected by a lack of star formation activity in their spectra and represented up to z=1.0) mainly occupies the RS and the majority of LTGs dominate the BC. Fig. 1.4 also features the fainter magnitudes of the late-type population, indicating they are not as massive as the ETG population (at least at these distances). Finally, this plot highlights the lack of low mass (faint), red galaxies in the CMR (e.g. Kodama et al. 2004).

Although originally the CMR was only validated for the local galaxy population, these studies were soon extended to higher redshifts in order to study the evolution of the CMR. Such studies of evolution with cosmic time indicate few changes since z$\sim$1 (Kodama & Arimoto 1997; Kodama et al. 1998; Stanford et al. 1998). Tanaka et al. (2005) indicate that the RS already appears to be in place at their highest observable redshift (z$\sim$0.83), but at this point there is no clear bimodality present; this is true for galaxies in low density environments. However, this bimodality becomes apparent for their sample at z$\sim$0.55. Somewhat conversely, Schade et al. (1999) found the CMR to become progressively bluer with redshift; they do however state that due to the poorness of their statistics their result is not conclusive.

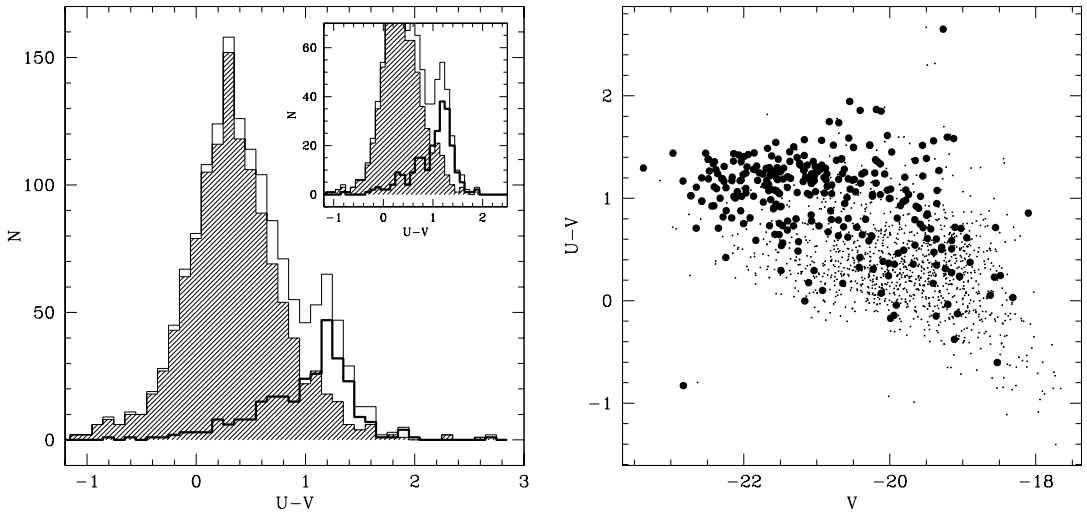

Figure 1.4: An example of the optical CMR from Franzetti et al. (2007). The left panel shows the distribution of rest-frame colours for their whole VMOS-VLT sample (up to z=1), where the shaded histograms represent their LTGs and the thick-line histograms their ETGS. The inset shows the same histograms drawn only for the higher signal-to-noise objects. The right panel shows the (U-V) vs V band CMR, with ETGs represented as filled circles and LTGs as tiny points.

1.1.2 ETG Formation and Evolution

There is currently a substantial amount of evidence pointing towards galactic evolution as a consequence of the hierarchical merging (ΛCDM) model; in this scenario mergers or tidal interactions between galaxies may destroy galactic disks and thereby convert spiral and irregular galaxies into bulge-dominated ETGs (Toomre & Toomre 1972; Farouki & Shapiro 1981). This is supported by observational evidence: the predicted conversion of irregular galaxies into spheroids via major mergers (mass ratios of 1:1; Somerville & Primack 1999; Steinmetz & Navarro 2002) is shown to be at least partially correct in a study by Prieto et al. (2013), who use observations of massive ($5{\times}10^{10}\,M_{\odot}$) RS galaxies over the Groth Strip to determine that the fraction of irregular galaxies decreases from $z \sim 1.5$, while the fraction of spheroids increases by the same amount. However it is as yet unclear

whether minor or major mergers play the dominant role in the build-up of mass that is known to take place at $z \lesssim 1$ (Bell et al. 2004; Drory et al. 2004; Conselice et al. 2005).

Mergers have been shown to operate most efficiently in galaxy groups or on the outskirts of rich clusters (Caldwell et al. 1993; Moss & Whittle 1993; Gnedin 2003). It also appears as though the majority of mergers take place at higher redshift; as an example, Huertas-Company et al. (2013) find that ∼80% of massive, passive systems are ETGs, and this appears true up to $z \sim 0.64$. It is possible that different types of interactions occur in different environments, resulting in different galaxies. Hopkins et al. (2009) suggest that the survival of a galaxy's original disk is less likely in a violent merger or multiple mergers; they further state that if all ETGs formed in this way, lenticulars would need their disks to survive the mergers or re-form the disk (and rotationally supported components) from gas that survives the mergers.

Hence the split between different merger scenarios becomes apparent. One theory supported by Shankar et al. (2013) amongst others predicts that low mass spheroids ($M_* < 10^{11} M_\odot$) are built up via a combination of disk instabilities and mergers, whereas in the second case massive galaxies mainly evolve via dry (gas-poor) mergers. Additionally, it is thought that present-day bulges grow their masses in a fast, early collapse at high redshift ($z > 1.5$), which is then followed by a smoother phase driven by mergers and disk instabilities (Obreja et al. 2013).

In the following subsections a discussion of the various relations supporting hierarchical merging scenarios is given.

Downsizing

The idea of downsizing, where massive galaxies have shorter formation timescales and formed at earlier times, was originally introduced by Cowie et al. (1996); this

has grown steadily more popular as an explanation for the differences seen in high and low-mass ETG cosmic time evolution within colour-magnitude, morphology-density and mass-metallicity relations (see upcoming subsections within Section 1.1.2).

Morphological downsizing is used to explain the evolution in number densities of galaxy types, for a given stellar mass. Observations with the CANDELS survey (Mortlock et al. 2013) find that higher mass galaxies form ETG structures before their lower mass counterparts. Earlier evidence comes from Kodama et al. (2004) who report a deficit of low-mass, red galaxies in the CMR; this would indicate that these low-mass galaxies are still star-forming, whereas massive galaxies are only passively evolving.

Downsizing is very much dependent on galactic environment: the CMR for ETGs in cluster environments shows redder galaxies are more massive and therefore indicate the majority of stars in these galaxies formed at high redshift, whereas the same relation for field ETGs suggests that star formation in low density environments is delayed by $\sim$1-2 Gyrs (Stanford et al. 1998; Gladders et al. 1998; Kodama et al. 1998). It is possible that ETGs form at different rates in the field, groups and clusters, with the more massive red galaxies assembling first; this would result in the bright end of the CMR being populated before the faint end (Tanaka et al. 2005).

De Lucia et al. (2006a) describe this phenomenon as less massive elliptical galaxies having more extended star formation histories than their more massive counterparts - this would of course result in a lower characteristic formation redshift. Thomas et al. (2005) depict this idea nicely in their Fig. 10 (shown as Fig. 1.5 here); galaxies in high density environments (equivalent to groups or clusters) are calculated to begin their star formation at higher redshift yet for a similar duration as those in low density environments. In the cases of massive systems, it is thought that early starbursts are triggered by merger events (see Thomas et al.

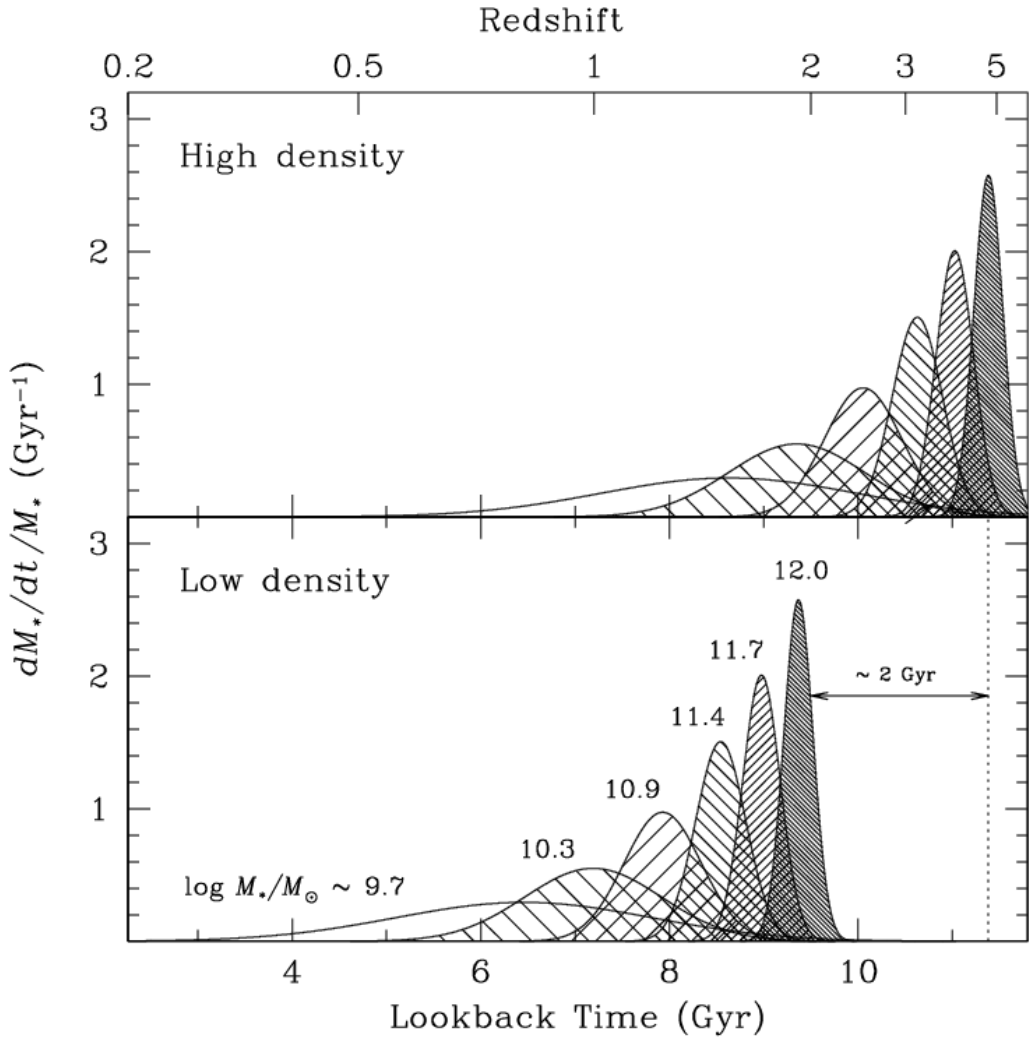

Figure 1.5: Thomas et al. (2005) show schematic star formation histories of early-type galaxies as a function of their stellar masses. The star formation histories are derived from the mean ages and [α/Fe] ratios calculated from real data and described in their paper. The dotted line marks the average age of a high-density object with M_*=10^{11} $M_\odot$ for comparison.

2005 and references therein). It is possible that the 2 Gyr delay in star formation observed in sparse environments is due to the decreased likelihood of mergers and interactions based on the lack of galaxies compared to dense environments.

Morphology-Density Relation

The morphology-density relation (MDR) was first realised by Oemler (1974) and Dressler (1980), and indicates that the fractional abundance of ETGs increases in comparison to that of spirals with increasing space density of galaxies. Initial results from Dressler (1980) are shown in Fig. 1.6, where population densities of elliptical, lenticular and spiral galaxies are seen to vary with environment. This relation has since been found in multiple studies: the MDR has been observed to occur over at least six orders of magnitude (Postman & Geller 1984) and S0s are shown to dominate at densities of $\sim$600 gals Mpc^{-3} in the local universe, with E fractions becoming dominant at densities as high as 3000 gals Mpc^{-3}. Red Es and S0s have been shown to dominate nearby galaxy clusters such as Virgo (e.g. de Vaucouleurs 1961b), whereas younger clusters (at $z \geq$0.4) contain substantial populations of blue spirals (Butcher & Oemler 1984; Moore et al. 1996). Follow-up work by Dressler et al. (1997) supports these observations, adding that the fraction of S0 galaxies decreases by 30-50% in higher redshift clusters, although the fraction of E galaxies is at least as high as that found in nearby clusters.

It is currently unclear what drives the evolution of the MDR: 'nature' or 'nurture'. The former requires galaxy properties to be determined by their initial conditions, whereby the morphological type is determined by the environment in which the galaxy is formed; the latter would indicate ram-pressure stripping (Lucero et al. 2005) and galaxy harassment (Moore et al. 1996; and hence the influence of environment) to be the dominant driver in evolution. It has been suggested that the MDR is not driven by processes that operate only in extreme

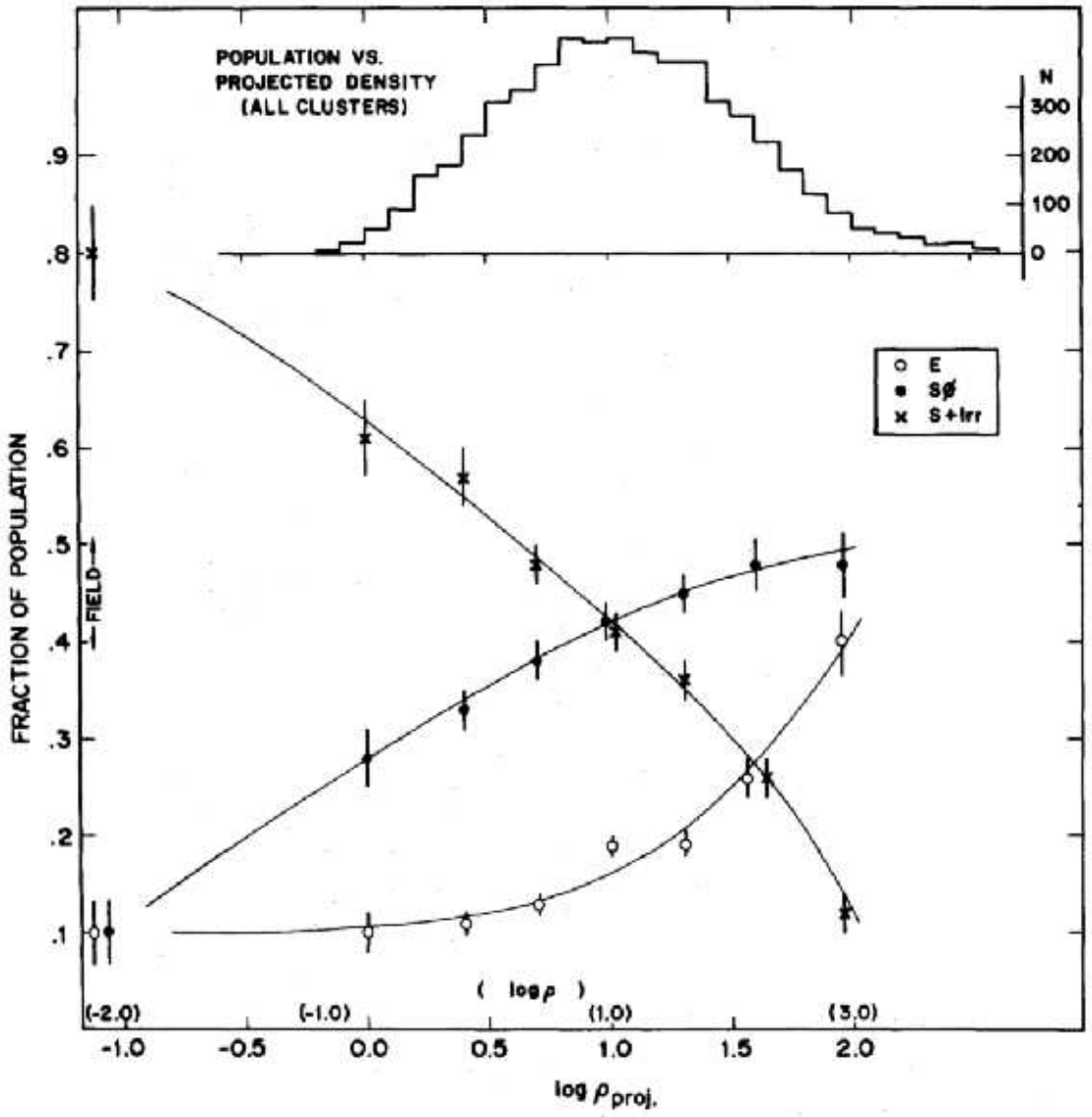

Figure 1.6: The Dressler (1980) relationship between galaxy number density and projected environment density, shown for three different galaxy morphologies: ellipticals (open circles), lenticulars (filled circles) and spirals/irregulars (crosses). The histogram in the top panel shows the overall distribution of densities for the sample.

environments, as the correlation between star formation history of a galaxy and its environment has been shown to extend down to low densities (Kodama et al. 2001; Pimbblet et al. 2002; Gómez et al. 2003; Balogh et al. 2004). Intrinsic galactic properties such as star formation, nuclear activity and most particularly specific star formation have been shown to depend strongly on the local density (Kauffmann et al. 2004), and massive galaxies in low-density environments have been shown to contain more dust (Kauffmann et al. 2004). Such results appear to be in favour of the 'nurture' scenario, although they could also be accounted for if galaxies in low-density environments are at an earlier stage in their star formation history than galaxies in dense environments (evidenced by downsizing models, Cowie et al. 1996)

Mass-Metallicity Relation

The metallicity of a galaxy is defined as the proportion composition of chemical elements other than Hydrogen or Helium. Metallicity levels and gradients within galaxies have therefore proven to be of great interest to both observers and theorists, due to the enormous range of properties metallicity can be associated with. For example, Kobulnicky & Kewley (2004) indicate that metallicity not only affects a galaxy's UV and optical colours at a given age, but also its dust-to-gas ratio (Issa et al. 1990; Dwek 1998), and possibly even its star formation rate (Nishi & Tashiro 2000).

As early-type galaxies are typically quiescent (or passive), their spectra are primarily comprised of absorption[1] line features. The comparison of such spectral line features to synthetic libraries of absorption line indices (e.g. Worthey et al. 1994) can lead to a determination of a stellar population's overall metallicity (e.g. Spolaor et al. 2009). It is important to note when undertaking such a task that both

[1]Absorption lines are caused by absorption by cold gas within stellar atmospheres at the atomic transition frequencies of the gas within our line-of-sight.

age and metallicity tend to redden the colours and strengthen the Mg_2 absorption line in similar ways; this is the age-metallicity degeneracy (Worthey et al. 1994). Techniques such as those in Proctor & Sansom (2002) can be used to break this degeneracy.

Results from studying metallicity levels in cores of ETGs have revealed a variation in metallicity from just below solar to ∼5 times solar levels (Bower et al. 1992; Kuntschner 2000; Trager 2004). To examine these trends on more subtle levels, α[2]-element to iron ratios are examined; these [α/Fe][3] abundances can be used to learn more about the stellar populations within galaxies. Enhanced [α/Fe] abundances indicate a variation in the ratio of Type II to Type Ia Supernovae (SNe), whereby the former produce both α-elements and iron, whereas the latter contribute only heavier iron-like elements (see Worthey 1998 for further detail on these processes). The relative populations of these two types of SNe are indicative of the types of populations currently inhabiting the galaxy. Studies thus far have indicated that [α/Fe] abundances are enhanced in massive ellipticals (Worthey et al. 1992; Vazdekis et al. 2001).

Metallicity is linked with colour, and radial gradients of both properties have been detected in elliptical galaxies, with the central regions showing the reddest colours and the highest metallicities (Kormendy & Djorgovski 1989; Franx & Illingworth 1990; Peletier et al. 1990). Such gradients are a result of a galaxy's star formation and metal enrichment history. However, these gradients have been found to behave differently at high and low galactic stellar masses, with a sharp transition being found at $\sim 3.5 \times 10^{10}\,M_\odot$ (Spolaor et al. 2009). The relationships found at different masses are shown in Fig. 1.7, with the low mass ETGs forming a tight

[2]These are elements whose most abundant isotopes are integer multiples of four, which is the mass of the helium nucleus.

[3]Square brackets denote taking the logarithm of the mass ratio of the two elements normalised to the solar abundance of those elements.

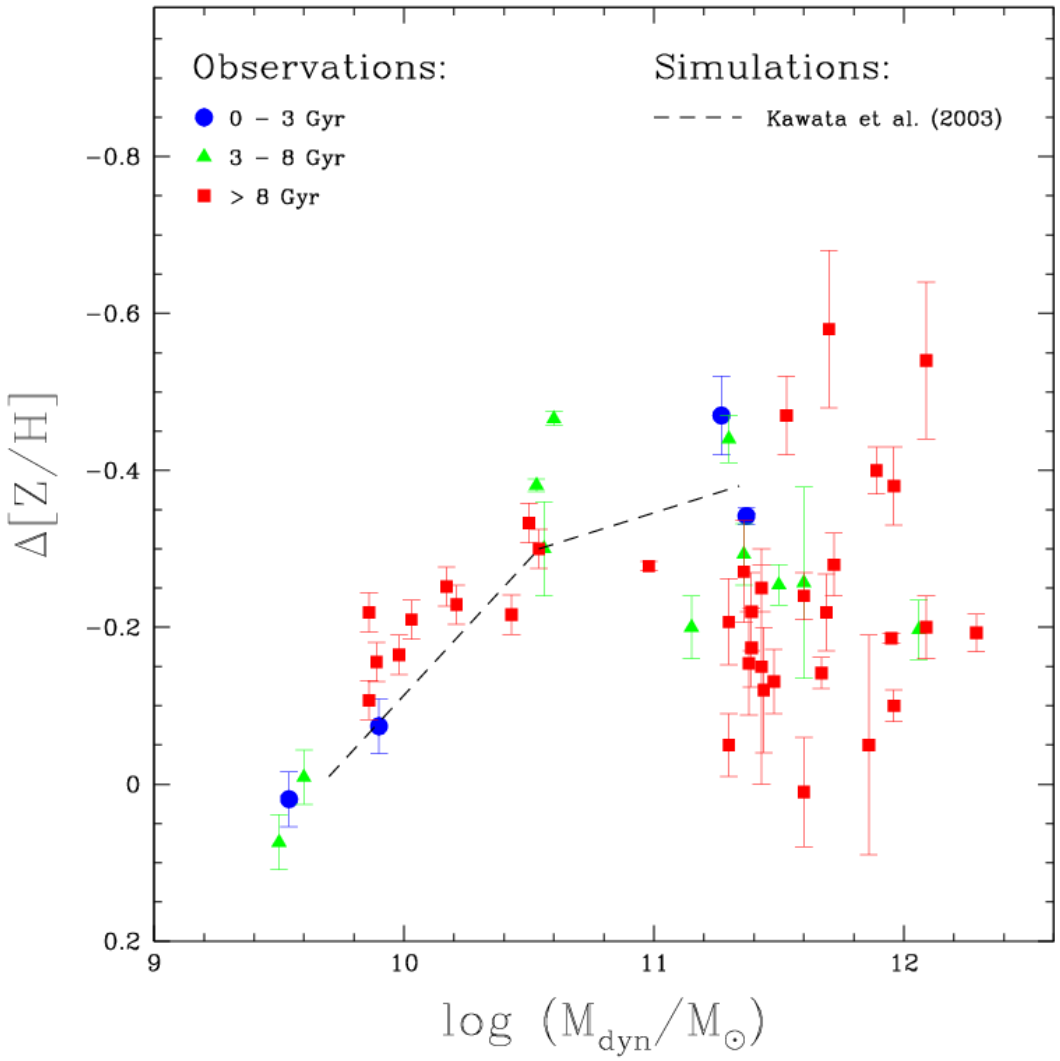

Figure 1.7: Spolaor et al. (2009) show the metallicity gradients Δ[Z/H] as a function of galactic dynamical mass (M_{dyn}) for a sample of 51 ETGs. They code their points by the central age value of the galaxies as described in the legend. They also show the mass-metallicity gradient predictions from the dissipative collapse models of Kawata & Gibson (2003) as a dashed line.

relation whereupon metallicity gradients become steeper with increasing mass and positive at the very low mass end. Above the so-called mass transition point, Spolaor et al. (2009) find a broad scatter with a clear downturn.

Fig. 1.7 includes the chemodynamical model from Kawata & Gibson (2003), which suggests an early star-forming collapse as the main mechanism for the formation of low-mass galaxies, and this model is consistent with the lower mass trend observed in this plot. The model does not account for the scatter observed at higher mass; this is due to the trend being based on only three simulations and therefore they have no true measure of the predicted scatter.

Theories for the formation of metallicity gradients require stars to form from metal-poor gas and then continue forming from self-enriched gas which flows into the galactic centre (Larson 1974; Pipino et al. 2008). Alternatively metal gradients might be created by changing the star formation rate as a function of galactic radius, thereby neglecting any gas or stellar flows. Merger events (as well as orbital mixing (White 1980) and the aging of the stellar population) are likely to flatten such radial gradients (Kobayashi 2004; Di Matteo et al. 2009); the differences in the properties of these merger events are thought to be the cause of the large scatter in high mass ETGs in the mass-metallicity relation. Such work is in support of hierarchical merging wherein ETGs are the product of merging events.

1.1.3 Accurate Selection of Early-Type Galaxies

Working with samples of ETGs is a daunting task, not the least of which is creating a sample of ETGs which is complete, unbiased and most importantly, uncontaminated by any LTGs. Creating such a sample from a large catalogue of mixed galaxies may require using proxies for galaxy morphology (e.g. Kaviraj 2010). This is advantageous because of the ease of cutting down catalogues to smaller samples by removing galaxies that don't conform to the typical ETG parameter

space. Hence proxies can be very efficient.

One commonly used proxy bases morphological selection on colour, as ETGs have been shown to dominate the red sequence region of the clear bimodality present in an optical CMR (Driver et al. 2006; Kaviraj 2010). However, Haines et al. (2008) argue that red optical colours do not fully correspond to the old stellar populations that reside in elliptical galaxies, but can be caused by high levels of dust extinction caused by starbursts in spiral galaxies. Therefore the RS is strongly contaminated by dust-reddened late-type systems. In addition to this, as optical colours reflect the luminosity-weighted mean age of a stellar population, they are sensitive to low levels of continuous SF. Hence if the star formation rate per stellar mass drops below a particular threshold, the optical colours will become uniformly red. Salim & Rich (2010) protest that these reasons are why photometry cannot distinguish a truly passive galaxy from one that has a young stellar population, whilst the solution presented by Haines et al. (2008) advocates using UV-optical colours[4] in the CMR to separate passive from active galaxies.

An alternative popular criterion for selection is that of Sérsic index (n). The single Sérsic profile is fully described in Section 2.3.3 of Chapter 2, and described by Eq. 2.6. The variation of this profile with radius is shown for a range of Sérsic indices in Fig. 1.8. Blanton et al. (2003) and Driver et al. (2006) state there is a clear bimodality for galaxies based on $\log(n)$, such that Sérsic index divides galaxies into red, high surface brightness, luminous galaxies (i.e. bulge-dominated ETGs) and blue, low surface brightness, lower luminosity galaxies (disk-dominated LTGs). One particular issue with this criterion that seems to stand out is that not all galaxies are so readily profiled by a single Sérsic or even a combined Sérsic and exponential model (Driver et al. 2006) - therefore for the Sérsic index to be used as a proxy the goodness-of-fit required from the profile fitting has to be high.

[4]UV-optical colours are an order of magnitude more sensitive to the ages of a stellar population.

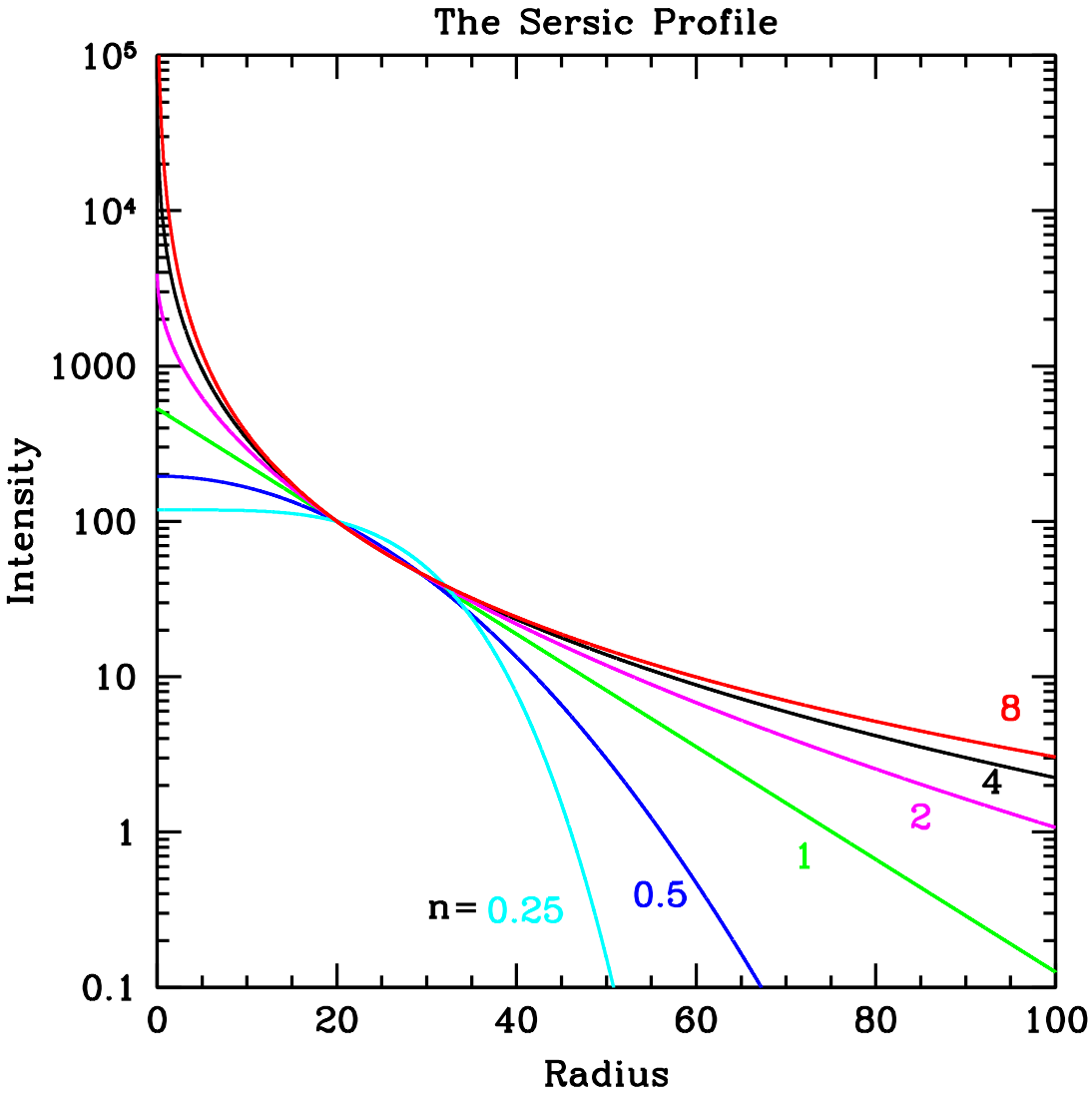

Figure 1.8: Peng et al. (2010) show the variation of the Sérsic model over radius for different Sérsic indices. Most notable are n=1 and n=4, which represent the exponential profile of a disk and the de Vaucouleurs profile of a bulge respectively.

Another parameter which has gained popularity in published sample selections is concentration index. This can be defined as the ratio of the Petrosian 90 radius (radius in which 90% of the galaxy's brightness is contained) to the Petrosian 50 radius (Blanton et al. 2003; see Chapter 2 for a full description of how this is derived); this is used based on the assumption that Es have more strongly peaked light profiles than spirals (e.g. Kaviraj 2010). Salim & Rich (2010) also use this criterion whilst Driver et al. (2006) argue that it is too susceptible to short-term transitory effects such as minor mergers, interactions or episodic starbursts to be used accurately.

There are other morphological proxies that have been used in the past which have similar success rates to the aforementioned systems; these include the CAS system (Conselice 2006) and the Gini coefficient. Bulge-to-total ratios are also commonly used in low redshift samples, but are restricted to these regions as detailed bulge-disk decompositions need to be carried out on the photometry to obtain these ratios (Lackner & Gunn 2012). Heuristic algorithms also exist for separating out morphologies - whilst these are overall quite successful, they need training samples to be provided to run and can be computationally quite expensive (e.g. Huertas-Company et al. 2011).

Recent work is leaning towards the use of multiple proxies for separating out galactic morphologies. Kelvin et al. (2014) use a combination of both optical colour and Sérsic index to divide galaxies into ETGs and LTGs, whilst Grootes et al. (2013) advocate a more conservative debiased probabilistic method with UV-optical colour and Sérsic index to pick out spiral galaxies.

Although there are many advantages associated with the use of morphological proxies, it should be noted that one of the preferred methods of sampling ETGs is to use direct visual inspection of the galaxy images (Kaviraj 2010), which is unfortunately subjective (Driver et al. 2006) and time-consuming for large samples.

It also requires high-quality and high-resolution imaging.

1.2 Dust in the ETG Interstellar Medium

In the past, lack of detections in 21cm line emission (e.g. Gallagher 1972) and CO molecular lines (e.g. Bregman et al. 1992) in ETG spectra was assumed to indicate a lack of neutral and molecular gas and by implication, cold dust. However, dust lanes and patches were then observed via optical extinction studies of some elliptical galaxies (Sadler & Gerhard 1985; Goudfrooij et al. 1994). Developments in FIR and sub-mm based observations have supported these claims, showing that a significant fraction of ETGs contain cold dust within their interstellar medium (ISM; Knapp et al. 1989; Goudfrooij & de Jong 1995). Some of these were subsequently shown to be spurious detections (see Bregman et al. 1998) but many remained. Studies at different wavelengths have shown this ISM to be complex: radio data at 21 cm led to the detection and mapping of cold neutral gas in some ellipticals (e.g. Morganti et al. 2006, and references therein); FIR and sub-mm data revealed significant cold dust masses (Leeuw et al. 2004; Savoy et al. 2009); X-ray observations showed that a substantial number of ellipticals have a hot ($\approx$ few $\times 10^6$ K) plasma component (e.g. Kim et al. 1992; Mulchaey & Jeltema 2010; Boroson et al. 2011), particularly in giant ellipticals (Kormendy et al. 2009) and older ellipticals (Sansom et al. 2006).

In order to fully understand the presence of dust in elliptical systems, the different proportions of dust in the multiple galaxy types should be considered, as well as the potential origins of this dust and possible mechanisms which can cause this dust to be moved or destroyed.

To accurately constrain dust properties within galaxies, frequencies in the radio to FIR should be observed. Within this range, dust is commonly detected by observing in the sub-mm regime because it is heated to emission by mechanisms such

as Active Galactic Nuclei (AGN), the interstellar radiation field, tidal heating or hot X-ray haloes (e.g. Gomez et al. 2010). Dust emission at shorter wavelengths is less well constrained: emission in the MIR is associated with warmer dust components in (for example) stellar birth clouds, but can simultaneously be dominated by emission from old stellar populations.

1.2.1 Dust Grain Composition

Studies have shown that grains within a galaxy's diffuse ISM are mainly composed of silicates, graphites and polycyclic aromatic hydrocarbons (PAHs). The presence of silicates was made apparent by two features in the MIR - a broad feature at $9.7\,\mu$m and a weaker feature at $\sim 19\,\mu$m. The shorter wavelength feature was of great interest because it was detected in both absorption and emission, and thought to be associated with reddened stars, O-rich circumstellar envelopes, HII regions, and galactic nuclei (Gillett et al. 1975a,b; Merrill & Stein 1976; Roche & Aitken 1984; Roche et al. 1991). Silicates have a continuous range of sizes up to $\sim 0.3\,\mu$m and own a tetrahedral shape with a negative charge.

Graphites were first detected when spectra of reddened stars were found to contain a strong absorption feature at 2175 Å in the UV; graphites associated with this feature are thought to be quite small with sizes of $<0.02\,\mu$m (Stecher 1965; Stecher & Donn 1965), and are constructed of regular stacks of platelets formed from planar groups of carbon rings. However in current models of dust grain distributions, graphites are no longer considered to be the main contributor to this absorption line (e.g. Weingartner & Draine 2001).

PAHs are large molecules (or small particles) composed of aromatic rings[5] with a common probability distribution of the electron density around the central carbon and external hydrogen atoms. The hydrogen atoms are linked in normal

[5] An aromatic ring is formed by the π orbitals of carbon.

sigma orbitals - a strong, covalent bond. Examples of PAHs are the well-known benzene (single-ring) and pyrene (four-ringed) molecules. While these PAHs are known to be constructed of benzene rings, the constituents of the PAH class are yet to be fully understood. This is because benzene rings have characteristic vibrational modes[6] which are excited by different temperatures, leading to emission features in the NIR/MIR (including but not limited to lines at 3.29, 6.2, 7.7, 8.6, 11.3 and 12.7 μm). However, it is unclear how many benzene rings make up these PAHs, as they will all result in the same emission features. Future work may lead to distinguishing these molecules, based on higher vibration modes being detected in the FIR/sub-mm; this is not currently possible with the data available.

The range of sizes these different grain types are assumed to exhibit are displayed in Fig. 1.9, where the dust grain composition is based on the Milky Way model of Weingartner & Draine (2001). PAHs and graphites (carbonaceous materials) are grouped together in this model, and display a range of characteristics: the carbonaceous materials have a double log-normal distribution for smaller grains[7] and a power-law for larger grains; the silicates also have a power-law. Both power-laws have a cut-off at large radii, with a smoothing function.

1.2.2 Effects of Dust

How does the presence of dust manifest itself? Stellar spectra of galaxies are modified by the dust grain absorption and scattering of short wavelength (UV, optical and NIR) photons and their re-emission at longer wavelengths (FIR and sub-mm). The former processes are defined as stellar extinction, and result in a reduction in the spatially integrated luminosity at a fixed UV/optical wavelength.

[6]Vibrational modes are caused by stretching modes of Carbon-Hydrogen and Carbon-Carbon bonds.

[7]PAHs are described by the small radius log-normal distribution and the smaller graphites are described by the larger radius log-normal distribution.

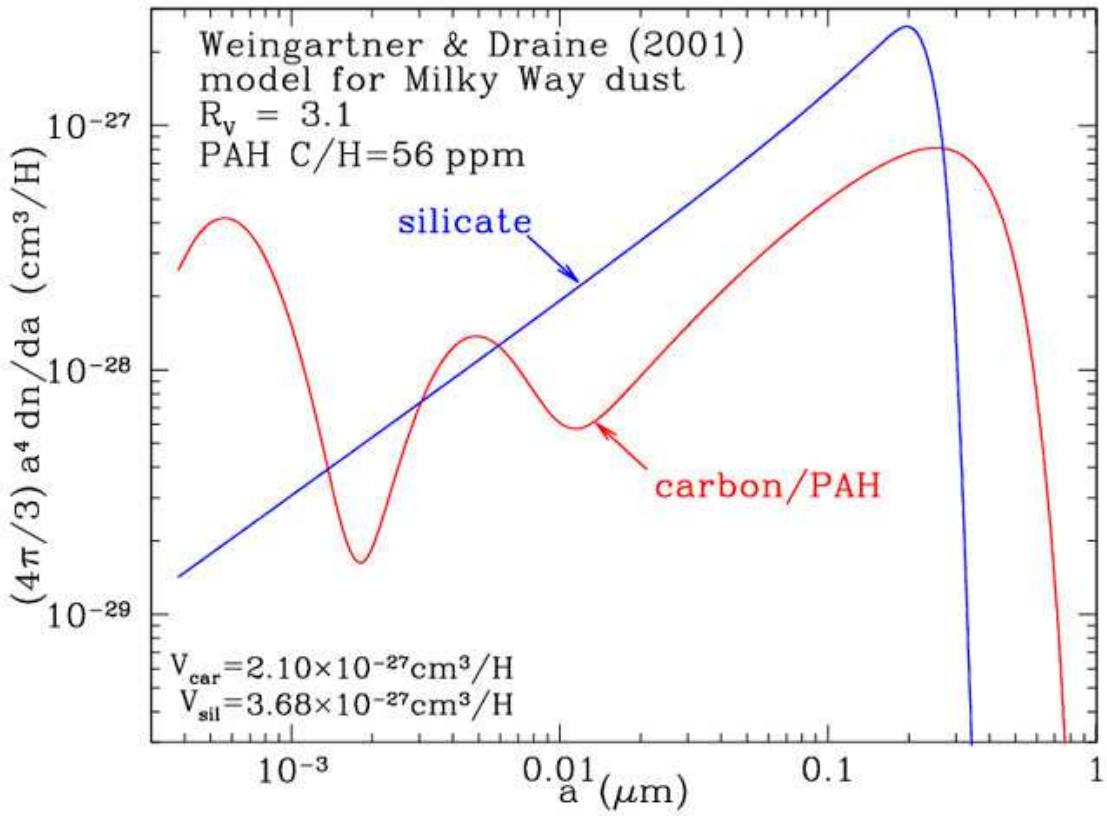

Figure 1.9: Weingartner & Draine (2001) show the distribution of grain sizes for their dust model of the Milky Way. Silicates and carbonates (PAHs and graphites) are plotted as blue and red solid lines respectively.

The subsequent emission by dust particles at longer wavelengths is often used as a tracer for current SFRs in galaxies, based on the assumption that young massive stars are the main source of heating of this dust (de Jong et al. 1985; Helou et al. 1985; Boulanger & Perault 1988) and the UV radiation from young stars is strongly attenuated by the dust (e.g. Savage 1975).

Extinction

Extinction is an effect that occurs when electromagnetic radiation travels through a medium containing small particles (dust grains). The radiation interacts with the particles and suffers a loss in intensity due to the two physical processes of absorption and scattering. In the former, a dust particle absorbs the light photon and this is converted into the internal energy of the particle which is subsequently heated. In the latter, the photon is scattered away from the original path. Extinction causes the reddening effect in starlight, as shorter wavelength photons are preferentially absorbed or scattered, leaving an excess of longer wavelength (redder) photons in the line of sight.

The reduction in intensity I of starlight resulting from extinction in a column of length dL is described as

$$\frac{dI}{I} = -n_{\rm d} C_{\rm ext} dL, \tag{1.2}$$

where $n_{\rm d}$ is the grain number density per unit volume and $\rm C_{ext}$ is the extinction cross-section. This can be integrated over the entire path of extinction to give

$$I = I_0 e^{-\tau}, \tag{1.3}$$

where $\rm I_0$ is the original intensity at the beginning of the cylinder and τ is the optical depth of the region.

The efficiency of extinction can be determined as the sum of the efficiency factors for absorption and scattering respectively:

$$Q_{ext} = Q_{abs} + Q_{sca}. \tag{1.4}$$

Further details on the derivation and calculation of these efficiency factors can be found in Whittet (1992). In brief, they are related to each other by the albedo α, which at its lower and upper limits of 0 and 1 represents perfect absorbers and perfect insulators respectively:

$$Q_{scat} = \alpha Q_{ext} \tag{1.5}$$

$$Q_{abs} = 1 - \alpha Q_{ext}. \tag{1.6}$$

Attenuation

The process of attenuation gives a physical meaning to the more theoretical idea of extinction. By definition, dust attenuation is a property of an extended distribution of light (i.e. a galaxy), whereas extinction describes absorption and scattering of light from a single point source such as a star, and is distinguished by line-of-sight observations. Attenuation effects vary for each galaxy depending on its distribution of stars and dust, as well as its particular dust characteristics and its orientation (see Popescu et al. (2011) and references therein).

Dust attenuation can be viewed directly as dark dust lanes in optical images of spiral galaxies, where the dense regions of dust grains are obstructing the passage of light and thereby distorting our view of the stellar population. This is a strong effect in all optical and even NIR bands for spiral systems (Driver et al. 2007; Shao et al. 2007; Choi et al. 2007) and as such results in galaxies' observed stellar profiles appearing less centrally concentrated, scale-lengths being overestimated and central surface brightnesses being artificially dimmed (Tuffs et al. 2004). Therefore

corrections need to be made to these extracted photometric properties. Photometric corrections are subject to large uncertainties due to the complex geometry of dust, as well as the range of interactions between the grains and different stellar populations of different ages (see Pastrav et al. (2013) for an analysis of such corrections).

Although the consequences of attenuation are apparent from the dust lanes in disks of spirals, bulges have also been shown to be affected as they are viewed through the dust layer of the disk, and therefore even more pronounced distortions are expected (Tuffs et al. 2004). It should be noted that the amount of UV and optical attenuation can be determined by the mass fractions of dust in clumps and diffuse structures (Kuchinski et al. 1998; Bianchi et al. 2000; Tuffs et al. 2004), and it is possible that these effects exist even in low opacity systems such as elliptical galaxies.

Stochastic Heating

Different dust grain distributions are present in a wide range of environments within a galaxy's ISM, but due to a lack of high resolution spectroscopy for galaxies outside the Local Group, details of these distributions and their respective grain properties (such as excitation temperatures) are still relatively unknown. Therefore properties of the diffuse distribution of grains in these galaxies need to be considered and studied as a whole, since the individual populations cannot be resolved.

Dust models should therefore incorporate stochastic heating to fully account for the temperature fluctuations of dust grains throughout a galaxy's ISM. Grains in very dense regions will be continuously bombarded by photons, especially those

grains in Photo-dissociation Regions (PDRs), which are in close proximity to additional UV photons emitted from young stars. These grains will exhibit a characteristic temperature which will be essentially constant; this temperature will be related to the dominant population large grains which do not experience large temperature fluctuations. However small grains residing in regions where the radiation field density is very low will experience very few interactions with photons, and therefore the absorption of photons by these grains is very rare. These grains will experience a rise in temperature by a single photon (possibly as high as 1000 K; Sellgren 1984). However, if the cooling timescale of the grain is less than the photon bombardment timescale, then the grain will cool down again. Such fluctuations in temperature will lead to a broad temperature distribution for the dust which is stochastically heated, peaking at low temperatures but extending to much higher values (Dwek 1986).

Larger dust grains are less susceptible to stochastic heating, as absorption of more than a single photon is required to increase their temperatures. PAHs are most affected by stochastic heating, as their small sizes lead to large temperature fluctuations (Whittet 1992). The modelled distributions of different grain compositions and sizes are shown in Fig. 1.10. The equilibrium temperature of larger grains is highlighted as delta function distributions (most notably in the central panels), whereas the smaller grains exhibit much broader temperature distributions.

Stochastic heating is not merely an effect of photon radiation heating, but can also affect the heating of dust particles when they collide with electrons and ions in the plasma in a hot, X-ray emitting medium. Once again temperature fluctuations are more apparent when the density of the plasma is much lower and electron interaction timescales are longer (Dwek 1986).

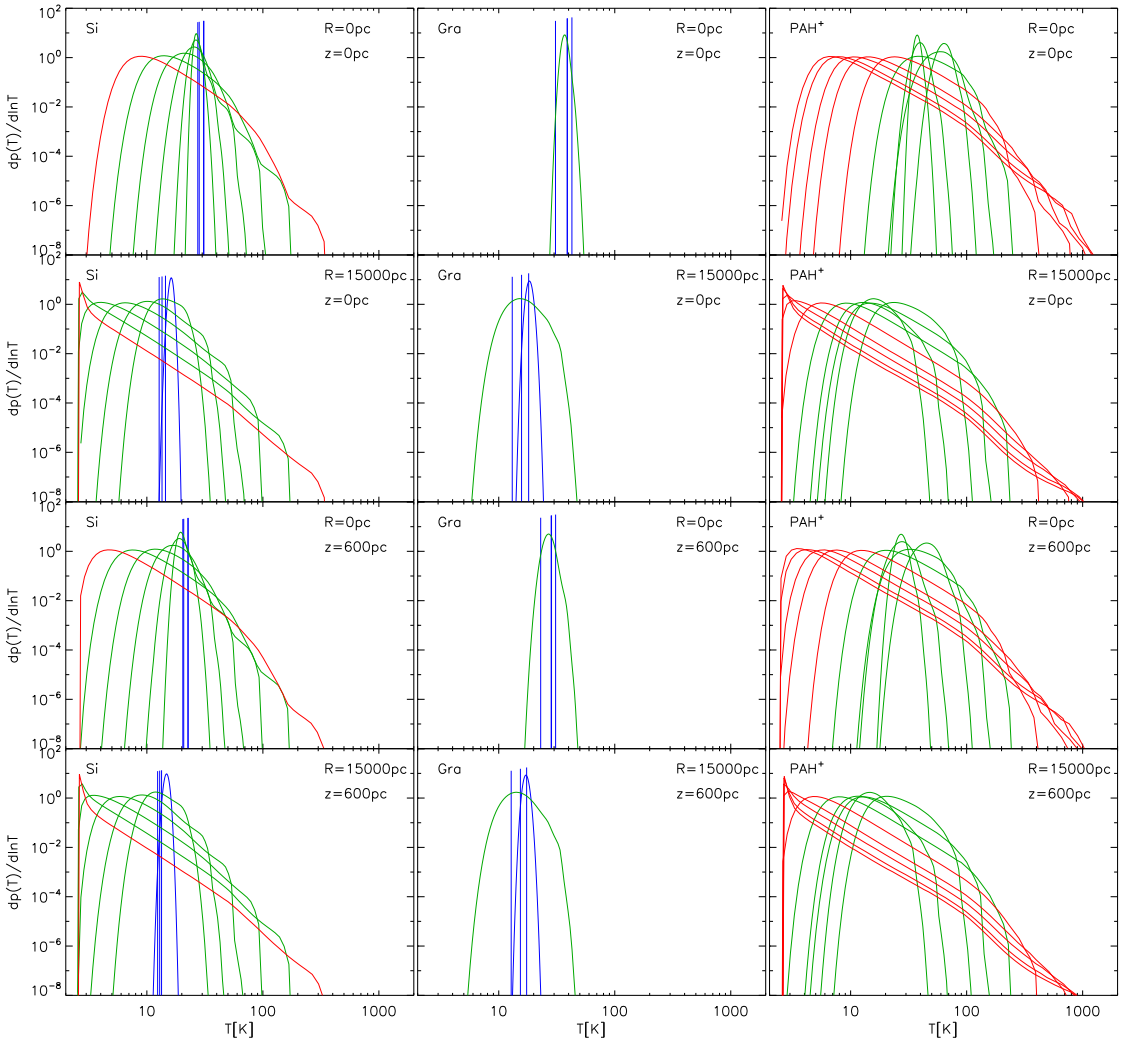

Figure 1.10: Popescu et al. (2011) show the dust grain temperature distributions for grains of different sizes (different curves in each panel) and compositions (silicates, graphites and PAHs from left to right), based on diffuse heating for their best fit model of a spiral galaxy. Curve colours represent different grain sizes: red is for the smallest grains ($a \leq 0.001\,\mu m$), green for intermediate sizes ($0.001\,\mu m < a \leq 0.01\,\mu m$), and blue for the largest grains ($a > 0.01\,\mu m$). From top to bottom, the panels represent grains at different positions in the galaxy.

Dust Emission

Emission of absorbed radiation at MIR to sub-mm wavelengths is the process by which dust grains can be directly observed. These observations are a necessary step in the study of galactic energy balance, as nearly half of the bolometric luminosity in the sky background is channeled through IR emission (see review by Hauser & Dwek 2001).

The process by which photons are absorbed and re-emitted by dust grains can be quantified using

$$\int_0^\infty Q_\lambda u_\lambda d\lambda = \frac{4\pi}{c} \int_0^\infty Q_\lambda B_\lambda(T_\mathrm{d}) d\lambda, \tag{1.7}$$

under the assumption that Kirchoff's law ($\mathrm{Q_{abs}}(\lambda)$=$\mathrm{Q_{em}}(\lambda)$) holds for any given wavelength. This way, the balanced absorption and emission factors are renamed as Q_λ, which is a function of the grain density and surface area. Eq. 1.7 shows the balance of the wavelength-dependent energy density (u_λ) absorbed (left-hand side) with the emitted energy density represented by the Planck function (B_λ; right-hand side):

$$B_\lambda = \frac{2hc^2}{\lambda^5} \frac{1}{\left(\mathrm{e}^{\frac{hc}{\lambda k_B T}}\right) - 1}. \tag{1.8}$$

The use of the Planck function to represent the grain-emitted luminosity indicates the significance of the grain temperature within this system. The above subsection on stochastic grain heating indicates the link between dust grain composition, size and their respective temperature distributions. The temperature utilised in the Planck function represents the equilibrium temperature of the dust grain composition as a whole; for classical sized grains in thermal equilibrium with the interstellar radiation field, the peak of the Planck function is located in the FIR with a representative temperature of $\sim$17-21 K (e.g. Schlegel et al. 1998; Dunne & Eales 2001).

1.2.3 Dust Grain Production and Destruction

Clemens et al. (2010) and Dunne et al. (2011) attribute low-to-intermediate asymptotic giant branch stars and Supernovae Ia as potential grain sources, producing dust at similar rates. Baes et al. (2010) maintain that alternative hidden dust sources are young stars deeply embedded in dusty molecular clouds. Neutral atomic gas origins may include accretion from gas-rich companions, gas fallback after possible major merger events, secondary infall and stellar mass loss (e.g.van Gorkom & Schiminovich 1997; Oosterloo et al. 1999; Lucero et al. 2005). Additional origins also include accretion processes from either the inter-galactic medium or intra-cluster medium. Dust and cold gas have been shown to be tightly correlated in galaxies (Knapp 1999), which may indicate similar origins for the two components. This particular correlation is highlighted in Fig. 1.11 for both elliptical and spiral galaxies. Note that the quantities of both cold gas and dust are shown to be lower than quantities within spirals in this plot; additionally the ellipticals show no correlation amongst themselves here.

Dust grains can be destroyed in a process called thermal sputtering, which involves collisions with electrons and ions in the hot, low-density gas emitting X-rays in bright ETGs (Savoy et al. 2009; Clemens et al. 2010). Astration[8] and supernova shocks may also cause intergalactic dust to be destroyed (Jones et al. 1994, 1996), and Draine & Salpeter (1979a) show that diffuse dust may come in contact with the ISM and be eroded in thermal collision with ions, with a destruction timescale of only $\sim 10^{7-8}$ yrs.

[8] Astration is defined as the incorporation of matter into a stellar interior during star formation.

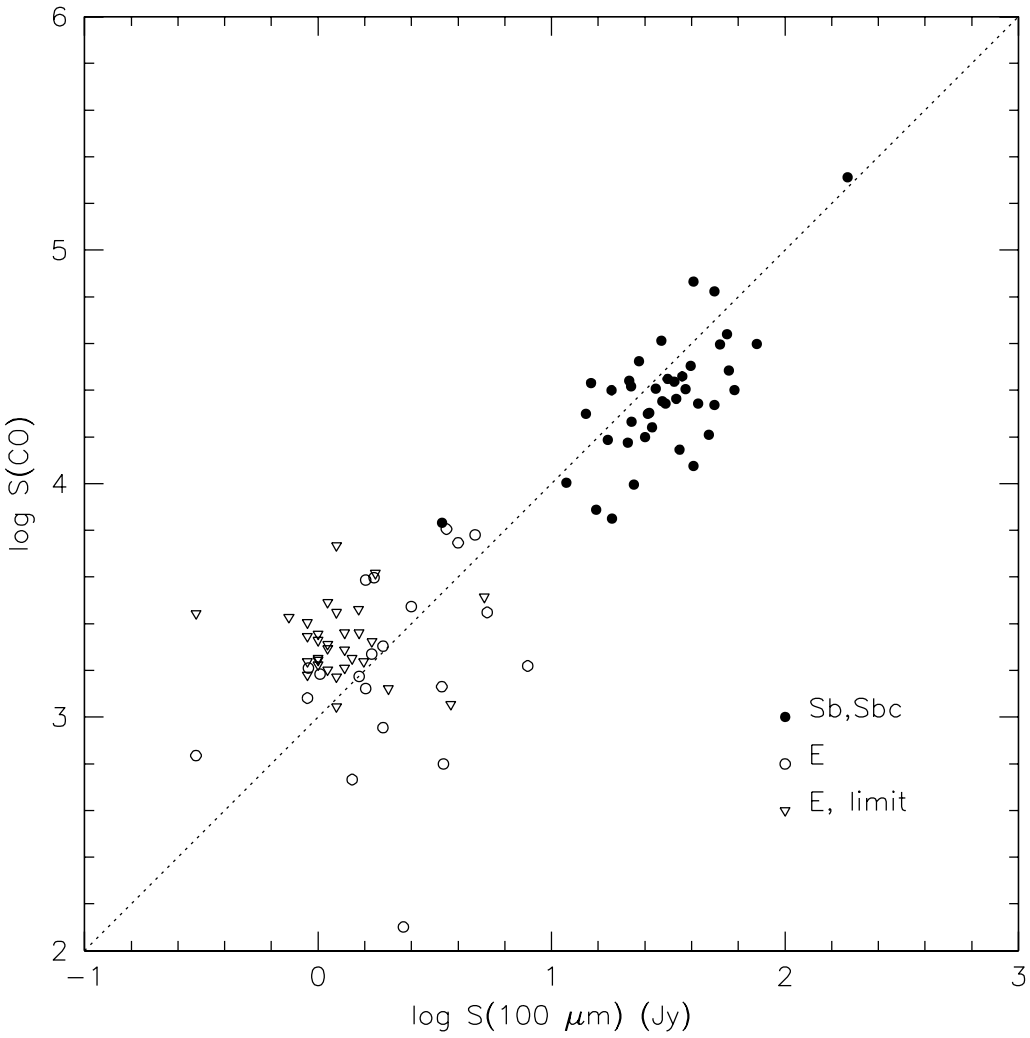

Figure 1.11: Knapp (1999) show CO line fluxes (which serve as a proxy for H_2 gas) and IRAS 100 μm flux densities for their sample of spiral and elliptical galaxies. Note in particular the inverted triangles, which are galaxies that do not have CO detections and are therefore only upper limits.

1.3 *Herschel* Astrophysical TeraHertz Large Area Survey

1.3.1 Consortium Long-Term Aims

The *Herschel*-ATLAS (H-ATLAS) is a survey designed to exploit a wavelength regime (100-500 μm) that up to this point has remained mostly unexplored. Defining sub-mm wavelengths as those between 100 μm$< \lambda <$1 mm (Eales et al. 2010), this consortium aims to fill this gap in our knowledge by using the *Herschel* Space Observatory's SPIRE and PACS instruments to measure the dust content and dust obscured star formation in large numbers of galaxies in the local Universe (Eales et al. 2010).

H-ATLAS is the largest Open-Time key project with *Herschel*, with 600 hours of time allocated during the observatory's lifetime. Relevant science aims named as key projects within H-ATLAS include making the first accurate estimates of the local sub-mm luminosity and dust-mass functions (Amblard et al. 2010; Davies et al. 2010; Baes et al. 2010), investigating how the dust-obscured SF depends on the local and large-scale environment (Serjeant et al. 2010) and how this and the dust content of the Universe have changed over the lifetime of the Universe (Eales et al. 2010). Science papers released for the Science Demonstration Phase (SDP) regions alone have contributed significantly to these aims; Dunne et al. (2011) showed that *Herschel*-detected galaxies as a whole demonstrate evolution in their dust properties: their dust mass and dust-to-stellar mass ratio is shown to increase with redshift. Serjeant et al. (2010) find evidence of downsizing in quasar host galaxy formation: their comoving star formation rates peak at higher redshift for higher luminosity quasars. Moving from galaxy sampling to single galaxies, Baes et al. (2010) find evidence that in the spiral galaxy UGC 4754, there exists large amounts of obscured star formation that contributes little to the optical

extinction. This last result in particular highlights the importance of studying dust in emission rather than in extinction alone.

1.3.2 Instrumentation and Data Reduction

Two of the three instruments on the *Herschel* Space Observatory were used by H-ATLAS. These are the Spectral and Photometric Imaging REceiver (SPIRE; Griffin et al. 2010) and the Photodetector Array Camera and Spectrometer (PACS; Poglitsch et al. 2010).

SPIRE contains a three-band imaging photometer working at 250, 350 and 500 μm with a field-of-view of 4×8 arcminutes and diffraction limited beams of 18″, 25″ and 36″. The primary calibrator for this instrument is Neptune (Griffin et al. 2010).

SPIRE's internal mechanisms are shown as a block diagram in Fig. 1.12. The Focal Plane Unit (FPU) is supported on the *Herschel* optical bench and contains all the cooling mechanisms, three photometer and two spectrometer detector arrays, optics, internal calibrators and thermometers. The detector arrays contain internal bolometers which detect emission at frequencies of 50-200 Hz, and these are further connected to the three SPIRE warm electronic units: the Detector and Control Unit (DCU) which provides the bias and signal conditioning for the arrays and cold electronics, the FPU Control Unit (FCU) which controls the cooler and reads out the FPU thermometers, and the Digital Processing Unit (DPU) which runs the software on-board and exchanges information with the spacecraft.

PACS performs integral-field spectroscopy and imaging in the 60-210 μm wavelength regime, with a photometric field-of-view of 3.5×1.8 arcminutes (Poglitsch et al. 2010). Standard stars are used as the primary calibrators for this camera.

PACS differs from the SPIRE instrument in the sense that the photometer contains a dichroic beam splitter which splits the light into long-wave (red) and

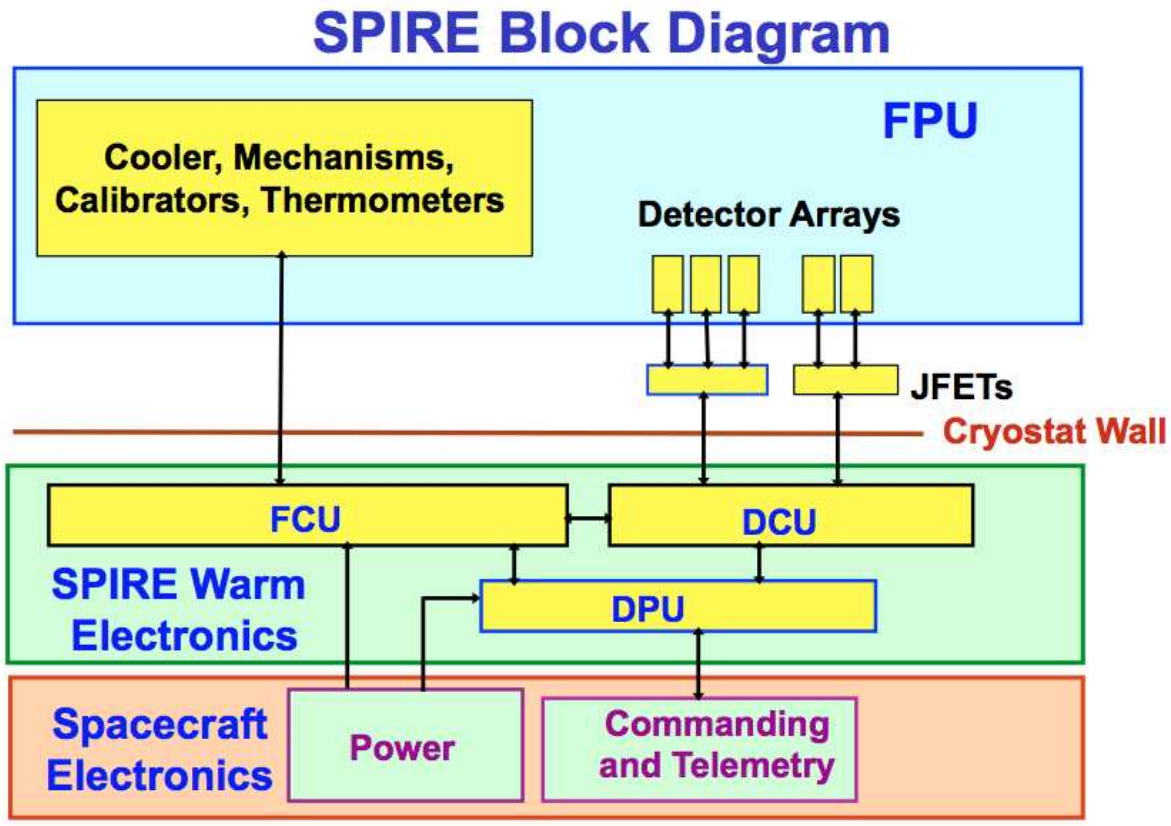

Figure 1.12: The block diagram from Griffin et al. (2010) depicting the internal structure of the SPIRE instrument. Five detector arrays are shown, where three are for the photometer and two are for the spectrometer. Acronyms are as follows: JFET = Junction Field-Effect Transistor, FPU = Focal Plane Unit, FCU = FPU Control Unit, DPU = Digital Processing Unit.

short-wave (blue, green) channels, with a transition wavelength of 130 μm. The red channel has sky-projected pixel sizes (6.4″) twice that of the blue/green channel. The bolometers on PACS are in 4×2 sub-arrays of 16×16 pixels each, and are mounted separately from the surrounding 2 K structure and are kept at an operating temperature of 0.3 K. The cold readout electronics from these bolometers flows first through the back of the focal plane arrays and then flows via ribbon cables to the buffer stage running at 2 K. The multiplexing readout samples each pixel at a rate of 40 Hz (Poglitsch et al. 2010).

The H-ATLAS consortium elected to use the PACS 100 and 160 μm combination of photometric bands due to their sensitivity, and ran the two cameras for all five wavebands in Parallel Mode (i.e. simultaneously; Eales et al. 2010). The regions of sky being surveyed were chosen based on a combination of complementary data available from other groups, and regions which are less affected by dust from the Milky Way Galaxy (Eales et al. 2010). The resultant fields, covering 550 deg^2 (Rigby et al. 2011), are hence:

One field near the Northern Galactic Pole (150 deg^2).

Three 36 deg^2 fields, each corresponding to the equatorial GAMA fields (see Section 1.4).

Two fields covering 250 deg^2 close to the South Galactic Pole.

These fields have FWHM angular resolutions of 9″, 13″, 18″, 25″ and 35″ at 100, 160, 250, 350 and 500 μm respectively, with map pixels of 2.5″, 5″, 5″, 10″ and 10″ in respective sizes and associated 5σ point source flux limits of 132, 126, 32, 36 and 45 mJy (Eales et al. 2010; Rigby et al. 2011).

1.3.3 Current Data

Whilst currently only the Science Demonstration Phase (SDP; covering 16 square degrees centred on 9 hrs 5 mins, +0 deg 30 mins) has been made available to the public, the full suite of H-ATLAS Phase 1 catalogues are in use by the consortium itself.

Catalogues for H-ATLAS were created from maps as described in Pascale et al. (2011) and Ibar et al. (2010). Sources extracted from these maps had to have emission greater than 5σ in any of the 3 SPIRE wavebands, described in detail for the SDP in Rigby et al. (2011). A more extensive description of the Phase 1 dataset will be given by Valiante et al. (in prep). A description of the likelihood-ratio analysis performed to identify robust counterparts to the sub-mm selected sources from the SDSS r band matched catalogue can be found in Smith et al. (2011). This uses both positional and photometric information of both individual sources and of the population in general to determine the reliability of an association between two sources. PACS flux densities are then measured by placing circular apertures at the SPIRE positions. For further descriptions of these methods, refer to Rigby et al. (2011).

1.3.4 Dusty ETGs with *Herschel*

FIR and sub-mm studies described in Section 1.2 have now been superseded by the higher resolution and sensitivity of the *Herschel* Space Observatory. *Herschel* SPIRE and PACS data are being used to examine more statistically representative samples of ETGs. Investigations of a volume-limited sample of 62 ETGs, largely in the Virgo Cluster, with the *Herschel* Reference Survey (HRS), has revealed that some early-types contain low levels of cool dust with temperatures comparable to those of LTGs (Smith et al. 2012). Further work with the HeViCs project, also on Virgo cluster ETGs, has identified a dependence of dust temperature on stellar

mass and on the average B-band surface brightness within an ETG's effective radius (di Serego Alighieri et al. 2013). Nearby galaxies have also been examined in the KINGFISH project, with ten ETGs revealing the possibility of ongoing star formation contributing to the dust heating, as well as heating from the radiation field associated with older stars (Skibba et al. 2011).

In the local Universe, H-ATLAS provides the opportunity to work with larger samples. Rowlands et al. (2012) used the SDP data to show that 42 detected ETGs (5.5% of luminous ETGs) contain as much dust as some spirals, and Bourne et al. (2012) used stacking of GAMA sources in H-ATLAS sub-mm imaging to examine the properties of red and blue GAMA galaxies. This thesis and associated publications (Agius et al. 2013, hereafter A13) progress beyond these studies with much larger samples of sub-mm detected ETGs.

1.4 Galaxy and Mass Assembly

1.4.1 Consortium Long-Term Aims

The GAMA[9] survey is a low-to-intermediate redshift, wide-area, multi-wavelength, spectroscopic and photometric, international galaxy search (Driver et al. 2009). The long-term aim of the survey is to study structure on scales of 1 kpc to 1 Mpc by building up a uniform galaxy database to deeper redshifts, fainter flux levels and higher spatial resolutions than other local surveys, which are used to augment the data[10] (Driver et al. 2011). Technological objectives are to improve spectroscopic efficiency, which will allow single surveys to comprehensively sample local low-mass galaxies and intermediate redshift high-mass systems. GAMA also seeks to improve the spatial resolution, allowing galaxies to be deconstructed into multiple features such as bars, bulges and disks, and provide increased wavelength coverage

[9] http://www.gama-survey.org.

[10] e.g. 2 Degree Field Galaxy Redshift Survey, Millenium Galaxy Catalogue.

of these systems.

These technological advancements all contribute towards the key science objectives chosen for GAMA. These include improving the community's understanding of galaxy structure using this high resolution data, improving data coverage of dust attenuation over a range of galaxy environments and morphologies, and augmenting the survey with improved radio data to probe the HI properties of galaxies (Driver et al. 2011). GAMA's contribution of multi-wavelength data for such a large catalogue of galaxies makes all of these objectives achievable (Driver et al. 2009).

1.4.2 Instrumentation and Data Reduction

The GAMA consortium is working to build up a comprehensive database of both spectroscopic and photometric multi-wavelength data. The spectroscopic element of the campaign is currently in progress collecting optical (3750-8850 Å) spectra with the AAOmega spectrograph (Saunders et al. 2004; Smith et al. 2004; Sharp et al. 2006) on the 3.9 m Anglo-Australian Telescope (AAT, Siding Spring Observatory, NSW, Australia), and is augmented by the Sloan Digital Sky Survey, the 2dF Galaxy Redshift Survey and the Millenium Galaxy Catalogue. The photometric side is being built up by utilising public surveys, GAMA's own campaigns and associations with other surveys. The following list gives a brief summary of the key telescopes and associated surveys contributing to the GAMA imaging database, with links to their websites for further information.

- Public Surveys
  - *Sloan* Digital Sky Survey [11]
  - *UK InfraRed Telescope*: UKIDSS-LAS [12]

[11] http://www.sdss.org/

[12] http://www.ukidss.org/

- GAMA Campaigns
  - *GALEX*-GAMA [13]
  - *Giant Metrewave Radio Telescope (GMRT)* [14]
- GAMA Associations
  - *VLT Survey Telescope*: KIDS [15]
  - *VISTA*: VIKING [16]
  - *Canada France Hawaii Telescope*: CFHTLenS [17]
  - *Herschel*: H-ATLAS [18]
  - *Australian Square Kilometre Array Pathfinder*: ASKAP-DINGO [19]
  - *X-Ray Multi-Mirror Mission*: XMM-XLL [20]
  - *Wide field Infrared Survey Explorer* (WISE) [21]

At this point in time, GAMA is utilising the SDSS seventh data release (DR7), which signified the end of the SDSS II phase. SDSS II has compiled spectroscopy and imaging over 9,380 square degrees (Abazajian et al. 2009) and is now complete over a large conterminous area of the Northern Galactic Cap. In total SDSS-DR7 has presented spectra for 930,000 galaxies (Abazajian et al. 2009; Hill et al. 2011), and SDSS photometry was used to help construct the GAMA target photometric catalogue (Driver et al. 2011). Hence the output catalogues presented by GAMA

[13] http://www.mpi-hd.mpg.de/galex-gama/
[14] http://gmrt.ncra.tifr.res.in/
[15] http://www.astro-wise.org/projects/KIDS/
[16] http://www.eso.org/sci/observing/policies/PublicSurveys/sciencePublicSurveys.html#VISTA
[17] http://www.cfhtlens.org/test/astronomers/content-suitable-astronomers
[18] http://www.h-atlas.org/
[19] http://internal.physics.uwa.edu.au/m̃meyer/dingo/welcome.html
[20] http://irfu.cea.fr/en/Phocea/Vie_des_labos/Ast/ast_technique.php?id_ast=3015
[21] http://wise.ssl.berkeley.edu/

are a combination of SDSS spectroscopic and imaging galaxies, including pre-existing redshifts, and galaxies being targeted by the AAT and redshifted by the GAMA team using the Fortran based RUNZ software (Driver et al. 2011).

1.4.3 Current Data

The GAMA database currently provides optical, UV, near and mid-IR photometry, as well as optical spectra, in a series of Data Management Units (DMUs), which are supplemented by additional work done by team members to create useful parameters from this data. Table 1.1 describes the key DMUs and the properties derived within these units, all of which are being used in this thesis.

Additional details on the physics being utilised to construct the parameters in some of these DMUs are given in later chapters, when the parameters themselves are first used.

1.4.4 GAMA Data Releases

At this point in time the GAMA team have publicly released two major sets of data: GAMA I and GAMA II. The first represents the original survey region of three equatorial regions of 48 square degrees each, centred at right ascension 9, 12 and 14.5 hours over the celestial equator. These fields have a survey depth of r_{Pet} <19.4, with an increased depth of 19.8 in the 12 hour field. GAMA I spectra were taken over 68 nights at the AAT, with 112,000 new galaxy spectra and redshifts initially obtained. Therefore by the end of 2010 the original survey was complete with a total of (including ancillary data) >130,000 redshifts collected.

GAMA II proposals to expand the survey were subsequently accepted, with the three equatorial fields increased in size (56 deg^2), depth (r_{Pet} <19.8) and region (two southern fields were included in the observations), resulting in a total area coverage of 280 square degrees for the survey. At time of publication, Hopkins et al.

Data Management Unit	**Parameter**	**Waveband**	**Reference**
Input Catalogue	GAMA CATAID†	-	Hill et al. (2011)
	SDSS OBJID	-	Driver et al. (2011)
	RA and Dec (J2000)	-	
	Petrosian Radius	r	
	Petrosian Magnitudes	$ugriz$	
Spectroscopy	Redshift	-	Hopkins et al. (2013)‡
	Redshift Quality	-	
Sérsic Photometry	Sérsic Index	$ugrizYJHK$	Kelvin et al. (2012)
	Effective Radius	$ugrizYJHK$	
	Apparent Magnitude	$ugrizYJHK$	
	Ellipticity	$ugrizYJHK$	
Stellar Masses	Absolute Magnitude	$ugrizYJHK$	Taylor et al. (2011)
(rest-frame)	Colour	$u-r$, $g-i$	
	Stellar Mass	-	
GALEX Photometry	Apparent Magnitude	FUV, NUV	Seibert et al. (2012)
WISE Photometry	Absolute Magnitude	W1-W4	Cluver et al. (2014)
Environment Measures	Surface Density	-	Brough et al. (2013)
	Comoving Distance	-	
K-corrections	K-corrections	FUV to K	Blanton & Roweis (2007)
Galaxy Groups	Group ID	-	Robotham et al. (2011)
	Group Multiplicity	-	

† GAMA CATAID refers to the catalogue index reference number, which is uniquely assigned to every GAMA galaxy.

‡ Note that the author of this thesis has contributed to the work done in calculating these redshifts, and is listed as one of the co-authors in this work.

Table 1.1: A summary of the parameters utilised throughout this thesis and their associated DMUs. Column 1 describes the formal name of the Catalogue within the DMU, Column 2 gives the relevant parameters associated with those catalogues, Column 3 gives the waveband the parameters are given in (where relevant) and Column 4 lists the appropriate reference describing the building of the associated DMUs.

(2013) boast a total of 215,458 redshifts collected by the survey with qualities (see Driver et al. 2011) considered to be good enough to do science with.

Scientific motivation, data processing and catalogue construction for GAMA I is fully described in Driver et al. (2009) and Driver et al. (2011); the latter includes full details on area of sky being surveyed, the data reduction and the details and quality control of the redshifting process. The photometric analysis is fully described by Hill et al. (2011).

The spectroscopic target selection for the GAMA survey is discussed in detail in Baldry et al. (2010), with emphasis on the overlap with completed and ongoing redshift surveys which are incorporated into the catalogues. The star-galaxy separation being used by GAMA is also described in full detail and current results at the time (79,599 unique redshifts in the first two years) are given. This paper has now been superseded by Hopkins et al. (2013), which details the full spectroscopic reduction and analysis completed by the team up to the year 2012.

1.5 Thesis Layout

This section will give a brief description of the layout of the rest of the thesis. Chapter 2 describes the studies carried out on various morphological proxies using a series of control samples which have been visually classified. These studies are motivated by the need to build up samples of ETGs which are complete, unbiased and uncontaminated.

Chapter 3 takes samples of ETGs which have been divided into those which have sub-mm detections with H-ATLAS ($SubS$) and those which are undetected and form the control sample ($OptS$). This chapter describes the work done on comparing the intrinsic and morphological properties of these galaxies, as well as their environments and dust properties. The latter set of properties are explored by fitting modified, single-temperature Planck functions to the H-ATLAS data and

studying the resulting cold dust temperatures and dust masses.

Chapter 4 investigates further properties of these sub-mm detected galaxies by fitting their panchromatic fluxes with more sophisticated, energy balance spectral energy distributions. These properties include ages of the ETGs, their star formation and specific star formation rates, as well as providing secondary results for dust masses and temperatures. Furthermore, the ETGs are compared with sub-mm detected ETGs in the local universe in an effort to understand differences in their physical makeup.

The final project in this thesis is described in Chapter 5, where geometrical distributions of dust in ETGs are explored in some case studies. This work requires both radiative transfer models and infrared/sub-mm SED fitting which can account for different dust heating mechanisms.

The thesis is concluded with a discussion (Chapter 6) on how current large samples could be used to assess predictions from different formation and evolution scenarios for ETGs, as well as some considerations on what future directions of study are available for dusty ETGs. These are followed by a conclusion section summarising and drawing out the main conclusions from this thesis.

Chapter 2

Sample Selection

There is nothing like looking, if you want to find something.
You certainly usually find something, if you look,
but it is not always quite the something you were after.

J.R.R. Tolkien, The Hobbit

2.1 Introduction

A thorough investigation of the available ETG selection methods is required in order to define appropriate classification criteria for this work. This chapter gives a break down of such an investigation, focussing in particular on advantages and disadvantages of different ETG classification criteria with respect to the type of sample needed for the remainder of this thesis.

One of the aims of this thesis is to study the properties of diffuse dust for a sample of ETGs. This sample should therefore be as large as possible so that the

results can be considered statistically significant. Additionally, given that studies of dust properties in late-type spirals have shown high dust masses and low temperatures, it is imperative that the ETG sample is completely (or at least to the best of our abilities) uncontaminated by late-types; otherwise dust parameters belonging to spiral galaxies could be falsely associated with the ETGs. An additional choice which must be applied to this sample selection is whether to create an optically-selected sample, or a FIR/sub-mm selected sample (i.e. whether galaxy selection is based on optical or FIR/sub-mm photometry). However, given the necessity for a both morphologically robust and large sample, an optical selection is the preferred choice over FIR selection. This is due to the wealth of selection mechanisms currently available which are based in the optical, and because the high resolution of the optical photometry available allows for visual inspection of the resultant sample to reduce the contamination by late-types.

Therefore the aim of this chapter is to define a selection method that can be utilised to create an optically-selected and complete sample of ETGs. Such selection methods are plentiful throughout the literature, with the most common process being that of visual inspection (Sandage 1961). This method (also known as 'eyeballing') is a simple but time-consuming process, where the optical photometry is examined by eye to determine the morphology of the galaxy. There are multiple catalogues of visually classified galaxies available to the general public, including the de Vaucouleurs 3rd Reference Catalogue of Bright Galaxies (de Vaucouleurs et al. 1991), the Virgo Cluster Catalogue (Binggeli et al. 1985) and the more recent Galaxy Zoo project (see Lintott et al. 2011 and Section 2.2.1). Unfortunately there are limiting factors to visual inspection - more distant galaxies are less easily resolved and therefore contain a large risk of misclassification. Additionally, different catalogues may have different criteria defining each morphology

and therefore may suffer from a lack of consistency. As an example, one classifier may give a late-type spiral classification to an object simply because of the spiral structure, and another classifier may base it on the apparent bulge-to-total fraction.

For the above mentioned reasons, automated classification methods have at times been preferred to visual inspection. Such methods include the use of a range of morphological proxies, or spectral or kinematic classification, or the use of artificial neural networks. Morphological proxies will be discussed in greater detail below in Section 2.3; they are chosen based on correlations found for particular galaxy types. For example, ETGs have been shown in the past to be largely passive with little or no ongoing star formation: this leads to the idea that ETGs occupy the red end of the colour-magnitude diagram and LTGs occupy the blue. Hence colour has often been used as a morphological proxy (Holmberg 1958; Roberts & Haynes 1994; Strateva et al. 2001; Blanton et al. 2003; Baldry et al. 2004; Balogh et al. 2004). Sérsic (Sérsic 1963; Peng et al. 2010) and concentration indices (Morgan 1958; Abraham et al. 1994, 1996; Postman et al. 2005), as well as bulge-to-total ratios calculated from bulge-disk decomposition (Baggett et al. 1998; Fisher & Drory 2008; Kormendy & Bender 2012; Lackner & Gunn 2012) are other frequently used proxies. Less well-known morphological proxies include the Concentration-Asymmetry-Clumpiness (CAS) parameters (Conselice 2006) and the Gini coefficient (Lotz et al. 2004).

The idea of neural networks is currently fashionable for the classification of large galaxy samples (Odewahn et al. 1996; Naim et al. 1997; Huertas-Company et al. 2011). They solve the time-consumption issue associated with visual inspection, and unlike the application of a proxy cut, they don't allow large levels of morphological contamination to affect the results. The issue with this automated

system is that it requires a previously classified, large, training sample to effectively 'learn' how to classify the galaxies. This can be difficult to produce. Such a classification process has the additional complication that galaxies that do not quite 'fit in' with the traditional galaxy types may be misclassified - only visual inspection can resolve such an issue.

The last few classification methods which should be mentioned are classification using either kinematics or spectral lines. The former process is based on the rotation speed of the stellar population with the galaxy (Emsellem et al. 2007; Cappellari et al. 2011a) - this method can be immediately disqualified for our purposes as there is no kinematic information available for the GAMA and H-ATLAS datasets. Additionally, it would be difficult to accurately observe the rotation speeds of galaxies at the redshifts found in these catalogues. Spectral classification on the other hand is a possibility given that GAMA has medium-resolution spectroscopy for its galaxies. However, such a classification method is tantamount to stating that there are no emission lines present in the spectra of ETGs and this has been shown to be untrue (Phillips et al. 1986; Macchetto et al. 1996; Sarzi et al. 2006; Yan et al. 2006).

The above selection methods are therefore the possibilities available for use in the creation of a sub-mm detected, optically selected ETG sample. The more accessible of these methods (i.e. a number of morphological proxies) will be discussed and investigated within the confines of this chapter. To this end, Section 2.2 gives an in depth description of the process of galaxy classification via visual inspection. This is indeed necessary if not for the ultimate ETG sample, but at least for the use of visually classified, control samples which are used to test the accuracy of the proxies. Following the description of these test samples, Section 2.2.2 deals with the diagnostics of the classifications in each of these samples. A fuller description of the different proxies to be investigated is given in Section 2.3 and these

are tested in full in Section 2.4. Section 2.5 gives an indication of what future classification methods may be available, and the conclusions for this Chapter are presented in Section 2.6.

2.2 Visual Classifications

This section identifies three control samples chosen to use for this proxy analysis. It is necessary to repeat the analysis for multiple samples because each sample has its own strengths and weaknesses. Moreover, although visual classification (or eyeballing) is employed to classify the galaxies in all these control samples, each sample is classified by different numbers of people (one versus the few versus the many), and different criteria are used in each classification process. These will be described in detail in the following sections.

2.2.1 Test Samples

Kelvin Sample

Kelvin et al. (2014) describe their volume-limited, visually classified sample of GAMA-I galaxies in the three equatorial regions. This is restricted to the redshift range 0.013<z<0.06, a Galactic extinction-corrected limit of r_{Pet} <19.8 and an additional absolute magnitude cut at M_r <-17.4 to ensure a volume-limited sample. After an additional 19 galaxies were removed due to poor imaging data or bad SDSS photometry, this resulted in a parent dataset of 4,110 galaxies, with a range of galaxy types.

The visual classification for this parent sample was carried out and is fully described in Kelvin et al. (2014). Briefly, they generate three colour postage stamps using UKIDSS H and SDSS i and g bands for red, green and blue colours respectively. These are then classified on a step-by-step basis by three independent

people across three tiers. The tiers are defined as follows:

Is the galaxy spheroid- or disk-dominated?

Is it a single- or multi-component system?

Is one component a bar?

These criteria allow an analysis of the broad-scale morphological properties of the galaxies, independent of colour. Classifications are assigned in cases where at least two of the observers agree, thereby allowing for objective visual classifications. Spheroid-dominated systems are all classified as ETGs, and then further subdivided into E (single-component) galaxies, S0a (multiple-component) galaxies and SB0a (multiple-component with a bar) galaxies. Note that the S0a grouping includes all sub-categories of S0, S0/a and Sa galaxies. Other spiral galaxy classifications, which are not the subject of this work, are assigned to systems that are classed as disk-dominated. For example, Sd galaxies are classified as disk-dominated, single-component systems. A full layout of these tiers, including the number of galaxies assigned to each classification criterion, is given in Fig. 2.1. Note that their irregular galaxy classification mainly ended up in the Sd class.

This could be considered an ideal parent sample to test proxies upon. However, there are several issues with this sample. The primary problem is the use of bulge versus disk dominance in determination of early or late-type. This quintessential use of bulge-to-total ratio is useful if spiral arms are always associated with disk-dominated galaxies but this is not the case as early-type spirals (Sa) also have spiral structure. As the presence of spiral arms is not taken into account in the classification process, it is uncertain whether ETGs in the sample contain early-type spirals. Re-classifying the ETGs based on spiral structure is not a possibility as the quality and resolution of SDSS imaging are limited. Therefore in all subsequent proxy tests it must be observed that early-type spirals may be present in

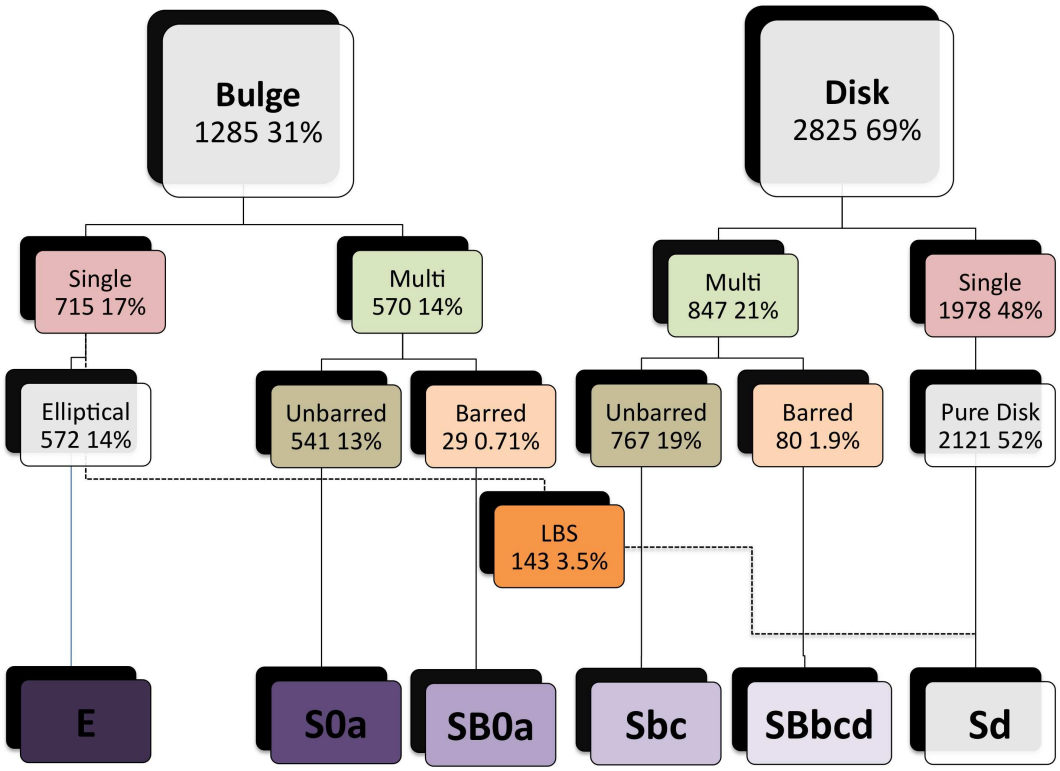

Figure 2.1: Flow chart showing the multiple tiers across which the galaxies from the Kelvin et al. (2014) parent sample were classified. Each tier within the flowchart shows the criterion within that level, the number of galaxies and their percentage of the whole sample. Note the Little Blue Spheroids (LBS) - galaxies fulfilling the criteria for ellipticals in terms of shape and structure, but which are significantly bluer and upon further analysis by Kelvin et al. (2014), considered to be dwarf irregulars/spirals.

the samples, and need to be considered.

Not considering spiral structure during classification is an issue that is further intensified by the classification groupings set by Kelvin et al. (2014). Due to the poor quality of SDSS imaging for some galaxies, it is necessary for S0, S0a and Sa galaxies to be grouped together as a single class S0a. The difference between these two types of ETGs is that S0 galaxies contain a disk but no spiral structure, and Sa galaxies contain both. Additionally, the classifications do not take into account the possibility of lenticulars with a small bulge[1] (Cappellari et al. 2011b; Kormendy & Bender 2012, and Fig. 1.2).

A final issue which must be acknowledged regarding this dataset is the low apparent fraction of barred spirals compared to unbarred spirals. Fig. 2.1 indicates that ∼10% of Sbc spirals contain bars - this is a significantly lower fraction than the expected ∼30-40% (e.g. Lee et al. 2012). This difference may be attributed to several different effects. In the first case, SDSS data is good enough to view strongly barred galaxies, but it is quite likely that weakly barred systems, or central isophotal twists, may be missed or lost in the flux from the central bulge. This may account for a missing 11% of barred spirals Elmegreen et al. 2004.

A secondary effect causing this low fraction is that KS14 did not make any cuts based on inclination. Any galaxies which appear edge-on in the images and have no obvious bar are classified as unbarred. Elmegreen et al. (2004) find that they need to scale up their barred fraction by a factor of two to account for this - therefore these two effects alone can scale the fraction up to around 40%, as predicted in the literature.

In spite of these minor issues, this GAMA sample is a large, complete, low redshift sample which overlaps with all SDSS samples and contains all the necessary parameters required for proxy analysis. In light of this, the associated issues are

[1]These are likely to be classified as disk-dominated and potentially Sbc or Sd galaxies.

quite minor and this has been chosen as the largest GAMA test sample for this chapter. This sample will be referred to as KS14 for the rest of this thesis.

Galaxy Zoo Sample

The second proxy test sample is taken from the Galaxy Zoo 1 (GZ1) database (Lintott et al. 2008, 2011). This is a large-scale citizen visual classification effort for nearly 900,000 galaxies in the SDSS, which is constantly being updated and statistically enhanced for every subsequent SDSS data release. Members of the public log onto the GZ1 website, and are presented with an interface containing a composite image of a galaxy. An example of this interface as published in Lintott et al. (2011) is shown in Fig. 2.2. Note that for the more recent Galaxy Zoo 2 (GZ2) project, which focusses on more detailed classifications, the user interface contains a more detailed line of questioning. This allows the database to make judgements about the following: do galaxies contain spiral arms, how many, how tightly wound the arms are, whether there is any evident tidal debris, dust lanes, rings or there are other interesting artifacts present. However, GZ2 is a subset of $\sim$300,000 GZ1 galaxies (Willett et al. 2013) and therefore we choose to use the more basic morphologies given by the larger GZ1 sample as there is a larger chance of finding GAMA counterparts.

The power of these classifications lies in statistics - thousands of people classify the galaxies and based on a combination of majority counts and weighting based on the galaxy's parameters, a classification is made. The GZ1 public data release is described in Lintott et al. (2011), with extensive notes on how they quantify bias and estimate confidence levels on the results. The bias quantification is an important factor in the classification of morphology: they use a technique which recognises that small, faint or distant galaxies will likely be classified as ellipticals but may yet be spirals whose arms are not distinctly visible in the SDSS images.

Figure 2.2: Galaxy Zoo 1 interface for users. The image panel shows the composite SDSS g, r and i band image being classified and the panel on the right gives the options for classification.

Section 3.1 of Lintott et al. (2011) gives a complete description of how such bias is applied to the final catalogue.

This GZ1 catalogue is position-matched to the H-ATLAS-GAMA equatorial data to achieve an overall match of 18,453 galaxies to all redshifts; this gives access to the full range of GAMA parameters. These matches are shown in Fig. 2.3, with classifications of elliptical and spiral highlighted. These classifications are assigned by the GZ1 catalogue itself, with 80 per cent of the vote in that category (following the debiasing procedure) required to attain that classification. Galaxies which do not achieve at least 80 per cent of a particular vote are assigned

'uncertain' status.

Visual classifications are known to be less reliable at higher redshift, due to increasingly poorer resolution at these distances and this is indicated in Fig. 2.3. At higher redshifts, spiral classifications become almost non-existent and elliptical classifications begin to dominate. This is true even after the debiasing procedure. Additionally, at these higher redshifts classifications are found only for the brightest galaxies, as poorly resolved (small radii) objects are dominated by the point-spread function and cannot be robustly identified; they are therefore classified as 'uncertain' and omitted from this diagram. This results in data points lying increasingly further above the dashed line in Fig. 2.3 - the 'uncertain' galaxies would fill this gap. All the above mentioned issues have to be considered in this proxy testing approach.

The primary reason for using this GZ1 sample is because there is enough data to judge the effect of using proxies for galaxies which are both detected and undetected in the FIR/sub-mm regime - an ultimate aim for this thesis. It is necessary to test proxies in a way that includes all galaxy types with a large range of luminosities. Ideally this would be done using a single low redshift volume-limited sample. However, although this one sample would extend down to the faintest galaxies, it would not fairly represent galaxies at higher redshift, nor would it indicate how morphological proxies become biased by redshift. Similarly, it is not possible to have a single volume-limited sample which extends out to slightly higher redshift, as this would have a brighter absolute magnitude cut and therefore would not include the faintest galaxies.

Therefore, the method utilised selects a range of volume-limited samples, with varying redshift and absolute magnitude limits, as described below:

Sample 1: $0.013 \leq z \leq 0.02$, $M_r \leq -17.00$ mag

Sample 2: $0.013 \leq z \leq 0.04$, $M_r \leq -18.40$ mag

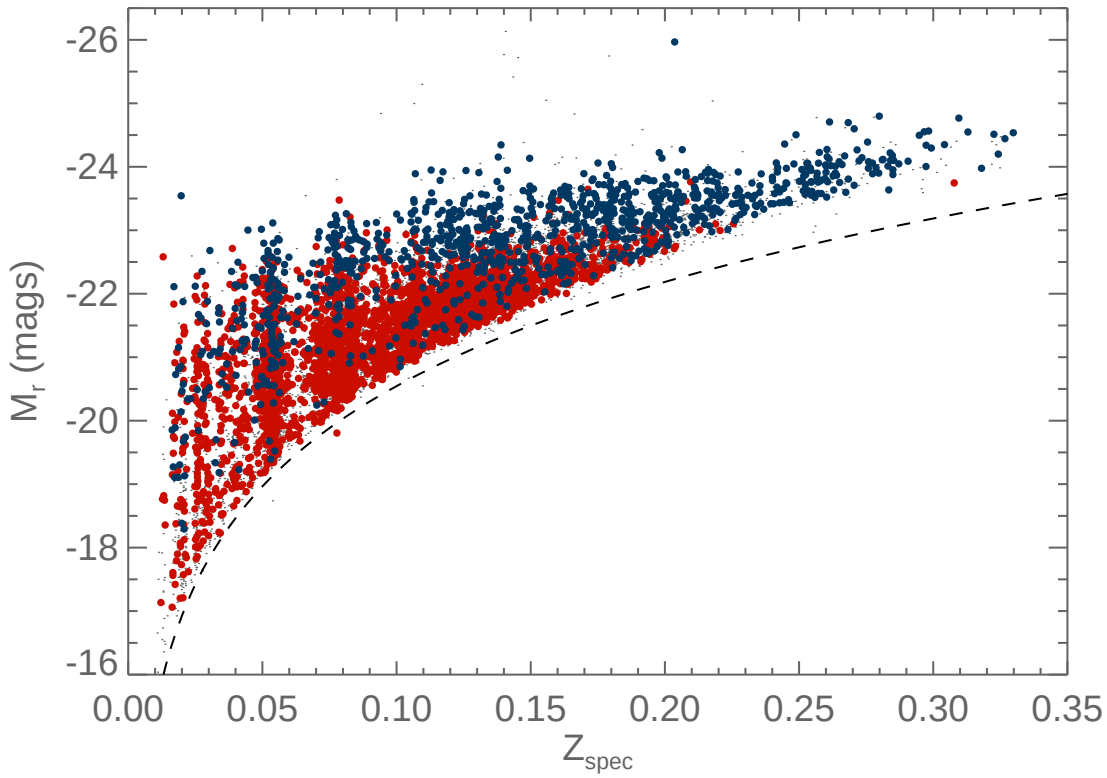

Figure 2.3: Absolute r-band magnitude plotted as a function of spectroscopic redshift for the GAMA catalogue matches with GZ1 (grey points). Blue points represent those galaxies classified as ellipticals, and red points those galaxies classified as spirals. The black dashed line indicates the Petrosian magnitude spectroscopic limit (r_{Pet} <17.77) used for the GZ1 sample (Strauss et al. 2002; Lintott et al. 2011).

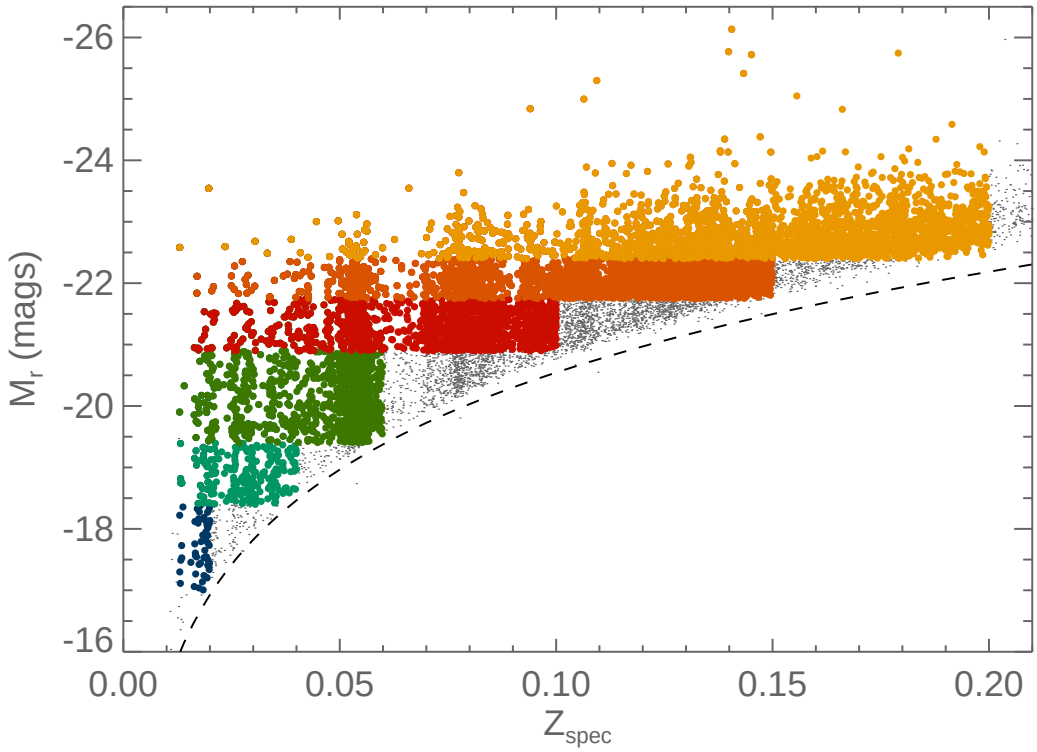

Figure 2.4: Absolute r-band magnitude plotted as a function of spectroscopic redshift for the GAMA catalogue matches with GZ1 (grey points). Our six volume-limited samples are shown (in order of increasing redshift limits) as the blue (Sample 1), cyan (Sample 2), green (Sample 3), red (Sample 4), orange (Sample 5) and yellow (Sample 6) points respectively. The black dashed line indicates the Petrosian magnitude spectroscopic limit (r_{Pet} <17.77) used for the GZ1 sample (Strauss et al. 2002; Lintott et al. 2011). See Table 2.1 for properties of these samples.

Sample	**Population**	**Bright Fraction**	**Ellipticals**		**Spirals**		**Uncertain**	
		($M_r \leq$-21.5)	*Num*	*Frac*	*Num*	*Frac*	*Num*	*Frac*
1	126	0.04	14	0.11	32	0.25	80	0.63
2	581	0.09	55	0.09	208	0.36	318	0.56
3	1528	0.16	157	0.10	533	0.35	838	0.55
4	2186	0.49	239	0.11	761	0.35	1186	0.54
5	3221	1.00	412	0.13	890	0.28	1919	0.60
6	2286	1.00	543	0.24	291	0.13	1452	0.64

Table 2.1: Tabulated information about the six volume-limited samples. Initial columns describe the sample numbers and populations. The third column gives the fractions of sample galaxies which have very bright absolute magnitudes ($M_r \leq$-21.5). Following columns describe the respective numbers and fractions of galaxies which have been assigned debiased GZ1 flags of elliptical, spiral and uncertain.

Sample 3: $0.013 \leq z \leq 0.06$, $M_r \leq$ -19.40 mag

Sample 4: $0.013 \leq z \leq 0.10$, $M_r \leq$ -20.90 mag

Sample 5: $0.013 \leq z \leq 0.15$, $M_r \leq$ -21.75 mag

Sample 6: $0.013 \leq z \leq 0.20$, $M_r \leq$ -22.40 mag

Fig. 2.4 shows how these samples are brightness-limited at the faint end. Each sample has its own strengths in the morphological testing that follows. Further properties for the six samples are shown in Table 2.1 and these will now be examined, so that a sample which is most representative of a wide range of galaxies can be chosen for the full proxy testing.

Sample 1, shown as blue points in Fig. 2.4, has the smallest redshift volume. Therefore, it has a small galaxy population which is representative of a broad range of luminosities, mostly dominated by fainter (including some dwarf) galaxies.

Table 2.1 indicates that the elliptical fraction is low here in comparison to the spiral fraction; however the 'uncertain' fraction is high and dominates the classifications for this sample. At such low redshifts we expect a high image resolution and classification should be less uncertain, yet it is likely that the low-luminosity galaxy fraction of the sample contains very faint, point-spread function (PSF) dominated images which were difficult to classify. These faint galaxies are likely to be the cause of the high 'uncertain' fraction in this redshift bin.

Due to the higher redshift limits, Samples 2 (cyan points) and 3 (green points) have larger populations and are more statistically representative of the local Universe. Both of them show similar morphological fractions, and indicate that spirals are more numerous in the nearby Universe than ellipticals. Uncertain galaxies will be omitted in the testing, and spiral and elliptical classifications will be considered to be fully representative of morphologies within each sample. For these two samples, the difference in the fractions of bright and faint galaxies is not too large, and does not appear to affect the morphological fractions.

Sample 4 (red points in Fig. 2.4) is approaching the cutoff point for which morphological detail is difficult to detect due to distance effects[2] (Nair & Abraham 2010). However, the sample size here is a significant improvement on the other samples and is only 50% dominated by brighter galaxies. Based on the morphological fractions for this sample (which are similar to those of Samples 2 and 3), it would appear that we are not seeing any brighter galaxy bias, and the classifications are as accurate as for the lower redshift samples.

Sample 5 (orange points) and 6 (yellow points) extend beyond z=0.1; at these redshifts SDSS imaging loses resolution and classification becomes much more uncertain. Although both these samples are large, they are completely dominated by brighter galaxies due to the absolute magnitude cuts. As high luminosity

[2]Including the variable seeing and relatively low signal-to-noise of SDSS data.

galaxies are typically early-type (Blanton et al. 2003; Baldry et al. 2004; Balogh et al. 2004; Kelm et al. 2005), this may be the cause of the increase in ellipticals and drop in spirals. However, the decrease in the spiral fractions is most likely attributed to the higher redshift range being classified. A morphological bias has already been established for classifications at higher redshift, which is the most likely cause of these larger elliptical fractions.

An additional point which is made apparent in Table 2.1 is the fraction of 'uncertain' galaxies remains approximately constant throughout these different samples. This might be balanced by different factors: Sample 1 goes down to faint magnitudes and the dwarf or faint galaxies that will be included here are likely to be classed as 'uncertain'. Sample 6 only contains very bright galaxies, but the effect of going out to higher redshift is that galaxies are less well resolved, leading to an 'uncertain' classification. The intermediate redshift samples have the lowest 'uncertain' fractions, a result of achieving a balance between these two main effects leading to 'uncertain' classifications. The 'uncertain' class is also likely to be dominated by lenticulars and early-type spirals. These galaxies have bulge-to-total ratios of $\gtrsim 0.5$[3] (e.g. Oohama et al. 2009), which will cause the classifiers to be more indecisive about whether the galaxies are ellipticals or spirals.

Having considered the properties of these six different samples, it seems wise to select Sample 4 as the Galaxy Zoo (GZ) sample and test morphological proxies on this. For this testing, the sample will be split into H-ATLAS detected ($F_\nu \geq 5\sigma$ in any SPIRE waveband) and H-ATLAS undetected galaxies. The number of galaxies in each subsample is 308 (14%) in the detected, and 1878 (86%) in the undetected sample.

[3]Although this is not always true - Kormendy & Bender (2012) found some lenticular galaxies have smaller bulges and reside parallel to the usual spiral sequence.

Nair Sample

The Nair & Abraham (2010) catalogue (NA10) comprises a sample of 14,034 low redshift ($0.01< z <0.1$), SDSS galaxies which were visually classified by the first author. Based on the parameters made available with this sample and the thoroughness of the NA10 classification process, this catalogue is exceptionally useful as a testing tool.

NA10 classifications are presented as T-types, based on the Carnegie Atlas of Galaxies (Sandage & Bedke 1994). T-Type is defined by associating numbers with morphological type. NA10 use different values of T-type to the Third Reference Catalog of Bright Galaxies (de Vaucouleurs 1963). The definitions of each T-type are given in Table 2.2, which is a summarised version of that shown in NA10 (their Table 1). The visual classifications by NA10 were run through twice, with a mean deviation in classified T-Type of $\approx$0.5. All galaxies with associated T-type ≤ 0 are considered to be ETGs for the rest of this work, and T-type = -5 are the elliptical galaxies.

NA10 is comprised of SDSS data, and therefore contains similar parameters to the GZ1 sample. These include optical colours and concentration index (see Sections 2.3.1 and 2.3.2). They also include r-band Sérsic index values (see Section 2.3.3) from Blanton et al. (2005), which are revised fits from Blanton et al. (2003). Lee Kelvin has identified multiple errors in these Sérsic profile measurements that make them unsuitable for the sort of analysis being done here (Lee Kelvin, priv. comm.). These include the type of fitting being done - they use 1-dimensional fits (believed to reduce the noise of the image), as opposed to 2-dimensional fits, which use all the possible data to minimise the model fit. They also use a double-Gaussian to represent the PSF, which will cause errors in Sérsic index for cases where the PSF is not well represented by a double-Gaussian in SDSS images. The Sérsic index measurement is most sensitive to a galaxy's core regions,

Class	c0	E0	E+	S0-	S0	S0+	S0/a	Sa	Sab	Sb	Sbc	Sc	Scd	Sd	Sdm	Sm	Im	?
NA10	-5	-5	-5	-3	-2	-2	0	1	2	3	4	5	6	7	8	9	10	99

Table 2.2: Table showing the NA10 adapted T-types, used to classify their galaxies. Note that c0, E and E+ galaxies are all given the same value, as are S0 and S0+ galaxies.

where there is the highest signal-to-noise ratio, and these regions are where the PSF has the highest impact. Additional problems with their Sérsic index include the narrow range they use to fit the models ($0< n <6$) and their treatment of the sky background. It should be noted that recent work by Bernardi et al. (2013) agree that there are large systematic differences between the Sérsic profile results included in NA10 (calculated by Blanton et al. (2003)) and those calculated by other parties; they also state the above reasons for the disagreement and suggest that the profile fits by Kelvin et al. (2012) supersede those of Blanton et al. (2003).

All these are reasons why proxy testing using the Sérsic profiles calculated in NA10 cannot be done. Therefore an alternative method is chosen using a subsample of the NA10 galaxies: counterparts to GAMA galaxies. Position-matches to the KS14 sample gives an NA10 subsample of 348 galaxies. This is statistically quite a small sample but it still provides the ability to complete the following tasks by making use of the combined parameters:

1. Compare the Blanton et al. (2005) Sérsic indices with those from Kelvin et al. (2012).

2. Compare the classifications from NA10 with those from KS14.

Fig. 2.5 shows the NA10 galaxies with GAMA counterparts; in this plot the Sérsic index of Blanton et al. (2003) has been plotted against the Sérsic index calculated by Kelvin et al. (2012). It is clear from this plot that the Blanton et al. (2003)

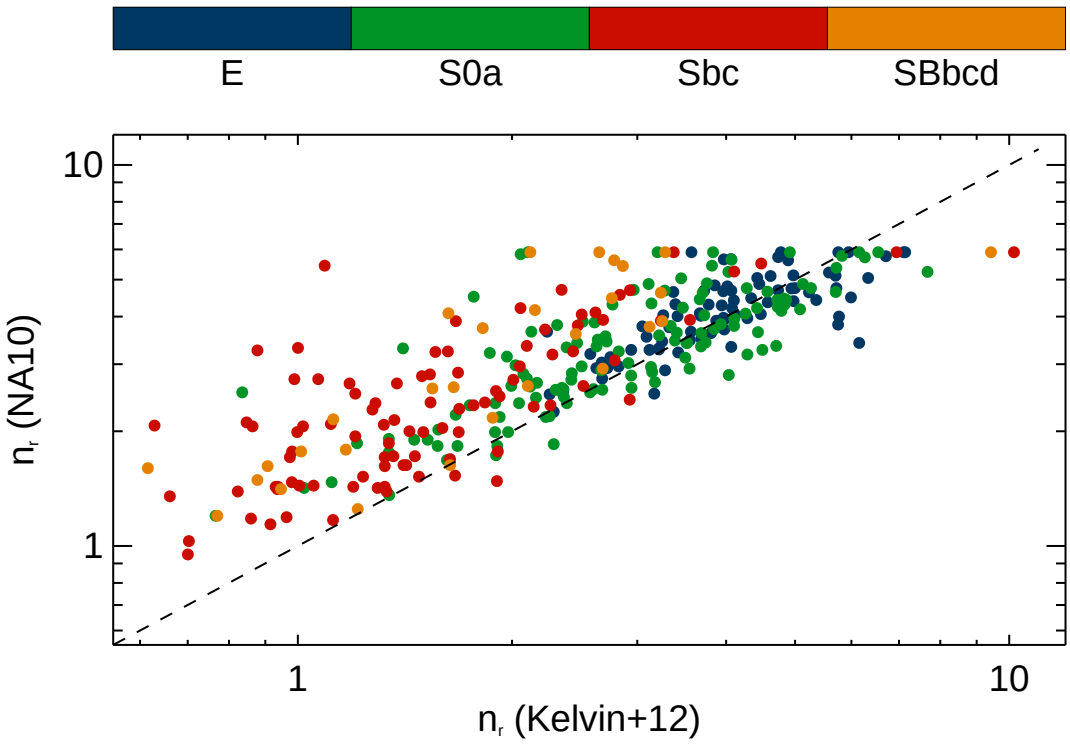

Figure 2.5: KS14's Sérsic index (x-axis) plotted against the Blanton et al. (2005) Sérsic index, for the NA10 sample. Points are coloured by KS14 classified morphology, with the colour bar showing the variation from early to late type from left to right. An x=y dashed black line is plotted for comparison. The Blanton et al. (2003) cutoff at n_r=6 is also apparent in this plot.

Sérsic indices are overestimated for ∼93 per cent of later-type galaxies. The profiles of ETGs do not show this same overestimation, but are instead underestimated in ∼ 39 per cent of cases. This analysis indicates that these cases can be linked to the Blanton et al. (2003) treatment of the PSF, as an incorrect PSF may falsely cause either an overly or under flattened Sérsic profile to be fit to the central regions of a galaxy, resulting in an under- or over-estimation of the Sérsic index n (see Fig. 1.8) which may be the correct fit to this region.

Overlapping Sample

A final sample we will be working with in this chapter is an overlapping sample, containing all position-matched overlaps with KS14, GZ1 and NA10. Such an overlapping sample will allow us to make a diagnosis of the suitability of the multiple proxies for each of their individual classifications, as well as the effect of visual classification carried out by the many (GZ) versus the few (KS14 and NA10).

Table 2.3 gives a summary of the classification results for each of the three main test samples before they are matched to create an overlapping sample. The high abundance of spiral galaxies is made apparent here for all samples, and while KS14's and NA10's classifications show ETG populations of ∼30-45%, the GZ1 classifications only provide elliptical classifications for a population of 11%.

NA10 and GZ1 samples are both derived from a large range of SDSS all-sky data, but KS14 is created directly from the GAMA equatorial regions and has both a redshift and absolute magnitude cutoff. Therefore the overlapping sample will also be limited to these redshifts, absolute magnitudes and regions of sky. Additionally the overlapping sample's population is limited by the smallest of these three test samples (i.e. 348 galaxies in NA10). After position-matching between samples is carried out, an overlapping sample of 245 galaxies is compiled.

	KS14 Classifications		**GZ1 Classifications**		**NA10 Classifications**	
	Number	*Fraction*	*Number*	*Fraction*	*Number*	*Fraction*
Total (T)	4110	1.0	2186	1.0	348	1.0
Elliptical (E)	572	0.14	239	0.11	51	0.15
Lenticular (S0/a)	570	0.14	-	-	103	0.30
Spiral (Sb/c)	847	0.21	761	0.35	171	0.49
Spiral (Sd)	2121	0.52	-	-	23	0.07
Uncertain (Un)	-	-	1186	0.54	0	0.0

Table 2.3: Numbers and fractions of classifications in each test sample. KS14 classifications are given as E, S0a+SB0a, Sbc+SBbcd and Sd. GZ1 classifications are based on debiased flag values of Elliptical, Spiral and Uncertain. NA10 classifications use the following T-types: E = -5, -3≤S0≤0, 1≤Sab/c≤5, 6≤Sd≤10, Un = 99.

KS14	**NA10**				**GZ**		
	E	*S0*	*Sabc*	*Sd*	*E*	*S*	*Un*
E	18.4%	10.2%	0.4%	0.0%	23.3%	0.0%	5.7%
S0a	0.8%	17.6%	23.7%	0.0%	3.7%	14.7%	23.7%
Sbc	0.0%	0.8%	26.9%	1.2%	0.0%	25.3%	3.7%

Table 2.4: Percentages of overlapping sample galaxies (245 galaxies), indicating how well visual classifications agreed for counterpart galaxies in each test sample.

As NA10 had already been matched to KS14, the removal of 103 galaxies from NA10 in the formation of this overlapping sample is due to these galaxies being missing from GZ1. Table 2.4 shows the classification results for the overlapping sample, based on each sample's classification, and these are discussed in further detail in Section 2.2.2.

2.2.2 Classification Diagnostics

Visual identification of galaxy morphology is known to be a subjective science, dependent on many factors such as the skill and training of the eyeballer, the quality, resolution and signal-to-noise ratio of the image, the waveband of the image, and even the time of the day that the image is being eyeballed. Therefore the differences in classifications between the three test samples should be quantified, so that a statement of the uncertainty on each set of classifications can be made.

The variation of classification between samples is first examined statistically by checking how consistent they are across the samples.

Figs. 2.6 and 2.7 are mosaic plots comparing classification results from KS14 with the NA10 and GZ1 samples respectively. These mosaic plots are used to visualise the percentages in Table 2.4 (see Robotham et al. 2013, Appendix A, for a description of mosaic plots and their interpretation). If the classifications

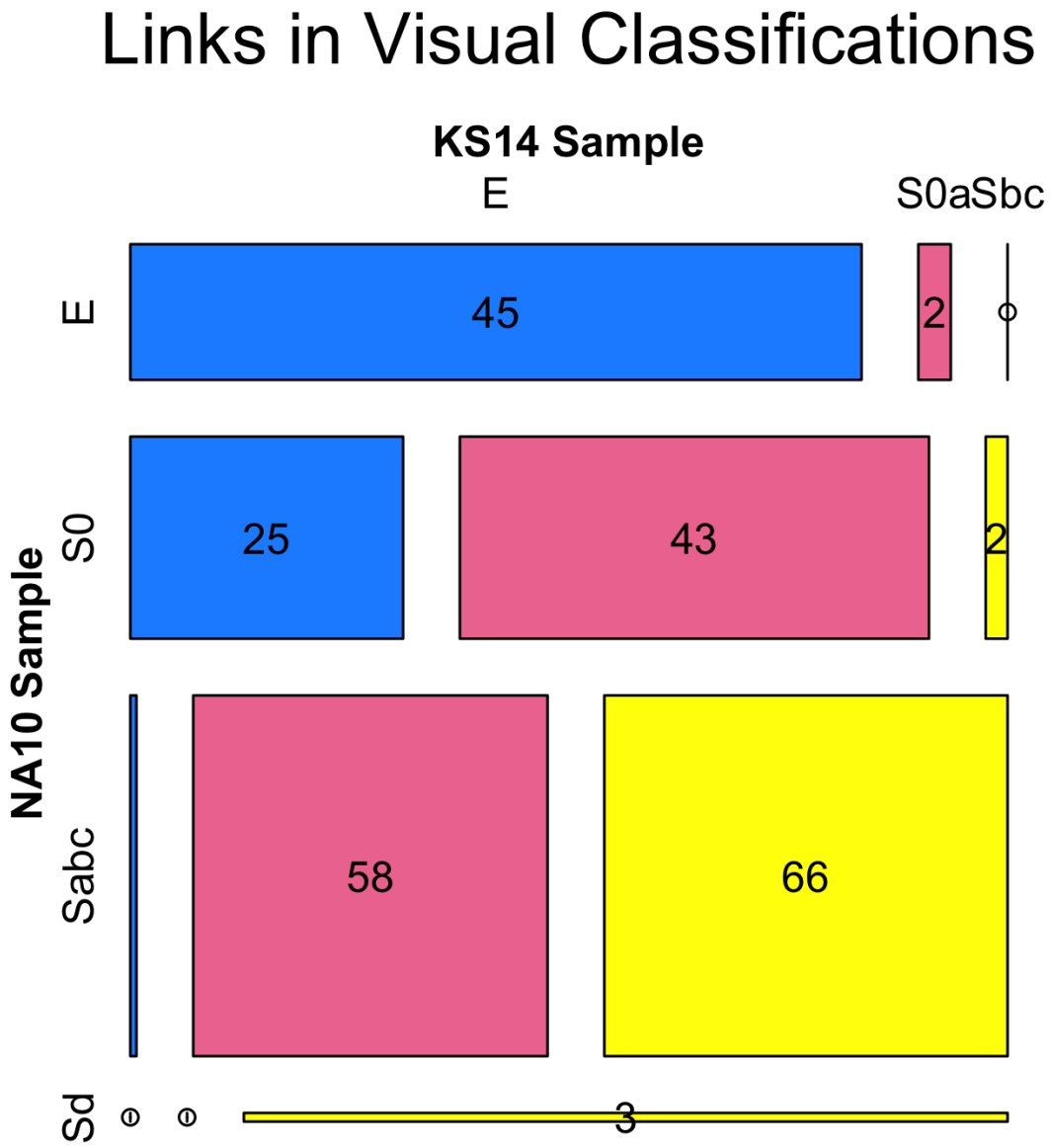

Figure 2.6: Mosaic plot comparing KS14 visual classifications with those from NA10 for 245 overlapping galaxies. From left to right and then down, boxes indicate matching E classifications, S0a classification by KS14 and E classification by NA10, Sbc classification by KS14 and E classification by NA10, and so on. Lines with a circle indicate no galaxies falling into that box. The numbers in each box represent the number of galaxies fulfilling the criteria for that box.

were identical between the samples, percentages on the downward diagonal from left to right in these tables would dominate over the other spaces. In general this seems to be the case: matches for the NA10 sample show high percentages on this diagonal[4], and low percentages in matched classifications are shown for (e.g.) E_{NA10} and Sbc_{KS14}, or E_{KS14} and Sd_{NA10}. However, there are some overly high percentage matches for E_{KS14} and $S0_{NA10}$, and for $S0a_{KS14}$ and $Sabc_{NA10}$. The difficulty in distinguishing between ellipticals and lenticulars is well known, however this overlap between $S0a_{KS14}$ and $Sabc_{NA10}$ classifications indicates some difference in the classification criteria. This is due to the KS14 classifications having included Sa galaxies in their S0a grouping, whilst NA10 classified the Sa galaxies separately (and therefore they are included in the NA10 Sabc group).

These statistics are also very similar when comparing KS14 with GZ1 classifications in Fig. 2.7. As the GZ1 classifications do not have an option to classify galaxies as S0, lenticulars are mostly grouped into the 'uncertain' category, making it difficult to ascertain how well the classifications truly match.

2.3 Morphological Proxies

As previously mentioned in Section 2.1, the ultimate aim in this chapter is to define a selection method that can be utilised to create an optically-selected, complete sample of early-type galaxies. There are many proxies that can be used to separate galaxies into late- and early-types, and this work concentrates on proxies available from optical images. Previous studies (e.g. Strateva et al. 2001) have shown strong correlations between morphology, galactic colour and the radial profiles of galaxies, which has led to the continued usage of such proxies throughout the literature (e.g. Strateva et al. 2001; Kauffmann et al. 2003a; Blanton et al. 2003; Bell et al. 2004; Baldry et al. 2004. However, the lack of information available on the strengths

[4]The area occupied in the mosaic plot is directly proportional to the percentage in question.

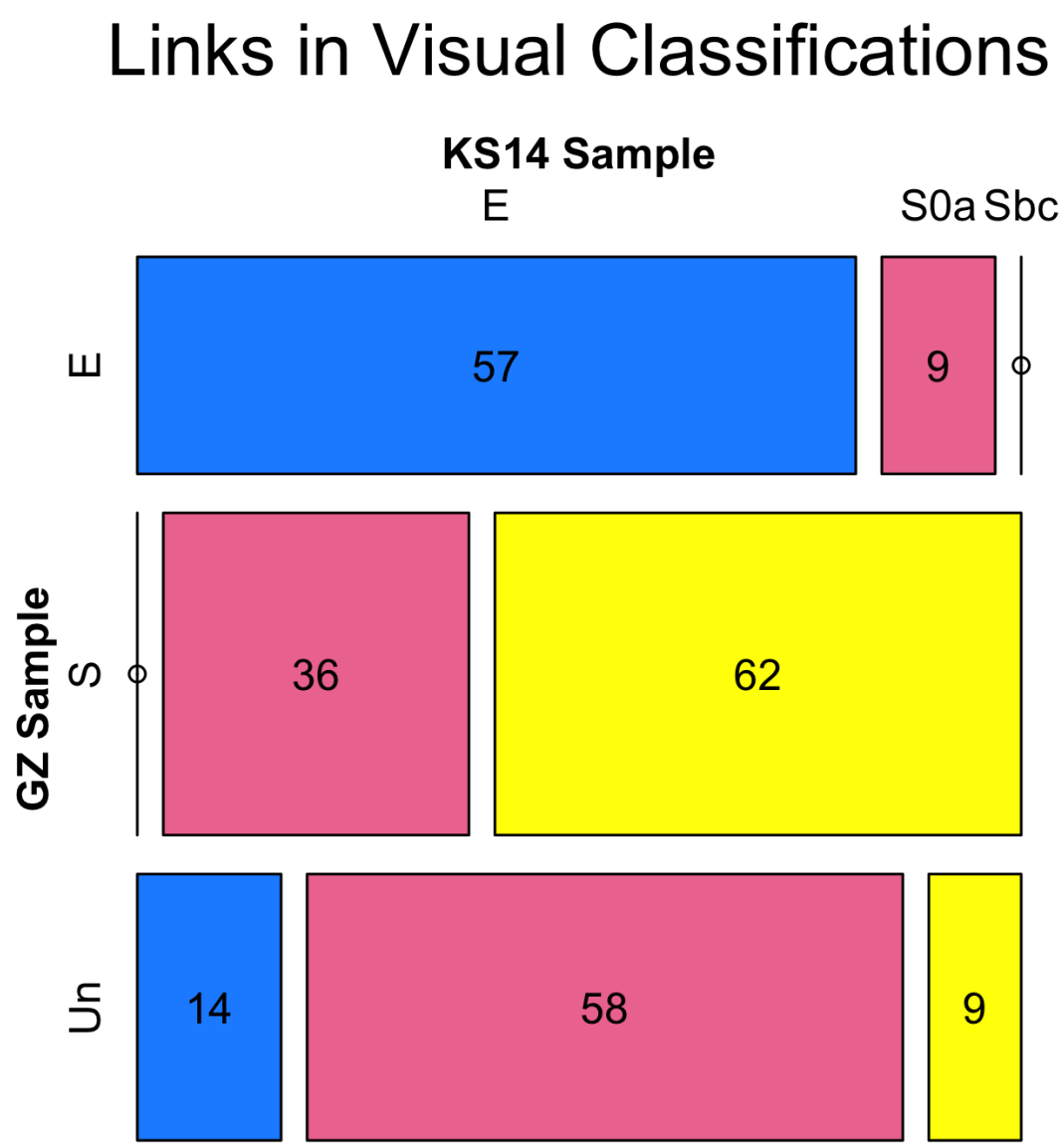

Figure 2.7: Mosaic plot comparing KS14 visual classifications with those from GZ1 for 245 overlapping galaxies. From left to right and then down, boxes indicate matching E classifications, S0a classification by KS14 and E classification by GZ, Sbc classification by KS14 and E classification by GZ, and so on. Lines with a circle indicate no galaxies falling into that box. The numbers in each box represent the number of galaxies fulfilling the criteria for that box.

and weaknesses of these proxies means that it is unknown how accurately a proxy corresponds with morphology.

Based on the data and subsequent parameters made available to the GAMA team through the database, certain optical proxies can be neglected. At this point in time, GAMA has not updated its photometry to include VST-KIDS and VISTA-VIKING, and data are limited to SDSS and UKIRT photometry and their corresponding resolution and quality. Bulge-disk decomposition can be removed as a realistic option, as the quality of SDSS data does not accurately allow the separation of bulge and disk components.

Three proxies are selected here and described in full detail in the remainder of this section.

2.3.1 Rest-Frame Colour

Colour is tested as a morphological proxy due to its popularity in past studies. The Colour-Magnitude Relation (CMR) has been used to divide galaxies into the RS and BC by multiple works (e.g. Baldry et al. 2004; Haines et al. 2008; Bernardi et al. 2010; Cappellari et al. 2011b), where the RS is used as a proxy for ETGs. Thus far the optical CMR has been discussed (see Section 1.1.1), but no reference has been made to the inclusion of UV data to derive these colours (as done in Grootes et al. 2013). Flux emitted at UV wavelengths is directly associated with emission from the young, hot stellar population and therefore should also be examined as a possible proxy.

UV-Optical Colour

UV-optical colours for GAMA galaxies can be calculated using a combination of Galaxy Evolution Explorer (GALEX[5]) and SDSS data. The GALEX bands are

[5]An orbiting space telescope observing galaxies in ultraviolet light as of 2003.

Far UV (FUV), with an effective wavelength of 1528 Å, and Near UV (NUV), with an effective wavelength of 2271 Å (Martin et al. 2005). The GAMA-GALEX catalogues seek to reconstruct the original UV flux for each given optical source, and include UV fluxes and AB[6] apparent magnitudes for both wavebands.

NUV CATAID-matched apparent magnitudes are corrected for Galactic extinction (for more details, see Wyder et al. 2007). The apparent magnitudes (m_{NUV}) can then be converted to absolute magnitudes (M_{NUV}) using NUV k-corrections which are also available through the GAMA database, derived from *kcorrect v.4.2* software, described in Blanton & Roweis (2007). This IDL code calculates k-corrections for the galaxies based on the best fit sum of templates to an SED and accounts for both the angular diameter distance and cosmological surface-brightness dimming for the distance modulus. The distance modulus equation is used for this conversion:

$$M_{NUV} = m_{NUV} - d_{mod} - K_{NUV}, \tag{2.1}$$

where d_{mod} is the distance modulus:

$$d_{mod} = 5\log_{10}D - 5, \tag{2.2}$$

with D calculated as the galaxy's luminosity distance. The UV-optical colour is then calculated as M_{NUV}-M_r. Given that SDSS r-band has a central wavelength of 6220 Å, this gives a wavelength difference of 3949 Å between the NUV and r bands. Higher values of (NUV-r) colour (red colours) require faint NUV magnitudes and bright r-band magnitudes, whilst the lower values (bluer colours) require bright NUV and faint r-band magnitudes. Other combinations result in intermediate colours.

UV emission is dominated by very hot, massive, young stars and therefore

[6]A standard magnitude system adopted by the SDSS (Oke & Gunn 1983)

NUV-r colours are more affected by the young stellar population in galaxies, unlike other colours which will be examined below. Recent work by, for example, Kaviraj et al. (2011) has used NUV detections to identify recent star-formation in ETGs. This indicates that (NUV-r) colours do not accurately separate out early- from late-type galaxies. Rather than being used as a successful proxy, it would be more useful to use NUV-r colours to identify NUV emission in ETGs and search for possible ongoing/recent star formation.

Optical Colour

SDSS u and r bands are considered to be the optimal wavebands for optical colour because they successfully straddle the 4000 Å break in the spectrum; a strong 4000 Å break represents a lack of hot blue stars in a galaxy and therefore the (u-r) colour is a crude indicator of the current star formation rate. The colour proxy itself is defined as those galaxies that sit on the RS in the Colour-Magnitude Diagram for this colour.

Although there have been many RS relations fit to the CM diagram, it seemed appropriate to fit an independent relation to act as a divider between RS and BC, due to the unique aperture photometry being employed by the GAMA team. This is calculated by bisecting the KS14 (g-i)[7] colour distribution at (g-i)=0.93, and fitting approximate straight lines to the (g-i) bimodalities representing the RS and BC in the (u-r) CM diagram. This RS divider is calculated as the line equidistant in magnitude from these fits. This is a similar method to other published works for different optical colours (e.g. Bell et al. 2003), and is shown to work well as a straight line separator for the (u-r) CMD in Fig. 2.8. A more sophisticated method such as that adopted by Baldry et al. (2004) assumes a bivariate distribution, however such a method need only be adopted if colour is found to be a suitable

[7] (g-i) colour is chosen here for being the closest to (u-r), which is used for the colour selection.

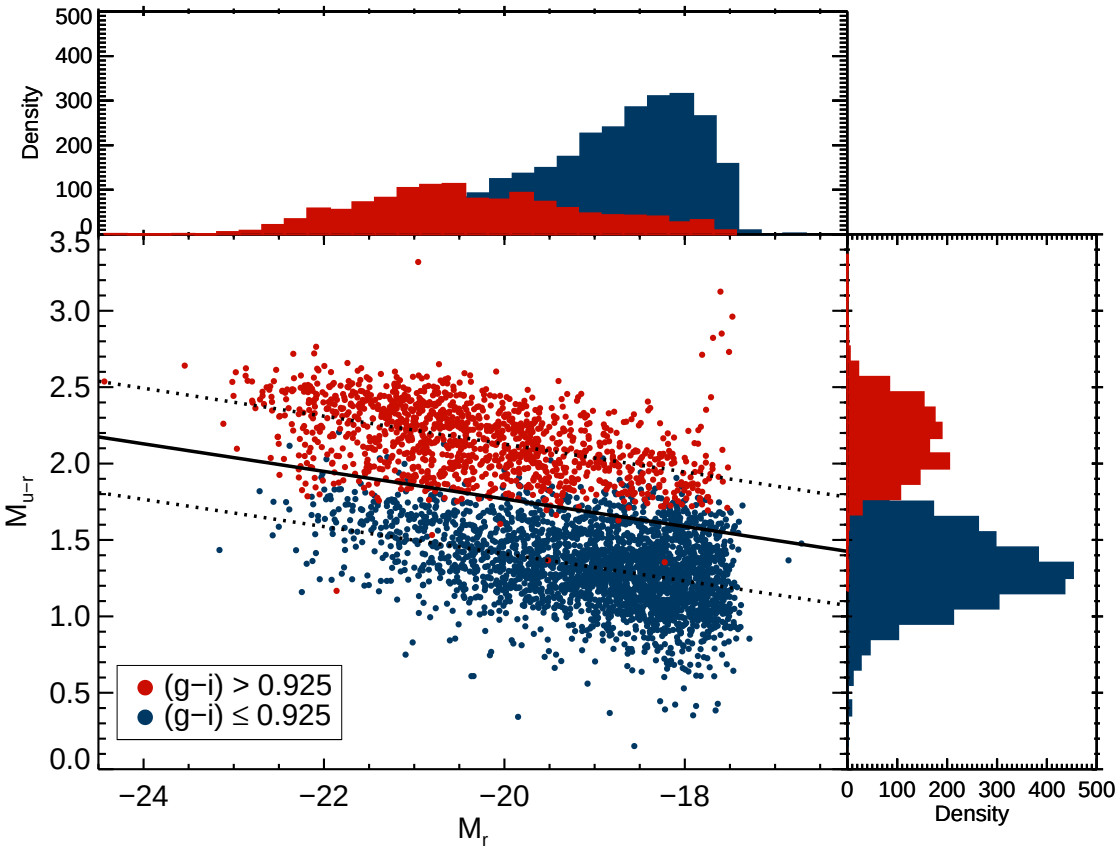

Figure 2.8: Colour-Magnitude diagram of KS14 galaxies in the (u-r) plane. Galaxies are coloured according to whether they occupy the blue region of the (g-i) bimodality, or the red region. Dotted lines indicate straight line fits to these two modes, and the solid line indicates the best fit RS divider for this plot. Histograms show the distribution of points in one dimension.

proxy for ETG selection. The resultant straight-line fit is given as

$$u - r = -0.09M_r - 0.0347 \tag{2.3}$$

and is shown in Fig. 2.8, as are the two lines which are used to fit the two (g-i) modes. In the proxy analysis given in Section 2.4, colour will be used to define ETGs as those galaxies within the RS, with a lower occupation limit given by Eq. 2.3.

2.3.2 Concentration Index

One commonly used morphological proxy is central concentration index (C_r), often defined as the ratio of the Petrosian r_{90} to r_{50} radii (Blanton et al. 2001; Mateus et al. 2006), where r_{90} and r_{50} are the SDSS circular aperture radii within which 90% and 50% of the flux are contained (Bell et al. 2003). The calculation of these quantities are shown in Blanton et al. (2001), where they define a Petrosian ratio (R_P) as the ratio of the local surface brightness in an annulus at radius r to the mean surface brightness within r:

$$R_P = \frac{\int_{\alpha_{low,r}}^{\alpha_{high,r}} dr' 2\pi r' I(r') / \left[\pi(\alpha_{hi}^2 - \alpha_{low}^2) r^2\right]}{\int_0^r dr' 2\pi r' I(r') / (\pi r^2)} \tag{2.4}$$

where $I(r)$ is defined as the averaged surface brightness profile in the azimuthal direction, and α_{low} <1 and α_{high} >1 define the annulus. The SDSS choice of annulus (and therefore the GAMA adopted value) is α_{low}=0.8 and α_{high}=1.25.

The Petrosian radius (r_P) itself can then be calculated as the radius at which $R_P(r_P)$ equals a specified value of $R_{P,lim}$, where for SDSS $R_{P,lim}$=0.2. At this point, the Petrosian flux F_P for any waveband can be defined as the flux within a certain number N_P of Petrosian radii in the SDSS r band:

$$F_{\rm P} = \int_0^{N_{\rm P} r_{\rm P}} 2\pi r' I(r') dr', \tag{2.5}$$

where N_P=2 for the SDSS (Blanton et al. 2001). Given this Petrosian flux one can calculate r_{90} and r_{50}, which are used to derive the concentration index. Objects with an exponential light profile can have their true fluxes virtually fully measured by Petrosian flux, but only 80% of the flux in a de Vaucouleurs profile is traced by the Petrosian flux. This is because the de Vaucouleurs profile contains flattened, extended wings which are not fully included in the Petrosian measurement.

A strong correlation between C_r and morphological type was identified by Strateva et al. (2001), Conselice (2006), Mateus et al. (2006), and Bernardi et al. (2010), amongst others, leading to the conclusion that this parameter is useful in differentiating between ETGs and LTGs. This is because ETGs tend to have light profiles which are more centrally concentrated, giving a high C_r. Strateva et al. (2001) ran a study on concentration index, quantifying strengths and weaknesses for different values of concentration index when used as a morphological separator. Based on the results in this work, a concentration cut of $C_r \geq 2.6$ has been chosen for testing in this Chapter.

2.3.3 Sérsic Index

The final proxy to be tested here is Sérsic index. The optical/NIR surface-brightness profiles of the GAMA/H-ATLAS galaxies are fit with a parametric model (Kelvin et al. 2012), which is a single-component Sérsic profile. The Structural Investigation of Galaxies via Model Analysis (SIGMA) wrapper around the GALFIT3 (Peng et al. 2010) profile fitting program is used for these systems. This catalogue is available within the GAMA database.

The single Sérsic distribution is given by

$$I(r) = I_0 \exp\left(-\left(\frac{r}{r_0}\right)^{1/n}\right), \tag{2.6}$$

where $I(r)$ is the surface brightness as a function of radius r, r_0 is a scaling radius which varies with the value of the third parameter n, and $1/n$ is the shape parameter that describes the amount of curvature in the light profile (e.g. MacArthur et al. 2003) and contains the Sérsic index n (see Fig. 1.8). This Sérsic index is commonly used as a morphological proxy as it defines the luminosity profile of a galaxy and gives us information on the concentration of light therein (Morgan 1958; Kelvin et al. 2012). Simmons & Urry (2008) show that Sérsic index is also closely linked to intrinsic Bulge-to-Total ratio. The de Vaucouleurs $r^{1/4}$ law is a particular case of Eq. 2.6, designed to fit large spiral bulges and ellipticals (illustrated by Peng et al. 2002), and therefore n=4 is the Sérsic index value typically associated with ellipticals, allowing for some errors in the fitted Sérsic index. The most massive ellipticals are not well-fit by a pure de Vaucouleurs law (e.g. Bernardi et al. 2010), which indicates that the link between Sérsic index and morphology is not perfect. Therefore, based on results from Kelvin et al. (2012), an r-band Sérsic cut of $n \geq$2.0 (half the de Vaucouleurs Sérsic index) is chosen as the third test proxy.

2.4 Testing the Proxies

We use all of the samples described above to investigate our selected morphological proxies. The methods we employ for these tests involve contrasting properties called Completeness (C) and Reliability (R) for each proxy in each sample.

The Completeness parameter describes the ability of the proxy to select all the possible ETGs available in the sample. This is calculated as:

$$C_{\rm ETG} = \frac{N_{\rm proxy,ETG}}{N_{\rm ETG}} \times 100\%, \tag{2.7}$$

where $\rm N_{proxy,ETG}$ is the number of galaxies selected by the proxy cut that have been visually classified as ETGs, and $\rm N_{ETG}$ is the total number of galaxies which have been visually classified as ETGs. This ratio gives a fraction that is then converted to a percentage. This is an important parameter for determining how complete the sample is.

The Reliability parameter is calculated in a similar manner, and is a measure of the robustness of the sample. It is described by the ratio of number of galaxies selected by the proxy cut which have been classified as ETGs ($\rm N_{proxy,ETG}$) to all the galaxies selected by the proxy cut ($\rm N_{proxy}$):

$$R_{\rm ETG} = \frac{N_{\rm proxy,ETG}}{N_{\rm proxy}} \times 100\%. \tag{2.8}$$

This value also leads to a percentage indicating the contamination of the sample by late-type galaxies:

$$\rm Contam_{LTG} = 100\% - \mathit{R}_{ETG}. \tag{2.9}$$

As well as these quantitative methods, we utilise a more qualitative set of tests which involve plotting the distributions of each morphological class and examining how these morphological distributions are split across the measured ranges of these proxies. These methods will now be employed for each identified proxy.

2.4.1 Colour

We highlight how the morphological classes from KS14 are distributed above and below the RS line in Fig. 2.9. Galaxy colours in this figure have had the RS divider (Eq. 2.3) subtracted so that offset from the RS is shown, with the dashed line representing the RS line. This plot shows the variation of colour offset with

morphology, with a transparency factor that allows the high number densities to be easily recognised as darker regions. This box-and-whiskers style of plot highlights mean values, as well as upper and lower quartiles for colour offset in each morphology.

Fig. 2.9 indicates that the very reddest galaxies are indeed ellipticals, and the ETGs are mostly located in the RS. However, it also indicates that there is a large proportion of LTGs that occupy the RS, which could partly be due to dust-reddening. The most important aspect of this plot is the 20% and 16% of ellipticals and lenticulars respectively that can be found outside the RS (it is unclear from this plot whether they can be found in the BC or GV). Such a proportion of blue colours for ETGs indicates that these galaxies may not be entirely quiescent, and these are the galaxies that we suspect are most likely to be significant emitters in the FIR/sub-mm. This is because dust is often associated with gas and recent star formation. This point alone indicates that colour is a weak option for our choice of morphological proxy.

When we examine the results from testing this proxy quantitatively, we get C_{colour}=82.4% and R_{colour}=65.0%. These numbers indicate a contamination by LTGs of 35.0% - this represents 17% of all the LTGs - these are proportionally large fractions that would significantly affect our sample results. Additionally, 17.6% of the bluest ETGs would be omitted in such a sample selection, and as mentioned above, these are potentially the ETGs with the strongest FIR detections. On this result alone, and for conciseness, colour tests will not be run on the other two samples.

The results from these colour tests highlight a key point that needs to be made about ETGs. Many results in the literature that contain samples consisting of red galaxies claim to be representative of elliptical galaxies in general. However, it is clearly impossible to claim that colour accurately represents any class of galaxy.

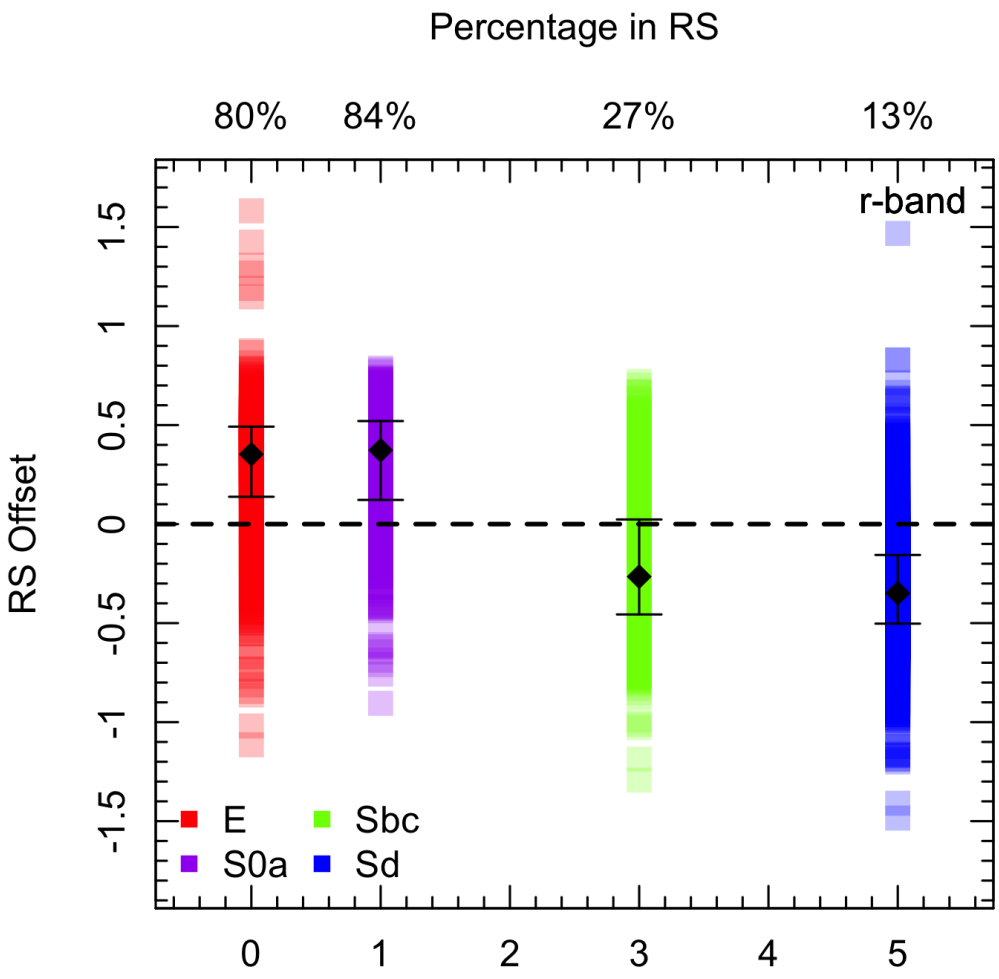

Figure 2.9: Plot showing how (u-r) colour varies with morphology for the KS14 sample. The x-axis does not represent any physical values, but is used to separate the four different morphologies. The dashed line indicates the RS (Eq. 2.3) offset line, calculated as described in the text. The percentages displayed above each distribution indicate the fraction of galaxies fulfilling this proxy within this morphological class. Diamonds represent median values for the distributions, with upper and lower quartiles shown as error bars.

Moreover, studies have shown that blue ellipticals/ETGs are what we are most interested in observing, as they are still evolving and have not yet reached the 'red and dead' stage (e.g. Kaviraj et al. 2011).

2.4.2 Concentration Index

The usefulness of concentration index for each test sample is demonstrated in Fig. 2.10, which shows plots made in the same style as Fig. 2.9. Each test sample will now be discussed based on its respective plot.

The KS14 sample indicates that using concentration index as a proxy works in an average sense - the mean points in Fig. 2.10 lie above the proxy cut for the ETGs and below for LTGs. However, a non-negligible percentage of late-types is found to lie above this line: 17% of Sbc and 10% of Sd respectively equates to 12% of all LTGs. Although lower than the 17% found for the colour proxy, this is not as low as would be preferred to create a truly robust sample. This also equates to a contaminated sample of 32%, which is unacceptable.

GZ1 classifications are plotted in a different manner to those of KS14. In this case, the elliptical and spiral classifications are further sub-divided into sub-mm detected and undetected, where detections are considered those galaxies with *Herschel* SPIRE 250 μm fluxes greater than 5σ. These divisions result in 7 detected ellipticals, 232 undetected ellipticals, 177 detected spirals and 584 undetected spirals. Unfortunately the number of detected ellipticals is very low, but this is unsurprising given the small size of the sample (1000 galaxies) with classifications that are not 'uncertain'.

Viewing the classifications in Fig. 2.10 reveals different results to those found for KS14. First of all, the majority of all ellipticals are above the proxy line. The small percentage of ellipticals lying below the line are H-ATLAS detected - these are the types of ellipticals this study is working to select, and therefore this plot

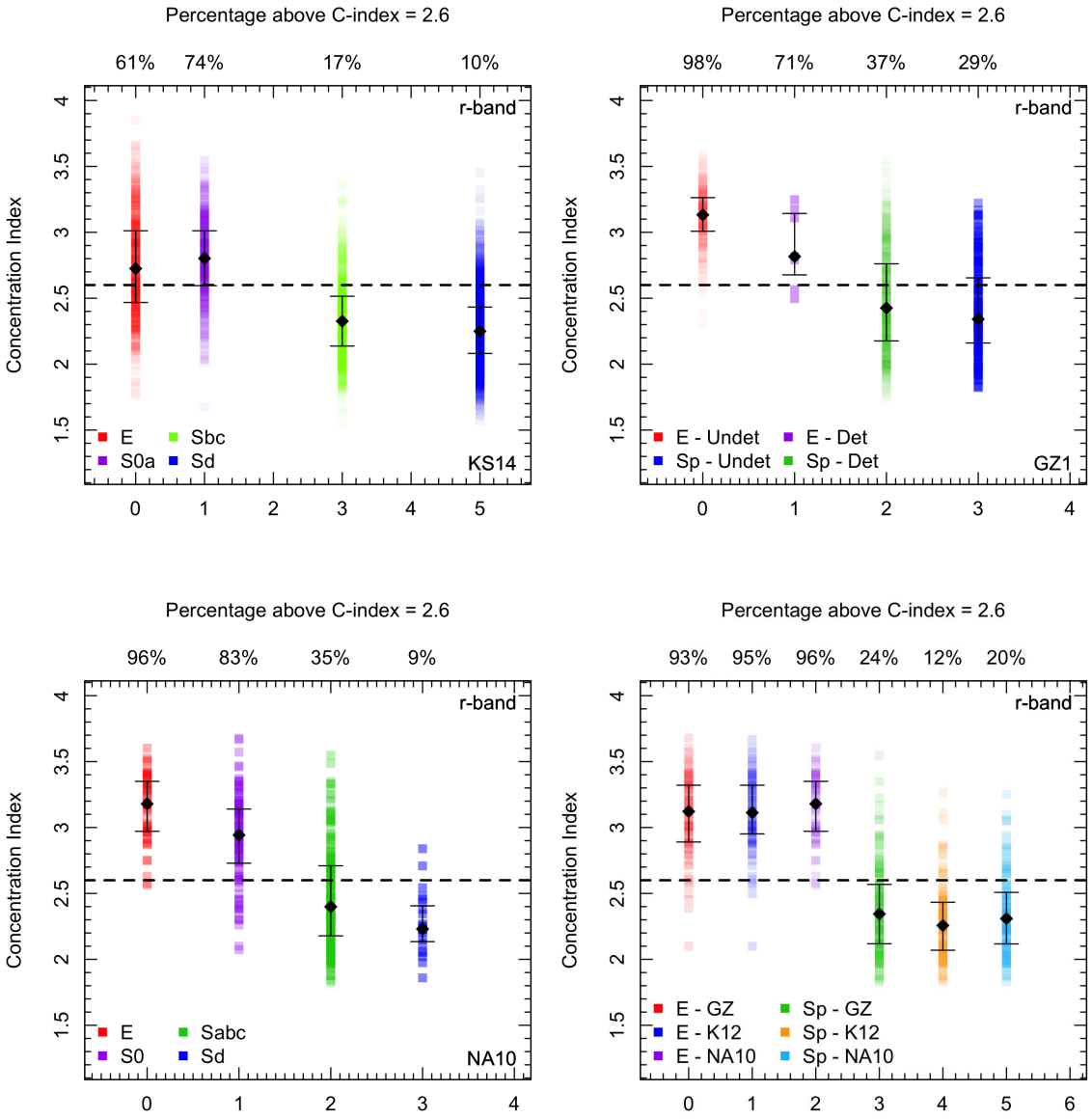

Figure 2.10: Plots showing how concentration index varies with morphology for the KS14 sample (top-left), GZ1 sample (top-right), NA10 sample (bottom-left) and overlapping samples (bottom-right). The x-axis does not represent any physical values, but is used to separate the different morphologies. Dashed lines indicate the concentration proxy cutoff. The percentages displayed above each distribution indicate the fraction of galaxies fulfilling this proxy within this morphological class. Diamonds represent median values for the distributions, with upper and lower quartiles shown as error bars.

indicates that concentration index may be a poor proxy for picking out these sub-mm detected ellipticals. Another point evident from this plot is the much higher percentage of late-types (31%) occupying the space above the proxy line compared to that from KS14. This is likely due to lenticulars being classified as spirals in GZ1 (see results in Table 2.4 and Fig. 2.7).

Moving on to the NA10 sample - given the more detailed classifications expectations are for similar results to KS14. This is not quite the case however - ETGs show higher percentages (86%) above the proxy line, as do LTGs (34%). The higher fraction of ETGs within the proxy cut is no doubt due to the separation of S0 and Sa[8] galaxies in their classifications. This should theoretically result in the percentage of LTGs within the proxy cut decreasing; as this is not the case, there is clearly some other issue in effect. This could be that a number of early-types were misclassified, or it may simply be a result of concentration index not acting as a very reliable proxy.

The final plot in Fig. 2.10 shows the results of this proxy cut for the overlapping sample. The population numbers are lower here, but it strengthens the point that concentration index has high levels of completeness for ETG selection, but also high levels of contamination by late-type galaxies (particularly Sb and Sc morphologies).

Fig. 2.11 shows the variation of both the reliability (left panel) and completeness (right panel) with concentration index value (based on KS14 classifications). The red line indicates the level for ETG selection and the blue line the level for LTG selection. The level chosen for this work (C=2.6) is also shown - it is clear from this plot that if the proxy level is increased the reliability of selection would also increase but the completeness decrease, and vice versa. Additionally, the results from GZ1 in Fig. 2.10 indicate that ETGs lost through increasing the proxy

[8]This choice of proxy groups Sa galaxies with the later-type spirals.

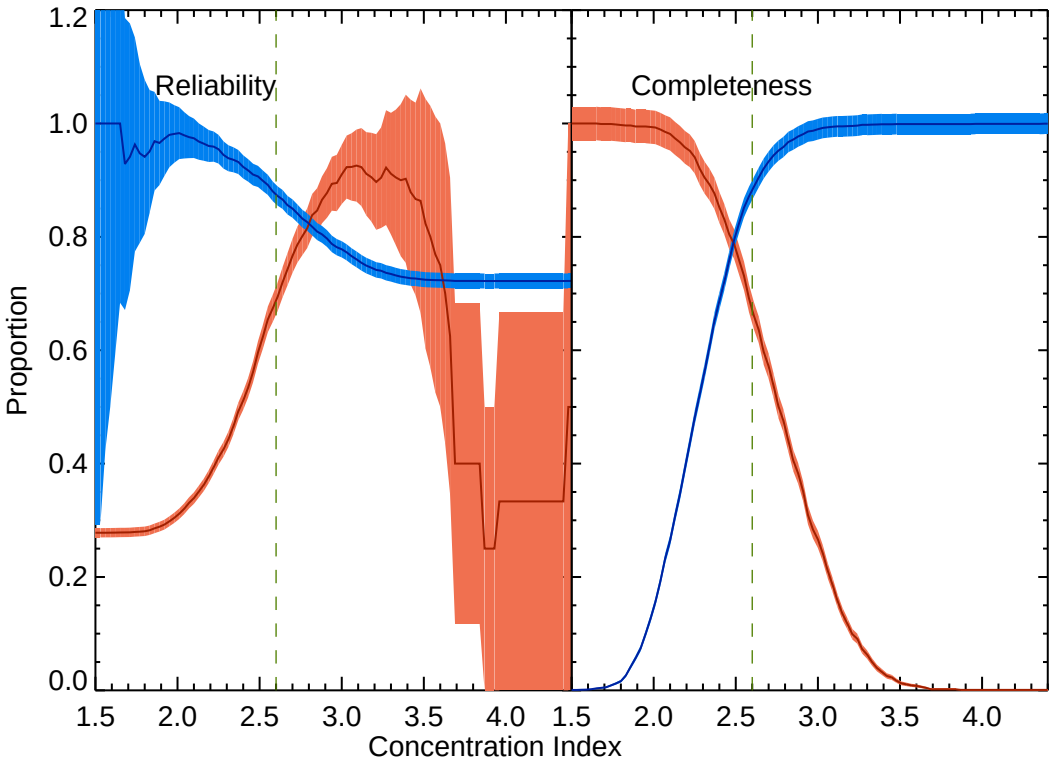

Figure 2.11: Plot showing reliability (left panel) and completeness (right panel; as defined in the main text) for the full range of possible concentration index proxy values. Red lines represent the results for a KS14 ETG selection, and blue lines represent the results for a KS14 LTG selection. The associated shaded regions represent Poisson errors on these values. Note the large dip in reliability at high concentration index is due to only one ETG fulfilling this criterion, evidenced by the large Poisson errors at C$\geq$3.7. The green, dashed line represents the selected value for the proxy cut (C=2.6)

level are likely to be sub-mm detected, compounding this issue. Therefore it is apparent that concentration index is not a proxy that should be used for this sampling.

2.4.3 Sérsic Index

As with concentration index, the variation of r-band Sérsic index with morphology is plotted for all four samples in Fig. 2.12. Beginning with the KS14 sample, the plot clearly shows the mean LTG points and quartile bars lie below the selected proxy value of n=2, but this is not the case for the ETGs, where the lower quartiles dip below n=2. The combination of eyeballing these distributions and the labelled percentages above each distribution indicates that the Sérsic proxy for this sample is generally quite strong, but has a completeness of 73% and a reliability of 69%. This leaves a 31% contamination factor within an ETG sample selected by this proxy.

The GZ1 classifications are once again shown in terms of sub-mm detected and undetected. Unlike with concentration index, the Sérsic index cut has full completeness for these classifications, even though once again the detected systems have a lower mean Sérsic index. Unfortunately, there is a very high level of contamination (38%) by LTGs in this plot.

NA10 classifications in the third plot show the mean Sérsic index of Sabc spirals is just above the proxy line, leading to a 53% contamination by these systems. Such high contamination will again be partially due to the inclusion of Sa galaxies which are dominated by a bulge component - a single Sérsic decomposition will mainly trace this component, resulting in a higher Sérsic index for the profile. In all there is a total 51% of NA10 late-types falling within this proxy cut. It would seem that the contamination from LTGs based on this proxy is worse than that from concentration index.

Once again the results from the overlapping sample show that in an average sense, Sérsic index as a proxy does work. Mean values for all the elliptical classifications are centred around n=4, and between $1 \leq n \leq 2$ for spirals. Completeness is very high for these samples, but there is a large amount of contamination by LTGs up to even higher Sérsic indices.

The value at which this Sérsic proxy cut is made is investigated in Fig. 2.13. Moving it lower does not make sense physically, as n=1 is the prescribed exponential profile used to fit a disk. Additionally, the reliability of the sample would become very small $\sim$35%, and completeness would not improve. However, shifting the proxy cut upwards to n=2.5,3.0 or 3.5 would cause the Sérsic profile to become more like a de Vaucouleurs (bulge) profile - a strong physical motivation. Whilst this would improve the reliability of such a cut (at n=3.5 the reliability would be 80%), it would also decrease the completeness severely (37% for n=3.5). Such a cut would be drastic, and would certainly decrease the size of any ETG sample by a large amount. For these reasons, it appears that there is no advantage in using a different Sérsix proxy cut.

2.4.4 To Proxy or Not to Proxy?

Finding a morphological proxy that can be used to create a simultaneously large, complete and uncontaminated sample of ETGs is a driving factor behind the work being done in this Chapter. The strengths of such a proxy are clear: it removes the need for the time-consuming process of visual inspection, and it is computationally inexpensive compared to other automated classification methods. However such morphological proxies are handicapped by their very definition: by associating a morphological type with a physical parameter the user is essentially making assumptions about a galaxy classification which might be inaccurate.

The combination of the proxy distributions by morphology and completeness

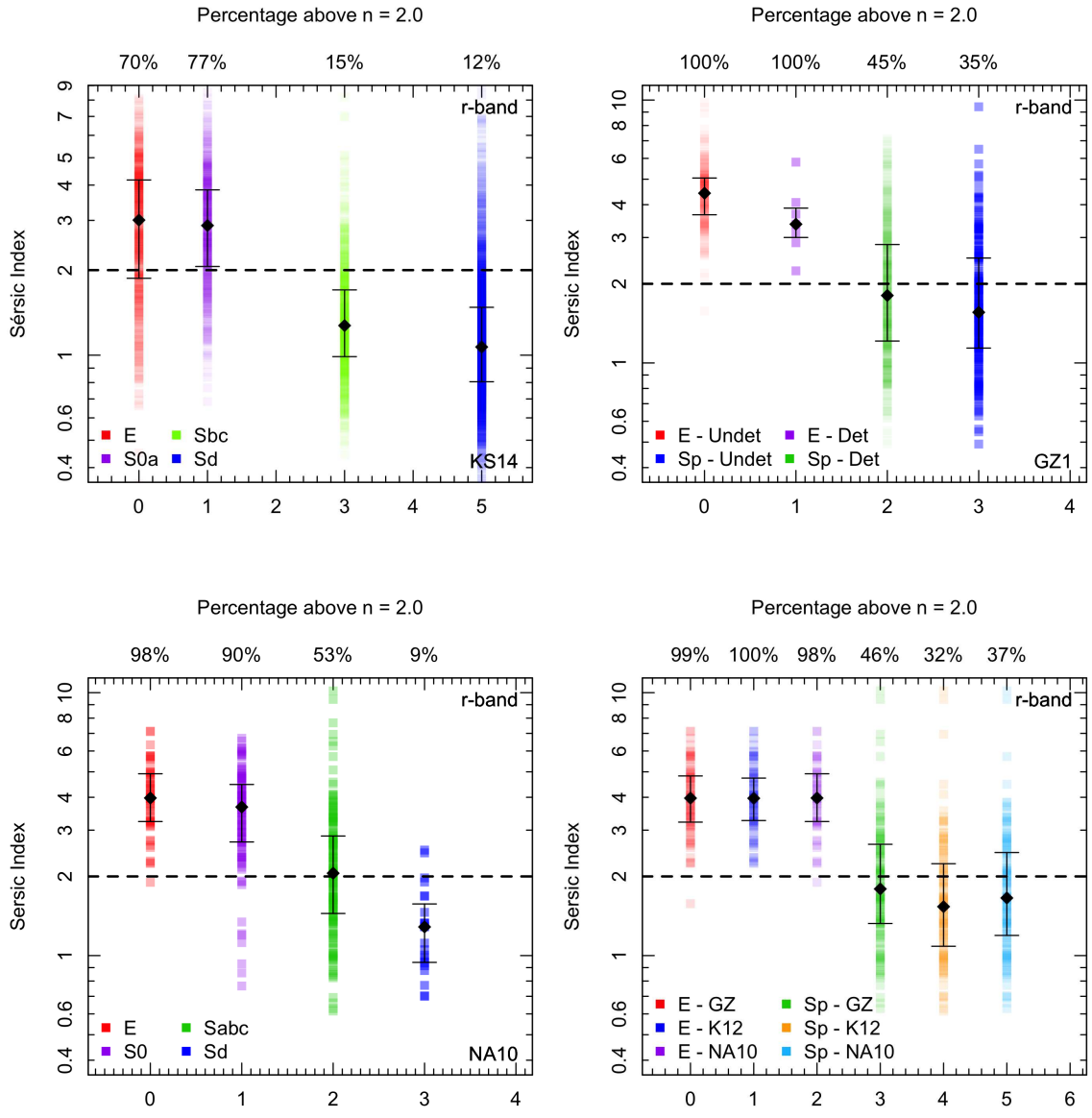

Figure 2.12: Plots showing how Sérsic index varies with morphology for the KS14 sample (top-left), GZ1 sample (top-right), NA10 sample (bottom-left) and overlapping samples (bottom-right). The x-axis does not represent any physical values, but is used to separate the different morphologies. Dashed lines indicate the Sérsic proxy cutoff. The percentages displayed above each distribution indicate the fraction of galaxies fulfilling this proxy within this morphological class. Diamonds represent median values for the distributions, with upper and lower quartiles shown as error bars.

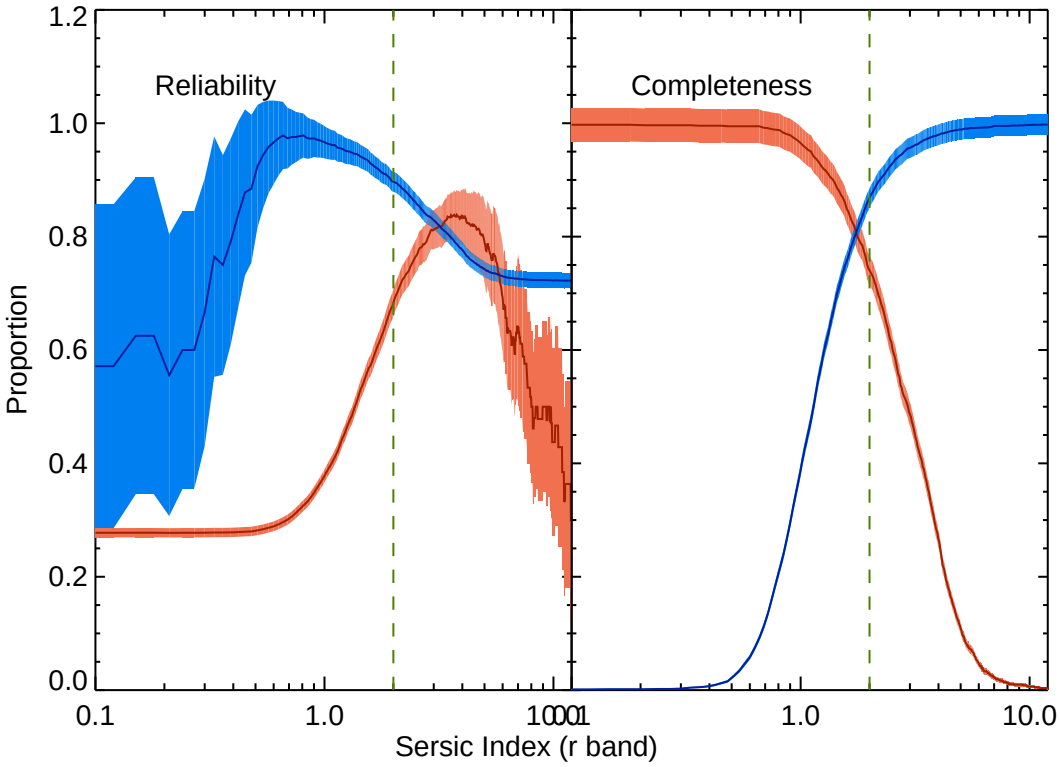

Figure 2.13: Plot showing reliability (left panel) and completeness (right panel; as defined in the main text) for the full range of possible Sérsic index proxy values. Red lines represent the results for a KS14 ETG selection, and blue lines represent the results for a KS14 LTG selection. The associated shaded regions represent Poisson errors on these values. The green, dashed line represents the selected value for the proxy cut (n=2.0)

versus the reliability results in the above sections gives a full overview of the advantages and disadvantages of each of the selected morphological proxies. This should allow for a decision to be made about which proxies can be utilised to create a robust, optically-selected, sub-mm detected sample of ETGs.

Colour is be ruled out due to the large contamination effects from reddened LTGs. Additionally colour relates directly to the ongoing or recent star formation within a galaxy; using red colour as a proxy for ETGs makes the assumption that there is no such activity ongoing within these systems.

Concentration and Sérsic index both have their justifications for being used as proxies. They are both linked to the surface brightness profile of a galaxy, although concentration index can be thought of as a cruder measurement of this property, whereas Sérsic index is calculated from a parameterised model that accounts for the effects of sky background and neighbouring objects. However, they are based on the physical assumption that ETGs are more centrally concentrated, whereas LTGs have a more extended light distribution due to their extended disks. Fig. 2.13 reveals the fallacy of this idea, since very high Sérsic index is not a reliable indicator of ETG morphology. Testing the level at which either a concentration or Sérsic index cut is made reveals that higher values will dramatically reduce ETG completeness whilst lower values will inject greater numbers of LTGs into the samples.

However, it is clear from the results shown above that neither of these parameters serves as an optimal proxy for ETG selection. The reliability of the concentration parameter is considerably better than that of Sérsic index, but completeness is not optimum. Should concentration index be used, a lot of potentially interesting ETG systems will be missed out from the samples. Sérsic index shows improved completeness to concentration index, but suffers from a deterioration in the reliability. A sample chosen based on this proxy would include most of the

interesting systems, but also many LTGs. A combination of the two parameters would also not work, as this would severely reduce the completeness, even though reliability might be improved.

Kelvin et al. (2012) advocated using a combination of colour and Sérsic index as a proxy for ETGs. However once again the inclusion of colour means that there are potentially many blue ETGs that are missed out of the resulting sample. Their argument is that by using a diagonal cut-off on the colour-Sérsic index diagram, red systems with low Sérsic index will be included within the ETG class, as will blue systems with high-Sérsic index. However, as shown later in this thesis, it is possible to have ETGs with both low Sérsic index and blue colours, and therefore such a classification method still suffers from a lack of completeness. Additionally, reddened spirals are likely to fit into the red systems with low Sérsic index category, thereby decreasing the reliability of such a method.

There is therefore a very clear conclusion from the above. Morphological proxies do work on average for the creation of samples, as long as the user is willing to put up with either a certain amount of contamination, or suffer from a lack of completeness (depending on the chosen proxy). However for our purposes, a sample with any form of contamination will significantly detract from the strength of our results, and a sample which is missing the 'rarer' ETGs due to lack of completeness will not represent the full distribution of systems that should be examined. Hence morphological proxies will not be used for this work, and visual classifications will instead be the selected method of galactic classification.

2.5 Wavelength effects on Derived Parameters

Both concentration and Sérsic index proxies described in this chapter are optical r-band parameters. This choice of waveband is based upon the following: SDSS and GAMA match all their photometry to r-band apertures, hence providing only

Petrosian r-band parameters, from which the concentration index is derived. The r-band is the central optical band with the least noisy data, therefore models fit to these data have less uncertainty than (for example) the u band, which has a very low signal-to-noise ratio. Furthermore the r band is longward of the UV bands which track young, massive star formation, and yet at shorter wavelengths than the NIR bands which trace the old, low mass stellar population.

However, this concept of different wavelengths tracing different stellar populations introduces the point that different wavebands also trace different components of the galaxy itself. Therefore both simple (e.g. concentration index) and parametric profile measurements (e.g. Sérsic index, size or magnitude) of a galaxy will be biased according to the waveband in which they are measured: bluer bands will better reflect the extent and light distribution of the young stellar population whereas redder bands will better trace the distribution of stellar mass.

The GAMA database contains multi-band photometry, allowing each band to be fit with a completely independent model (Kelvin et al. 2012). This is where the r-band Sérsic index values in this section are taken from. However, fitting light profiles to each waveband in this way means that no information can be carried across and throughout the photometry. For example, a light profile fit to a g-band image might find a spiral galaxy to contain a low Sérsic index which is based on the contribution from the disk. However, when an independent profile is fit to the H-band image of the same galaxy, a much higher Sérsic index may give the best model fit as the disk might fade into the background noise and the image will be dominated by the spiral galaxy's bulge. It is likely that light profile fitting will be more meaningful if multi-band images can be fit simultaneously, thereby utilising all the available information in the fitting process.

This is the approach adopted by the MegaMorph team (Häußler et al. 2013; Vika et al. 2013). It has adapted the Sérsic profile fitting program GALFIT3 (Peng

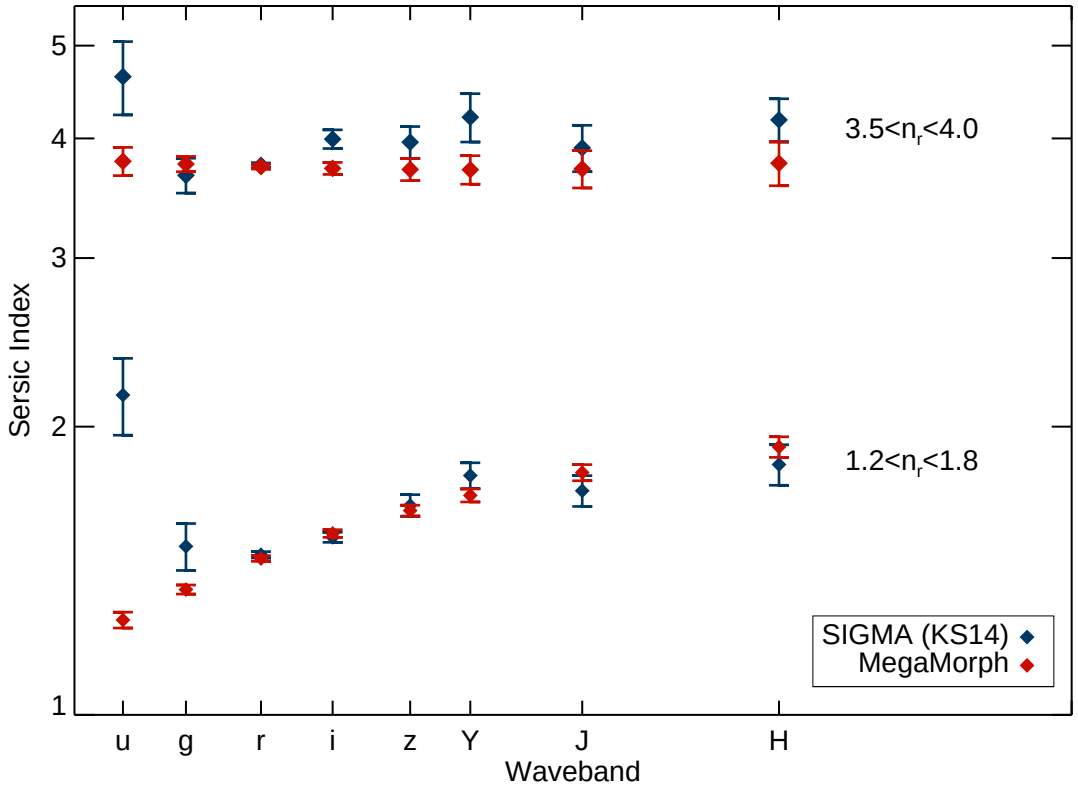

Figure 2.14: Variation of Sérsic index as calculated by SIGMA (blue) and MegaMorph (red) for KS14 galaxies matched to MegaMorph data. The top subset represents average values for those galaxies with $3.5 \leq n_r \leq 4.0$ (48 in SIGMA and 49 in MegaMorph) and the bottom subset those galaxies with $1.2 \leq n_r \leq 1.8$ (243 in SIGMA and 268 in MegaMorph). Error bars represent the error on the mean for each subset.

et al. 2010) to fit a full wavelength-dependent model to a subset of the GAMA galaxies (primarily the G09 field). In its original form, GALFIT3 performs a profile fit with free galaxy model parameters, of which we are interested in the galaxy effective radius, magnitude, and Sérsic index. The modified form (called GALFITM), replaces each of these parameters with a wavelength-dependent function. MegaMorph's function of choice is currently a Chebyshev polynomial and is not intended to be physically meaningful, but it can be used to calculate the value of each free parameter in between the observed bands (i.e. it can be used to calculate rest-frame results). This code is still a work in progress but is currently working well for single Sérsic profile fits. The ultimate aim of the project is to have a MegaMorph code which can fit multi-component Sérsic profiles to a large, multi-wavelength, galaxy dataset.

At this point in time, MegaMorph has provided fits for 52,266 galaxies in the GAMA I G09 database (Boris Häußler, priv. comm.). There are 43,493 (83%) galaxies within this set that have not hit any of the hard-coded or user-set constraints. These are put into effect to ensure that output parameters are physically meaningful (e.g. removing negative sizes) as well as to improve the efficiency of the fitting process. Combining these results with the galaxies in the KS14 sample gives a subset of 1186 'good' fits, which allows some flexibility in examining the effect of this fitting process in comparison to single-band fits with SIGMA.

Fig. 2.14 compares the single-component Sérsic indices from SIGMA (used in KS14) with those from MegaMorph. The plot shows the variation of Sérsic index with wavelength for two subsets of the MegaMorph sample. The upper points are mean values for all galaxies with fit r-band Sérsic index between 3.5 and 4.0, whilst the lower set of points are those galaxies with fit r-band Sérsic index between 1.2 and 1.8. Note that the r-band values for both types of fitting sit on top of each

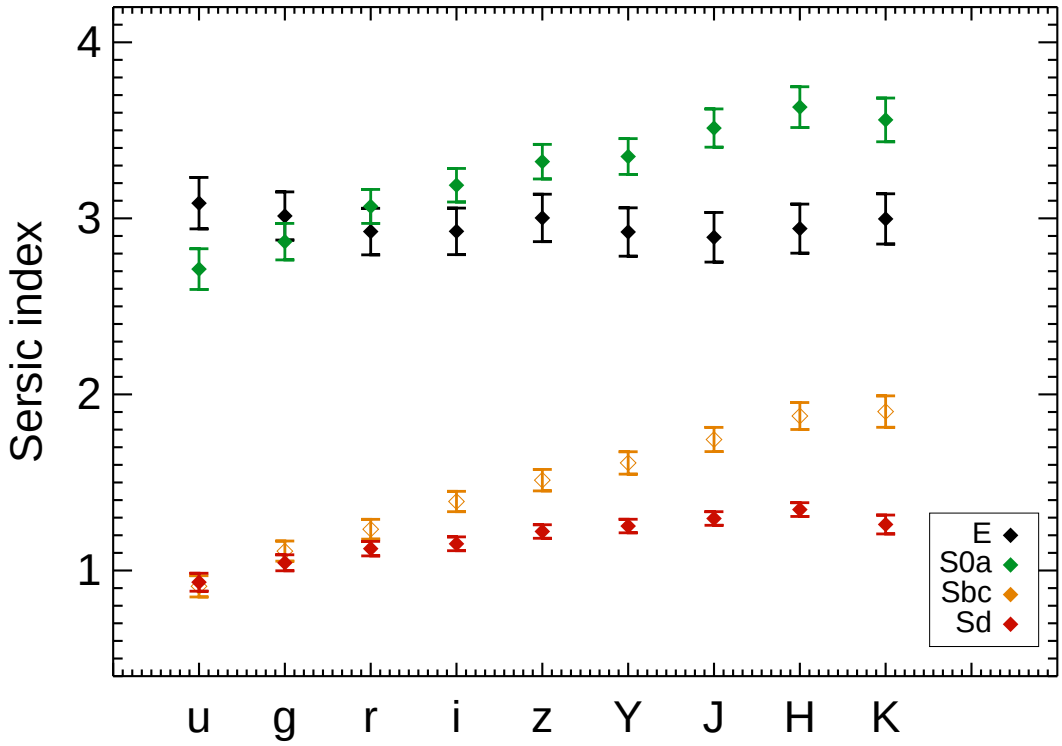

Figure 2.15: Mean values of the Sérsic index and associated standard deviations are presented as diamonds and error bars respectively. KS14 morphological types are coloured as described in the legend. Sérsic indices are derived using MegaMorph, where a function is fit to images in all wavebands simultaneously.

other, indicating the constraints on each subset.

Fig. 2.14 clearly shows the smooth variation of Sérsic index with wavelength for the MegaMorph fits. More importantly, it highlights the noise in fitting independent profiles to each waveband, as done with SIGMA. The bands which have a lower signal-to-noise ratio (e.g. u, z and Y) show the most scatter in this respect. There is no physical reason why a galaxy would have a profile of n_u ∼2.2 which then dramatically decreases to n_g ∼1.6 over a wavelength gap of only ∼1200 Å, which is what is being seen in Fig. 2.14 for the SIGMA fits. This would be more understandable if the variation took place over a much larger wavelength range, such as from the u band to the H band.

It is clear from Fig. 2.14 that there is a strong physical motivation for this type of Sérsic profile fitting. For the purposes of this thesis, it is useful to understand how the wavelength variation of Sérsic index differs for all morphological types. This is explored in Fig. 2.15, where the mean Sérsic index for the KS14 morphological types is plotted as a function of wavelength. As expected, ETGs have higher average Sérsic indices than LTGs. However, the interesting aspect of this plot is the difference in the wavelength variation. ETGs have a fairly steady average Sérsic index with wavelength, although lenticulars do tend to higher Sérsic index with longer wavelength. However LTGs (particularly Sbc type LTGs) demonstrate a smooth increase in Sérsic index with increasing wavelength. This is the result of longer wavebands better tracing the stellar mass of a galaxy, the majority of which resides in the bulge. Note that the Sd morphologies do not show this same increase with wavelength - this is likely due to their bulges being almost non-existent.

This variation lead to the MegaMorph team investigating further correlations with morphology. They found that normalising the derived Sérsic indices and effective radii by a single band value (in this case we normalise by the g-band Sérsic index and effective radius) effectively separates the morphologies quite neatly (Boris

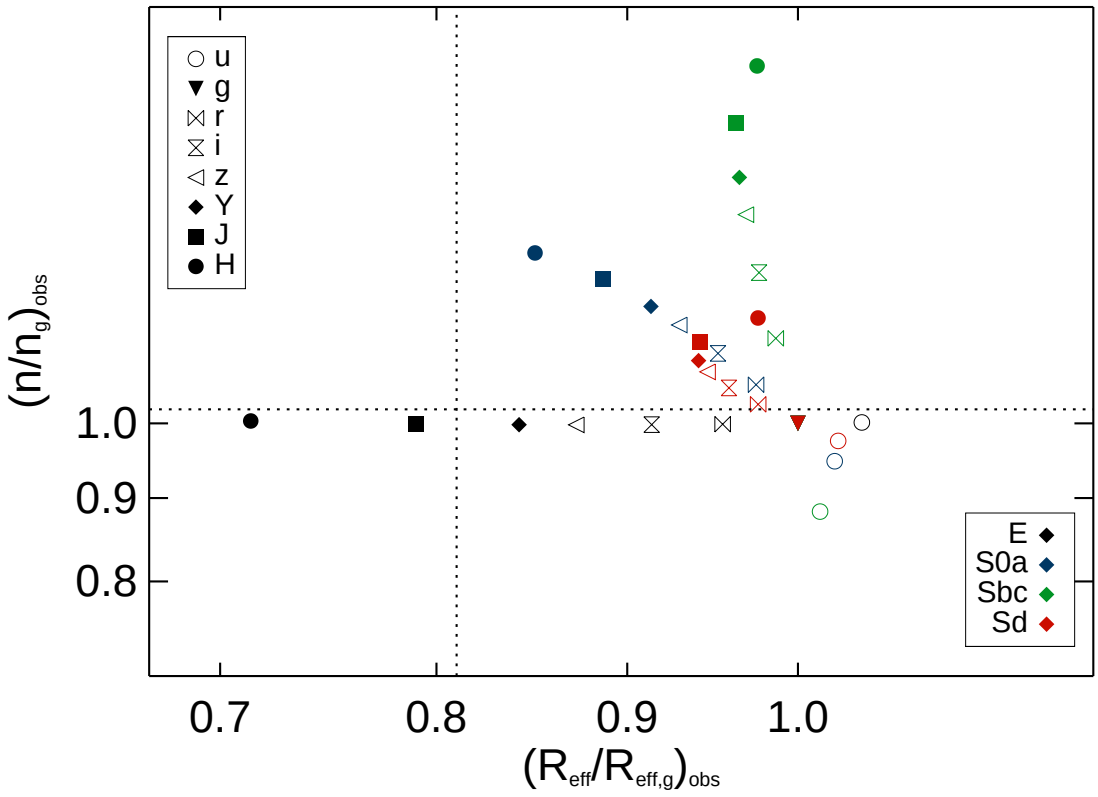

Figure 2.16: MegaMorph's mean normalised Sérsic index plotted against the average normalised effective radius, coloured by morphology. Different symbols represent different wavebands.

Häußler, priv. comm.). However, they currently do not have a visually classified sample with which to test this - their tests are run on samples divided by colour and Sérsic index (Vulcani et al. 2014). This normalisation is replicated with the larger KS14 sample in Fig. 2.16, where the galaxy morphologies are plotted in different colours for average normalised Sérsic indices and average normalised effective radii. Observe the lack of variation in normalised Sérsic index for the elliptical morphologies but significant variation of effective radius - this points to substantial differences in the stellar population age as a function of radius, but these will not result in any change in profile shape. This is reversed for Sbc morphologies, which show almost no variation in their sizes - this suggests that the bulge component in these systems is not substantially smaller than the disk. Otherwise the effective radius would vary as MegaMorph preferentially fits the disk as shorter wavelengths, and the bulge at longer wavelengths.

Within these morphological types, the Sd population shows the most unexpected variation for these normalised parameters. Neither the effective radius nor Sérsic index varies more than $\sim$0.1 in either direction, yet the values do not remain constant with wavelength either. These galaxies are possibly the most homogeneous in terms of stellar populations, hence the lack of variation in size. The lack of bulge in these systems is likely to be the cause of the almost constant Sérsic index.

Vulcani et al. (2014) indicate that this plot may be the starting point of a new type of morphological classifier. It is possible that in future years this may be the case; MegaMorph has provided new insight into the world of galaxy profiling and with further work this may become the standard for fitting parametric models to galaxies.

2.6 Conclusions

This Chapter gives a full account of the work completed in testing a number of different morphological proxies on three test samples. The visual classifications associated with each of these samples have different defining criteria, each of which has its own merits. Below is a summary of each of these samples.

1. Kelvin et al (KS14) Sample:

   4110 galaxies in GAMA I equatorial regions.

   Classifications of E, S0a, SB0a, Sbc, SBbc, Sd.

   Three classifiers with previous classifying experience.

2. Galaxy Zoo 1 (GZ1) Sample:

   2186 galaxies matched to GAMA I equatorial region data.

   Classifications of elliptical, spiral and uncertain.

   Numerous classifiers with little/no classifying experience.

3. Nair & Abraham (NA10) Sample:

   348 galaxies matched to GAMA I equatorial region data.

   Classification by T-type (see Table 2.2).

   Single classifier with previous classifying experience.

The visual classifications associated with each of these samples are compared for an overlapping sample consisting of 245 galaxies. On average the KS14 and NA10 samples show good consistency in their classifications (they agree on 65% of defined ETGs; Fig. 2.6), but this is less true when contrasting the KS14 and GZ1 samples (27% agreement in this case). However when comparing with the GZ1 sample it

is important to note that ∼50% of the classifications are uncertain. This is due to the restrictions on their classification percentages (see Section 2.2.1).

Once the strength of the classifications was determined, three different morphological proxies were identified as being candidates for ETG selection. These are optical colour, concentration index and Sérsic index. Colour was dismissed as a viable option as it became clear that most ETGs are red, but not all red galaxies are ETGs. Studies in the literature have suggested that there is also a population of blue, FIR detected ETGs; this coupled with the high LTG contamination (35%) indicates that colour is an unsuitable proxy for ETG selection.

Concentration and Sérsic indices are next examined and both show high completeness for ETG selection. However the contamination from LTGs is at $\gtrsim$30% for both concentration and Sérsic index (see Figs. 2.11 and 2.13). Therefore, should an ETG sample be created by using either of these parameters to set a proxy cut, the results for said sample would have a 10% weighting by parameters associated with LTGs. When taking FIR emission into account, and the calculated dust masses associated with such FIR emission, this 10% could equate to at least a factor of two higher average dust mass. This is non-negligible when attempting to trace the dust properties of ETGs.

Given the results of this proxy testing, it is clear that morphological proxies have not advanced to the stage where they can be used to accurately define a complete sample of ETGs. Therefore, visual classifications will be used to classify ETGs for the remainder of this thesis.

Chapter 3

Linking the Properties of Sub-mm Detected and Undetected Early-Type Galaxies

It does not do to leave
a live dragon out of your calculations,
if you live near him

J.R.R. Tolkien, The Hobbit

3.1 Introduction

Properties typically associated with ETGs include red colours, lack of star formation and smooth, spheroidal structures. Chapter 1 has given a detailed account

of where ETGs lie in many relations, including the Hubble Sequence, colour-magnitude diagram and MDR. Chapter 2 discussed how these associated characteristics might be utilised as proxies for sample selections; the main result of this study indicated that proxies such as concentration index, Sérsic index and colour result in $\gtrsim$30% late-type contamination and therefore should not be used to create a fully complete and uncontaminated sample. Additionally, proxy completeness results indicate that many ($\sim$80%) ETGs can be associated with a high concentration or Sérsic index but this is not the case for all ETGs. The ETGs that are not characterised by these properties may be rare objects in the Local Universe and, furthermore, will be difficult to select as they lack the aforementioned ETG-like properties. Therefore we choose to base our ETG selection only on visual morphology. In this Chapter, sub-mm detected ETGs (i.e. those which contain significant dust in emission) will be studied and compared to undetected ETGs.

There are several aims which will be addressed in this Chapter. First of all, to create a sample of sub-mm detected ETGs that is statistically representative and larger than previously studied samples. This presents several challenges: it is clear from Chapter 2 that proxies are not ideal for the creation of such samples, particularly when trying to resolve between galaxies in the ETGs class. Moreover, as studying the dust properties of these ETGs is a primary motivation for this thesis, even small numbers of LTGs (which are known to contain large amounts of cold dust and gas) contaminating this sample might change the results significantly.

The next goal for this chapter is to identify how such a sample compares to non-detected ETGs when considering structural, colour and environmental properties. The results from such comparisons are required to address questions about where these ETGs sit on the aforementioned colour-magnitude and morphology-density relations. More specifically, do these sub-mm detected ETGs have more in common

with undetected ETGs or with the LTG class? Do they have star formation rates consistent with quiescent ETGs or active LTGs? This topic in particular has been explored for small samples in the past years: Combes et al. (2007) find that CO-rich ETGs have higher star formation rates than CO-poor ETGs; Kuntschner et al. (2010) also find that some ETGs that are fast rotators contain flattened components, which display active star formation signatures, whereas slow rotator ETGs don't display this feature. More recently Bayet et al. (2013) discovered that ATLAS^{3D} CO-rich ETGs display star formation activity analogous to that at the centre of the Milky Way.

Another primary goal within this study is to derive dust temperatures and masses for the sub-mm detected ETGs. Once again these can be used to compare with published LTG dust properties, as well as those presented for small samples in previous *Herschel* literature (as described in Section 1.3.4). Such properties also also make it possible to observe what correlations exist with this dust - previous works have typically contained biases or selection effects in the sample creation, or have been too small to pick out any real trends. Additionally, with the availability of GAMA multi-wavelength data and parameters for ETGs in this analysis, it is possible to explore a large number of potential correlations with the dust.

This chapter utilises the GAMA UV/Optical/NIR Phase 1 data and H-ATLAS FIR/sub-mm Phase 1 GAMA-matched sources to study different subsets of ETGs. The creation of sub-mm detected and undetected samples, with particular emphasis on the reduction of contamination at all wavelengths whenever possible, is described, as are the tests and results based on these samples. A ΛCDM cosmology of Ω_M=0.3, Ω_Λ=0.7 and H_0=$100h\,\mathrm{km\,s^{-1}Mpc^{-1}}$ with h=0.7 is assumed, and used to calculate any cosmological parameters including luminosity and angular distances. The selection criteria for the two samples of ETGs used in this chapter are described; these are the optically selected GAMA/H-ATLAS matched

sample and the optically selected sub-mm undetected GAMA sample. Diagnostic plots and tests are presented in Section 3.3, including host galaxy properties such as stellar mass, UV luminosities and environments. Dust temperature and dust mass properties are derived and examined in Section 3.4. Conclusions are given in Section 3.6.

3.2 Early-type Galaxy Sample Selection

We choose the KS14 sample as our parent sample; this is fully described in Section 2.2.1. Choice of this sample was based on the need for visual classifications at relatively low redshift, completed by multiple separate classifiers; this latter requirement is to reduce the level of subjectivity as much as possible.

The distribution of this KS14 parent sample in optical colour and Sérsic index space is shown in Fig. 3.1, where Sérsic indices are extracted from GAMA Sérsic photometry fits (Kelvin et al. 2012) and colours are the restframe colours taken from Stellar Population Synthesis modelling of the optical spectral energy distributions (SEDs; Taylor et al. 2011). The classifications resulting from the previously described eyeballing are illustrated by colours identified in the colour bar. This plot gives us an indication of the properties of each galaxy type. It shows that as we go to later types, both colour and Sérsic index properties decrease on average. This can be interpreted as earlier types tending towards redder colours and less exponential Sérsic profiles (n >1), a result consistent with previous studies such as Peng et al. (2002),Blanton et al. (2003),Driver et al. (2006),Haines et al. (2008),and Kaviraj et al. (2011). This plot highlights once again the difficulty of separating galaxy morphologies based on these parameters.

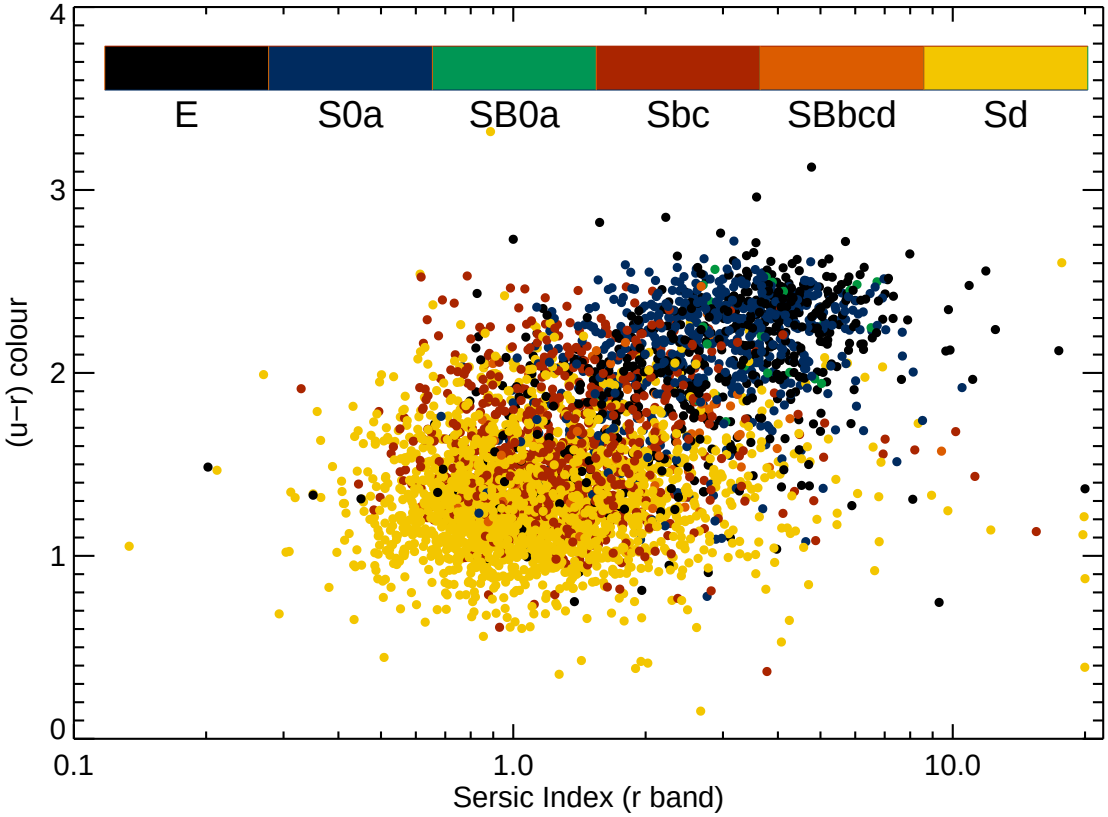

Figure 3.1: Optical colour versus Sérsic index of the visually classified KS14 parent sample, coloured by galaxy type.

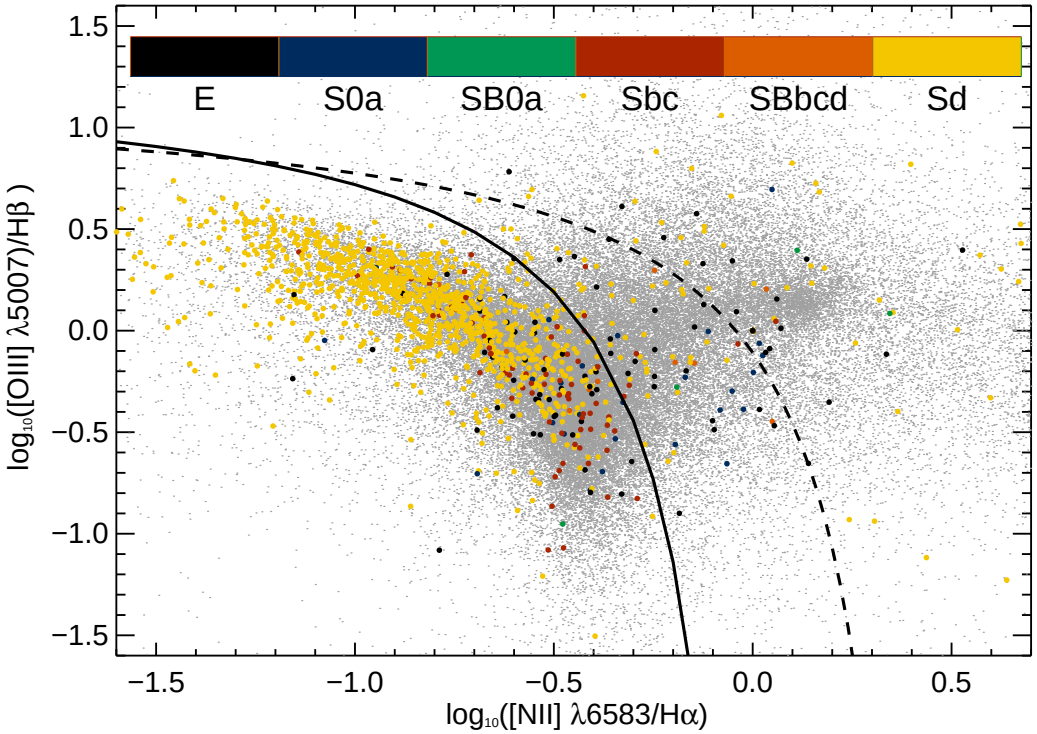

Figure 3.2: This BPT diagram shows the flux ratios of [OIII] λ5007/Hβ emission lines against [NII] λ6584/Hα emission for all GAMA emission line galaxies (grey points), with the Kauffmann et al. (2003a) AGN dividing line shown as the solid black line and the Kewley et al. (2001) dividing line as the dashed black line. Visually classified galaxies with ID-matched emission lines are shown and coloured according to their morphological classification.

	E		**S0a**		**SB0a**		**Sbc**		**SBbcd**		**Sd**	
	SF	*AGN*	*SF*	*AGN*	*SF*	*AGN*	*SF*	*AGN*	*SF*	*AGN*	*SF*	*AGN*
Emission-line galaxies	71	83	20	18	1	3	74	10	6	5	1136	224
H-ATLAS detected	2	2	7	6	0	1	39	5	6	4	27	3
H-ATLAS undetected	69	81	13	12	1	2	35	5	0	1	1109	221

Table 3.1: Galaxies in our KS14 parent sample with emission lines are divided into star-forming (SF) and active galactic nuclei emitting (AGN). Numbers shown here are divided into H-ATLAS detected (102 galaxies) and those which are undetected by H-ATLAS (1549 galaxies). They are additionally separated into their morphological classifications.

3.2.1 Removal of Active Galactic Nuclei

As the key focus of this work is to compare the properties of two samples of ETGs, it is necessary to make sure the properties obtained accurately represent the ISM of the host galaxies. Therefore the dust heating contribution (or sub-mm emission) from AGN should be avoided for these purposes. For these reasons AGN are now selected and removed from the KS14 parent sample.

Foster et al. (2012) use the Gas and Absorption Line Fitting (GANDALF; Sarzi et al. 2006) algorithm to measure stellar emission lines from flux calibrated GAMA spectra. They define galaxies with significant emission lines as those with 3σ levels in Hα, Hβ and [NII]λ6584 lines. With their results, a BPT diagram (Baldwin et al. 1981) is produced for GAMA galaxies with these and [OIII] lines (see Fig. 3.2). Emission-line galaxies in the KS14 parent sample are over-plotted to indicate their distribution and are again coloured by eyeballed morphology. Based on the prescription by Kauffmann et al. (2003a) (Eq. 1), the dividing line between star-forming galaxies and AGN-dominated galaxies is shown, in the form:

$$\log\left(\frac{[\mathrm{OIII}]}{\mathrm{H}\beta}\right) = \frac{0.6}{\log\left(\frac{[\mathrm{NII}]}{\mathrm{H}\alpha}\right) - 0.05} + 1.3. \tag{3.1}$$

This line identifies the upper limit for emission line measurements which are representative of pure star formation in the BPT plot. Fig. 3.2 also shows the Kewley et al. (2001) upper limit line (Eq. 3.2) for extreme starburst limits:

$$\log\left(\frac{[\mathrm{OIII}]}{\mathrm{H}\beta}\right) = \frac{0.61}{\log\left(\frac{[\mathrm{NII}]}{\mathrm{H}\alpha}\right) - 0.47} + 1.19. \tag{3.2}$$

Note that this latter relationship is not the AGN identifier of choice, and is only shown for comparison as a soft limit. All galaxies above and to the right of the Kauffmann dividing line are considered to have optical AGN emission.

Matching the KS14 parent sample to the GANDALF emission lines catalogue (Foster et al. 2012) gives 1651 (40%) matches for emission lines. From this selection, 343 (21%, and ∼8% overall) galaxies are dominated by AGN and 1308 (79%, and ∼32% overall) are star-forming. Lack of significant emission lines is the chief cause of unmatched galaxies. The colour selection in Fig. 3.2 indicates how these are divided by morphology and quantitative results are shown in Table 3.1. The first row in Table 3.1 shows that early-types (E, S0a and SB0a) have larger proportions of their emission-line galaxies identified as AGN (∼59%) than later-types (∼26%). However, both Table 3.1 and Fig. 3.2 show that late-types preferentially occupy the BPT diagram and for the KS14 parent sample, emission from these late-types is most likely powered by young stars rather than AGN.

For the next stage of this sampling, all galaxies with optically identified AGN emission are removed from the KS14 parent sample, leaving 3767 galaxies to pick ETGs from. The following section describes how those galaxies classified as E or S0a by Kelvin et al. (2014) are used to form the two samples which are the subject of this chapter.

There are some potential impacts associated with the removal of those galaxies with AGN signatures. If the presence of AGN emission correlates with any of the parameters that we are planning to probe later, the results and trends found for such parameters may be biased in some way. In particular, it is well known that AGN emission correlates with the presence of dust (e.g. Jaffe et al. 2004); however, as shown in Table 3.1, only eight galaxies with *Herschel* detections have AGN signatures (a significantly small proportion compared to the number of potential ETGs with *Herschel* detections). Such a small percentage is therefore unlikely to bias the results associated with dust.

The number of non-detected ETGs with AGN signatures is significantly higher, and if star formation rates were to be examined for these ETGs, the removal of such a percentage would likely bias the results quite strongly. However, star formation is not one of the parameters that will be examined for the non-detected ETGs, and therefore this is not considered to be an issue.

3.2.2 H-ATLAS Detected and Undetected Samples

Two samples were created from the remaining visually classified ETGs: the optically selected, sub-mm detected, ETG Sample (*SubS*), and the optically selected, sub-mm undetected, ETG Sample (*OptS*). *SubS* is the eyeballed sample of E (elliptical) and S0a (lenticular/early Sa spiral) galaxies which have highly reliable positional matched detections in both GAMA and H-ATLAS. *OptS* is the eyeballed sample of GAMA ETGs which do not have H-ATLAS detections (5σ in any SPIRE waveband).

Additional selection criteria were also imposed to form these samples. These included an independent visual check on these galaxies to remove any objects with obvious spiral arms. This was a necessary additional criterion as spiral structure was not accounted for in the eyeballing by Kelvin et al. (2014). As described in

Criterion	***SubS***	***OptS***
Detected/Undetected	326	787
Remove spiral structure	−5	−19
Remove AGN/LINER signatures	−8	−93
Remove high ellipticity	−39	−92
Remove low effective radius	−30	−32
Remove low reliability	−15	−0
Final count	229	551

Table 3.2: The selection criteria for the creation of *SubS* and *OptS* samples, as described in the main text. A full accountancy of the number of galaxies removed in each step is also given. The first step shows the initial division of the 1113 KS14 ETGs into H-ATLAS detected and undetected.

Section 3.2.1, galaxies characterised by optical AGN and LINER emission were removed. An ellipticity cut of $(1 - (b/a)) \leq 0.7$ was set to remove any edge-on disk galaxies. Additionally all sample ETGs with an effective radius less than the seeing FWHM ($1.2''$) were removed to minimise any uncertainty in parameters related to seeing. For the H-ATLAS detections, fifteen galaxies which had low reliabilities were removed, as they are considered likely to be false counterparts. These classification steps are all described in Table 3.2, and the number of galaxies removed in each step are also accounted for here.

The resultant samples included 229 ETGs (29% ETGs, divided into 33% E and 67% S0a) in the *SubS* and 551 ETGs (71% ETGs, divided into 54% E and 46% S0a) in the *OptS*. Therefore the sub-mm detected ETGs are more dominated by lenticulars. Examples of *SubS* Es are shown in Fig. 3.3 and S0as in Fig. 3.4. Photometric data and properties for both *SubS* and *OptS* samples are shown in Table A1 and A2 of Appendix A (see attached CD).

As described in Section 2.2.1, these samples contain Sa galaxies, but the assumption is made that they are not numerous and should not significantly skew subsequent results. We estimate this to be true by considering published Sa population percentages (∼29% of early-types with disks; Nair & Abraham 2010, their Table 3). Assuming, in the worst case scenario, that all Sa galaxies that have not been weaned out during the classification process are in the *SubS*, and these constitute 29% of the S0 classifications. This translates to an upper limit of 44 (19%) Sa contaminants. The additional imposed selection criteria described above and in Table 3.2 are partly geared towards removing this contaminants, so we don't expect a contamination of more than 10% at the absolute maximum. This should not significantly impact our future work with these samples.

3.2.3 Selection Effects and Completeness

Both *SubS* and *OptS* are affected by selection effects and completeness issues. In this section we will examine these and try to assess how they will affect our comparisons.

First of all, both samples are affected by a lack of GAMA catalogue ID (CATAID) completeness. The 229 and 551 ETGs in the *SubS* and *OptS* respectively all have GAMA CATAIDs and redshifts with normalised redshift qualities nQ≥3 (good for science). However, due to the failure of the extraction of derived parameters for a small subset of galaxies in the GAMA database, our samples do not 100% match CATAIDs in all GAMA internal catalogues used in this work. In particular, NUV magnitudes are not complete for both samples. We explore the level of this incompleteness in Section 3.3.1.

Fig. 3.5 shows the GAMA absolute r-band magnitude of the two samples, as a function of redshift. The plot marks the r-band spectroscopic completeness limit of r_{Pet} =19.4 in all three fields as the dashed line (Driver et al. 2011). Note that

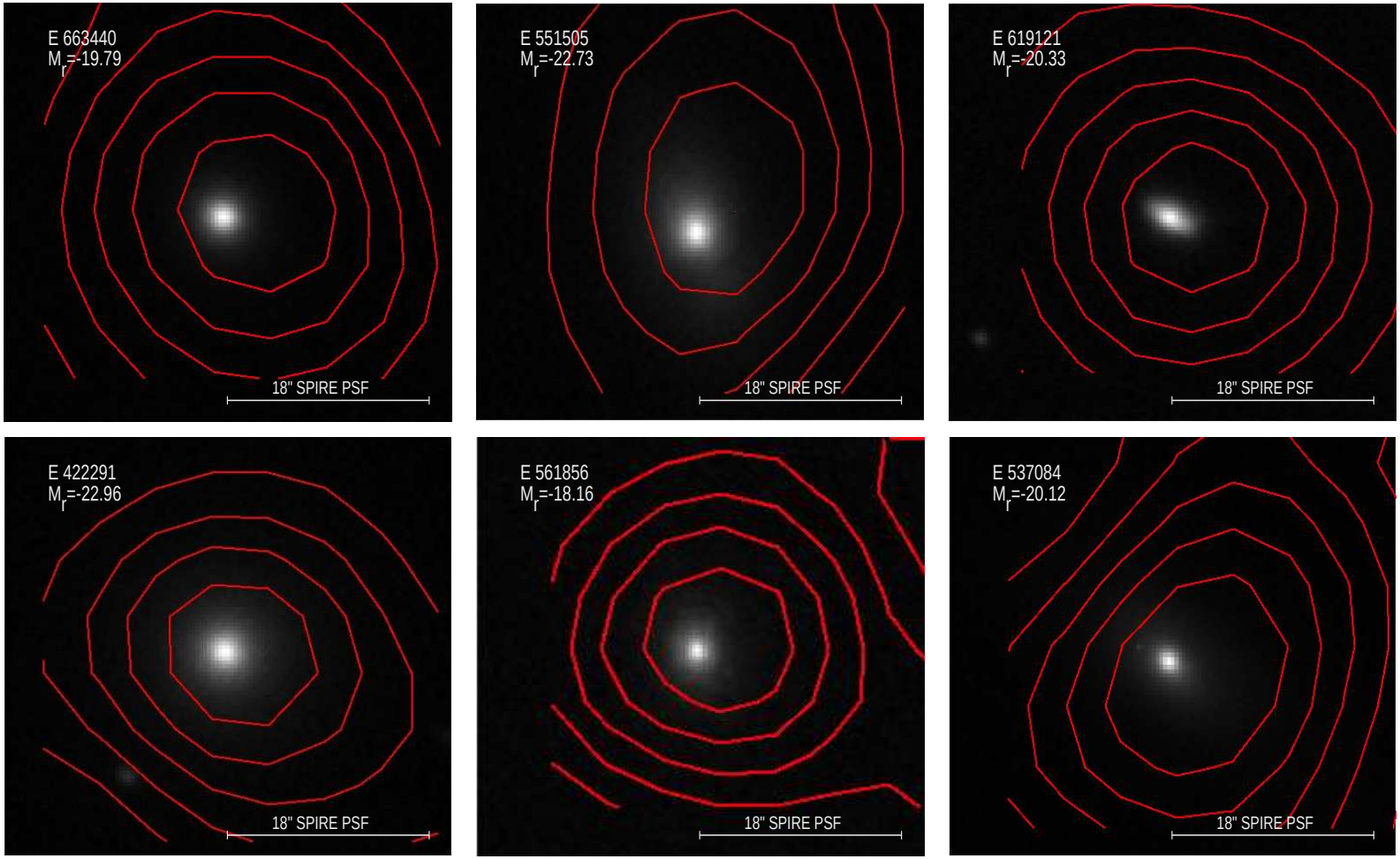

Figure 3.3: Example images of sub-mm detected galaxies with E classification. The images are 40″ SDSS g-band cutouts with superimposed H-ATLAS 250 μm contours in red. Galaxy classification, catalogue ID and absolute r-band magnitudes are shown on the top-left of the images. The 18″ SPIRE PSF is also shown in these images.

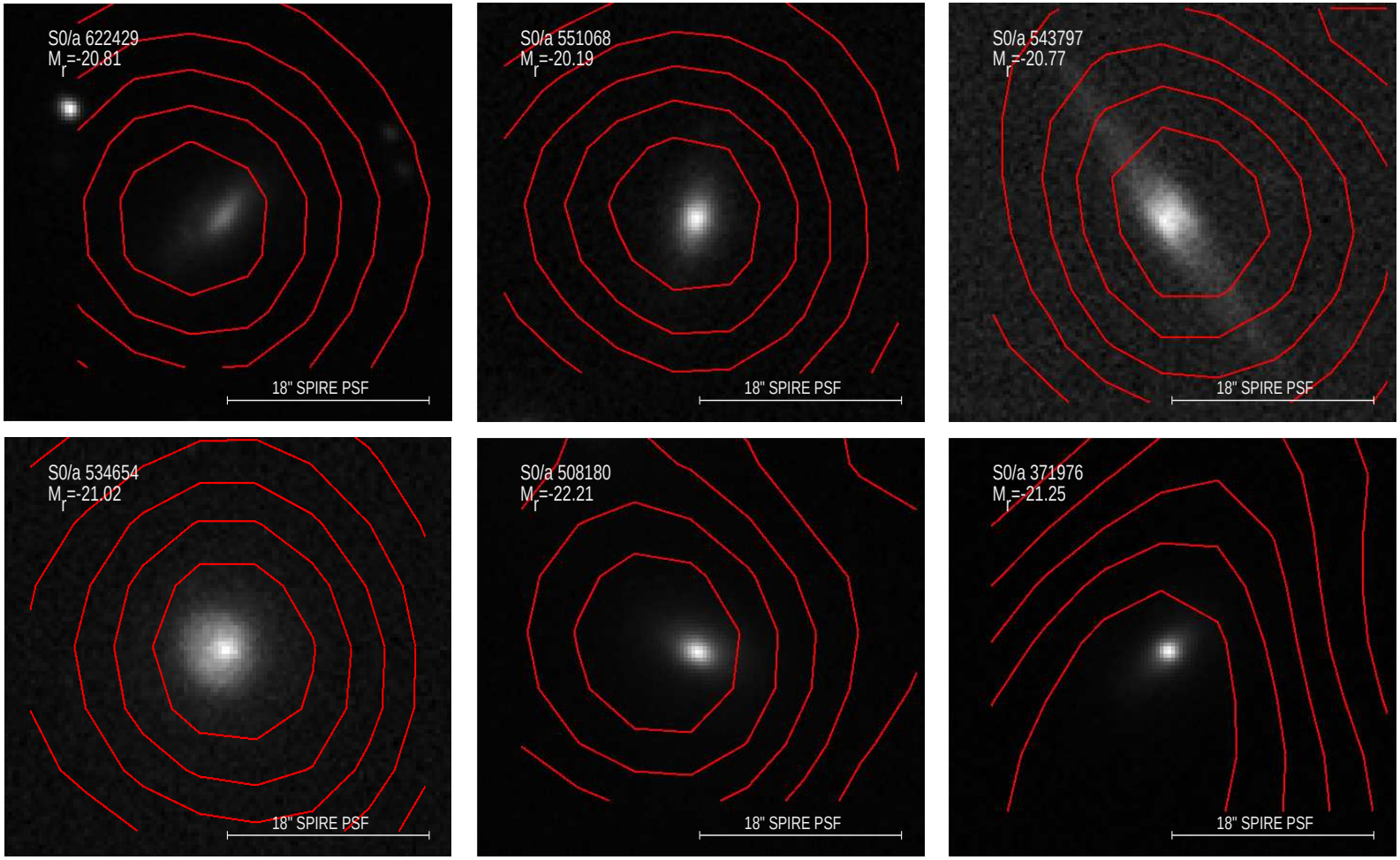

Figure 3.4: Example images of sub-mm detected galaxies with S0a classification. The images are 40″ SDSS g-band cutouts with superimposed H-ATLAS 250 μm contours in red. Galaxy classification, catalogue ID and absolute r-band magnitudes are shown on the top-left of the images. The 18″ SPIRE FWHM PSF is also shown in these images.

there are galaxies plotted below this limit which will be as faint as r_{Pet}=19.8: the magnitude limit for the ongoing GAMA-II data collection. This plot also highlights the absolute magnitude cutoff used here to form a volume-limited sample (down to $M_r = -17.4$ mag., i.e. slightly brighter than the Small Magellanic Cloud). Less luminous galaxies are removed from our samples in this work.

This plot shows an apparent lack of completeness at higher redshift and faint absolute magnitudes for these samples. The KS14 parent sample is complete even in this regime and therefore this effect is a result of the methods used to create the two samples. This phenomenon was investigated on a galaxy-by-galaxy basis; the main cause of this incompleteness was found to be the removal of AGN and galaxies with a low effective radius. However, this effect is true for both samples, indicating that comparative measures between the two are unlikely to be biased.

Completeness issues specific to *SubS* also need to be considered. These sources were selected based on H-ATLAS SPIRE detections greater than 5σ in any wave-band. As shown in Fig. 3.6(a), detections in other bands, and 100% detection at 250 μm is a non-imposed or predicted outcome for this sub-mm sample. A study in Rigby et al. (2011) shows H-ATLAS SDP as having greater than 80% catalogue number density completeness; this means that >80% of the optical sources were found to have sub-mm counterparts. This missing ∼20% is due to a number of undetected faint sources indicated by random noise fluctuations in the simulated maps, or because of source blending. This is likely to be larger for the Phase 1 data due to its deeper region. Dunne et al. (2011) also shows a slight breakdown in ID completeness, as they cannot guarantee that all detections which are given an SDSS ID counterpart have been correctly identified. This is due to positional uncertainties, close secondaries and the random probability of finding a background source within $10''$.

Based on recommendations by Smith et al. (2011), all the sub-mm galaxies

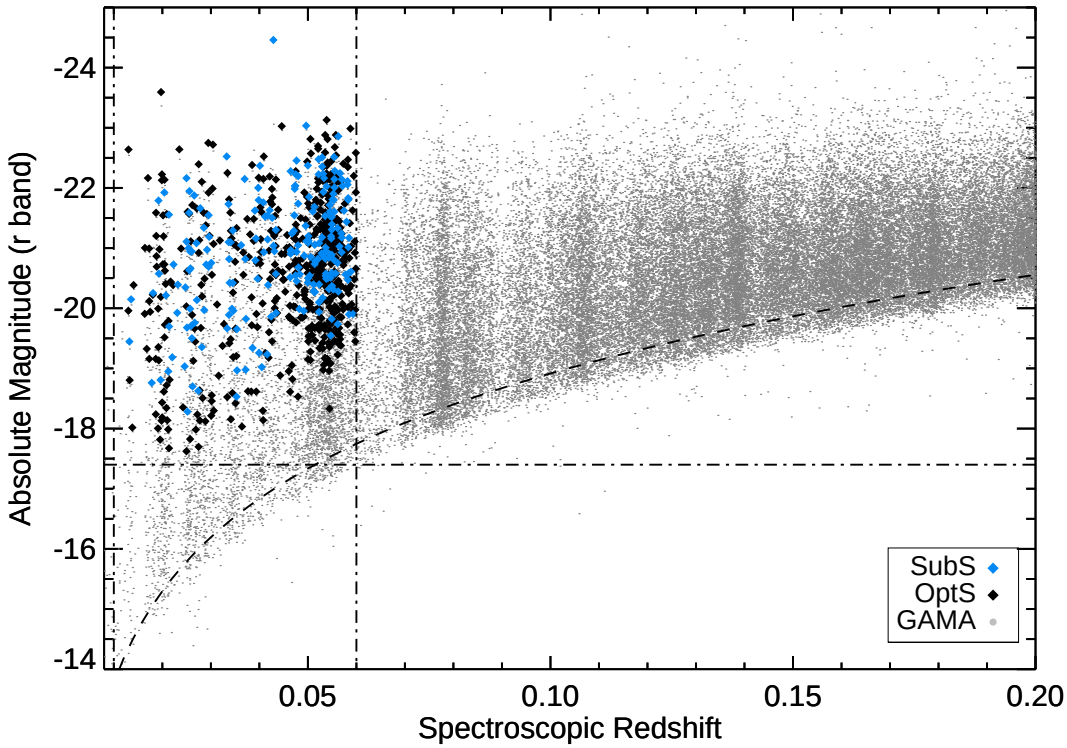

Figure 3.5: The distribution of all GAMA detections (grey points) plotted as a function of redshift up to z=0.2. The dashed line shows the GAMA r-band spectroscopic completeness limit of m_r=19.4. The vertical dot-dashed lines illustrate the redshift cutoffs for our early-type samples and the horizontal dot-dashed line indicates the absolute magnitude cutoff. The sub-mm detected sample is shown as blue diamonds and the undetected sample as black diamonds.

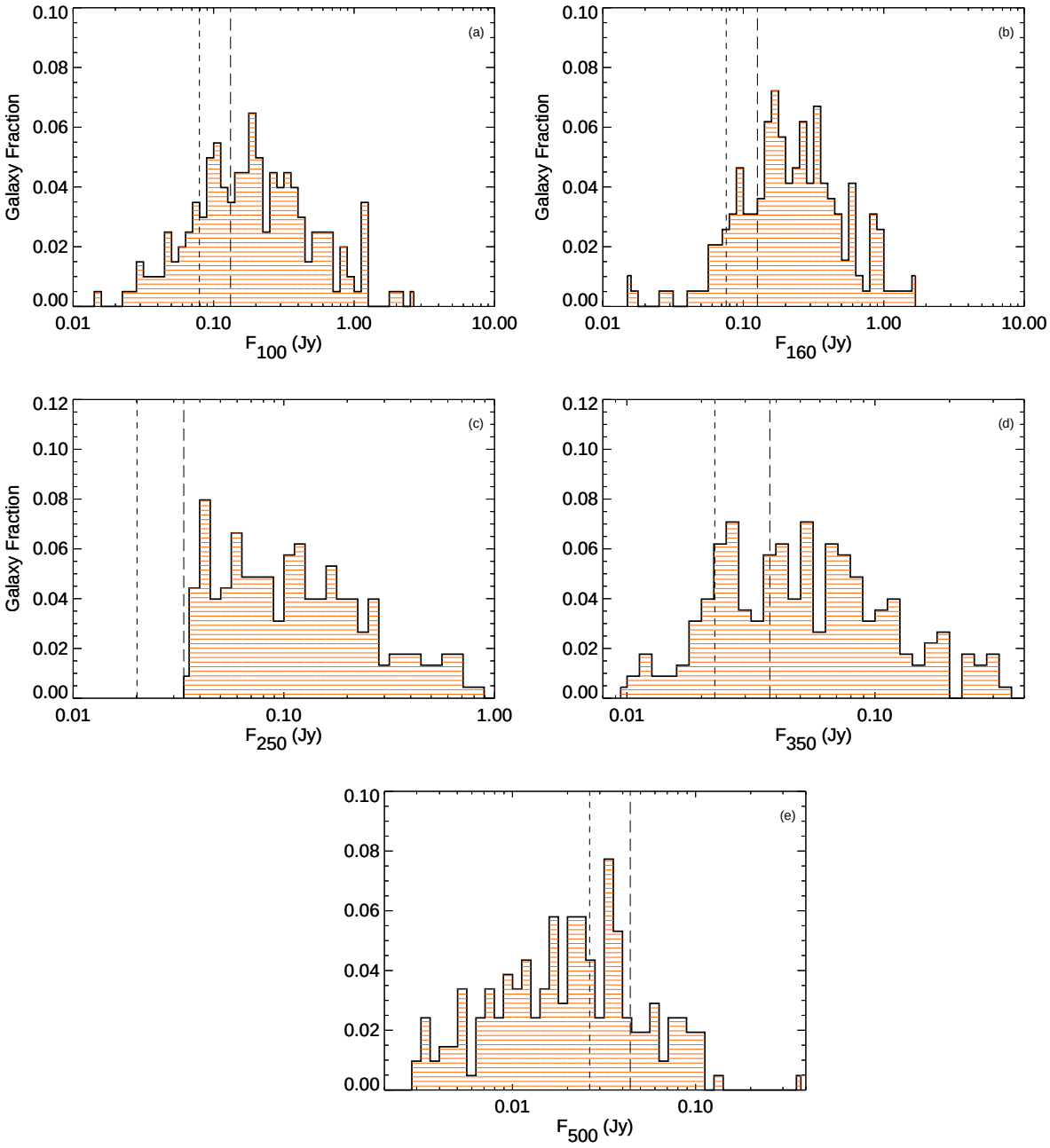

Figure 3.6: The orange histograms show (a) PACS 100 μm, (b) PACS 160 μm, (c) SPIRE 250 μm, (d) SPIRE 350 μm and (e) SPIRE 500 μm H-ATLAS flux values for our sample of optically-selected, early-type galaxies with 5σ detections in at least one SPIRE band. The short dashed line gives the 3σ flux level, and the long dashed line the 5σ flux level (Eales et al. 2010). The distribution of the *SubS* is entirely above these levels in the 250 μm regime, but $\sim$35% of 350 μm fluxes are below the 5σ level and most of the distribution lies below the 5σ flux level for the 500 μm band.

have an imposed reliability R >0.8, where reliability is the likelihood that each object is the correct counterpart out of all the counterparts within a search radius. This ensures that the contamination rate is kept to a minimum and that the SDSS r-band source is linked to the FIR emission. Based on this value, it is possible to estimate the likely number of false IDs in the *SubS*. This is done using Eq. 12 from Smith et al. (2011):

$$N(false) = \sum_{R>0.8} (1 - R). \tag{3.3}$$

This results in ∼3 galaxies (1%) in this sample having a possibly false ID. This fraction is judged low enough to not be a major problem for the rest of this work.

The galaxies in *SubS* are checked for the likelihood of contamination from strong lensing sources. Two methods are used to check for lenses. The first method relies on a study by Negrello et al. (2010), where galaxies with SPIRE 500 μm emission $\geq$ 100 mJy are likely to be strong lenses. Seven of the galaxies in the *SubS* fulfill this criterion. The second method is that of González-Nuevo et al. (2012), where galaxies fulfilling all the following criteria have a 50% likelihood of being strong lenses:

SPIRE 250 μm flux emission $\geq$ 35 mJy

SPIRE 350 μm flux emission $\geq$ 85 mJy

SPIRE 350/250 μm ratio $\geq$ 0.6

SPIRE 500/350 μm ratio $\geq$ 0.4.

Based on this second set of criteria, two ETGs in the *SubS* are 50% likely to be strong lenses. However, these two methods do not pick out the same galaxies as being possible strong lenses. Altogether, these tests indicate low (∼4%) levels of contamination from lensing, but these nine galaxies are removed from the *SubS*

to avoid including any possible strong lenses or background contaminants in the sample. This reduces the *SubS* to 220 ETGs.

The fourth and fifth plots in Fig. 3.6 indicate that in the 350 μm band, 65% (142 detections) of the galaxies are above 5σ, while only 14% (31 detections) are above this limit in the 500 μm waveband. This causes some problems, as will be discussed later in Section 3.4, with fitting SEDs to the data to obtain dust-related parameters.

In subsequent sections everything is examined on a comparative basis between the *SubS* and *OptS* whenever possible. This comparative approach is used to investigate the relative behaviours of sub-mm detected versus undetected ETGs in the nearby Universe.

3.3 Sub-mm Detected vs Undetected Diagnostics

Kormendy et al. (2009) split elliptical galaxies into two main classes: Giant Ellipticals and Normal/Dwarf Ellipticals. The primary class can be defined as having a brightness $M_r \leq -21.5$ and $n \geq 4$, whilst the Normal/Dwarf class has the reverse criteria. To gain understanding of the characteristics of galaxies seen in the two ETG samples, distributions of multiple parameters are plotted in Fig. 3.7 for both *SubS* and *OptS*. At a glance, most of these distributions are seen to differ for the *SubS* and *OptS*. Based on the Kormendy et al. (2009) brightness definition, both samples contain a broad range of r-band absolute magnitudes, indicating a mix of both giant and normal ETGs.

To compare the structural properties of ETGs in these samples, a series of Kolmogorov-Smirnov (KS) tests are carried out for both these samples and subsets thereof, the results of which are shown in Table 3.3. The samples are tested as a

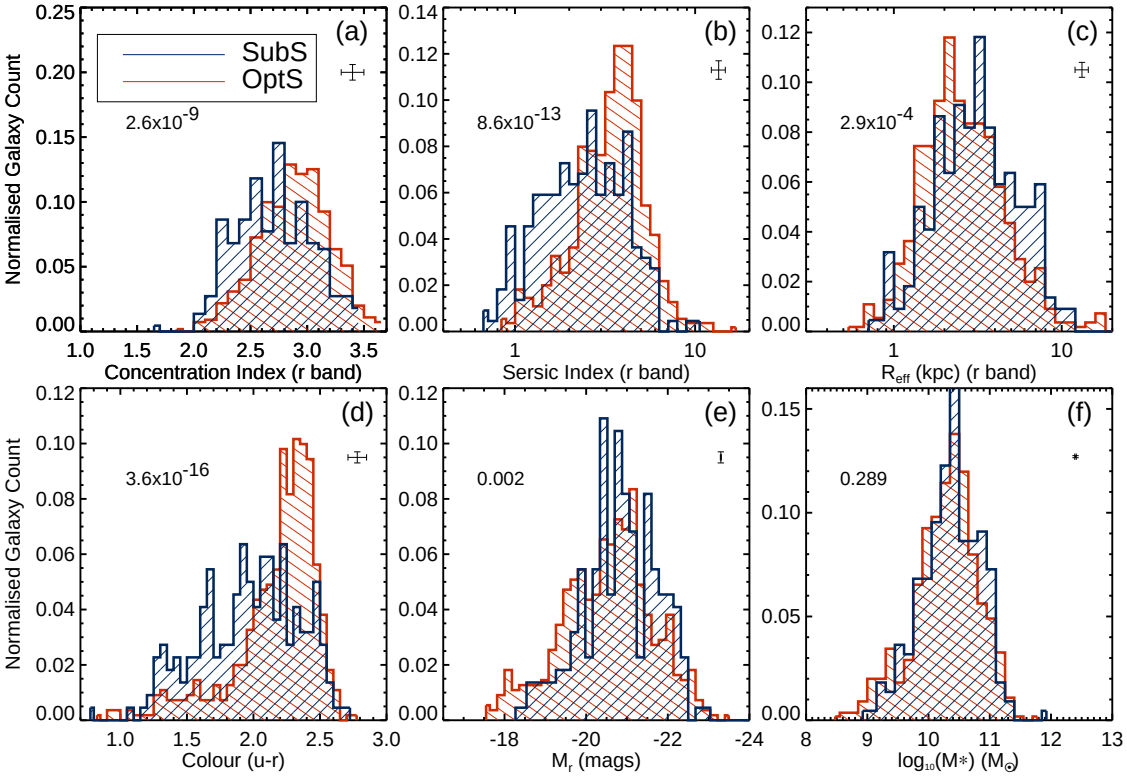

Figure 3.7: Histograms representing distributions of ETGs in the *SubS* and *OptS* for the optical parameters discussed in Section 3.3. From left to right, top to bottom, the distributions of concentration index, Sérsic index, intrinsic effective radius, (u-r) colour, absolute r-band magnitude, and stellar mass are shown. Plots include average errors for these parameters, as well as error bars for the normalised binning. KS-probabilities from Table 3.3 are also included for each set of distributions.

whole because they are volume-limited, and therefore the testing is unlikely to be biased by, for example, redshift or mass effects. Two subsets are also tested: the first containing those galaxies classed as Giant ETGs ($M_r \leq$-21.5) and the second classed as Normal/Dwarf ETGs ($M_r >$-21.5). The aim of this subset testing is to investigate whether these two so-called separate populations have their own unique set of properties for sub-mm detected and undetected ETGs. Within the Giant ETG subset, 36% are found to be sub-mm detected, whereas only a quarter of the Normal ETGs are detected.

Table 3.3 subsequently shows parameters which appear to be most representative of the characteristics of the two samples of galaxies. A combination of Table 3.3 and Fig. 3.7 is used to investigate how these distributions vary for these two samples. The KS-test is chosen because of its usefulness as a non-parametric test for checking a null hypothesis for unbinned distributions that are functions of a single independent variable (Press 1992). KS-probabilities of 1% are chosen as the significance level for this distribution testing.

By examining the spectroscopic redshift values in this table, it was found that the typical redshift for the galaxies in both samples does not differ for the whole sample or Giant subset, although there is a difference in the distributions for the Normal subset.

Concentration index, as defined in Section 2.3.2, is the first parameter plotted in Fig. 3.7. It is linked to the concentration of light in the centre of a galaxy, and it has higher values in ETGs than in LTGs (Strateva et al. 2001; Conselice 2006). Both Table 3.3 and Fig. 3.7(a) show that the concentration index for galaxies in the two full samples differs significantly, with the probability of getting the null hypothesis of no difference approaching zero. The distribution for the $SubS$ is offset towards low concentrations for the full samples and for both low and high luminosity subsets. These differences indicate that H-ATLAS detected ETGs are

likely to have less concentrated light distributions, and therefore may have more perturbed internal structures than those which are undetected, indicating some past merging or formation activity.

Sérsic profile properties are next examined for the samples. Kelvin et al. (2012) describe how their SIGMA wrapper around the GALFIT3 profile fitting program (Peng et al. 2010) is used to fit the entire GAMA database with 2D Sérsic profiles in multiple wavebands. The key parameters this study requires from this profile fitting are the Sérsic indices and effective radii of the galaxies in these samples. Initially, the Sérsic index, which gives information on the distribution of light within a galaxy, is tested. This parameter is more useful than the concentration index as it is less affected by seeing, having been convolved with the point-spread function (PSF) before comparison, and therefore it does not vary so much with redshift. The recovered Sérsic index distributions show similar trends to those observed for the concentration index. The distribution of the samples in equal log spacing shown in Fig. 3.7(b) indicates that ETGs in the *SubS* have lower Sérsic indices, and KS-testing the samples shows them to be significantly different. One possible interpretation of this result is that the difference found in the two samples is due to the effect of dust, which has been shown (e.g. Pastrav et al. 2013) to lower values of measured Sérsic indices. Alternatively, these results for both the Sérsic and concentration index may be caused by morphological disturbances, or problems with the morphological selection process, which is limited by the resolution of the SDSS.

Table 3.3: Two-tailed Kolmogorov-Smirnov (KS) test results for the distributions of host galaxy parameters of our ETGs, tested as follows: (1) testing the full samples, (2) testing those ETGs in the samples with $M_r \leq$-21.5, and (3) testing those ETGs with $M_r >$-21.5. The first column gives the parameter which has been tested, with the two distributions being the sub-mm detected and undetected samples respectively. The second column gives the KS-statistic D, which is defined as the maximum value of the absolute difference between two cumulative distribution functions. The third column gives the KS-probability, which is the probability for the null hypothesis that these data sets are drawn from the same distribution. The fourth and fifth columns show the numbers of *SubS* and *OptS* galaxies tested. The final two columns show the mean values for the *SubS* and *OptS* parameter distributions. The test is carried out using the IDL routine KSTWO.

Parameter	**KS-stat (D)**	**KS-prob**	**Sample Size**		**Mean Value**	
(1) Full Samples			*SubS*	*OptS*	*SubS*	*OptS*
Redshift	0.122	0.017	220	551	0.044	0.046
Concentration index (r-band)	0.253	2.6×10^{-9}	220	551	2.71	2.88
Sérsic index (r-band)	0.298	8.6×10^{-13}	220	551	2.72	3.67
Effective Radius (r-band)	0.166	2.9×10^{-4}	220	551	4.02	3.13
Colour (u-r band)	0.336	3.6×10^{-16}	220	551	1.97	2.17
Absolute Magnitude (r-band)	0.148	0.002	220	551	-20.84	-20.52
Stellar mass	0.078	0.289	220	551	10.36	10.28
UV Colour (NUV-r band)	0.517	4.5×10^{-32}	181	481	4.05	5.33
Surface Density	0.257	1.6×10^{-9}	219	551	7.20	12.63
(2) Giant ETGs			*SubS*	*OptS*	*SubS*	*OptS*
Redshift	0.116	0.684	57	99	0.047	0.046
Concentration index (r-band)	0.362	7.8×10^{-5}	57	99	2.93	3.16

Continued on next page

Parameter	**KS-stat (D)**	**KS-prob**	**Sample Size**		**Mean Value**	
Sérsic index (r-band)	0.295	0.003	57	99	3.71	4.41
Effective Radius (r-band)	0.257	0.013	57	99	7.76	5.82
Colour (u-r band)	0.363	9.5×10^{-5}	57	99	2.28	2.41
Absolute Magnitude (r-band)	0.149	0.367	57	99	-22.01	-22.08
Stellar mass	0.231	0.036	57	99	10.93	10.99
UV Colour (NUV-r band)	0.667	1.5×10^{-12}	50	88	4.99	5.33
Surface Density	0.316	0.001	56	99	4.12	18.22
(3) Normal ETGs			*SubS*	*OptS*	*SubS*	*OptS*
Redshift	0.154	0.006	163	452	0.043	0.046
Concentration index (r-band)	0.292	1.8×10^{-9}	163	452	2.64	2.82
Sérsic index (r-band)	0.388	1.9×10^{-16}	163	452	2.37	3.50
Effective Radius (r-band)	0.150	0.008	163	452	2.71	2.54
Colour (u-r band)	0.413	1.2×10^{-18}	163	452	1.85	2.12
Absolute Magnitude (r-band)	0.154	0.006	163	452	-20.43	-20.18
Stellar mass	0.067	0.649	163	452	10.16	10.12
UV Colour (NUV-r band)	0.570	4.6×10^{-30}	138	396	3.74	5.33
Surface Density	0.262	1.0×10^{-7}	163	452	8.25	11.52

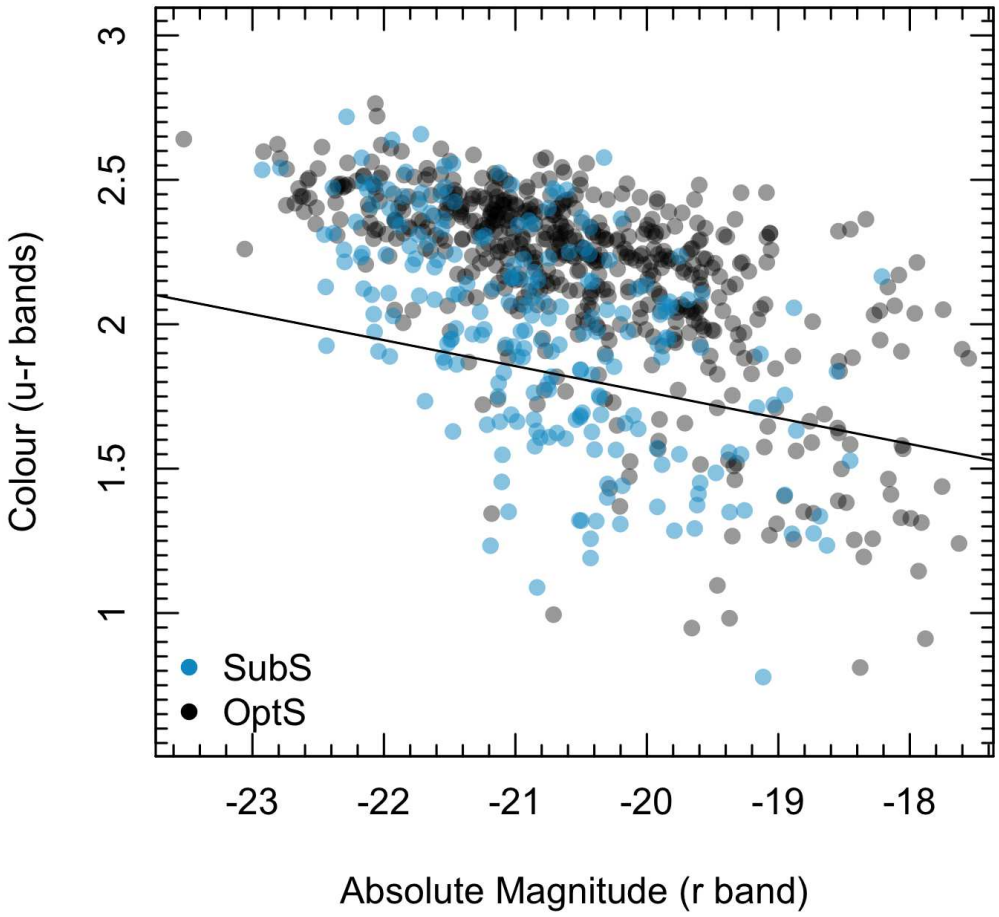

Figure 3.8: Scatter plot showing the colour-magnitude (CM) distribution of galaxies in the *SubS* (blue circles) and *OptS* (black-grey circles). The division between Red Sequence and Blue Cloud defined in the text is shown as the black solid line.

It is interesting to note that mean Sérsic indices for the two samples are higher for the Giant ETGs subset than the Normal ETGs subset, as is predicted by the Kormendy et al. (2009) separation criteria. In addition, the observed differences in the distributions of Sérsic index affects mainly the Normal ETG subset (see Table 3.3). Thus, if this difference is believed to be caused by dust, the Sérsic index would appear to be most affected by its presence in low-luminosity ETGs. This could indicate that higher luminosity ETGs contain lower normalised dust masses, leading to higher Sérsic indices and profiles more similar to *OptS* ETGs. This effect with respect to specific dust mass is explored in Section 3.4.

Apparent effective radii are also calculated for the galaxies through the Sérsic profile fitting, and these are converted to intrinsic radii using simple geometry and angular diameter distances. The distributions are plotted in log space in Fig. 3.7(c). It appears that *OptS* ETGs typically have smaller effective radii than those in the *SubS*, although this result is not robust when the sample is divided into luminosity subsets.

Optical (u-r) colours of both samples are examined; galaxies in the optical Red Sequence (RS) are separated from the Blue Cloud (BC) using Eq. 2.3 (described in Section 2.3.1). ETG colours are explored in Fig. 3.8, where the (u-r) CM scatter plot is shown for both samples. The diagram highlights the point that ETGs, whether detected in the sub-mm or not, have a multitude of both blue and red colours. Interestingly, the *SubS* does not show as dense a clustering in the Red Sequence as the *OptS* and is more evenly distributed towards the blue end. Both Figs. 3.7(d) and 3.8 indicate that the *SubS* contains a larger proportion of blue ETGs. Table 3.3 also shows the distribution of optical colours is quite different, even when testing separate subsets.

The full sample testing of absolute magnitudes indicates different distributions. However, results from subset testing indicate that the Giant ETGs have similar

distributions, whilst Normal ETGs are different with ∼0.6% probability. This is also seen in Fig. 3.8, where the *OptS* ETGs are shown to extend to fainter magnitudes than *SubS* ETGs.

Given the link between the luminosity and stellar mass of galaxies, equivalent results are expected for the stellar mass distributions. However, all the samples have similar mass distributions, although as with effective radius the result is less robust for the Giant subset. On average, the *SubS* reaches to brighter absolute magnitudes than the *OptS*, whereas mass differences between the samples are not significant. This may mean a decrease in mass-to-light ratios for *SubS* ETGs.

Altogether, after testing these intrinsic properties, sub-mm detected ETGs are found to be bluer than undetected ETGs (see also results by Dariush et al. 2011), and they are also shown to be likely to have similar masses, lower Sérsic indices, be less centrally concentrated and less compact than undetected ETGs in the *OptS*.

3.3.1 UV Parameters

Availability of GALEX data means that ultraviolet (UV) bands can be examined for both *OptS* and *SubS*; these are typically used as an indicator of recent star formation. GALEX NUV detections are found for 481 and 184 galaxies in the *OptS* (87%) and *SubS* (83%) respectively. *SubS* galaxies are brighter on average in the NUV by ∼2 mags. The NUV-r colours are shown in Fig. 3.9, where the *SubS* displays bluer UV-optical colours than the *OptS*, similar to the H-ATLAS result for ETGs in the SDP field of Rowlands et al. (2012). As in Section 3.3, KS-tests are performed on the full *SubS* and *OptS* samples and their luminosity subsets. The results of these tests are presented in Table 3.3 and show the distributions of UV colours are very different for ETGs in all these cases, with *SubS* ETGs showing much bluer colours overall.

Colour Region	***SubS***		***OptS***	
	Galaxies	*Fraction*	*Galaxies*	*Fraction*
Red Sequence	50	0.27	373	0.78
Green Valley	88	0.48	77	0.16
Blue Cloud	46	0.25	31	0.06

Table 3.4: Numbers and Fractions of ETGs residing in the UV-Optical Red Sequence, Green Valley and Blue Cloud, as defined by Bourne et al. (2012).

For comparison, H-ATLAS detected LTGs (visually classified in the same process as ETGs in our samples) are also plotted on this histogram. The colours of these LTGs are bluer on average than both ETG samples, but the *SubS* straddles the gap between the blue and red modes filled by LTGs and *OptS* galaxies respectively. This indicates that H-ATLAS detected ETGs are forming a colour population of their own.

The UV-optical CM diagram is given in Fig. 3.10, and following the method of Bourne et al. (2012), NUV-r colour boundary cuts are applied as Eqs. 3.4, 3.5 and 3.6 below, to define regions as the Red Sequence (NUV-RS), Green Valley (NUV-GV) and Blue Cloud (NUV-BC) respectively.

$$1.23 - 0.17M_r \leq (\mathrm{NUV} - r)_{\mathrm{rest}} \leq 7.0 \tag{3.4}$$

$$-0.27 - 0.17M_r \leq (\mathrm{NUV} - r)_{\mathrm{rest}} < 1.23 - 0.17M_r \tag{3.5}$$

$$1.0 \leq (\mathrm{NUV} - r)_{\mathrm{rest}} < -0.27 - 0.17M_r. \tag{3.6}$$

The results of applying these boundary conditions to define different regions are shown in Table 3.4. This highlights a key difference between the *SubS* and *OptS*. There is a large fractional difference between the populations in all these regimes, with *OptS* galaxies most prominently located in the NUV-RS, and *SubS* ETGs

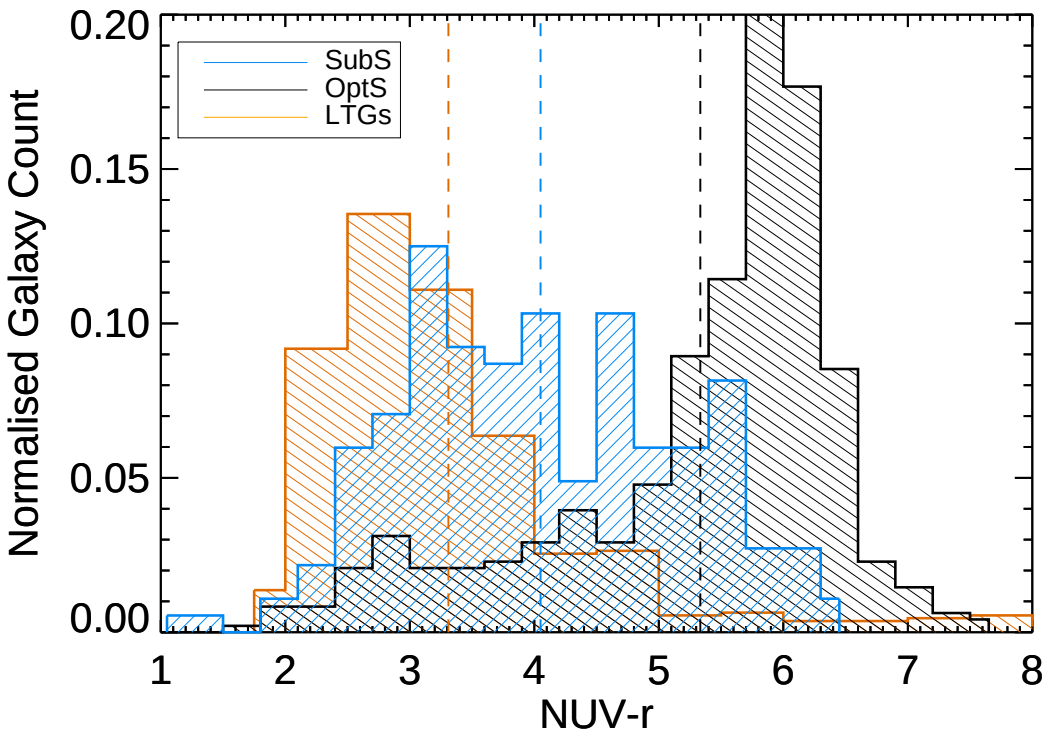

Figure 3.9: Histograms of UV-optical colour for the *OptS* (black) and *SubS* (blue), as well as H-ATLAS detected LTGs (orange). The *SubS* appears to be skewed towards the bluer end, whilst the peak of the *OptS* is decidedly within the red end of the plot. The blue, black and orange dot-dashed lines show the respective mean colour for the *SubS*, *OptS* and LTG sample (4.05, 5.33 and 3.31 mags).

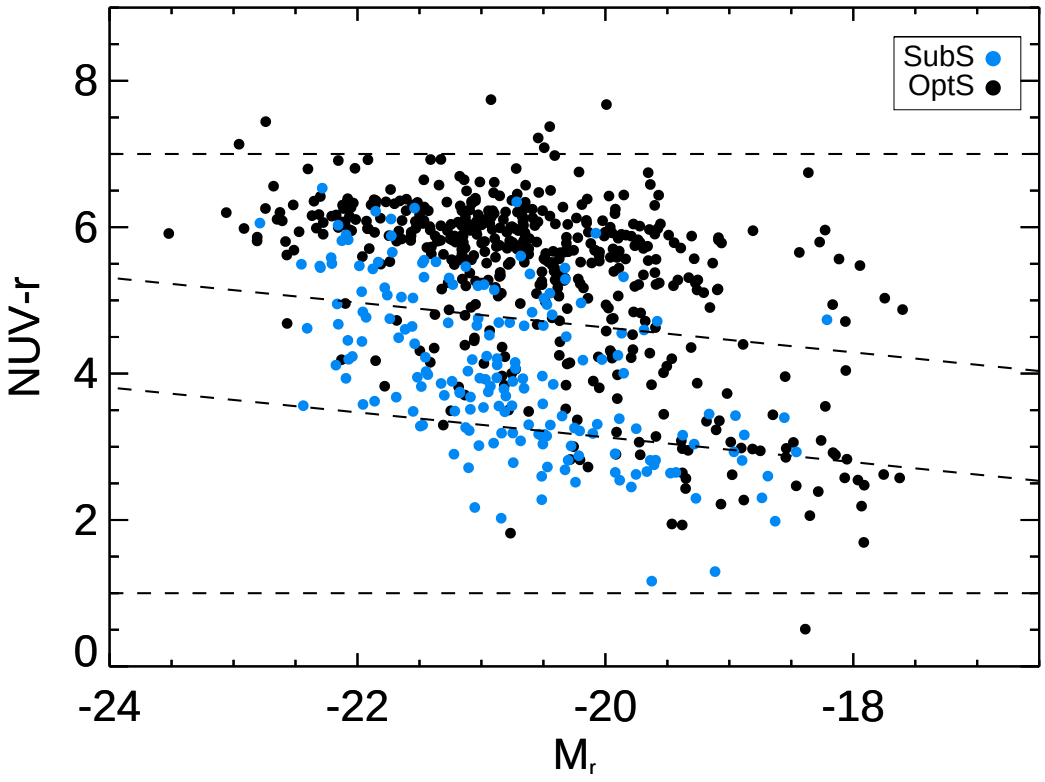

Figure 3.10: The distribution of *SubS* (blue filled circles) and *OptS* (black filled circles) galaxies on the UV-optical colour-magnitude diagram. Dashed lines indicate the cutoffs taken from Bourne et al. (2012) to separate galaxies into Red Sequence, Green Valley and Blue Cloud respectively.

mostly dominating the NUV-GV. It is difficult to determine whether the 48% sub-mm detected galaxies in the NUV-GV are ETGs in transition from the Blue Cloud to the Red Sequence, or whether they are NUV-BC ETGs that are dust-reddened to appear in the NUV-GV, although absolute NUV flux levels do suggest ongoing or recent star-formation in *SubS* ETGs.

The sub-mm detected ETG occupation of the NUV-BC is a factor of three more than that of undetected ETGs, possibly indicating more ongoing or recent star formation in the former. If the UV emission in ETGs is dominated by emission from recent star formation and dust is predominantly heated by photons from the young stellar population, then *SubS* ETGs may be partially dust-reddened and driven towards the NUV-RS. The fact that the *SubS* ETGs occupy mostly the NUV-GV implies that one of these assumptions may not be dominating factors. Additionally, the dust may be predicted to lie within a different geometry to the star formation, potentially implying star formation is not the main source of heating the dust.

3.3.2 Environment Parameters

The Dressler (1980) morphology-density relation is a key driver for investigating the varying environments of ETGs. Although it has been shown that bulge-dominated galaxies are more commonly found in the densest regions of the Universe, it is unclear whether ETGs with differing dust properties are typically found within different environments.

Disk-dominated galaxies are thought to be transformed into bulge-dominated galaxies via processes which occur in dense environments (see Boselli & Gavazzi (2006) for a review of such processes). This thesis is only concerned with bulge-dominated galaxies, or ETGs. However, this is a comparison of sub-mm non-detected passive ETGs, which may be at the end stages of their lives (*OptS*) with

dusty ETGs, which are likely to have active star-formation (*SubS*). It would be interesting to see whether these two classes of ETGs reside in different environments.

The surface density information used to investigate environments for the ETG samples was taken from the GAMA EnvironmentMeasures database (Brough et al. 2013). These surface densities ($\Sigma_{\rm gal}$) in galaxies Mpc^{-2} were calculated based on the N^{th} Nearest Neighbour method, using

$$\Sigma_{\rm gal} = \frac{N}{\pi D_N^2}, \tag{3.7}$$

where N is the nearest neighbour number, set at a value of 5, and $\rm D_N$ is the projected distance in co-moving Mpc to the N^{th} nearest neighbour within a velocity cylinder of $\pm 1000\,{\rm km\,s^{-1}}$, from a volume-limited, density-defining population. This population is defined by an r-band absolute magnitude $\rm M_r$ $\leq$-20 and a redshift selection of $0.002 \leq z \leq 0.18$ (Wijesinghe et al. 2012; Brough et al. 2013). ETGs situated at the angular edge of the velocity cylinder are allocated upper limits and are also included. Only one galaxy within these two samples is removed because the density cannot be estimated, reducing the *SubS* to 219 ETGs. Surface density is an extremely useful parameter to work with because it provides information about the area around the galaxy and whether there are likely to be any real interactions occurring between it and its neighbours.

Fig. 3.11 shows the surface densities for both the reduced *SubS* and *OptS*. The *SubS* ETGs on average occupy lower surface density environments compared to the *OptS* ETGs. As in Section 3.3, the distributions of densities for the samples are KS-tested, as are the luminosity subsets. Results given in Table 3.3 show that sub-mm detected and non-detected ETGs have different density distributions in the main sample, as well as both luminosity subsets, with probabilities of below 1%.

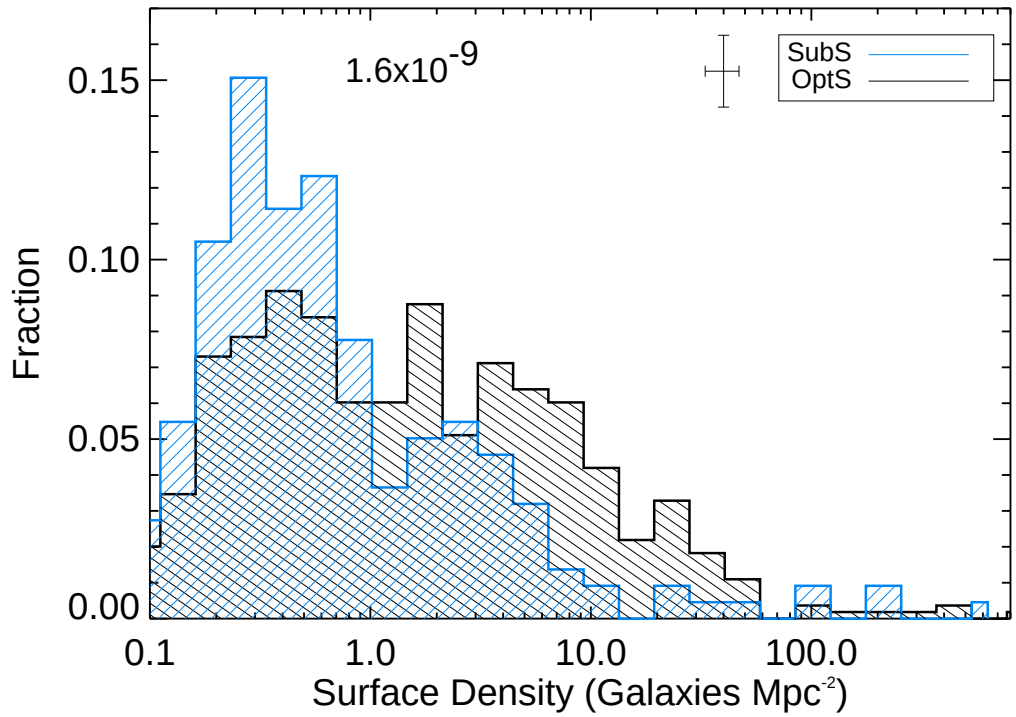

Figure 3.11: Normalised histograms of surface density in log bins, where the blue histogram is for the *SubS* and the black histogram is the *OptS*. The error bars represent average errors on both surface density and the normalised binning. The KS-probability for comparison of the surface density distributions from Table 3.3 is also included.

Robotham et al. (2011) produced a GAMA Galaxy Group Catalogue (G^3C) that identifies which group the GAMA galaxies belong to, as well as assigning each group a set of properties. It is assumed here that if the galaxies are not assigned a Group ID, then they are in the field. This G^3C is used to assign ETGs in the *SubS* and *OptS* either field or group status by splitting the *OptS* and *SubS* into two: grouped and ungrouped galaxies. The two samples are then compared to find that the *SubS* appears to have galaxies which are almost equally split between the field (52%) and groups (48%), whereas the *OptS* shows more of a difference with 62% in the field and 38% in groups. ETGs within the groups can be further split according to the multiplicity of the group: ETGs in small groups with less than five galaxies (32% and 24% for the *SubS* and *OptS*, respectively), and larger groups with five or more galaxies (15% and 14% respectively).

Fig. 3.12 shows the distribution of surface densities with stellar mass for the two samples. The galaxies have been coloured by the multiplicities of their groups, making it simple to identify lone ETGs, ETGs in small groups and those in large groups. Both plots show no direct link between higher surface densities and larger groups and furthermore, that there are some ETGs with high surface densities that do not seem to share a group. This may be an effect of the groups data selection function, which changes with redshift; this is essentially a selection effect based on the fact that at higher redshift, only the brightest galaxies can be observed. This explains why some of the highest surface density ETGs may not have a group classification, but it weakens the usefulness of this Groups Catalogue for this analysis.

Fig. 3.12 highlights the similar *SubS* and *OptS* galaxy mass ranges, but different galaxy surface density ranges. Testing for Spearman correlations does not reveal any trends between surface density, group multiplicity and stellar mass, although these same tests suggest that the *OptS* contains more ungrouped ETGs in

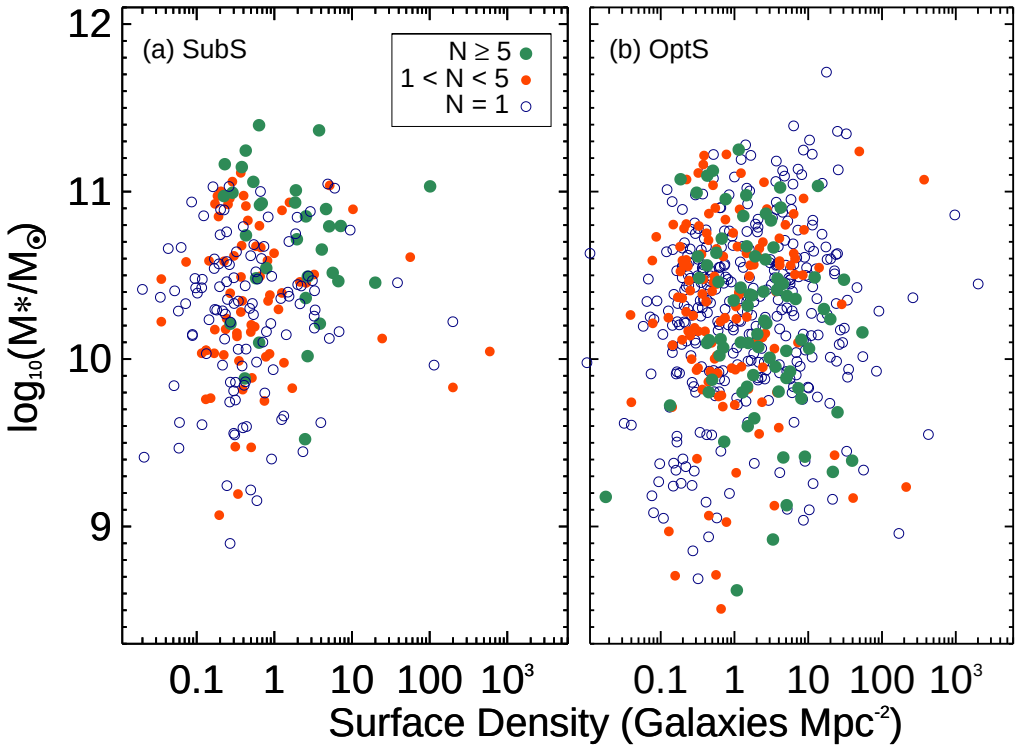

Figure 3.12: Variation of stellar mass with surface density. (a) shows results for *SubS* galaxies and (b) for *OptS* galaxies. Both plots are coloured by group multiplicity: open blue circles are galaxies which are ungrouped and assigned a group size of 1, red filled circles represent ETGs in small groups (< 5 galaxies) and large, green filled circles those in large groups (≥ 5 galaxies).

high density areas (r_s=0.005) than the *SubS* (r_s=0.24).

There also appear to be some missing galaxies in Fig. 3.12(a). The *OptS* shows galaxies of quite low stellar mass ($M_* < 10^{10} M_\odot$) going to higher densities, but these do not appear for the *SubS*. In general, H-ATLAS is known to preferentially detect higher mass galaxies, which could partially explain this. In addition, the larger H-ATLAS PSF when compared to that of the optical may result in low counterpart reliability for ETGs in the densest regions, resulting in their removal from these samples. The sparsity of low mass, dusty ETGs at high surface densities may thus be caused by sample completeness effects. However, the sparsity of dusty ETGs in general (i.e. even at high mass) at high densities suggests that dusty ETGs do not occupy the densest regions of groups and clusters, unlike their non-dusty counterparts. Kauffmann et al. (2004) showed that generally, massive galaxies in low density environments in their SDSS sample contain the most dust, based on evidence of optical attenuation. Kaviraj et al. (2012) studied optical images of ETGs with visible dust lanes and patches. They found that dusty ETGs occupy less dense environments than those with no sign of dust obscuration. Findings for the *SubS* and *OptS* are qualitatively consistent with these results.

3.4 Dust Properties of Detected ETGs

3.4.1 Fitting Modified Planck Functions

The *SubS* ETGs have both *Herschel* PACS 100 and 160 μm measurements, as well as 250, 350 and 500 μm fluxes from the SPIRE instrument. A subsample (3σ sample) of 188 ETGs is selected which has at least 3σ flux levels (22.6 mJy) in the 350 μm SPIRE waveband, as well as the requisite 5σ emission in at least one SPIRE sub-mm waveband (see Section 3.2.3). PACS measurements are missing for 27 of these galaxies, and for these only SPIRE flux densities are fit. Uncertainty values

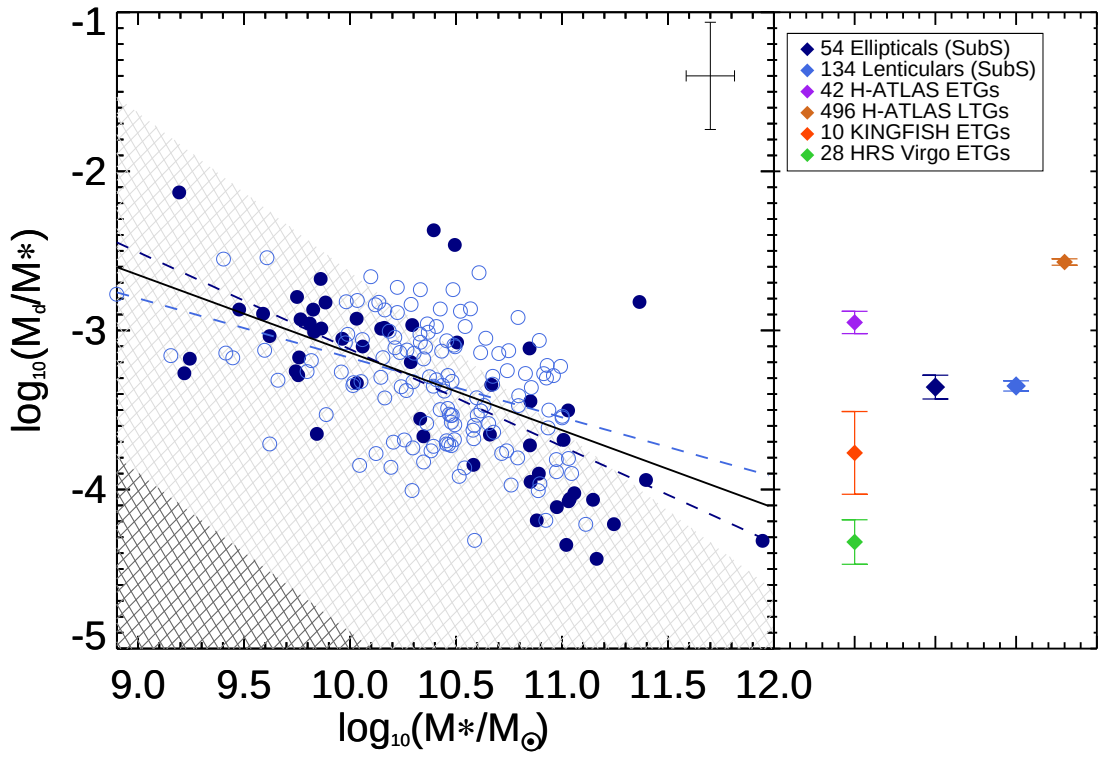

Figure 3.13: Specific dust mass of *SubS* 3σ sample ETGs as a function of stellar mass. The points are coloured by morphology: dark blue filled circles for ellipticals (E) and light blue open circles for lenticulars (S0a). Average errors are shown as bars on the top right. Same colour dashed lines represent best fit straight lines through the respective points. The black solid line is the overall fit to all points. The dark grey cross-hatched region denotes the area where galaxies can't be detected due to the 250 μm flux limit: this is derived using a dust temperature of 30 K for a galaxy at z=0.013. The underlaid light grey cross-hatched region shows the region up to where a typical galaxy with a dust temperature of 15 K at z=0.06 cannot be detected: these parameters are the limits of our sample. This light grey cross-hatched area shows a region of partial detectability, due to the redshift range and dust temperature range in the samples. In the panel to the right, filled diamonds and error bars represent mean specific dust masses for a range of studies with *Herschel* data, described in the text.

are calculated as the sum in quadrature of the instrumental noise and the confusion noise (see Rigby et al. 2011). Flux calibration errors of 7% of the catalogue flux values are added in quadrature to these errors to account for the uncertainty in the SPIRE photometric calibration (Pascale et al. 2011), and 10% to the PACS fluxes.

In order to estimate dust temperature and mass we then fit isothermal, modified Planck functions to the rest-frame data for each galaxy, of the form:

$$F_\lambda = \Omega B_\lambda \lambda^{-\beta}, \tag{3.8}$$

where B_λ is the Planck function (see Eq. 1.8), Ω is the amplitude parameter for the model fit, and β the dust emissivity index which is kept fixed as 2.0 (e.g. Galametz et al. 2011; Davies et al. 2012; Cortese et al. 2012b). This modified blackbody (modBB) model is fit to the FIR/sub-mm flux densities, which are corrected for redshift. The characteristic rest-frame temperatures of emission by the dust distributions in these galaxies can thereby be measured.

The best fit model to the five fluxes is selected using the χ^2 goodness-of-fit statistic. This is calculated as

$$\chi^2 = \frac{\sum_{i=1}^{N} \left(F_{\mathrm{mod},i} - F_{\mathrm{obs},i}\right)^2}{\sum_{i=1}^{N} E_i^2} \tag{3.9}$$

where $\mathrm{F_{mod}}$ is the modified Planck function model used for the fit, $\mathrm{F_{obs}}$ refers to the observed fluxes, E represents the instrumental and calibration errors on these observed fluxes, and the sum is over all available wavebands. This is calculated for each iteration of the code, and the best fit is selected as that model which gives the minimum χ^2 value (χ^2_{min}). This best fit will have an associated cold dust temperature which is assigned to that galaxy.

Errors on the dust temperature are calculated by checking the grid of χ^2 values, and finding which model parameters fit the 1σ confidence level such that

$$\chi^2_{\rm lim} = \chi^2_{\rm min} + 1\,\sigma, \tag{3.10}$$

where 1σ=1.0 for a single degree of freedom; the fits with $\chi^2_{\rm lim}$ goodness-of-fit results give the upper and lower limits for the dust temperature.

Dust masses for this subsample are calculated using

$$M_{\rm d} = \frac{F_{250} D_{\rm L}^2 K}{\kappa_{250} B(T)_{250}\,(1+z)} \tag{3.11}$$

(Whittet 1992, Eq. 6.12), where $\rm F_{250}$ is the observed flux value in the $250\,\mu$m waveband in Jansky (Jy), $\rm D_L$ the luminosity distance to the source and K is the k-correction as defined in Eq. 2 of Dunne et al. (2011). The assumed mass absorption coefficient (κ_{250}) is $0.89\,{\rm m^2\,kg^{-1}}$ at $250\,\mu$m (Dunne et al. 2011). The value of $\rm B(T)_{250}$ in Jy for Eq. 3.11 is calculated using the best fit, cold dust, rest-frame temperature from the SED fitting of each galaxy. The dust mass is measured using this waveband because of the relatively smaller errors when compared to the other SPIRE wavebands.

Dust mass errors cannot be calculated directly using confidence intervals. Dust mass errors are derived instead using the formal dust temperature uncertainties, which fold into the blackbody equation within Eq. 3.11. The propagation of these errors was therefore done using partial derivatives of Eq. 3.11 as follows:

$$\frac{\partial(M_{\rm d})}{\partial T} \propto \exp^{\frac{h\nu}{kT}} \left(\frac{h\nu}{k}\right) \frac{\partial(\frac{1}{T})}{\partial T} \tag{3.12}$$

$$\partial(M_d) \propto \exp^{\frac{h\nu}{kT}} \left(\frac{h\nu}{k}\right) \times (-T^{-2}) \tag{3.13}$$

$$\frac{\partial(M_{\rm d})}{M_{\rm d}} = -\frac{h\nu}{kT^2} \frac{dT}{\left(1 - \exp^{\frac{-h\nu}{kT}}\right)} \tag{3.14}$$

$$\frac{\Delta M_{\rm d}}{M_{\rm d}} = \left(\left(\frac{\partial(M_{\rm d})}{M_{\rm d}}\right)^2 + \left(\frac{\partial(F_{250})}{F_{250}}\right)^2 \right)^{1/2}, \tag{3.15}$$

where Eq. 3.12 is converted to 3.13 by substituting for the temperature derivative, and 3.13 is then converted to 3.14 by dividing by M_d. This partial derivative $\frac{\partial(M_d)}{M_d}$ is added in quadrature to the flux error ($\frac{\partial(F_{250})}{F_{250}}$) in Eq. 3.15. Further uncertainty resulting from the values of the luminosity distance, redshift, k-correction and absorption coefficient also need to be considered. Baldry et al. (in prep) quote uncertainties for GAMA redshift of $\pm 50\,\mathrm{km\,s^{-1}}$, which, depending on the redshift of the galaxy, range from 0.3% to 1% - these are omitted from our error calculations as they are negligible in comparison to temperature and flux uncertainties. Likewise, luminosity distance and k-correction values are derived from redshift parameters, and also have negligible uncertainties. The mass absorption coefficient also has an associated uncertainty - given the current lack of understanding of dust emission, this coefficient is not well constrained at all. However, given that any uncertainty added for this coefficient will have a systematic and not random effect on the resultant errors, we choose to omit its associated uncertainty. Therefore, the chief contributors to the uncertainty on the dust mass are the flux and derived dust temperatures. Due to the exponential dependence on temperature in this error analysis, dust mass errors increase very rapidly with higher temperature errors.

The complete results of this fitting give the mean cold dust temperature for the ETGs as $22.1^{+2.7}_{-2.0}\,\mathrm{K}$ with 5^{th} to 95^{th} percentiles of 14-28 K, with no obvious variation of fit temperature with stellar mass. The mean cold dust mass is calculated as $(1.8\pm0.5)\times10^7\,\mathrm{M_\odot}$ with a percentile range of $(0.19\text{-}5.41)\times10^7\,\mathrm{M_\odot}$. The resultant average specific dust mass ($\log_{10}(\mathrm{M_d/M_*})$) is calculated as -3.37. Due to the non-linearity of the propagation of dust mass uncertainties, we only show average dust mass errors for those galaxies with full PACS and SPIRE data. Thus the correlation between dust temperature and mass is accounted for within dust mass errors. See Table A3 of Appendix A for the full set of FIR/sub-mm data and subsequent modBB derived parameters.

Specific dust masses are presented in Fig. 3.13, plotted against stellar mass. Overall, the galaxies show a clear trend for lower mass galaxies to contain higher normalised dust masses, with a straight line fit to the distribution yielding a Pearson coefficient ($r_{\rm p}$) of -0.55. The dependency on morphology within ETGs is addressed in Section 3.4.3. Here the average normalised dust mass is compared with those from other works with *Herschel*. These results and the standard errors on the means are also shown in Fig. 3.13 (right) for the *SubS* 3σ sample ellipticals and lenticulars separately.

This ETG sample does not contain many low mass ETGs, which indicates that it may be missing galaxies at the low stellar mass and specific dust mass end of Fig. 3.13. To test for this, two cross-hatched regions are shown on the plot, representing the 250 μm 5σ limit. Both regions are based on the same dust mass calculations as the ETGs, with a representative upper limit dust temperature of 30 K and minimum redshift of 0.013 for the darker, smaller region, and a lower limit dust temperature of 15 K and maximum redshift of 0.06 for the lighter, larger region. The smaller excluded region becomes larger with decreasing temperature and increasing redshift, eventually expanding to the size of the larger region; the former represents the region of the plot which H-ATLAS is insensitive to and galaxies cannot be detected in this region. H-ATLAS can detect galaxies with redshift smaller than 0.06 and dust temperatures warmer than 15 K within the light-grey region. These combined regions (and the lack of points directly above the dark grey limit) indicate that the trend being observed in this diagram is real and ETGs of similar dust and stellar masses are not being excluded as a direct result of this flux limit.

Based on the results found in Section 3.3, the properties of the ETGs can be further explored for high and low luminosity subsets. Luminosity and stellar mass

are known to be linked, and these properties are plotted to find that values of M_r=-21.5 mag or M_*=$10^{10.2}$ $M_\odot$ can be used as high and low luminosity/stellar mass dividers. From Fig. 3.13 it appears that while lenticulars dominate the median range of stellar masses, ellipticals appear to be separated into low and high stellar masses. Those ETGs with the highest stellar masses show the lowest specific dust masses. The brightest ETGs have been shown to contain Sérsic indices most similar to undetected ETGs (see Section 3.3) and this therefore indicates that ETGs with low specific dust masses have high Sérsic indices and are not dissimilar to ETGs in the *OptS* in this respect.

Next results obtained with other H-ATLAS data are compared. Recent multi-wavelength SED fitting by Rowlands et al. (2012) on a sample of 42 detected ETGs in the H-ATLAS SDP gave an average cold dust mass of 5.5×10^7 $M_\odot$ for an allowed distribution of temperatures of 15-25 K. Improving upon Rowlands et al. (2012), a more straightforward single-component fitting approach has been selected here and applied to all *SubS* ETGs with 3σ detections at 350 μm (this latter criterion is not applied in the case of Rowlands et al. (2012)). This low-redshift *SubS* alone contains over four times the number of galaxies in the SDP and therefore yields a more statistically significant result. Results in this section indicate a lower mean specific dust mass for ETGs than in Rowlands et al. (2012), which may be partly due to the nearer redshift limit of the *SubS* sample presented here. For the sake of comparison, the average normalised dust mass for their larger sample of LTGs has been shown in Fig. 3.13. This is clearly a lot higher than the ETGs, as is to be expected for spiral galaxies, which are known to have high dust masses.

Dust mass results are also compared with those from the KINGFISH survey, where Skibba et al. (2011) also calculate dust temperatures and masses for a sample of 10 nearby ETGs using single-temperature modified blackbodies. Their specific dust masses are lower than those calculated here, but fall well within the range of

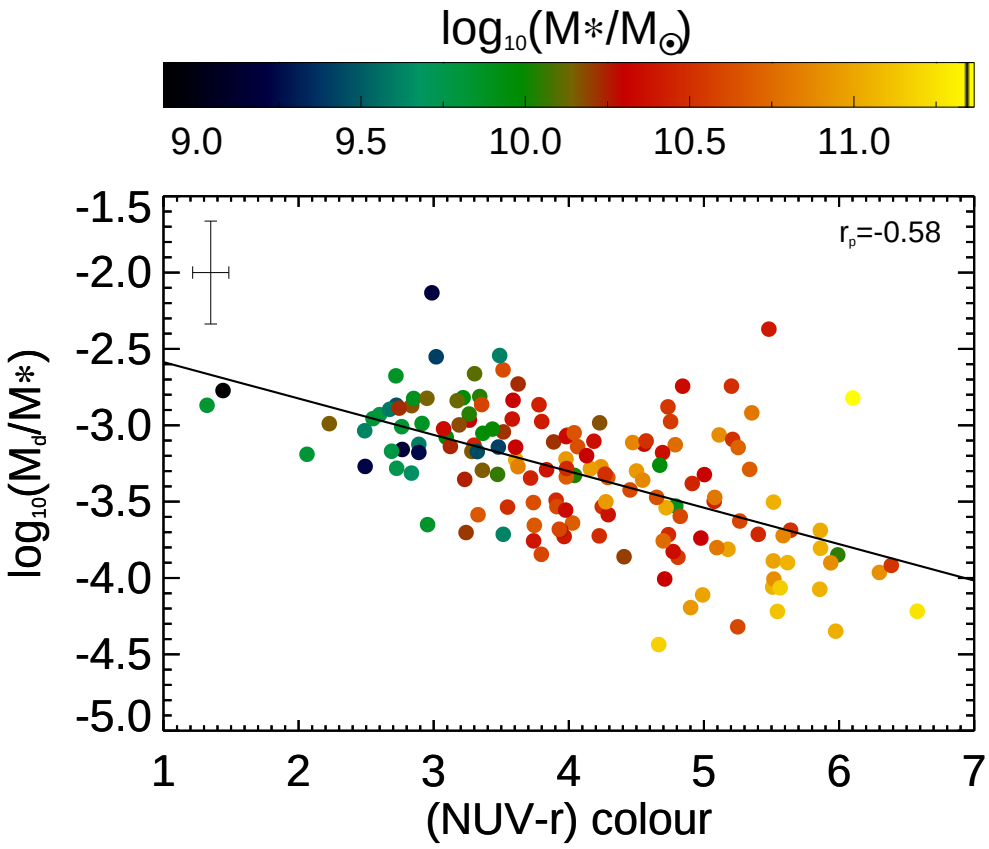

Figure 3.14: Distribution of specific dust masses with (NUV-r) colour for the *SubS* 3σ sample. Points are coloured by the log of their stellar mass. The solid black line is the best fit straight line through the points, with the Pearson coefficient for the fit indicated in the top right-hand corner. Typical error bars for the points are shown in the top left corner.

masses exhibited by *SubS* galaxies. Therefore the difference in mean masses can partly be attributed to sample size, but also to a difference in the nature of the KINGFISH sample (i.e. differences in their selection criteria, and the location and distance of their galaxies). Size is less of an issue with the Smith et al. (2012) study in the HRS, where they select a sample of 62 ETGs, mainly in the Virgo Cluster, of which 45% are detected in the sub-mm. They also calculate dust masses for the 28 detected ETGs using single-temperature modBB fitting, and their average specific dust mass for detected ETGs is much lower than any of the aforementioned works, including this work. However, they do not seem to sample as large a range of environments as these other works, since their sample is restricted mainly to galaxies in the high densities of the Virgo Cluster. Further HRS work by Cortese et al. (2012b) shows that in clusters such as Virgo, the dust fraction of galaxies of a given mass is significantly lower than that of galaxies in isolation or in small groups. This bias for dusty ETGs to reside in lower density environments is also hinted at in Table 3.3 and Figs. 3.11 and 3.12 for the *SubS*. The KINGFISH and HRS studies look at galaxies in the very nearby Universe, and therefore they are able to detect the lowest dust masses in galaxies. Additionally, Smith et al. (2012) emphasise that they only study the most massive ellipticals in the nearby Universe. Given this information, the differences in average normalised dust masses between this and these other two *Herschel* works are understandable.

Next the variation of computed dust masses with UV-optical colours is considered. This is presented in Fig. 3.14, where the galaxies are also coloured by stellar masses. Here a very clear trend is identified. As the ETGs get bluer, they also increase their specific dust masses and decrease in stellar mass. This highlights a key result: the most massive ETGs are redder and therefore more quiescent, and they also contain proportionally less dust. This strengthens the link between dust and star formation and, assuming the more quiescent ETGs do not host many young

blue stars, predicts that low mass red stars do not contribute as highly towards the dust presence in ETGs as bright young stars. This sort of evolution has been shown before: Bourne et al. (2012) show a similar strong anti-correlation between stellar mass and dust-to-stellar mass ratio for their sample of red galaxies. This trend may be further understood if the ETGs are shown to be of different ages, and therefore in different stages in their evolution, or if they are shown to be two completely different populations and types of ETGs.

3.4.2 Contamination Issues

Rigby et al. (2011) found that a significant number of sources may have 350 and 500 μm flux densities that are overestimated by a factor of $\sim$2 in the H-ATLAS SDP fields. This is due mainly to source confusion where the signal-to-noise levels are low. This would result in SED fitting underestimating dust temperatures and overestimating dust masses. There is nothing that can be done to remedy this on an object-by-object basis, but it should be made apparent that such an effect may have carried through to the Phase 1 data.

The presence of radio-emitting AGN within these ETGs is investigated by referring to the Very Large Array FIRST survey, which covers 10,000 degrees over the North and South Galactic Caps, currently with 30% optical counterparts in the SDSS (Becker et al. 1994) and covering the GAMA equatorial regions down to the SDSS DR6 brightness limit. Potential counterparts within a 20″ search radius are searched for, and two *SubS* ETGs are found within search radii of 18.9″ and 9.4″, and 1.4 GHz integrated flux densities of 1.17 and 3.59 mJy respectively. Given the likelihood of these being false counterparts and the low associated flux densities, it would appear radio emitting AGN are not an issue for *SubS* ETGs.

If the *SubS* ETGs do host radio-emitting AGN which have remained undetected through FIRST counterpart matching, it is necessary to consider their implications

for our results. Synchrotron emission from AGN would be modelled as a radio power-law, which may extend into the longest sub-mm wavebands. The modBB fit parameters would then represent not only the thermal FIR/sub-mm emission, but also the synchrotron emission component. This could lead to false cooler temperatures in the fits, as the apparent modBB peak would be pushed to longer wavelengths.

SPIRE 250/350 and 350/500 colours can also be used to check for the presence of radio-loud AGN. Boselli et al. (2010a) show that SPIRE colours are useful for discriminating thermal from synchrotron emission in radio galaxies, with the colours becoming very small for those galaxies with synchrotron emission. The low redshift sample fit in this section has high (f_{350}/f_{500} >1) SPIRE ratios, providing further evidence that the 500 μm waveband is unaffected by synchrotron emission in the sample.

Free-free emission (thermal bremsstrahlung) from ionised HII regions is also a potential contamination factor in the 500 μm waveband. As it seems quite likely these ETGs have HII regions, it is important to quantify the contribution of this free-free emission. Based on the mapping of the starburst galaxy M82, we estimate the typical ratio of free-free emission to dust continuum emission to be approximately 0.016 (1.6%) for HII regions (Fig. 3, Klein et al. 1988) at 500μm, and therefore negligible for this work.

As discussed in Section 3.2.3, the Negrello et al. (2010) and González-Nuevo et al. (2012) selection criteria are used to remove nine galaxies which are quite likely to be lensed. These galaxies did have high enough flux emission to run modBB fits across them. The results of these fits were a range of dust masses of $10^{7-8}\,M_\odot$ (-3.1<$\log_{10}(M_d/M_*)$ <-1.9) and temperatures of 20-35 K, with only one lens galaxy candidate exhibiting a temperature as low as 11 K. Although these galaxies are not included within the presented dust mass plots, upon inspection it

should be noted that if they had been included they would not have changed the straight line fits in Figs. 3.13 and 3.14, or have affected the results, significantly.

Finally, as a check, the modBB fitting was re-run on the ETGs for just the four shortest waveband fluxes, thereby excluding the 500 μm points. The resultant rest-frame temperatures did not change greatly for many of the galaxies, except in the cases ($\sim$4%) where flux from the 250 μm band was much greater than the 350 μm flux. The lack of a strong systematic bias occurring when running this test gives further evidence that the dust characteristics of the *SubS* galaxies are not significantly affected by synchrotron emission or other contamination issues affecting the 500 μm band fluxes.

3.4.3 Elliptical vs Lenticular Dust Characteristics

It is necessary to consider the implications that S0a galaxies have created by being included within these ETG samples, as they may have had an effect on dust results.

It is possible that lenticular galaxies are in fact spirals which have had their star-formation cut off (e.g. Aragón-Salamanca et al. 2006). Supposing ellipticals are formed in a different way, possibly via mergers, the two different formation methods will result in different proportions of dust left within the galaxy systems. If this is the case, one of three possible scenarios need to be considered. Either the dust masses and temperatures being fit to the sample are representative of dusty ETGs overall, or they are representative of either dusty S0a galaxies or E galaxies separately.

Fig. 3.13 shows the trend of normalised dust mass with stellar mass for all ETGs, coloured by morphology. These are plotted separately because lenticular and elliptical galaxies are not necessarily at the same stage of their lives, and may have different evolutionary patterns. Additionally, the presence of a disk in lenticular galaxies points towards them possibly having higher dust masses than

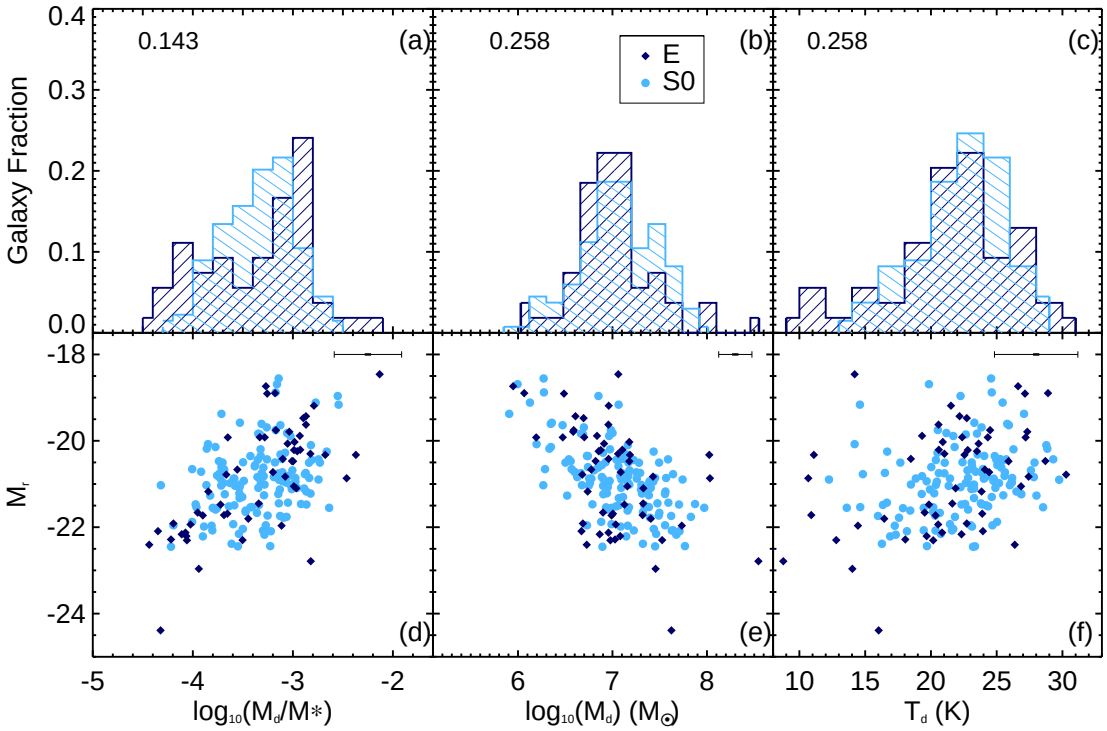

Figure 3.15: Scatter plots and normalised histograms for *SubS* ellipticals and lenticulars. Ellipticals are represented by black filled diamonds and black histograms, and lenticulars by light blue filled circles and light blue histograms. From left to right: (a) histograms of dust mass normalised by stellar mass, (b) histograms of dust mass, (c) histograms of rest-frame dust temperatures calculated by modified Planck function fitting, (d) absolute r-band magnitude (M_r) plotted against normalised dust mass, (e) M_r plotted against dust mass, and (f) M_r plotted against best fit dust temperature. Average errors are shown in the top-right corners. KS-probabilities described in the main text are also included for each histogram.

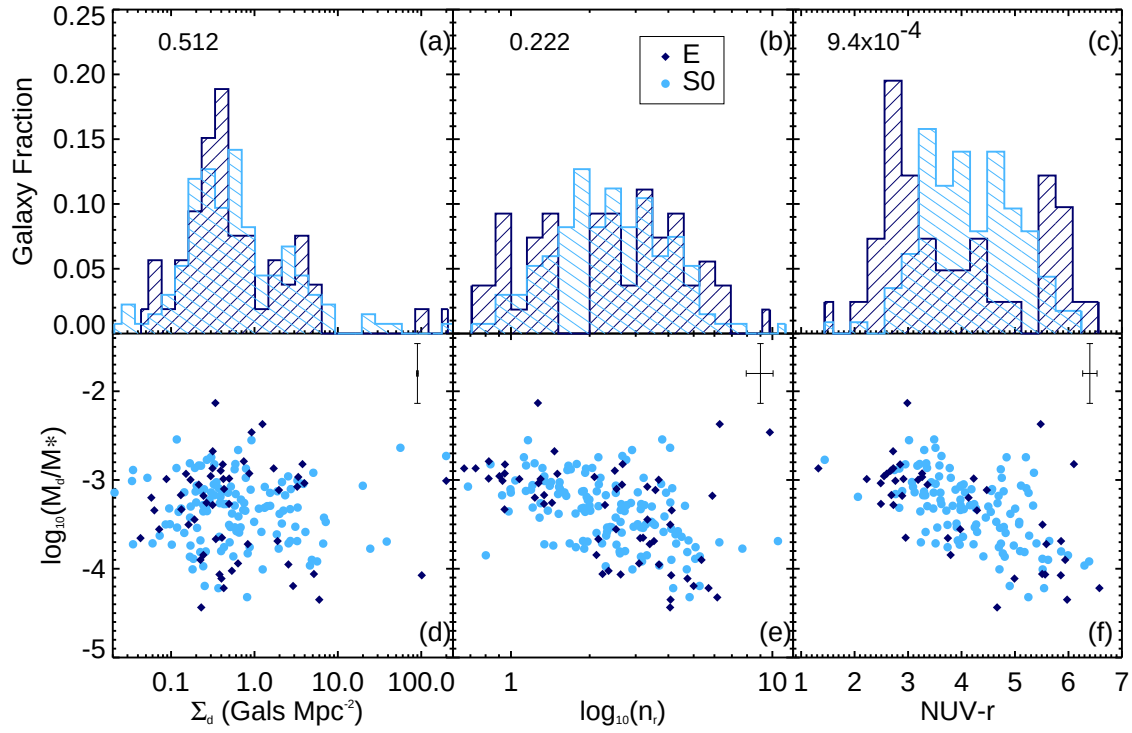

Figure 3.16: Scatter plots and normalised histograms for *SubS* ellipticals and lenticulars. Ellipticals are represented by black filled diamonds and black histograms, and lenticulars by light blue filled circles and light blue histograms. From left to right: (a) normalised histograms of surface density $\Sigma_{\rm d}$, (b) histograms of r-band Sérsic index, (c) histograms of UV-optical colour (NUV-r), (d) scatter plot showing the specific dust mass against surface density, (e) specific dust mass against Sérsic index, and (f) specific dust mass against NUV-r colour. Average errors are shown in the top-right corners. KS-probabilities described in the main text are also included for each histogram.

ellipticals, thus skewing the perception of the dust contents of elliptical galaxies. Such a result is not indicated in Fig. 3.13, where the lenticulars are shown to have the same mean specific dust mass (-3.35) as the ellipticals (-3.36). However, a KS-test of the stellar mass distributions shows them to be marginally different at the 1% level (KS-prob=0.009). The straight-line fit to the ellipticals suggests a slightly stronger trend for specific dust mass to change with stellar mass ($r_{\rm p}$=-0.71) than the trend for lenticulars ($r_{\rm p}$=-0.41). Smaller number densities for the ellipticals weakens this trend somewhat. This result nevertheless indicates that the two different types of ETGs have similar dust properties and therefore that there is some similarity in the way dust in these galaxies evolves and consequently, in the evolution of the galaxies themselves.

The separate morphological properties are explored further in Figs. 3.15 and 3.16 by plotting different parameters against the absolute r-band magnitudes and normalised dust masses respectively. Figs. 3.15(a) and (b) show how both normalised dust mass and total dust mass vary with absolute magnitude. For both galaxy types a clear trend emerges here, which is similar to the trend identified earlier in Section 3.4.1. This is expected since magnitude and stellar mass are related (see discussion in Section 3.4.1). These plots show that the brightest ETGs contain proportionally the least dust and vice versa (Fig. 3.15(d)). Once again, by breaking ETGs down into ellipticals and lenticulars, their comparative properties are explored to find the brightest ETGs are ellipticals, with low specific dust masses (Fig. 3.15(d)) and high dust masses (Fig. 3.15(e)). On the faint end, a well mixed distribution is evident for both types of ETGs. This, and a KS-test, indicates no preference for lenticulars to have different specific dust masses than ellipticals.

The wide distribution of dust temperatures arising from the modified Planck function fits is also highlighted in Fig. 3.15(c) and (f). *SubS* ETGs extend to very

low dust temperatures, with errors of typically ±2 K. This could be attributed to the fact that this is a very large sample of ETGs observed by very sensitive detectors and the galaxies may contain dust temperatures which could not physically have been measured up until now. However, it should be noted that the galaxy with the lowest temperature (∼9 K) has large PACS measurement errors.

All the other ETGs in this sample have dust temperatures higher than 10 K. The distributions of ellipticals and lenticulars look quite similar, although the lowest temperatures (<15 K) belong predominantly to ellipticals. KS-testing shows the distributions are not significantly different. Based on this result, it appears that lenticulars not only contain similar (specific) dust masses to ellipticals, but also similar dust temperatures. The lack of an observable trend of temperature with luminosity also implies that there is no direct correlation between the distributions of dust temperature and stellar mass for the two types of ETGs - this was confirmed using a Pearson correlation test.

The distributions of environment, Sérsic and colour properties of the galaxies as a function of normalised dust mass are examined in Fig. 3.16. Fig. 3.16(a) indicates that there is no significant difference in the distribution of surface densities for the two morphologies, which is confirmed by a KS-test. Its counterpart scatter plot (Fig. 3.16(d)) shows no observable trend for these properties, although the few ellipticals with an intermediate specific dust mass seem to be clustered towards the lower densities.

Figs. 3.16(b) and (e) show the Sérsic index (n_r) distributions of these morphologies and highlight a useful characteristic of ellipticals. Although there are only small numbers of ellipticals, approximately a third of them are at low Sérsic indices (n ∼1). However, Fig. 3.16(e) also indicates that, on average, these low Sérsic index ellipticals are those with the highest specific dust masses ($r_{\rm p}$=0.1). This again supports the idea that dust is causing the lowering of the Sérsic index,

as predicted by Pastrav et al. (2013).

Finally UV-optical colour is examined in Figs. 3.16(c) and (f). Although this trend was seen previously in Fig. 3.14, in this plot the significance of different morphologies becomes apparent. Once again different groupings of ellipticals appear, unlike the solidly filled range presented by the lenticulars. A KS-test shows the NUV-r distributions to be significantly different at well below the 1% level (KS-prob=0.0009). Ellipticals are grouped either as very blue and dusty, or red with a range of specific dust masses. Such a distribution of specific dust mass at the red end indicates that dust may be contributing to reddening in this plot, otherwise galaxies with such high levels of dust (and therefore presumably more star formation) would be expected to occupy the bluer end of this distribution.

3.5 Discussion

The work completed in this chapter has uncovered some key differences in the properties of sub-mm detected and non-detected ETGs. Naively, we would expect the presence of dust in ETGs to be present due to recent merger activity, which may have sparked some low levels of star formation and resulting dust formation. However, there are more profound implications indicated by the trends presented in this chapter than simply a coincidence of mergers.

Sub-mm detected ETGs within the GAMA/H-ATLAS fields have here been shown to represent a significant percentage (29%) of the ETG population, indicating that such objects are not as rare as previously considered. This percentage agrees with other fractions indicated in the literature (e.g. Smith et al. 2012), although cluster-based studies report lower fractions (e.g. di Serego Alighieri et al. 2013). However, given the H-ATLAS detection limits, and the redshift range utilised here, it is likely that lower levels of dust have been missed in ETGs grouped within the *OptS*. Isolating these ETGs from ETGs that are virtually

dust-free would be a next step in strengthening the trends observed in this chapter.

One of the key results observed for the *SubS* ETGs is their more exponential-like (i.e. disky) Sérsic profiles. As described in Chapter 1, Section 1.1.1, elliptical galaxies in particular are being grouped into two classes: boxy, slow-rotator, bright ellipticals, and fainter, fast-rotating, disky ellipticals (Kormendy & Bender 1996; Kormendy et al. 2009; Cappellari et al. 2011b). In the case of our two samples, the *OptS* has properties (such as high Sérsic index) that slot into the first grouping, and the *SubS* has properties that fit the latter. The only disagreement with such a bimodal classification evidenced here is that the *SubS* on average exhibits brighter optical luminosities than the *OptS*. However, this leads to a further point that was expanded upon in Section 3.4.3: a parameter bimodality is clear in the trends exhibited by the dusty ETGs. The *SubS* is in fact composed of the low Sérsic index, high dust-to-stellar mass ratio, low stellar mass ETGs (thought to be the fast rotators) and the high Sérsic index, low dust-to-stellar mass ratio, high stellar mass ETGs that in fact are probably more appropriately placed within the *OptS* than the *SubS*, and would have been had the selection process been dependent on properties other than *Herschel* detections.

For clarity and the purposes of this discussion, we shall describe the ETGs not as sub-mm detected or undetected, but as fast and slow rotators based upon the assumptions and descriptions given above[1]. The differences in properties exhibited by these two different classifications indicate some difference in their evolutionary processes, which should be identified. Let us begin with the the slow rotators. On average their UV-optical and optical colours are red, indicating that these galaxies are largely quiescent[2]. Although their environment surface densities are higher on

[1]Investigating the rotation properties of these galaxies in the future will be the next step to confirming these assumptions.

[2]Dust reddening is not considered likely here, as the majority of these ETGs are non-detected.

average than that of the fast rotators, they are still relatively low, indicating low likelihoods of having endured multiple mergers with other galaxies. The lack of star formation indicators in these ETGs suggests that merger events of gas-rich, disky galaxies are unlikely to be the principle contributors to the formation of these ETGs. In fact, it is more likely that the mergers that contributed to the mass and radius increase of these ETGs will have been dissipationless ("dry"; Naab et al. 2006, 2009), although whether they were minor or major mergers cannot be said.

On the other hand, it is likely that the history of the fast rotators is quite different. Their colours are much bluer, indicating some ongoing level of star formation and therefore the presence of gas. Similar mass ("major") mergers are unlikely to have featured in the evolution of these galaxies, at least in the recent past. Dry major mergers would not result in any star formation in these galaxies, and wet major mergers will have caused a massive spark of star formation (i.e. there would be a massively increased star formation efficiency) and most of the galaxy's gas would be used up during this period. This would also lead to a quiescent ETG. Therefore, it is thought that minor mergers are the main source of evolution of these fast rotators (Naab et al. 2006; Kaviraj et al. 2009). These mergers are more likely to be dissipative than gas-poor, supplying the fuel for the ongoing star formation being observed here. The sparsity of the environment that these ETGs reside in may have had an additional effect on their evolution: lack of galaxies to interact with could explain their slow mass build-up and their high dust levels. In fact, the difference in dust-to-stellar mass ratio identified in Fig. 3.13 between H-ATLAS ETGs and cluster *Herschel* surveys may be caused by this difference in environment. Cluster galaxies undergo processes such as ram-pressure stripping (e.g. Takeda et al. 1984; Lucero et al. 2005) and increased galaxy interactions that galaxies in low-density environments are not subject to.

3.6 Conclusions

This chapter describes the work done in exploring structural and dust properties of early-type galaxies. By using visual, morphological classifications applied to a low-z sample of GAMA galaxies from Kelvin et al. (2014), two ETG samples were created from the GAMA data. These are the *SubS* - galaxies classified as ETGs with H-ATLAS SPIRE 5σ detections - and the *OptS* - galaxies classified as ETGs without H-ATLAS SPIRE detections.

A series of optical and UV properties for these two samples was explored. These included concentration and Sérsic indices, stellar masses, luminosities, optical colours, and effective radii. GALEX NUV detections were used to explore the UV-optical colours of these galaxies and the environments of the ETGs were examined by way of 5^{th} nearest neighbour surface densities and group membership data. The results for these tests are summarised here:

(i) A 29% H-ATLAS detection rate was found for ETGs in the equatorial field. The detection rate for sub-mm detected ellipticals is 22%, and 37% for sub-mm detected lenticulars (see Section 3.2.2).

(ii) H-ATLAS detected (*SubS*) ETGs are shown to have lower concentrations and Sérsic indices than undetected (*OptS*) ETGs. It has been shown that the presence of dust can lower Sérsic index (Pastrav et al. 2013), an effect regarded as a possible explanation for these findings.

(iii) H-ATLAS detected ETGs are shown to be typically optically brighter, bluer and larger than undetected ETGs. However, differences in the stellar mass distributions of the samples are found to be not significant.

(iv) The H-ATLAS detected sample shows significantly brighter NUV luminosities and bluer colours in the UV-optical than the undetected sample. This

suggests that the observed dust emission is linked with changes in the optical and UV colours, which are indicative of young star formation. Such a colour trend is in agreement with previous works such as Rowlands et al. (2012) and Dariush et al. (2011). However, the H-ATLAS detected ETGs are redder than LTGs from the same KS14 parent sample, and therefore dominate an intermediate NUV-r colour space.

(v) The H-ATLAS detected ETGs are shown to inhabit sparser environments, particularly for the lower luminosity ETG subset. No links are found between ETG surface density and group membership or multiplicity.

Modified single-temperature Planck functions were fitted to the 250 μm 5σ detected *SubS* galaxies containing $\geq$3σ emission in the SPIRE 350 μm waveband. Characteristics of the *SubS* galaxies based on resultant best-fit temperatures and associated dust masses were then presented, and trends with optical and UV properties explored. These results can be summarised as follows:

(i) ETGs in the H-ATLAS detected sample are shown to contain dust masses ranging from 8.1×10^{5}-3.5×10^{8} $M_{\odot}$, with a range of rest-frame temperatures from 9-30 K. These dust masses are consistent with previous *Herschel* work such as Skibba et al. (2011), but lower than results from previous H-ATLAS work in Rowlands et al. (2012). These results may differ due to larger sample size, lower redshift limit, or uncertainties in morphological classifications.

(ii) A strong trend for specific dust mass to decrease with redder (NUV-r) colour was discovered. This implies that the dustiest ETGs have the bluest colours, linking recent star formation with a higher specific dust presence.

(iii) The faintest H-ATLAS detected ETGs with the lowest stellar masses are shown to have higher specific dust masses and lower Sérsic indices compared

to the brightest H-ATLAS detected ETGs. This result is consistent with downsizing, as the most massive, brightest galaxies are more similar to the *OptS* ETGs in terms of their specific dust masses and Sérsic profiles.

(iv) Splitting the dusty ETG sample into separate morphologies of elliptical and lenticular galaxies indicates how they contribute to the measured dust properties. No difference in the dust masses (whole or specific) or temperatures of both ETG types is found. However, significant differences in their NUV-r colour and stellar mass distributions are noted.

(v) Ellipticals may therefore be grouped into two sets: the faint, blue, low mass, relatively dusty ellipticals and bright, red, massive, ellipticals with lower specific dust masses. This leads to the conclusion that two different populations of ellipticals, or at least two different age ranges, are being studied.

The ETG samples in this chapter have been selected and analysed to set up future work in examining the *SubS* galaxies' cold dust properties. The isothermal SED fitting described in Section 3.4 outputs some basic properties for the sub-mm selected galaxies, but doesn't contribute information about which mechanism powers the dust emission within their interstellar media. More about the distribution and physical properties of the dust in ETG ISM will be discussed in Chapter 5. Such properties include the grain temperatures and overall dust masses, but also the physical mechanisms which heat galactic dust. The future work will begin with fitting the MIR/FIR/sub-mm waveband data with several template models. The first model will account for the more well-known radiative heating by photons in the ISM, whereas the second model will fit the data with parameters based on collisional heating. Our primary aims are to develop an understanding of what the main source of dust heating is within sub-mm emitting ETGs.

Before beginning this new study, we first look at how ETGs in the *SubS* compare with results for a very nearby, sub-mm detected sample, based on ETGs in the

Virgo Cluster (HeViCS team; di Serego Alighieri et al. 2013). This will improve our understanding of whether GAMA/H-ATLAS ETGs exhibit typical properties of sub-mm detected ETGs or whether they represent an extraordinary class of ETG.

Chapter 4

A GAMA/H-ATLAS Comparison with Nearby Cluster ETGs

The world is indeed full of peril
and in it there are many dark places.
But still there is much that is fair.

J.R.R. Tolkien, The Two Towers

4.1 Introduction

Although ETGs typically comprise a relatively passive and homogeneous class, it has been shown in Chapter 3 of this thesis that this is not always the case. ETGs with strong FIR luminosities are preferentially detected by the PACS and SPIRE instruments aboard the *Herschel Space Observatory* with H-ATLAS, and these ETGs in particular have been shown to contain blue UV-optical colours (representative of ongoing or recent star formation), large dust masses and cold

dust temperatures, thus sharing similar properties with late-type spiral galaxies rather than their native ETG class. These results are similar to those found for smaller samples of H-ATLAS detected ETGs (Rowlands et al. 2012; Kaviraj et al. 2013).

What remains to be seen is whether these sub-mm detected ETGs are atypical of all ETGs in general. This is a possibility because this sample is derived from a 144 deg^2 region of sky (equivalent to a volume of $\sim$76,000 Mpc^3), resulting in the selection of ETGs from many different environments and potentially undergoing extreme mergers or interactions. An alternative to this scenario consists of these galaxies representing younger versions of the 'standard' ETG; i.e. they may have formed recently, or have had more extended star formation histories. It is possible to test both of these hypotheses by comparing the *SubS* ETGs to *Herschel* detected ETGs in the very local Universe (i.e. the Virgo Cluster) and examining how their respective properties vary.

There is significant evidence in support of the latter ETG scenario (i.e. the 'downsizing' effect; Cowie et al. 1996). As discussed in Section 1.1.2, downsizing is a model whereby the most massive galaxies form on shorter timescales than their less massive counterparts. If downsizing is a consequence of environment (e.g. Thomas et al. 2005), ETGs in sparse environments are more likely to be at an earlier stage in their evolution than ETGs in dense environments. There have been multiple *Herschel* studies on ETGs in cluster environments, primarily within the nearby (17-32 Mpc) Virgo Cluster (e.g. Smith et al. 2012; di Serego Alighieri et al. 2013), but Chapter 3 is the only large *Herschel* study within a range of environments. All of the cluster studies have utilised similar modified blackbody (modBB) fitting approaches to that undertaken in Section 3.4.1 in order to constrain the dust properties of ETGs observed with *Herschel*. Summarily, their fits have shown Virgo Cluster ETGs to contain dust masses of order $10^{4-6}\,M_{\odot}$

- a factor of ten on average lower than the results found for the *SubS*.

Temi et al. (2009a,b) and Amblard et al. (2014) have further investigated the diversity of ETGs by studying the physical properties of a sample of local E and S0 galaxies. They find that many local S0 galaxies are quite distinct from Es, containing dust and cold gas in amounts that may be sufficient to generate appreciable star formation at rates as large as several $M_{\odot}\,year^{-1}$. However in this thesis we cannot investigate the differences between E and S0 galaxies in detail, since they are difficult to distinguish in the H-ATLAS/GAMA sample because of their distance.

Although a single modBB fitting approach gives a good estimate of the mass of cold, diffuse dust grains in the ISM of galaxies at all redshifts (Dunne et al. 2000; Blain et al. 2003; Pope et al. 2006; Dye et al. 2010; Bianchi 2013), it does not account for the emission from dust in warmer media, such as the grains surrounding the birth clouds of hot, young stars. The addition of further blackbodies peaking at higher temperatures and shorter wavelengths would improve such fits (Dunne & Eales 2001; Galametz et al. 2011; Dale et al. 2012). Furthermore, given the wealth of panchromatic data for these ETGs, it is possible to exploit multi-wavelength SED fits which consider stellar emission at UV/optical wavelengths, the attenuation by dust and resultant emission in the infrared.

The most robust approach of modelling the full SED includes a full treatment of attenuation within the galaxy, by using radiative transfer to calculate the integrated MIR/FIR/sub-mm emission due to stellar extinction and re-emission by dust grains. This has been done for various specifications of the dust and stellar geometry in disk galaxies (Siebenmorgen et al. 1992; Silva et al. 1998; Popescu et al. 2000a) - however ETGs have not yet been successfully modelled in this way as the dust geometry in these systems is currently unconstrained. Therefore in this Chapter we utilise an energy balance code to model the panchromatic SED,

described fully in Section 4.4.1 (da Cunha et al. 2008). This allows us to account for emission from dust in warmer media. Thus it is possible to characterise dust grain properties for both the *SubS* and nearby cluster ETGs in a uniform manner, as well as taking into account data at shorter wavelengths to help constrain further parameters such as the star-formation rate and galactic age. Here we choose a *Herschel* Virgo Cluster Survey (HeViCS) sample (di Serego Alighieri et al. 2013) to compare with our ETGs, because the sample contains a full complement of *Herschel* and panchromatic data. Additionally, all the ETGs in this sample are located within the Virgo cluster, unlike some of the other samples available that contain a range of environmental properties.

This Chapter is laid out in the following manner. Section 4.2 summarises the work done in Chapter 3 and di Serego Alighieri et al. (2013) in creating statistically significant samples of ETGs at low redshift and in the Virgo Cluster, respectively. A brief comparison of the ETG samples is also given, based on the results of these studies. Section 4.3 describes the calculation of nearest neighbour environmental densities for the two samples, and compares the results therein. Panchromatic SED fitting is shown in Section 4.4, followed by a discussion of the results so far. Finally, a pilot study examining further properties of the *SubS* galaxies in contrast to the Virgo ETGs is described in Section 4.5. A discussion and some conclusions are given in Section 4.6 and 4.7.

4.2 Overview of ETG Samples

This Chapter compares and contrasts two ETG samples, which are described below. Particular emphasis is placed on the differences between the classification criteria for these two samples. A summary of the results from their parent papers is also given.

4.2.1 H-ATLAS Sample

The H-ATLAS Sample comprises 220 Es and S0s with 5σ 250 μm detections with *Herschel*, and optical counterparts in GAMA (i.e. the *SubS* described in Chapter 3). The classification process for these ETGs is fully described in Chapters 2 and 3; briefly it was based on visual classification of blue, green and red optical galaxy cutouts into six groupings of E, S0, SB0a, Sbc, SBbc and Sd galaxies (see Kelvin et al. 2014 for a full account of this process). The galaxies classified in this way are GAMA I galaxies within a redshift range of $0.013 \leq z \leq 0.06$ and complete to an absolute magnitude cutoff of $M_r \leq -17.4$ - these limits are therefore also applicable to the ETG sample; although the faintest ETG within this sample is almost a magnitude brighter than this faint limit.

The ETG sample was constructed from the H-ATLAS detected E and S0 (which include both S0 and S0a galaxies) galaxies from within this classified set of galaxies, with additional criteria imposed to remove any potential spiral structure, edge-on disks, or small objects which may be dominated by the PSF and thereby possibly misclassified. Galaxies with AGN and LINER signatures in the optical BPT diagram (Baldwin et al. 1981) were also removed, so as to only consider galaxies with a FIR/sub-mm SED dominated by thermal dust emission. This resultant sample contains 73 Es and 147 S0s, a few examples of which are shown as colour composites in Fig. 3.3. The detailed creation of this sample is also described in Chapter 3, Section 3.2.2.

Chapter 3 showed the H-ATLAS sub-mm detected ETG sample to contain unusual characteristics in comparison to undetected ETGs. In particular, both optical and UV-optical colours were typically quite blue, indicating some ongoing star formation in these systems. The galaxy light profiles indicated more exponential (or less centrally concentrated) luminosity distributions, which might indicate some recent merging activity, or may be an effect of dust attenuation. Finally an

investigation of nearest neighbour galaxy surface density revealed that these ETGs inhabit sparser environments than the non-detected ETGs.

ModBB models with emissivity spectral index β=2 and 350 μm mass absorption coefficient κ_{250}=0.89 $\mathrm{m^2\,kg^{-1}}$ (Dunne et al. 2011) were fit to the PACS and SPIRE data for this sample. These fitting parameters are fixed to these values throughout this Chapter. Chapter 3 reports a range of rest-frame dust temperatures of 9-30 K and a range of dust masses of 8.1×10^5-3.5×10^8 $\mathrm{M_\odot}$, with a mean dust-to-stellar mass ratio of $\log_{10}(\mathrm{M_d/M_*})$=-3.37. These results are the key parameters which will be investigated within this Chapter, in comparison to the nearby ETGs in the Virgo Cluster. A summary of the characteristics of H-ATLAS and HeViCs Samples (described in Section 4.2.2) is given in Table 4.1.

4.2.2 HeViCs Sample

The *Herschel* Virgo Cluster Survey (HeViCS[1]; Davies et al. 2010; Davies et al. 2012) is an audit of a large fraction (84 square degrees) of the Virgo Cluster in the same five *Herschel* bands as the H-ATLAS survey. This specifically samples the dense environment of a nearby cluster, going down to fainter stellar luminosities than H-ATLAS. Additionally their observations are deeper than the H-ATLAS observations, with four linked cross-scans for HeViCS compared to a single cross-scan for H-ATLAS. HeViCS observations were performed in fast-parallel mode with PACS and SPIRE, with a scan rate of 60″ $\mathrm{s^{-1}}$. The HeViCS 5σ sensitivity at 250 μm is 25-33 mJy for sources smaller than the PSF (Auld et al. 2013; di Serego Alighieri et al. 2013); depending on the dust temperature this corresponds to a dust mass of $\sim$0.2-1$\times10^5$ $\mathrm{M_\odot}$ at the 17 Mpc distance of the main Virgo Cluster cloud. A detailed account of the data collection, reduction and flux measurements can be found in Auld et al. (2013) and di Serego Alighieri et al. (2013).

[1]http://wiki.arcetri.astro.it/bin/view/HeViCS/WebHome

Parameter	**H-ATLAS Detected**		**HeViCS Detected**	
	min	max	min	max
Sample Size (galaxies)	220		33	
Distance (Mpc)	57.2	265.4	17.0	32.0
$\log_{10}(M_*)$ ($M_\odot$)	8.9	11.4	8.7	11.4
M_r (mag)	-18.2	-23.1	-17.4	-23.1
m_r (mag)	17.7	13.3	14.1	8.1
m_{NUV} (mag)	22.7	16.6	18.1	13.8
F_{250} (Jy)	0.033	0.770	0.013	7.992
L_{250} (ergs s^{-1} Hz^{-1})	1.62×10^{29}	4.3×10^{31}	4.4×10^{27}	2.8×10^{30}
$\log_{10}(M_d)$ ($M_\odot$)	5.91	8.54	4.48	6.67
$\log_{10}(M_d/M_*)$	-4.44	-2.13	-6.29	-3.07
Σ_{gal} (gals Mpc^{-2})	0.001	37.08	29.19	463.10

Table 4.1: Parameters indicating the types of ETGs found in the sub-mm detected H-ATLAS and HeViCS samples. Note that the parameters for the HeViCS sample only include the 33 ETGs with $M_r \leq$-17.4. The parameters shown include sample size, stellar masses, r-band absolute magnitude, r- and NUV-band apparent magnitude, total 250 μm flux and luminosity. Dust mass, dust-to-stellar mass ratio and environmental density ranges are also shown, calculated as described in the main text.

A very large set of data is available for galaxies in the Virgo Cluster. The original source of information is the Virgo Cluster Catalogue (VCC, Binggeli et al. 1985, 1993) which, together with Virgo SDSS data (Davies et al. 2014), will remain the most complete optical catalogue until the New Virgo Cluster Survey Catalogue (NGVS, Ferrarese et al. 2012) becomes available. The VCC is complete to a photographic magnitude $m_{pg} = 18.0$, but also contains fainter galaxies. GOLDMine (Gavazzi et al. 2003) provides a compilation of data on VCC galaxies. Useful additions are the GALEX Ultraviolet Virgo Cluster Survey papers (GUViCS, Boselli et al. 2011; Boselli 2012) and the HI survey of ETGs of di Serego Alighieri et al. (2007).

For HeViCS, di Serego Alighieri et al. (2013) (S13) utilise an input optical sample from the VCC, constrained by ETG morphology (as compiled in GOLDMine; Gavazzi et al. 2003) but not limited in any other respect. Therefore their sample of 925 ETGs spans a range of magnitudes, from dwarf systems to the most massive ETGs, and contains classifications equal or earlier than S0a-S0/Sa types.

S13 found 52 ETGs by searching for *Herschel* counterparts within one pixel ($6''$) of the expected position ratios and with signal-to-noise (S/N) greater than 5, in the parent sample described above. The reliability of these counterparts is fully discussed in S13. In order to make a fair comparison with the brighter galaxies in the GAMA/H-ATLAS sample, we selected a bright subsample of these 52 ETGs by applying a cutoff of $M_r \leq$-17.4, as with the GAMA galaxies. This subsample is complete for the Virgo Cluster and contains 33 ETGs whose main properties are given and contrasted to the H-ATLAS sample in Table 4.1. Sixteen of the nineteen galaxies removed have formal GOLDMine dwarf classifications. From here on, these 33 ETGs will form the HeViCS detected sample. The magnitude cutoff $M_r \leq$-17.4 also has the effect of removing all those ETGs identified as possible contaminating background sources in S13. Therefore all the 33 HeViCS

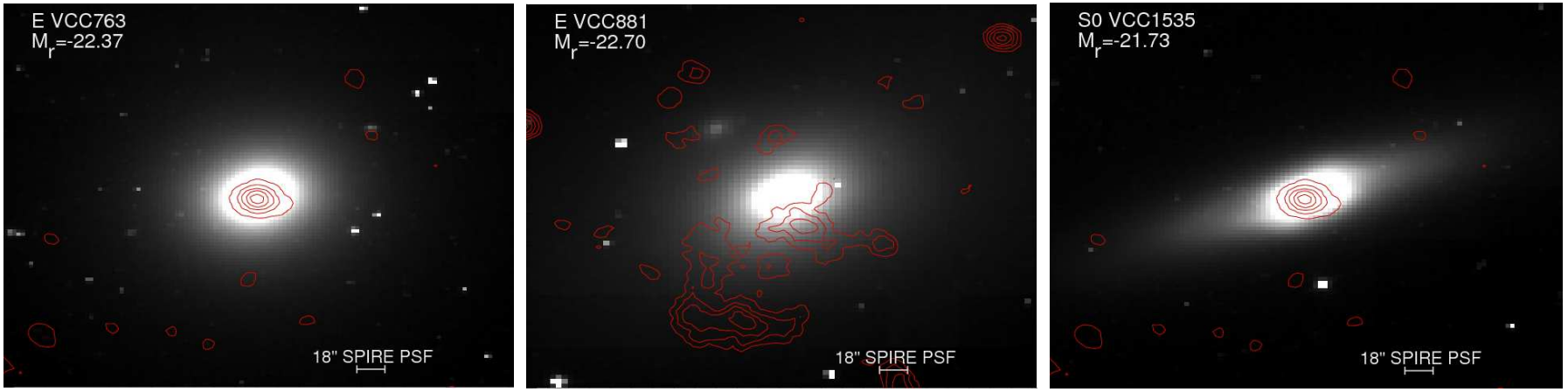

Figure 4.1: Example images of sub-mm detected HeViCS galaxies with a variety of classifications. The images are 6′ SDSS g-band images with superimposed HeViCS 250 μm contours in red. These contour levels represent the following percentages of the 250 μm flux: 14, 43, 71 and 100% (VCC763); 18, 36, 55, 73 and 100% (VCC881); 3, 28, 52, 76 and 100% (VCC1535). Galaxy GOLDMine classification, identification and absolute r-band magnitudes are shown on the top-left of the images. Note that VCC 763 has a synchrotron component. The 18″ SPIRE FWHM PSF is also shown in these images.

ETGs considered here have secure identifications. Fig. 4.1 shows a few examples of Virgo ETG detected in HeViCS.

Apparent r-band magnitudes for this ETG sample have been obtained from the work by Cortese et al. (2012a), where they calculated UV and optical asymptotic magnitudes for the HRS galaxies, some of which are in the Virgo Cluster. This provided AB r-band magnitudes for 148 HeViCS galaxies; the remaining HeViCS galaxies have magnitudes calculated from the combination of B-band magnitudes from GOLDMine and the average (B-r) = 1.02±0.26 colour obtained from these 148 galaxies. These apparent magnitudes are then converted to absolute magnitudes using the GOLDMine distances and the appropriate Galactic absorption.

Stellar masses were estimated for these galaxies using the method of Zibetti et al. (2009), whereby optical (and NIR when available) photometry and synthetic libraries are compared. Dust temperatures and masses were derived from modBB model fits to the FIR/sub-mm data. For the 33 massive (i.e. non-dwarf) ETGs and the same values of β and κ_{250} as Chapter 3, the dust temperatures and masses are calculated as 14.6-30.9 K and 3.0×10^4-4.7×10^6 $M_\odot$ respectively. The mean dust-to-stellar mass ratio is $\log_{10}(M_d/M_*)$=-3.93. These dust mass parameters are lower by approximately a factor of ten, even though the morphologies of the galaxies are similar and stellar mass ranges overlap. This is due to the fact that the closest H-ATLAS ETGs (those at $z \leq$0.013) are more than three times further away from us than the main Virgo cloud at 17 Mpc, and on average the H-ATLAS ETGs are still much further away (see Table 4.1). Therefore smaller quantities of dust (at least ten times smaller) can be detected in HeViCS ETGs than in H-ATLAS. These differences need to be understood in the broader context to avoid possible biased conclusions about the properties of ETGs as a class.

Dust appears to be much more concentrated than stars in Virgo ETGs and more luminous ETGs have higher dust temperatures (Smith et al. 2012; S13).

The dust mass does not correlate clearly with stellar mass, while the dust-to-stellar mass ratio anticorrelates with galaxy luminosity. The dusty ETGs appear to prefer the densest regions of the Virgo Cluster. Contrary to H-ATLAS/GAMA ETGs, the HeViCS ETGs detected at 250 μm are not bluer than the undetected HeViCS ETGs (di Serego Alighieri 2013).

4.2.3 Sample Comparison

There are some clear differences between the two samples which need to be addressed before proceeding with a comparison of their properties. A primary concern is the difference in galaxy distance (see Table 4.1): HeViCS ETGs are located in the nearby Universe at a distance between 17 and 32 Mpc, whereas H-ATLAS ETGs are further away within a redshift range of $0.013 \leq z \leq 0.06$; this equates to an average distance of $\sim$195 Mpc. As a consequence, H-ATLAS ETGs will have lower spatial resolution, larger luminosity at the optical detection threshold, and a higher dust-mass detection threshold. HeViCS ETGs are very well resolved and have lower detection thresholds at all wavebands. For H-ATLAS, this results in the morphological classification not being as detailed as that completed for HeViCS. Therefore H-ATLAS ETGs can be identified as either E or S0 galaxies, but cannot distinguish any dwarf galaxies, which in any case are excluded by the $M_r \leq$-17.4 limit.

Given that this work will contain a statistical analysis of the properties of the two samples, it is important to consider whether the ETG sample sizes are statistically significant. Additionally, when comparing properties of the samples using statistical testing, it is preferable for the sample sizes to be of similar orders of magnitude in order to obtain a fair analysis. The H-ATLAS sample contains 220 ETGs detected in the FIR, whereas HeViCS contains 33 ETGs (within the H-ATLAS magnitude cutoff of $M_r \leq$-17.4). Both samples are large enough to run

a Kolmogorov-Smirnov (KS) test[2] to check whether the populations are similar. The sample sizes themselves are different with the HeViCS sample only containing ∼15% of the H-ATLAS numbers, but the difference is not so large that such a test would be invalid.

4.3 Exploring Environments

As HeViCS ETGs are extracted specifically from the Virgo Cluster environment, their environments are likely to be quite dense, although exact densities will depend on the physical positions of the ETGs within the cluster. Conversely, because the ETGs in the H-ATLAS sample were taken from a wide area of sky over a large volume, they are likely to belong to a range of environments, reaching low densities. In order to quantitatively decide whether these above points are true, it is necessary to calculate some form of environmental density in a consistent manner for the two samples.

4.3.1 Nearest Neighbour Densities

To calculate environmental densities we utilise nearest neighbour environment surface densities. This has already been done to some extent for the H-ATLAS sample (Brough et al. 2013, A13 and Chapter 3), although a bright magnitude limit of $M_r \leq$-20 was imposed that may not accurately sample the true densities of these ETGs. Nearest neighbour densities are now calculated which do not incorporate so bright a magnitude limit.

Chris Beaumont's IDL library[3] is used to calculate a smoothed map of the coordinates of all the galaxies in the HeViCS and H-ATLAS sample regions, respectively, based on the method in Gutermuth et al. (2005). Although only the

[2]The KS-test is sensitive to fairly small differences even in small sample populations

[3]http://www.ifa.hawaii.edu/~beaumont/code/

environments of the sub-mm detected ETGs are of interest to this work, it is necessary to perform this routine on the entire galactic population within these regions to accurately depict the true density; this is the density-defining population (DDP). For every galaxy, the algorithm calculates the distance D_N to the N-th closest object and thus the surface density

$$\Sigma_{\rm gal} = \frac{N}{\pi D_N^2}. \tag{4.1}$$

The value of N chosen for these calculations is five, for consistency with Chapter 3. Additional calculations are then required to convert the coordinates of the surface densities from objects per square degrees to objects per square Mpc. For the HeViCS galaxies, this is a straightforward conversion using the distance of the galaxy.

These calculations are not as simple for the H-ATLAS sample. Because of the large redshift range of the galaxies, Brough et al. (2013) and Chapter 3 limited the DDP for each sample galaxy to a velocity cylinder of $\pm 1000\,{\rm km\,s^{-1}}$ over which the surface density is calculated, so that the latter is not influenced by galaxies at large distances, which clearly cannot have any environmental effect. This is also repeated here. Once each DDP has been created, the procedure described above for the HeViCS densities can be run, and surface densities calculated.

An additional restriction for these calculations is the imposed magnitude limit on the galaxies used to create the DDP. The Virgo Cluster galaxies can be detected down to much fainter magnitude limits than the higher redshift galaxies, and therefore surface densities for the latter are likely to be underestimated because dwarf galaxies which are detected in the Virgo Cluster cannot be detected at higher redshifts. To avoid this, a magnitude limit $M_r \leq$-17.4 is applied to the DDP of both samples. This is the faintest limit which still ensures completeness for the H-ATLAS/GAMA sample at $0.013 < z < 0.06$.

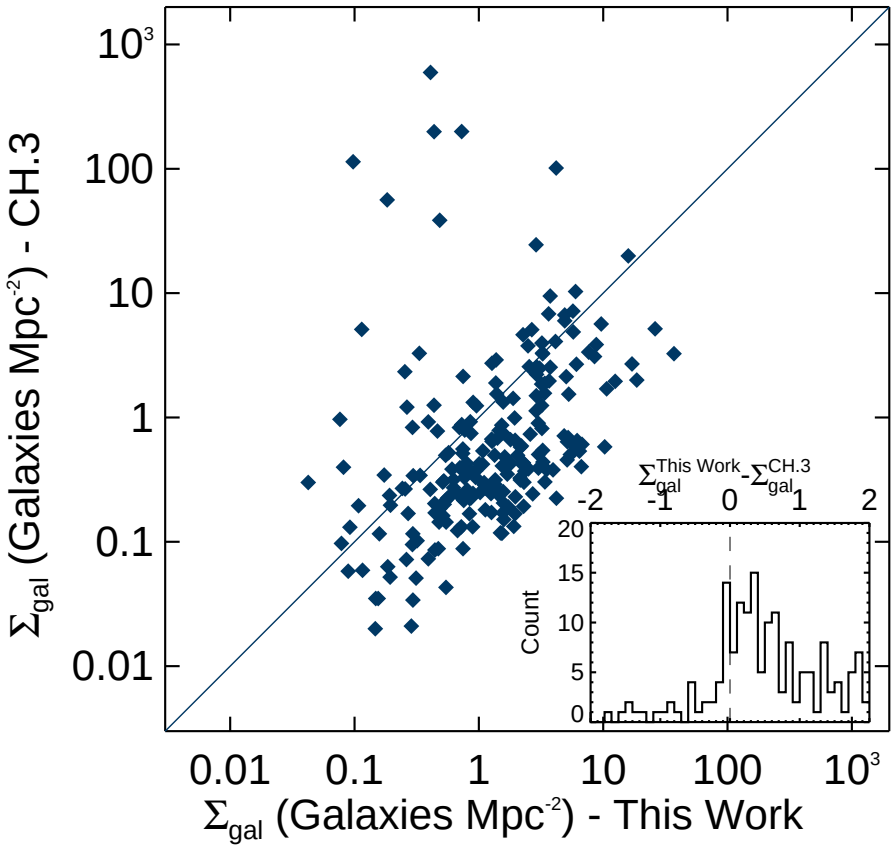

Figure 4.2: A comparison of the nearest neighbour densities for the H-ATLAS sample calculated in this chapter with those calculated in Chapter 3. The key difference in the calculation of these densities is the magnitude limit of the DDPs required to calculate these values. A one-to-one correlation is shown to aid comparison. The inset plot shows the quantitative difference between the two in histogram form.

The calculated surface densities are tested by comparing them with those derived by Brough et al. (2013) and displayed in Chapter 3; see Fig. 4.2. This shows a direct comparison between the two parameters, with a mostly linear relation defined. There are some galaxies from Chapter 3 which have randomly higher surface densities than those calculated here: this can be attributed to the upper limit surface densities which were calculated for those galaxies flagged as lying at the edge of a DDP. More importantly, the surface densities calculated in this work are systematically higher than those in Chapter 3. This is as expected, as the fainter DDP magnitude limit will include more galaxies in the calculation, resulting in higher densities.

4.3.2 Sample Environments

There are three key points to be investigated when comparing the environmental densities of ETGs in the H-ATLAS sample with those from the HeViCS sample. Firstly, do the respective sub-mm detected samples vary in environment? Next should this study be extended to all ETGs in Chapter 3 compared to all ETGs in S13? Finally, it is also of interest whether the sub-mm detected versus non-detected ETGs in these respective samples vary in environment between themselves and if so, what the direction of this variation is.

The trends of these multiple possible distributions of densities are investigated in Figs. 4.3 and 4.4. A KS-test of the sub-mm detected samples' surface densities in Fig. 4.3(a) reveals a probability of only 1.95×10^{-26} (i.e. virtually zero) of the two distributions being similar. This very clearly indicates that, based on these calculations of nearest neighbour densities, H-ATLAS and HeViCS ETGs reside in very different environments. Where HeViCS ETGs are dominated by the dense cluster environment, the H-ATLAS ETGs on the other hand mostly occupy sparse and non-cluster environments.

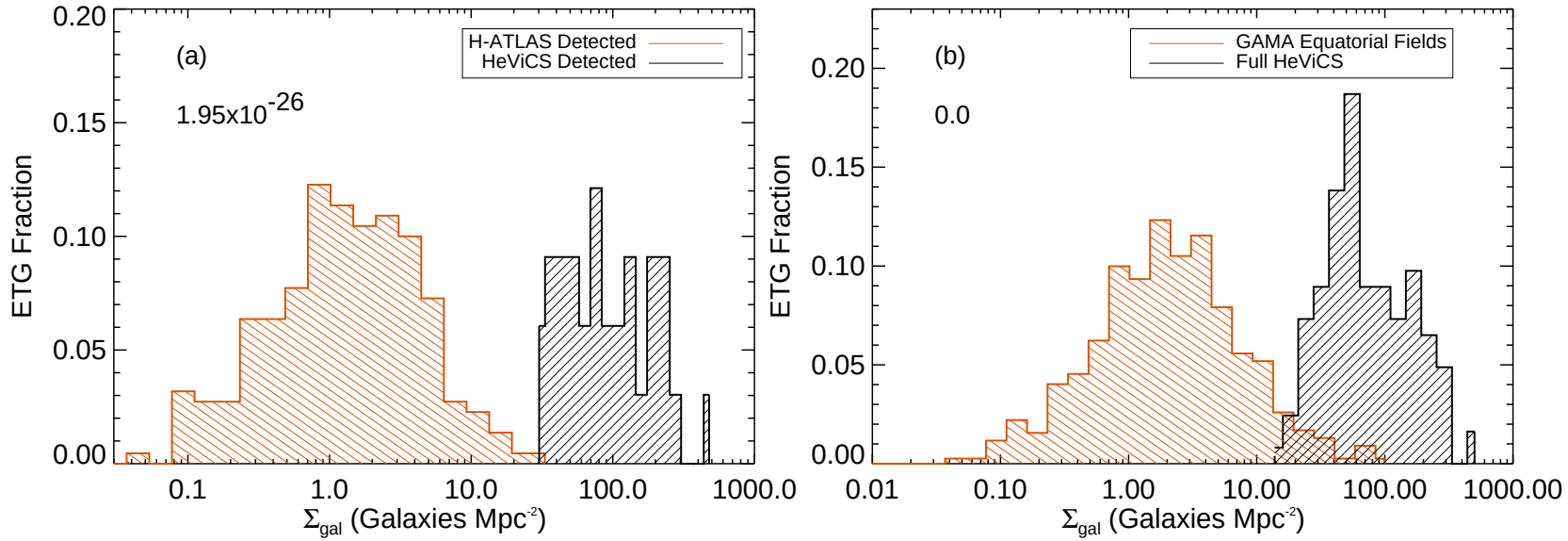

Figure 4.3: Left panel: normalised distributions of sub-mm detected ETGs in the H-ATLAS (orange histogram) and HeViCS (black histogram) samples. Right panel: distributions of the combination of sub-mm detected and undetected ETGs in the H-ATLAS (orange histogram) and HeViCS (black histogram) samples. KS-probabilities of the presented samples being drawn from the same distribution are shown in the top left of the plots.

Examination of the samples including those ETGs without sub-mm detections in Fig. 4.3(b) reveals the probability of ETGs residing in the same environments drops to zero, yet there is a modest overlap in the environments for the two samples between $20< \Sigma_{\rm gal} <100$ gals Mpc^{-2}. This overlap can mostly be associated with those ETGs which are not detected at sub-mm wavelengths and is explored further in Fig. 4.4. Note that such an overlap is not apparent in Fig. 4.3(a) for the sub-mm detected samples. Furthermore, in spite of this overlap, the H-ATLAS undetected sample does not contain densities as high as the HeViCS ETGs.

The GAMA survey as a whole is deep and wide enough to sample a broad range of galaxy environments, from isolated field galaxies, to pairs, and both small and large groups (e.g. Robotham et al. 2011). However, it does not well sample the densest regions of the Universe as found in large clusters, since these are very rare environments. This can be seen in Fig. 4.3(b), which shows that the GAMA galaxies in the three equatorial fields sampled in Chapter 3 do not extend up to the densities found in the Virgo Cluster. Thus this ETG study is contrasting largely different environments.

Fig. 4.4 explores the trend of surface density between sub-mm detected and undetected ETGs for the respective samples. KS-tests for both sets of distributions indicate that there is a significant difference of less than 1% between the H-ATLAS distributions, but that the HeViCS distributions are very similar. This indicates no environment density preference within Virgo ETGs (for the subsample of data used here). An additional result made apparent in these plots is that for H-ATLAS (see Fig. 4.4(a)), the sub-mm detected ETGs have lower surface densities with respect to those of the undetected ETGs - this is the same result shown in Fig. 3.11 in Chapter 3. In Fig. 4.4(b) for the HeViCS sample, the opposite effect is found, with the sub-mm detected ETGs occupying higher density regions within the cluster than the undetected ETGs. This latter result was noticed by S13 (and

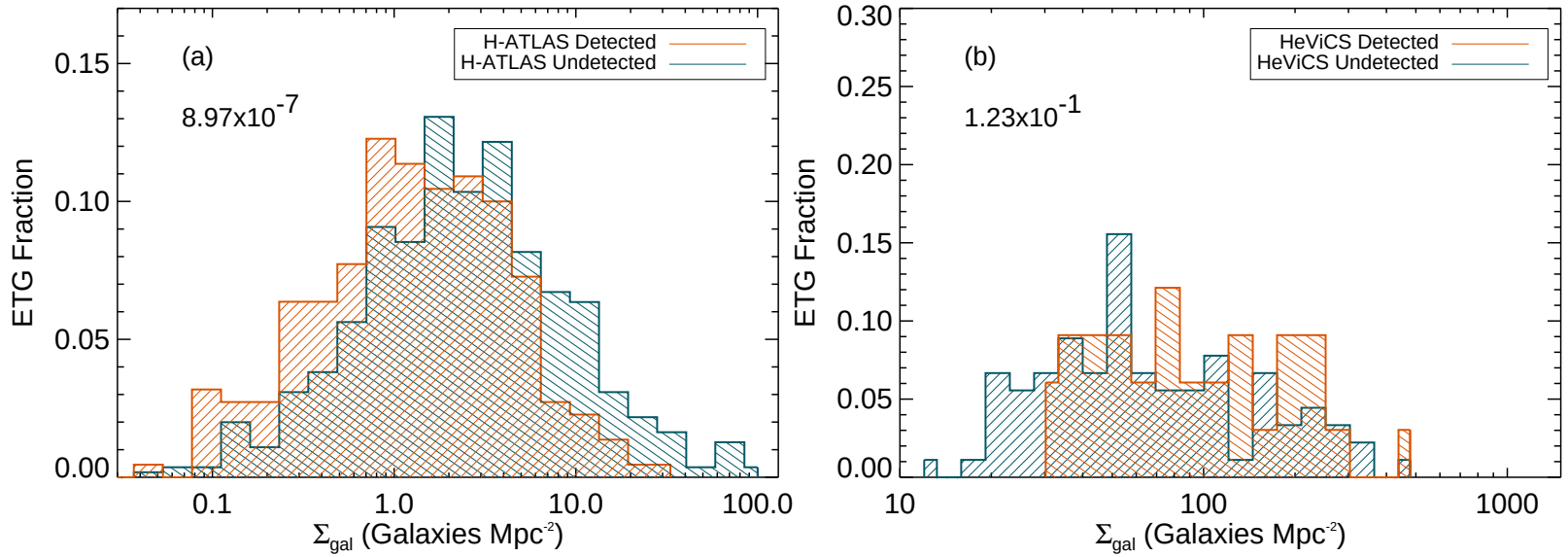

Figure 4.4: Left panel: normalised distributions of sub-mm detected (orange histogram) and sub-mm undetected (blue histogram) ETGs in H-ATLAS. Right panel: distributions of sub-mm detected (orange histogram) and sub-mm undetected (blue histogram) ETGs in HeViCS. KS-probabilities of the presented samples being drawn from the same distribution are shown in the top left of the plots.

contrasted with the result for HI detections and non-detections), but is shown here in a quantitative way.

This particular difference may be attributed to the fact that the two samples are environmentally very different (as explicitly shown in Fig. 4.3), with the H-ATLAS sample occupying sparse environments and the HeViCS sample occupying a high density environment. However, given that both strangulation and ram pressure stripping in dense environments are known to typically remove the ISM from galaxies[4], it is expected that sub-mm detected galaxies would be in lower density regions than undetected galaxies. The fact that the Virgo galaxies are exhibiting the opposite behaviour indicates some other processes governing the presence of dust within these systems. Attention could be drawn to the case of M86, a Virgo elliptical which appears to have acquired its ISM via the stripping of gas and dust from a nearby spiral (Gomez et al. 2010). Smith et al. (2012) also suggested that all their ETGs acquired their dust through mergers. Such a process may be one of the key elements contributing to the result seen here for the Virgo ETGs, although it is unclear how common a case such a process is. In fact, based on the lack of evidence for externally acquired material, Davis et al. (2013a) argue against accretion as a general mechanism for getting gas and dust in Virgo ETGs.

An additional effect which may be contributing to this difference is the ability of HeViCS to detect dust to lower levels than H-ATLAS: S13 amongst others found Virgo ETGs with dust masses as low as $10^5 M_\odot$, and these lower dust masses dominate the average values found for Virgo ETGs. Therefore by definition the Virgo ETGs are different to those being found by H-ATLAS. From the point of view of the H-ATLAS sample, HeViCS does not detect 250 μm luminosities above 2.77×10^{30} ergs s^{-1} Hz^{-1}, which is equivalent to the threshold luminosity of H-ATLAS at the redshift upper limit. This is unexpected given that the samples are

[4]For example, dust stripping has been observed to be ongoing in the Virgo Cluster (Cortese et al. 2010a,b).

matched in optical luminosity ($M_r \leq$-17.4), however it does explain the differences in dust masses currently being observed. Therefore this difference in environments may be a cause of the differences in dust levels in these ETGs (dust is destroyed in denser environments), or it may be an effect of dusty ETGs simply preferring sparser environments for some other, unknown reason.

Another possible cause for this difference is the morphological classification of the ETGs. HeViCS ETGs have high enough optical resolution that they can be definitively categorised into their separate morphologies. Given that H-ATLAS ETGs lie at higher redshifts, their associated classifications cannot be assigned the same level of detail as the HeViCS ETGs. Since specific dust ratio of galaxies systematically increases when moving from early- to late-type galaxies (Cortese et al. 2012b; Smith et al. 2012), it is possible that even a slight change in the threshold between ETG and late-type classification can skew the results. It is also well known that earlier-type galaxies prefer denser environments (e.g. Dressler 1980). Therefore any spurious LTGs which may exist in the H-ATLAS sample are likely to have both high dust-to-stellar mass ratio and sparser environments, thereby skewing the sample in the direction being seen.

This last possibility can be investigated further by estimating possible contamination levels for the H-ATLAS sample. Original classifications for these galaxies revealed 1113 ETGs (see Section 2.2.1), of which 30% were only agreed on by two of the three classifiers (Kelvin et al. 2014). Assuming that the majority of the time ($\geq$80%) the two classifiers in agreement are correct, then there is only a small ($\lesssim$20%) chance of false ETG classification. Considering the extra classification criteria introduced for the H-ATLAS sample removed 30% of the H-ATLAS detected ETGs (see Section 3.2.2 and Table 3.2), this percentage can be reduced to $\lesssim$5% contamination for the H-ATLAS sample.

Next consider the proportion of H-ATLAS ETGs that would need to be late-type contaminants to explain all the claimed ETGs with high dust-to-stellar mass ratios. We estimate $\lesssim$29% contamination to explain such high normalised dust mass levels - this is much higher than our contamination estimates, indicating that this environmental difference cannot simply be explained by a difference in morphologies.

4.4 Multi-Wavelength SED Fits

Similarities in the methods utilised to derive dust temperature and mass parameters for the two samples of galaxies have already been highlighted in Sections 4.2.1 and 4.2.2. However differences also exist in the methods of deriving further properties such as galaxy stellar mass. Therefore to ensure consistency for comparison of galaxy parameters, a single fitting method is now adopted to constrain each galaxy's multi-wavelength spectral properties.

4.4.1 MAGPHYS

The Multi-wavelength Analysis of Galaxy Physical Properties (MAGPHYS; da Cunha et al. 2008) code utilises a Bayesian approach to simultaneously model the UV to sub-mm SED of galaxies. This energy balance code is based on a single underlying assumption: that all attenuated starlight is conserved and re-emitted at longer wavelengths.

The code works by computing huge libraries of stochastic models at each point on a redshift grid. Libraries containing the light produced from stars are generated using the stellar population synthesis (SPS) model of Bruzual & Charlot (2003), using an initial mass function from Chabrier (2003), and the Charlot & Fall (2000) dust extinction model. These libraries enable wide ranges of star formation history,

metallicity and dust content. The predictions for unattenuated stellar light span a range of wavelengths from 91 Å to 160 μm, and a range of stellar ages from 1×10^5 to 2×10^{10} years. During the calculation of these models, the fraction of interstellar light absorbed by dust in the ISM (f_μ) is calculated, as is the specific star formation rate (sSFR; defined as the average star formation rate over the past 10^8 years divided by the current stellar mass).

In addition to the computation of optical libraries, a set of infrared libraries is simultaneously created for the same redshift grid. These are required to represent the MIR-sub-mm emission from the heated dust grains. Diffuse dust emission is here modelled using a series of modBBs and a fixed template for PAH features[5] to build up the IR luminosity. Three of the five modBBs represent hot dust and have fixed peak temperatures of 130 K, 250 K and 850 K and emissivity β =1. Warm dust surrounding stellar birth clouds and cold dust in the ambient medium are represented by modBBs with β =1.5 and 2 respectively. We use an expanded version of MAGPHYS such that warm and cold dust temperatures have extended ranges from the standard version: ranges from 30 to 70 K and 10 to 30 K respectively are used instead (Sebastién Viaene, Elisabete da Cunha, priv. comm.). Although this increases the computation time, these extended ranges allow temperatures consistent with those found in Chapter 3 to be fit to the observed fluxes.

The combination of the stochastic libraries of attenuated stellar spectra and the dust emission spectra allows the construction of theoretical SEDs, whereby the theoretical SED is constructed from models with matched[6] values of f_μ - hence a forced energy balance ensues. There are a number of parameters derived from these combined models - each parameter has an associated marginalised likelihood distribution, allowing a statistical estimate to be given for the properties of each

[5]This is chosen based on the MIR spectrum of the local Galactic star-formation region M17 (Madden et al. 2006).

[6]Matches are within a tolerance of f_μ=0.15.

galaxy based on the reduced χ^2 goodness-of-fit. Certain parameters have been shown to be better constrained than others (da Cunha et al. 2008), based on this we are limited to the following parameter probability distributions:

- The equilibrium cold dust temperature of the ambient ISM (T_C^{ISM}).
- The equivalent temperature of warm dust in birth clouds (T_W^{BC}).
- The total infrared luminosity emitted by the dust grains (L_{dust}), which is dictated by the amount of energy absorbed at UV and optical wavelengths.
- The total dust mass (M_d), which is comprised of multiple components including the warm dust surrounding birth clouds, warm dust in the ambient ISM and cold dust grains in the ISM. These are combined as follows:

$$M_{dust} = 1.1(M_W^{BC} + M_W^{ISM} + M_C^{ISM}), \tag{4.2}$$

  where the multiplicative factor of 1.1 accounts for the excess dust mass contribution from small, stochastically heated grains.
- The total stellar mass (M_*) as derived from the SPS models.
- The star formation rate (SFR), which is an average of the amount of stars formed per year over the last 10^8 years. This is based on an underlying star formation law whereby a continuous exponentially declining SFR starts from the birth of the galaxy. There is a random chance of a starburst (Kauffmann et al. 2003b) lasting between 3×10^7 and 3×10^8 years taking place at any point during the galaxy's lifetime.
- The specific SFR (sSFR; e.g. Brinchmann et al. 2004; Walcher et al. 2008), which is the ratio of SFR to the current stellar mass.
- The formation timescale (T_{form}) - defined as the age of the oldest stars in the galaxy, which is a representation of the galaxy's age.

- The time of the last burst of star formation ($T_{lastburst}$)

4.4.2 Data coverage of the SED

Due to the panchromatic fitting nature of MAGPHYS, it is necessary to input fluxes at as many wavelengths as possible, which must additionally be as accurate as possible. This allows the code to better constrain each component of the SED fit. For example, fluxes at wavelengths greater than 100 μm constrain the modBB assigned to fit the cold dust in the ambient ISM.

The two samples examined in this Chapter are derived from different datasets, and so have different sources of photometry. The GAMA/H-ATLAS dataset is quite straightforward to handle because it comprises self-consistent photometry based on a standard format. Therefore through GAMA, the H-ATLAS ETG sample has the following data coverage of the SED: GALEX FUV and NUV, SDSS *ugriz*, UKIDSS YJHK, WISE W1-W4, PACS 100 and 160 μm and SPIRE 250, 350 and 500 μm. Note that there is missing data for the following numbers of galaxies in the following bands:

GALEX FUV: 38 galaxies (17%)

GALEX NUV: 36 galaxies (16%)

WISE W1-W3: 5 galaxies (3%)

WISE W4: 90 galaxies (41%)

PACS 100 μm:19 galaxies (9%)

PACS 160 μm:26 galaxies (12%)

Missing galaxies in these wavebands are due to an inability to match the optical source to a counterpart in the specific waveband (i.e. no detection). The 22 μm WISE W4 band in particular suffers from a low detection rate due to the wavebands low signal-to-noise ratio.

The H-ATLAS galaxies are all at high enough redshift and small enough that their magnitudes are well estimated by GAMA photometry (see the publications listed in Table 1.1). However this is not the case for the HeViCS ETGs, which are all extended sources. The additional photometry for these galaxies has been handled by Sebastién Viaene and will be fully described in Appendix A of Agius et al. (in prep). In brief, photometry has been derived for similar wavebands as the H-ATLAS sample, but with a slight difference of origin, as follows:

GALEX FUV: 10 (Cortese et al. 2012b) and 23 galaxies (GALEX)[7]

GALEX NUV: 14 (Cortese et al. 2012b) and 19 galaxies (GALEX)

GOLDMine U: 23 galaxies (Gavazzi et al. 2003)

GOLDMine B: 33 galaxies (Gavazzi et al. 2003)

GOLDMine V: 28 galaxies (Gavazzi et al. 2003)

GOLDMine JHK: 33 galaxies (Gavazzi et al. 2003)

WISE W1-W4: 33 galaxies (Agius et al. in prep)

PACS 100-160 μm: 33 galaxies (S13)

SPIRE 250-500 μm: 33 galaxies (S13)

4.4.3 SED Results

MAGPHYS was used to fit energy balance models to each of the HeViCS (Sebastién Viaene) and H-ATLAS (this author) ETGs, as described above. Figs. 4.5 and 4.6 show example MAGPHYS fits to one each of the H-ATLAS and HeViCS ETGs respectively, with the resultant probability distribution functions (PDFs) of a variety of fit parameters shown beneath the SEDs themselves. An additional fit is shown for HeViCS elliptical galaxy VCC763 (Fig. 4.7), which is known to

[7]http://galex.stsci.edu/

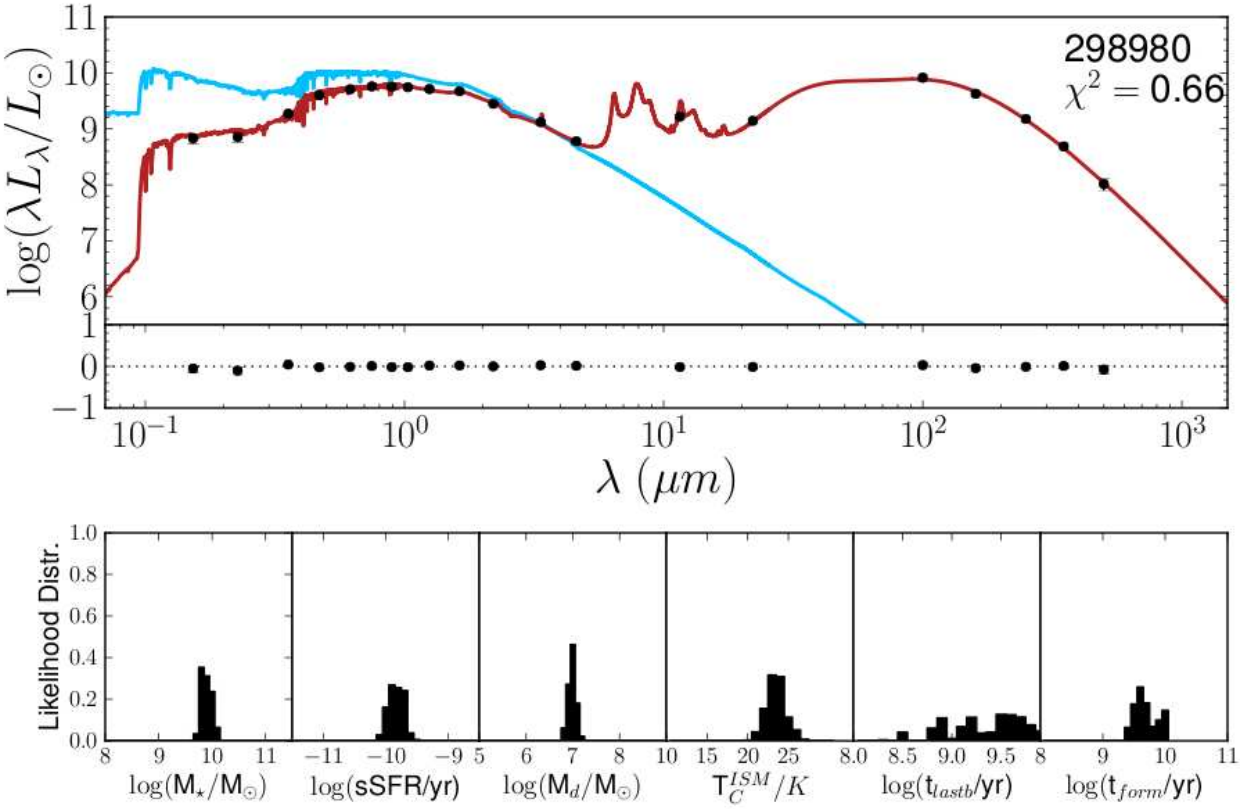

Figure 4.5: MAGPHYS rest-frame SED fit to H-ATLAS elliptical galaxy 298980 (GAMA CATAID). The SED is fit to the observed photometry in the GALEX FUV, NUV, SDSS *ugriz*, UKIDSS YJHK, WISE W1, W2, W3 and W4, PACS 100, 160 μm and SPIRE 250, 350 and 500 μm wavebands (black points). The red line shows the overall attenuated model fit, whilst the blue line shows the unattenuated optical model. Below are the likelihood probability functions for the derived parameters of this elliptical.

emit significant synchrotron radiation. MAGPHYS cannot currently include a synchrotron component, neither does removing the synchrotron component using a power-law (S13) improve the fits. The effect of the synchrotron component is apparent in Fig. 4.7, where the sub-mm points are not well fit by the cold temperature modBB model. To account for this, the four HeViCS radio galaxies are highlighted in all future plots, to ensure that they do not adversely influence any results.

In order to gain some insight on the goodness-of-fit for each galaxy, the 33 HeViCS fits were eyeballed by Sebastién Viaene and assigned a flag for 'good' or 'poor' fit. Four galaxies were assigned 'poor' fit status - each of these fits had an associated reduced χ^2 value[8] greater then four. This was then chosen as the criterion to assess whether the H-ATLAS fits were 'good' or 'poor'. Eleven H-ATLAS systems were found to have 'poor' fits. These fifteen galaxies are also highlighted in future plots as a separation mechanism from the trustworthy results. Additionally, all ETGs with 'poor' fits or a radio component are excluded in any further statistical analysis in this section.

Contrasting Derived Parameters

As described in Section 4.2.1 and Section 4.2.2, A13 and S13 fit modBBs to their FIR/sub-mm data to obtain dust masses for their ETGs. These dust masses are normalised by and plotted against stellar mass in the left panel of Fig. 4.8[9]. This figure shows a key difference in the normalised dust levels of the two ETG samples. It indicates that the HeViCS ETGs have a factor of $\sim$10 less dust than the H-ATLAS ETGs. This is also self-evident from the ranges of dust masses displayed for the two samples in Table 4.1. One of the ultimate aims of this work is to

[8]The MAGPHYS χ^2 is a constraint on the best fitting theoretical template SED and hence the most likely fit.

[9]This figure is equivalent to the H-ATLAS Fig. 3.13.

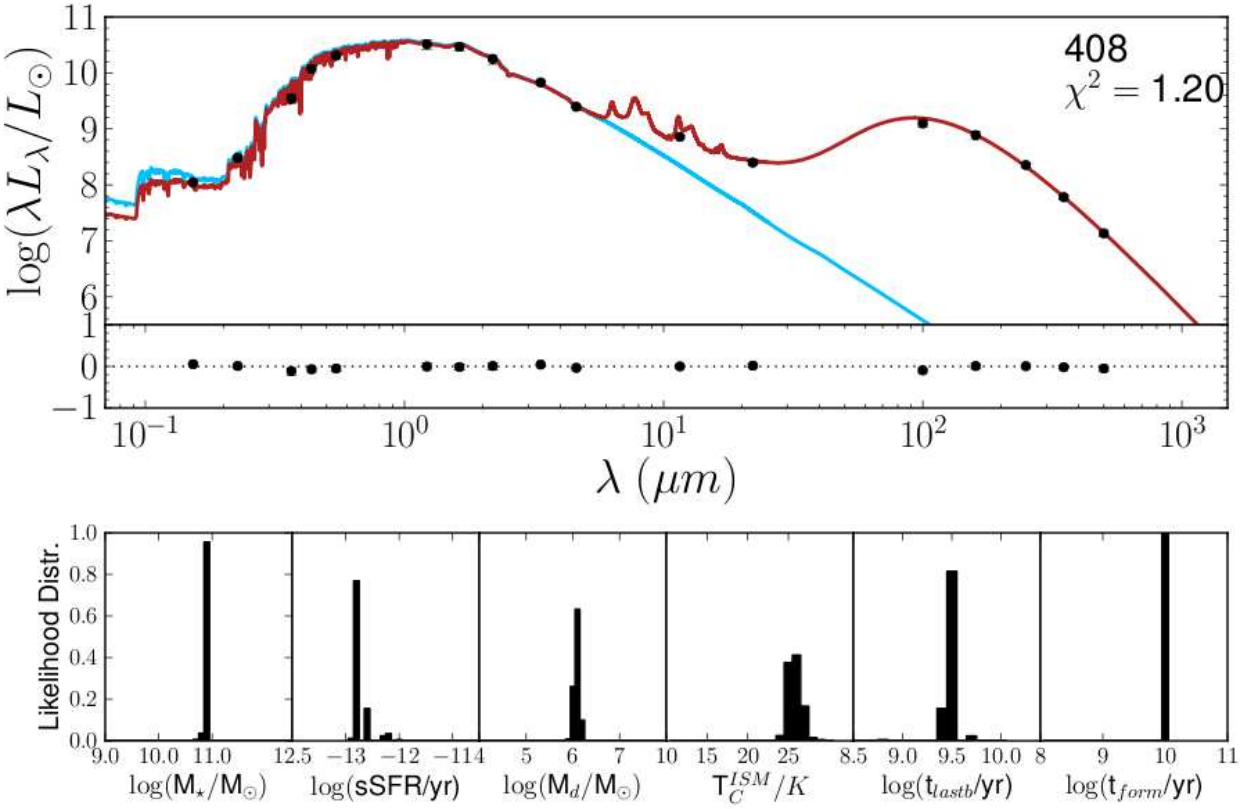

Figure 4.6: MAGPHYS rest-frame SED fit to HeViCS elliptical galaxy VCC 408. The SED is fit to the observed photometry in the GALEX FUV, NUV, GOLDMine UBV, 2MASS YJHK, WISE W1, W2, W3 and W4, PACS 100, 160 μm and SPIRE 250, 350 and 500 μm wavebands (black points). The red line shows the overall attenuated model fit, whilst the blue line shows the unattenuated optical model. Below are the likelihood probability functions for the derived parameters of this elliptical.

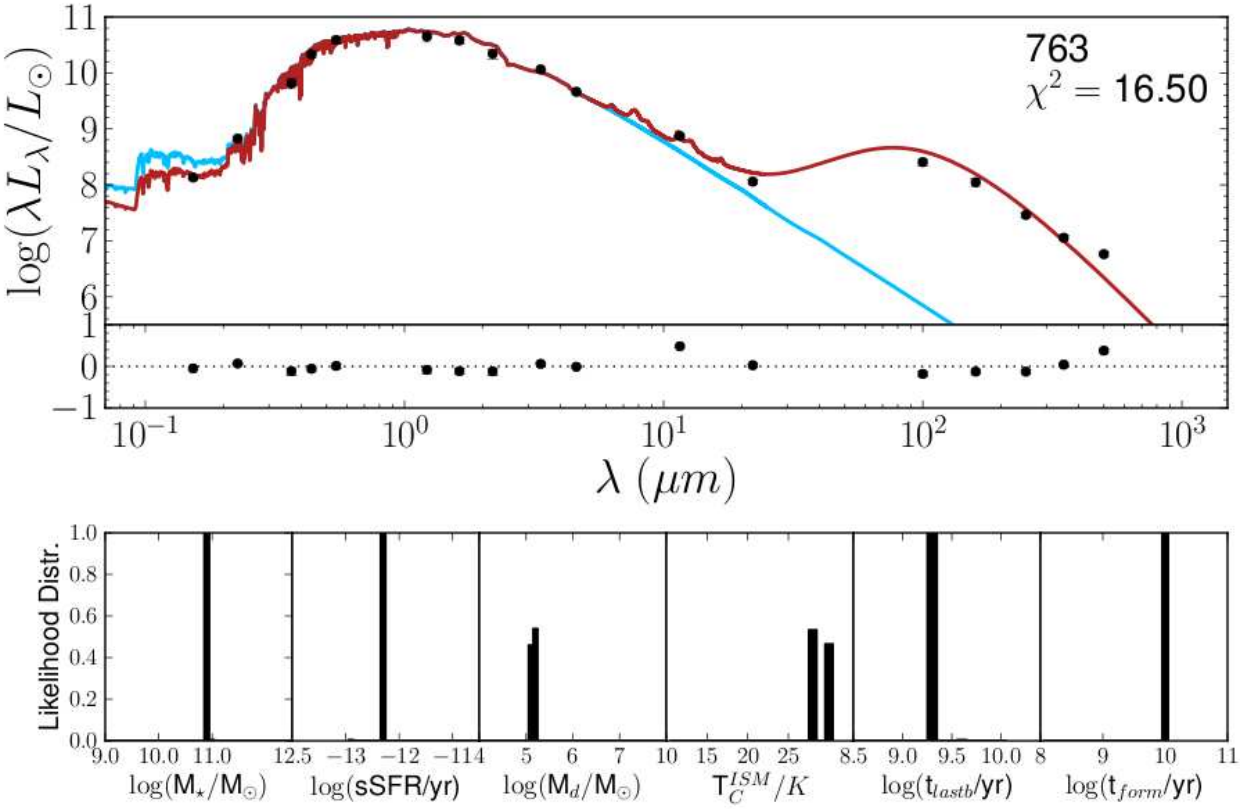

Figure 4.7: MAGPHYS rest-frame SED fit to HeViCS radio elliptical galaxy VCC 763. The SED is fit to the observed photometry in the GALEX FUV, NUV, GOLDMine UBV, 2MASS YJHK, WISE W1, W2, W3 and W4, PACS 100, 160 μm and SPIRE 250, 350 and 500 μm wavebands (black points). The red line shows the overall attenuated model fit, whilst the blue line shows the unattenuated optical model. Below are the likelihood probability functions for the derived parameters of this elliptical.

attempt to understand this particular difference.

Normalised dust masses calculated from MAGPHYS are shown plotted against stellar masses in the right panel of Fig. 4.8. Both ModBB and MAGPHYS plots are shown here side-by-side for ease of comparison. Qualitatively it appears as though there is little change between these plots. In order to get a quantitative measure of the difference between these results, a linear regression is run across each of the two samples in these two dust-to-stellar mass ratio plots. There is a strong negative correlation found for this relationship for each of these samples. In the case of the modBB fitting, a correlation coefficient ($r_{\rm P}$) of -0.553 is found for H-ATLAS ETGs and -0.793 for HeViCS ETGs. This indicates a stronger negative gradient for the Virgo ETGs. Running the regression across the MAGPHYS results leads to a slightly stronger correlation for H-ATLAS ($r_{\rm P} = -0.600$) and a weaker trend for HeViCS ($r_{\rm P} = -0.622$) than those found from the modBB fits. The cause of this difference is further examined by running KS-tests across the three parameters of stellar mass, dust mass and dust-to-stellar mass ratio to determine whether the two samples are drawn from the same parent population.

Dust properties from MAGPHYS fits are examined and contrasted to the modBB solutions in Figs. 4.9 (left) and 4.9 (centre). MAGPHYS' most likely[10] cold dust temperature and overall dust mass is shown on the x-axis, and modBB solutions are shown on the y-axis for both samples of ETGs. As previously stated, radio galaxies and 'poor' fits are shown as different symbols to separate them from the good fits.

Fig. 4.9 (left) shows that dust temperature varies significantly between the fitting methods. The scatter observed here is due to MAGPHYS assigning higher likely cold temperatures to the dust grain distributions. This difference may be

[10]The most likely value of a parameter is chosen as the mode of the probability distribution function output by MAGPHYS.

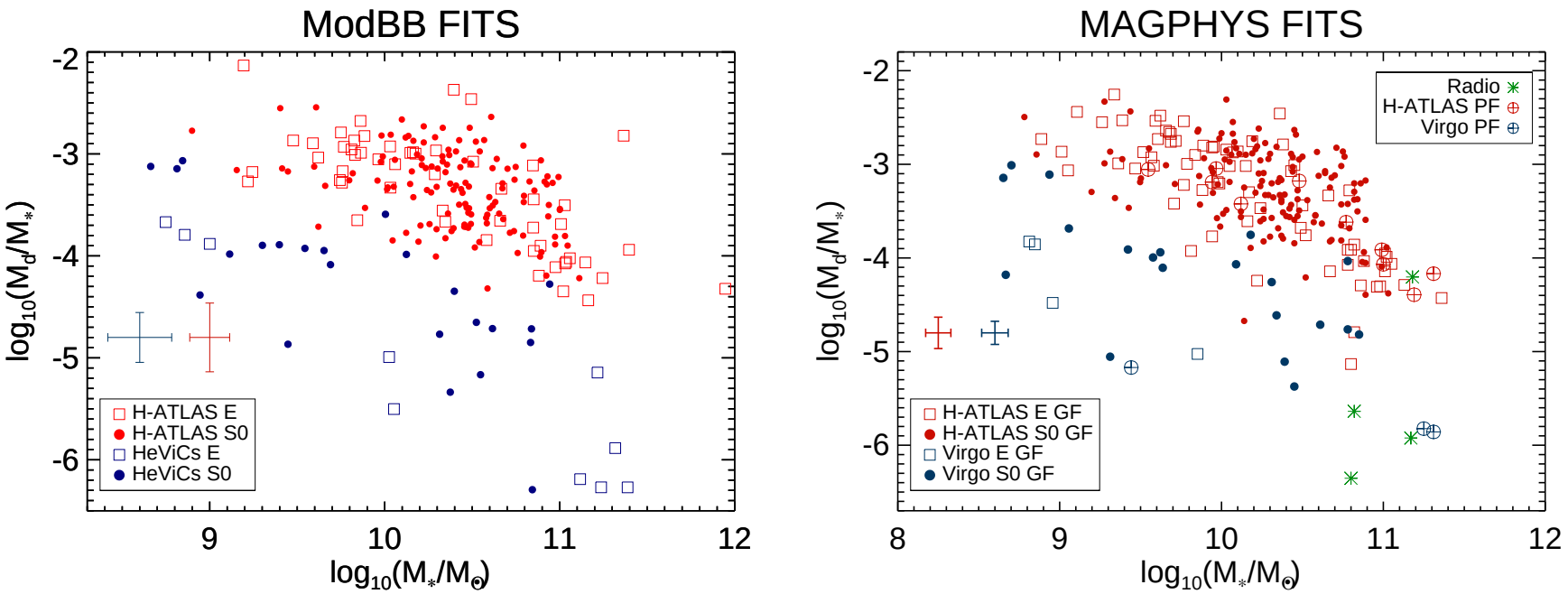

Figure 4.8: Dust-to-stellar mass ratio plotted as a function of stellar mass calculated using ModBB models (left panel) and MAGPHYS (right panel). HeViCS (blue points) and H-ATLAS (red points) samples are shown in both plots, and galaxies are subdivided into E (red open squares for H-ATLAS and blue open squares for HeViCS) and S0 (red dots for H-ATLAS and blue dots for HeViCS) classifications. In the MAGPHYS plot, galaxies with 'poor' fits are shown as encircled crosses in the samples' respective colours, and the four HeViCS radio galaxies are shown as green asterisks. Error bars in the left panel give the mean overall uncertainty on the points from ModBB fits, in the same colours as their respective samples. Error bars in the right panel give the 1σ range to each side of the PDF, in the same colours as their respective samples.

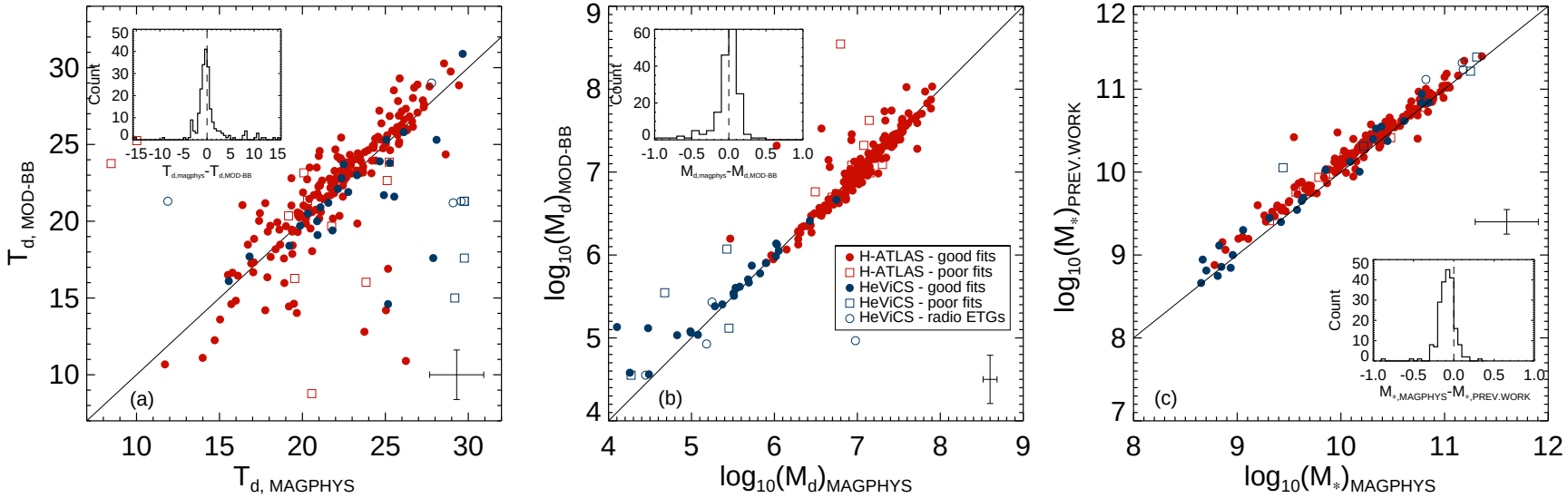

Figure 4.9: A comparison of derived dust temperatures (top), dust masses (center) and stellar masses (bottom), where the y-axis represents values from the modBB fitting and the x-axis represents the MAGPHYS fitting results. For the stellar mass comparison, the y-axis represents stellar mass values from Chapter 3 and S13. The H-ATLAS sample is plotted in red and HeViCS ETGs are plotted in blue. Galaxies with 'poor' fits (reduced χ^2 $\geq$4.0) are shown as open squares in their respective colours, and the four HeViCS radio galaxies are shown as open circles. The solid line is an x=y line for ease of comparison and error bars represent the mean 1σ errors in either direction for both samples. Inset plots show the parameter's difference for the combined samples.

induced by the fact that MAGPHYS fits multiple temperature components, unlike the single component modBB. Therefore the temperature of the warm dust component influences the temperature of the cold dust component as the fitting routine searches for the best fit. Such a degeneracy is aggravated by the poor MIR data coverage. However these differences in temperatures do not necessarily cause similar scatter in other derived parameters.

MAGPHYS dust mass shows a better correspondence with dust masses derived from modBB fitting (see Fig. 4.9(b)). There is a slight offset for some galaxies in both samples from the x=y plane - typically the modBB fitting appears to overestimate the dust mass rather than MAGPHYS. This is likely because modBB fitting assumes a single grain distribution of temperature and thereby also assumes all the grains are of a similar size (on the larger end of the dust grain scale). By accounting for multiple temperature distributions for the grains, as well as the stochastic heating of smaller grains, MAGPHYS is a better representation of the true mass of diffuse dust grains.

This comparison is furthered by testing the relationship between the derived dust and stellar mass (see Fig. 4.10). Correlations are found for both H-ATLAS and HeViCS ETGs, with correlation coefficients of $r_{\rm P}$=0.42 and 0.58 respectively. The difference in dust mass between the samples is highlighted by the ranges exhibited: $4.4 \leq \log(M_d/M_\odot) \leq 6.7$ for HeViCS and $5.5 \leq \log(M_d/M_\odot) \leq 7.9$ for H-ATLAS.

Two clear conclusions about the choice of modelling are revealed from these tests. First of all, the dust mass parameter is well described by both a modBB and MAGPHYS, as the mean results for the two samples do not change substantially, nor do the KS-test probabilities. However, a clear difference is found between the stellar masses derived by the GAMA/HeViCS teams and the stellar masses derived by MAGPHYS. We investigate this further by comparing the stellar masses in Fig.

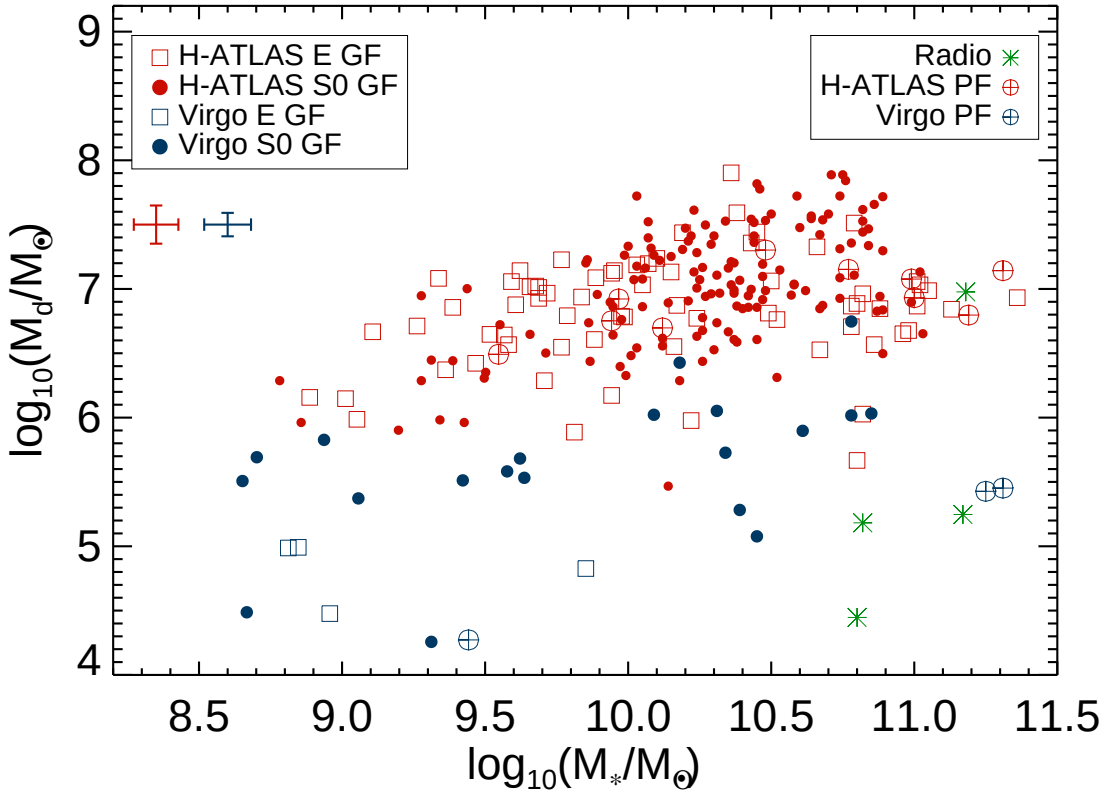

Figure 4.10: MAGHPYS dust masses plotted as a function of stellar masses. HeViCS (blue points) and H-ATLAS (red points) samples are shown, where galaxies are subdivided into E (red open squares for H-ATLAS and blue open squares for HeViCS) and S0 (red dots for H-ATLAS and blue dots for HeViCS) classifications. Galaxies with 'poor' fits are shown as encircled crosses in the samples' respective colours, and the four HeViCS radio galaxies are shown as green asterisks. Error bars in the right panel give the 1σ range to each side of the PDF, in the same colours as their respective samples.

4.9 (right), and find that stellar masses from the previous works are systematically overestimated. Finding the root of this difference is beyond the scope of this thesis, but it is likely that this is due to the previous models using only a subset of the available data to calculate the stellar masses. This stellar mass difference ultimately also leads to different values of the dust-to-stellar mass ratios and hence to different gradients in subsequent correlations.

4.5 An Investigation of ETG Parameter Space

As it has been shown that MAGPHYS successfully reproduces the modBB results for dust mass, further study can be done on this and some other derived parameters with peaked probability distribution functions. We begin by examining the relationship between environment and dust-to-stellar mass ratio in Fig. 4.11. In spite of the large scatter in this plot, there is an overall log-log anti-correlation ($r_{\rm P}$=-0.3) over four orders of magnitude between nearest neighbour density and normalised dust mass.

The substantial range of normalised dust mass displayed by the Virgo ETGs is a feature which needs to be subjugated to more scrutiny. ATLAS^{3D} is an ongoing survey investigating the kinematic properties of a volume-limited sample of ETGs including the Virgo Cluster, finding that elliptical galaxies tend to be either slow rotators or rotate as fast as than lenticulars. They find that non-rotating ETGs tend to be found in highly overdense environments (Krajnović et al. 2011) - their results also indicate that in dense groups and clusters gas accretion is suppressed (Davies et al. 2014). Although twenty of the ETGs in the HeViCS sample overlap with those studied by ATLAS^{3D} (Emsellem et al. 2011), it is inconclusive from such a comparison whether the rotation speed of a galaxy is related to its respective dust-to-stellar mass ratio. However it has been shown that a galaxy's stellar angular momentum and stellar mass are negatively correlated (e.g. Emsellem et al.

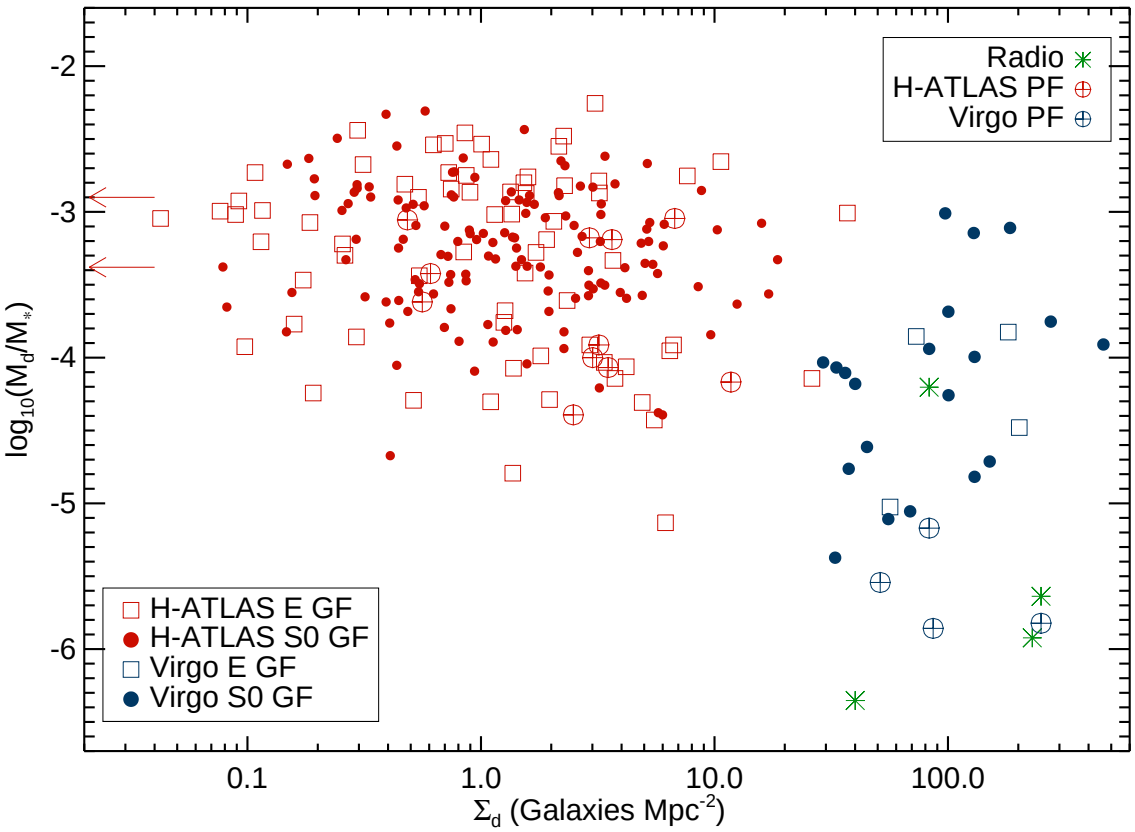

Figure 4.11: Dust-to-stellar mass ratio derived from the MAGPHYS fits plotted against environment surface density for the two ETG samples. H-ATLAS ETGs are plotted in red (Es as open squares and S0s as filled circles) and HeViCS ETGs are plotted in blue (Es as open squares and S0s as filled circles). 'Poor' SED fits are shown as encircled crosses (in red or blue based on the sample) and radio galaxies are highlighted as green asterisks. Arrows indicate the dust-to-stellar mass ratio for two H-ATLAS S0s at $\Sigma_{\rm d}$ =0.001 gals Mpc^{-2}.

2011), and normalised dust mass is negatively correlated with stellar mass (A13; Chapter 3). Therefore it can be postulated that dust-to-stellar mass ratio is positively correlated with a galaxy's rotation speed. This is a suggestion that might be investigated in the future with high-resolution, kinematic observations of the cold dust or gas in GAMA/H-ATLAS ETGs.

4.5.1 Star Formation Properties

In previous chapters UV-optical colour was used as a proxy for the star formation rate (SFR) in a galaxy. However blue colours can also be induced by the presence of a very old stellar population in the galaxy (Greggio & Renzini 1990; Horch et al. 1992; Bressan et al. 1994) and therefore a direct investigation of the SFRs in these galaxies is a necessity to confirm the results found thus far. This must be handled with care, as SFRs derived from MAGPHYS are also related to the UV emission. However, the inclusion of longer wavelength information and energy balance in the SFR calculations gives a better estimation than a simple proxy.

The interpretation of SED fits to ETG data must account for the potential contribution to UV light from old, evolved stars on the horizontal branch (HB). Kaviraj et al. (2007a) (K07a) confirmed that populations of stars older than $\sim$10 Gyrs can cause an upturn of the UV flux, due to UV emission from HB stars. Younger populations do not have this component contributing to the integrated UV light. Populations younger than $\sim$3 Gyrs again have excess UV emission but from the young, massive, main sequence stars. Thus intermediate age populations ($\sim$3 to 10 Gyr) do not have significant UV upturns in their spectra and hence will show no sign of a UV excess that could be erroneously attributed to the presence of young stars. The GALEX NUV flux is less affected by the UV flux from old, evolved stars than the GALEX FUV band (see K07a, Fig. 1).

A concern with using MAGPHYS for the interpretation of parameters such

as SFR, is that they are based on UV and FIR data, and are calibrated only for galaxies where dust heating is primarily contributed to from the young stellar population. However, if the photons heating the dust come primarily from an old stellar population, then the results obtained with MAGPHYS may be meaningless, because they are based on a misguided interpretation of the physics in these galaxies. However, the contribution to dust heating from the old stellar population is a known effect, which is incorporated into the models of Bruzual & Charlot (2003) and therefore into MAGPHYS; additionally, eyeballing the fits done here indicates that the UV upturn of the ETGs is not a strong effect.

We can further strengthen our argument that the old stellar population is not the driving mechanism for the dust heating by examining the NUV-r colour link to the UV upturn. Even with UV contamination from old stars, ETG colours are expected to be redder than NUV-r >5.0 (from the sample of K07a; their Fig. 11). Their ETGs classified as old (ages>1 Gyr from stellar population model fits) all have NUV-r>5.0. For example, NUV-r = 5.4 is the colour of the strong UV-upturn galaxy NGC 4552 (see Yi et al. 2005). In the H-ATLAS/GAMA sample, the majority of ETGs (141 of 184 NUV detections) are bluer than NUV-r=5.0. This majority in the H-ATLAS sample indicates that the blue colours cannot be explained by a UV upturn from old, evolved stars alone. Therefore the blueness and large scatter of their NUV-r colours (ranging from ∼1.5 to 6.5) indicates that these colour and UV fluxes are dominated by different amounts of recent star formation rather than by UV emission from old, evolved stars. The fractional mass involved in the star formation does not need to be very large in order to strongly influence the NUV-r colour of a stellar population (see review by Kaviraj 2008, Fig. 1).

Approximately 23% of H-ATLAS ETGs, and 33 ETGs in the HeViCS sample do not exhibit such blue colours, with an average NUV-r ∼5.3. This should be

kept in mind when considering the parameters extracted based on MAGPHYS fits to these galaxies, and may in fact result in star formation rate overestimates for Virgo Cluster ETGs, and a small proportion of H-ATLAS ETGs.

We examine the specific star formation rate (sSFR; defined in Section 4.4.1) as derived by MAGPHYS below. Fig. 4.12 shows sSFR plotted against stellar mass, where a similar trend to Fig. 4.8 emerges in the form of an anti-correlation between sSFR and stellar mass of the ETG for the two samples. Regression lines are fit to the two samples, revealing correlation coefficients of $r_{\rm P}$ =-0.572 and -0.733 for the H-ATLAS and HeViCS samples respectively. This corresponds to what was observed for dust-to-stellar mass ratios: H-ATLAS ETGs show a weaker correlation for both dust-to-stellar mass ratio and sSFR against stellar mass in comparison to HeViCS.

The side panel of Fig. 4.12 shows the distribution of galaxies in sSFR space for the two samples. This quite clearly identifies the higher on average sSFR for H-ATLAS ETGs compared with HeViCS ETGs, further strengthening the point that H-ATLAS ETGs are not only dusty, but actively star-forming. The most star-forming end of this distribution displays sSFRs on par with that of the Milky Way, which sits at log(sSFR)$\sim$-9 $(\mathrm{yr})^{-1}$.

This anti-correlation between sSFR and stellar mass has previously been observed in both the local and medium-redshift Universe (Salim et al. 2007; Somerville et al. 2008; Firmani et al. 2010). The study by Salim et al. (2007) took observations of 50,000 SDSS galaxies with a range of morphologies and stellar masses and, after measuring their sSFRs using synthetic population models including dust attenuation, constrained this relation for purely star-forming galaxies as

$$\log(\mathrm{sSFR}) = -0.35 \log M_* - 6.33. \tag{4.3}$$

In contrast with this, the HeViCS ETGs display a steeper slope with

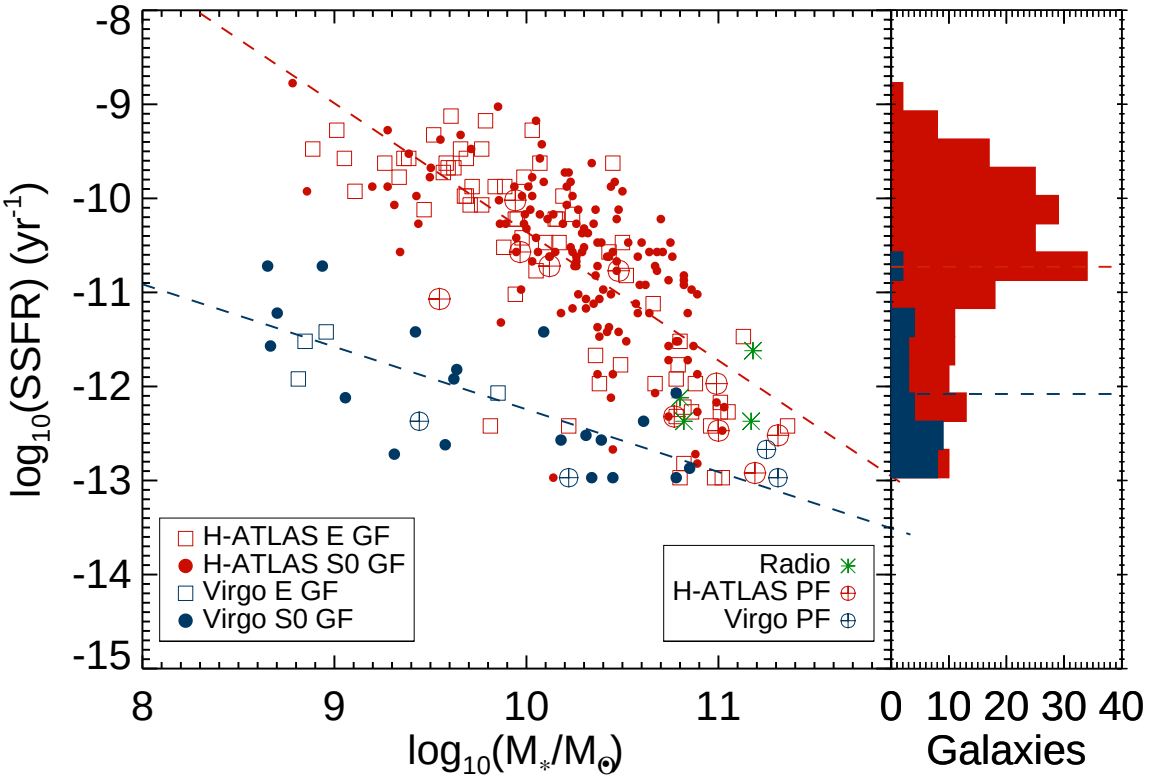

Figure 4.12: MAGPHYS derived specific star formation rate plotted against stellar mass for the two ETG samples. See Fig. 4.11 for symbols and labels. Red and blue dashed lines show best linear fits to H-ATLAS and HeViCS data respectively.

$$\log(\mathrm{sSFR}) = -0.59 \log M_* - 6.39, \tag{4.4}$$

and the H-ATLAS ETGs produce the steepest gradient of all with

$$\log(\mathrm{sSFR}) = -1.37 \log M_* - 3.40. \tag{4.5}$$

These differences may be attributed to both the larger sample size and the different galaxy types (presumably dominated by later-type galaxies) making up the relation in Salim et al. (2007). The ETGs used in our work span a large range of sSFRs and the relation's gradient is likely to be steepened by these extreme sSFR values. Regardless, such a steep relation for the H-ATLAS ETGs, coupled with the extreme levels of dust content for lower stellar mass H-ATLAS ETGs, is consistent with sSFR downsizing where lower mass ETGs harbour star formation in even the local Universe. These low mass ETGs also occupy the sparsest environments ($\leq$1 galaxy Mpc^{-2}), further strengthening this downsizing theory and in accordance with previous results shown for galaxies in the local Universe (Cassata et al. 2007; Cooper et al. 2007).

We next calculate the lookback time for the H-ATLAS ETGs as defined by Eq. 29 of Hogg (1999):

$$t_{\mathrm{L}} = t_H \int_0^z \frac{dz'}{(1+z')E(z')}, \tag{4.6}$$

where t_H is the Hubble time and $E(z)$ is the time derivative of the logarithm of the scale factor $a(t)$, evaluated as

$$E(z) = \sqrt{\Omega_{\mathrm{M}}(1+z)^3 + \Omega_{\mathrm{k}}(1+z)^2 + \Omega_{\Lambda}}, \tag{4.7}$$

where Ω_{k} represents the curvature of the Universe and equals zero for ΛCDM. See Hogg (1999) for a full description of these parameters. Lookback time is defined as the time between the age of the Universe now and the age of the Universe when

the photons being observed were emitted - therefore it is directly related to the redshift of the galaxy.

Models for downsizing predict that lower mass galaxies have more extended star formation histories (e.g. De Lucia et al. 2006a). To test whether H-ATLAS ETGs fit into this model, mean sSFR is plotted against lookback time and redshift in Fig. 4.13, where the H-ATLAS sample is divided into low mass ($\log(M_*/M_\odot)<10.5$) and high mass systems ($\log(M_*/M_\odot)\geq 10.5$). These two subsamples are binned to find mean (and respective quartile) values, and the average over time and redshift is also indicated. Additionally, a mean sSFR value is shown for the HeViCS ETGs for comparison.

Although it is unlikely that galactic evolution can be observed over such a small redshift range, it is interesting to see that the lower mass systems exhibit higher average sSFRs over the full redshift range (consistent with recent results by Firmani et al. 2010), whereas the higher mass systems show a factor of $\sim$1.5 dex lower sSFR overall. Additionally, the higher mass systems show the most similar sSFR to the average sSFR displayed by the HeViCS ETGs, indicating greater similarity between these systems than the lower mass ETGs have with either of these groupings.

4.5.2 Age Properties

Ideally, an exploration of the ages of these ETGs would begin by using spatially resolved, population synthesis modelling for these systems as a whole. In the case of the H-ATLAS ETGs, this has not been done yet because current imaging does not have good enough resolution. Therefore we chose to run a pilot study on the ages of these galaxies using the MAGPHYS results. Caution must be applied to the use of these results, as they are fully dependent on the stellar population synthesis (SPS) code used to compute the short-wavelength light produced by stars, which

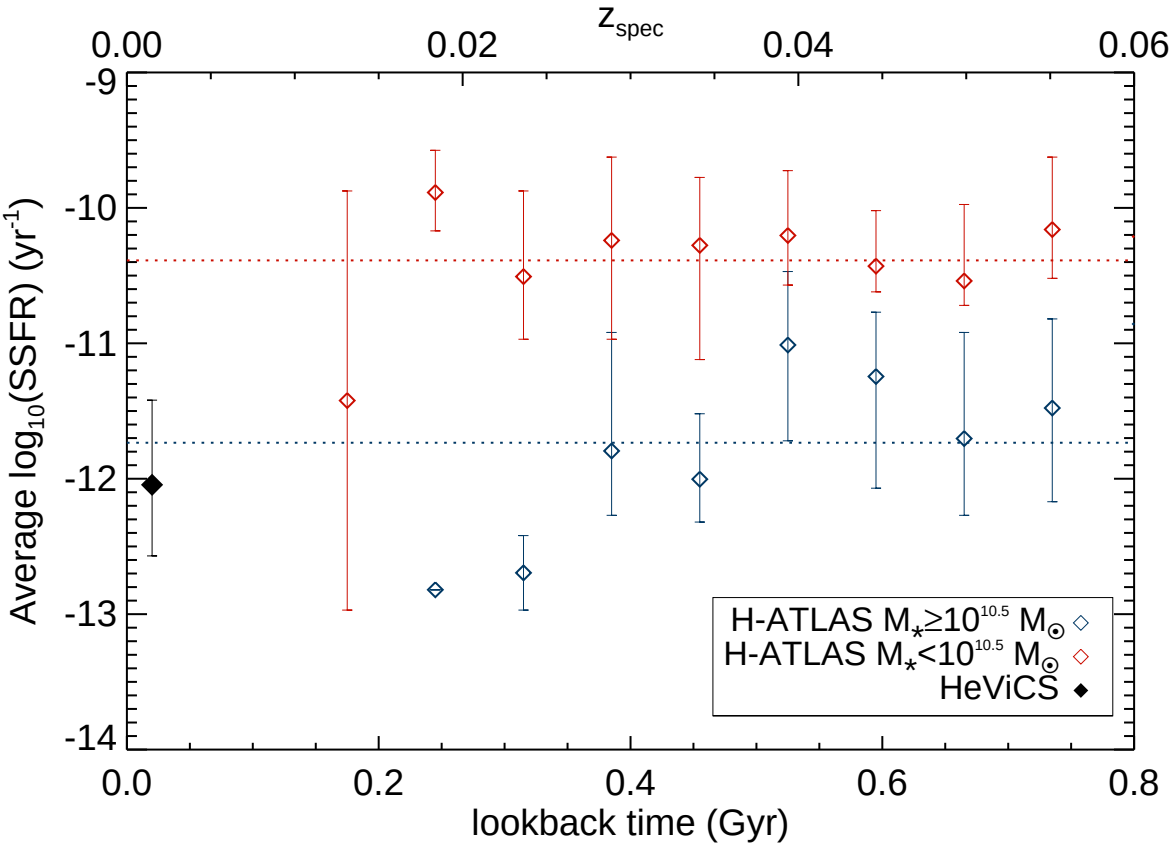

Figure 4.13: Mean sSFR value for the H-ATLAS galaxies as a function of binned lookback time and redshift, divided into low (red diamonds) and high (blue diamonds) mass samples. Upper and lower quartiles are shown as error bars on the points. The mean value for the binned averages are shown as dotted lines in the respective colours. A mean value with upper and lower quartiles (black diamond) has been plotted for the HeViCS ETGs at a lookback time of virtually zero.

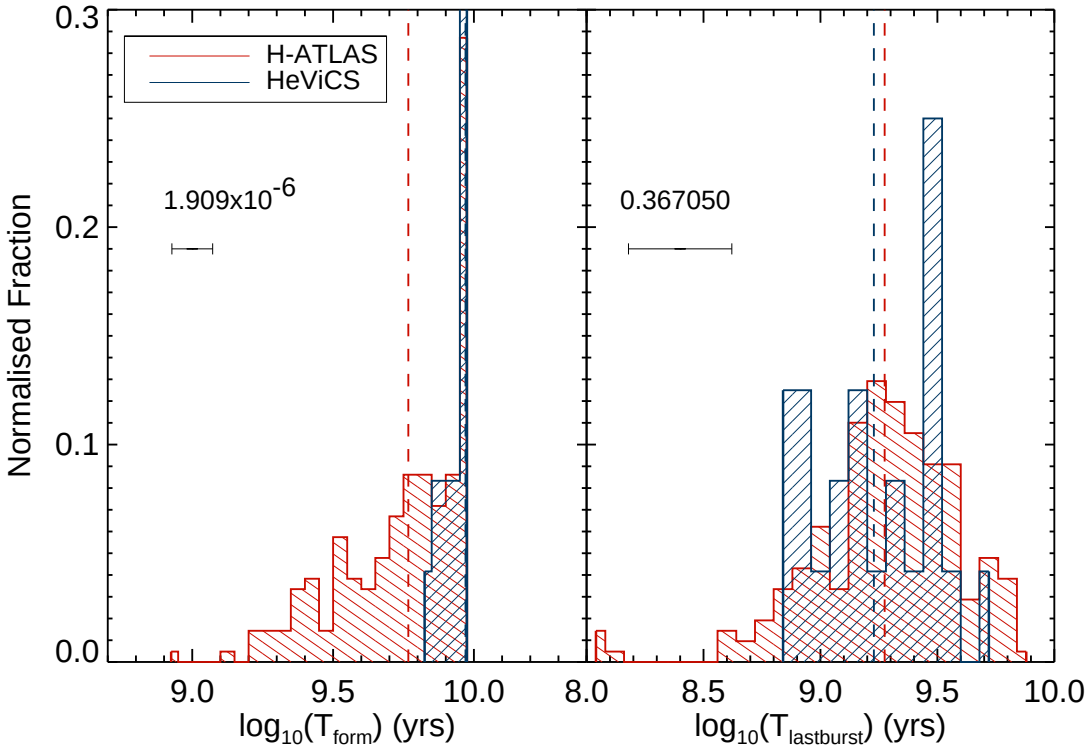

Figure 4.14: Distributions of T_{form} (left) and $T_{lastburst}$ (right) for H-ATLAS (red) and HeViCS (blue) populations. Numbers in the plots represent the KS-probabilities that the two parameter distributions come from the same parent sample. Dashed lines represent mean values in the samples' respective colours.

is likewise dependent on the model's choice of metallicity, initial mass function (IMF) and star formation history. In this case, the SPS code is that of Bruzual & Charlot (2003), and they adopt a range of exponentially declining SFHs and a Chabrier IMF (Chabrier 2003). Here we will only consider relative numbers, and not absolute ages.

We choose to examine both T_{form} and $T_{lastburst}$ here (defined in Section 4.4.1). The distributions of both these parameters and the means thereof are shown in Fig. 4.14. Probability results from KS-testing the distributions are also included in these figures. The left panel indicates that the two samples have significantly different formation timescales. However, the results for $T_{lastburst}$ indicate that there is no difference at the 1% level for the two sets of galaxies. This is an interesting result as it is the first point at which any similarity between the parameters of the two sets of ETGs has been found. Further detailed study on the galactic stellar populations is required to determine whether these results are real or simply a result of the assumptions made in the SPS fitting.

4.6 Discussion

Based on the results discussed in Section 4.5, a clear conclusion about the two samples is reaffirmed: that the ETGs in each of the samples have differing dust properties, with HeViCS ETGs demonstrating consistently low dust levels, whilst the H-ATLAS ETGs have significantly higher dust levels which bridge the gap between HeViCS ETGs and late-type spirals. The dust-to-stellar mass ratio is shown to be strongly driven by the stellar mass of the galaxy, particularly for the HeViCS systems. This work has synchronised the calculations of stellar and dust mass for two samples; this has served to strengthen the result that there is no overlap between dust-to-stellar mass ratio for fixed stellar mass for ETGs from different samples and in separate environments.

This lack of overlap should be considered from two points of view: why do the H-ATLAS ETGs not have low normalised dust masses, and why does no HeViCS ETG occupy the same regions as the H-ATLAS sub-mm detections? The first point is easily addressed: the different dust detection limit between both samples, caused by the shorter distance to HeViCS ETGs and the deeper observations, results in much smaller levels of dust being detected at fixed stellar mass in the HeViCS sample.

It is more difficult to understand the cause of the second point, i.e. why there is no HeViCS ETG with high dust-to-stellar mass ratio at fixed stellar mass, such that it overlaps with H-ATLAS ETGs. This cannot be explained by a detection limit, but may be due to the larger area surveyed by H-ATLAS. Some of the more extreme cases in H-ATLAS could be explained as unusual ETGs, but given that all H-ATLAS ETGs occupy the top region of Fig. 3.13, this effect is most likely explained by the difference in environment.

There are only three HeViCS ETGs which demonstrate normalised dust mass levels on par with the H-ATLAS ETGs - these all have GOLDMine classifications of S0 and are found in high density regions of Virgo ($\Sigma_{\rm d}$ $\sim$100-200 gals Mpc^{-2}). It may be possible that these galaxies have been recently accreted into the Virgo Cluster (e.g. Kraft et al. 2011), and have not yet been subjected to the effects of dust stripping and destruction in the intra-cluster medium.

We run a simple test to check whether this may be a possibility. Based on Virgo infall velocities provided by Mould et al. (2000) and assuming a Virgo Cluster radius of 2.2 Mpc (Mei et al. 2007), we calculate typical crossing times for these three Virgo ETGs of $\sim$0.7, 0.8 and 2.2 Gyr. If we assume ram-pressure stripping is responsible for the majority of dust loss in Virgo ETGs, with typical removal timescales of a few $\times10^8$ yr (Takeda et al. 1984; Murakami & Babul 1999), then it may be possible to relate these high relative dust levels with recent galactic infall

into the Virgo Cluster.

The dust masses detected in these galaxies can be used to estimate total (both atomic and molecular) gas masses: a typical gas-to-dust ratio of 100 (e.g. Parkin et al. 2012)[11] gives a range of $\sim 1\times10^{7}$-$8\times10^{9}\,M_{\odot}$ for the H-ATLAS sample and $\sim 10^{6}$-$5\times10^{8}\,M_{\odot}$ for HeViCS. ATLAS^{3D} estimated molecular gas masses for some of the Virgo galaxies in this sample, finding an upper limit of $10^{8.59}M_{\odot}$ for these particular galaxies (Young et al. 2011), which is consistent with our estimations of the total gas masses. Additional results from ATLAS^{3D} indicate a strong HI detection rate dependence on surface density, whereby HI in ETGs is preferentially detected outside the Virgo Cluster (Serra et al. 2012). Again these results are quantitatively consistent with our findings for the two samples, whereby H-ATLAS ETGs demonstrate a factor of ten dust and hence gas mass increase over HeViCS ETGs in the dense regions of Virgo.

Similar studies run on samples of LTGs in the Virgo cluster have demonstrated appreciably low levels of HI gas compared to LTGs in sparser environments. Additionally, lower star formation activity has been identified in these spiral galaxies, and possibly lower dust levels (Boselli & Gavazzi 2006 and references therein). Models indicate that ram pressure stripping, gas compression (Byrd & Valtonen 1990; Tonnesen & Bryan 2009) and starvation due to the cluster potential (Balogh et al. 2000) are possible causes of these decreased levels of gas and dust in LTGs. Theoretically, ETGs in the same environment would also be subjected to these same physical mechanisms, resulting in the lower levels of gas and dust currently being observed.

The *Herschel* Reference Survey (HRS, Boselli et al. 2010b) sampled a wider range of galaxy environments than just the Virgo Cluster. Although it includes very few luminous ETGs other than those in the Virgo Cluster, it is still useful

[11] Although it should be noted that S13 find very little overlap between dust detections and atomic gas detections for HeViCS ETGs.

to consider where their ETGs reside in terms of parameter space, and how this compares to the two samples investigated here. Smith et al. (2012) find 31 ETGs in the HRS parent sample with 250 μm detections: these all have stellar masses $\gtrsim 10^{10}\,M_{\odot}$ and modBB fits to the sample reveal a dust mass range of $10^{5.0-7.1}\,M_{\odot}$ and dust temperatures of 16-32 K. Most notably, however, while they find a similar trend for the dust-to-stellar mass ratio with stellar mass, their elliptical galaxies are found to present the lowest normalised dust masses. This is not what is seen here, particularly for the H-ATLAS/GAMA sample. It should be noted that the HRS sample only contains seven sub-mm detected elliptical galaxies, and therefore this result may be due to poor statistics. The majority ($\sim$68%) of the HRS ETGs reside within the Virgo Cluster, which explains the similar dust mass range to that of the HeViCS survey; in fact Smith et al. (2012) explicitly state that there is overlap between their ETGs and those of S13. Therefore we choose not to perform a further study with HRS ETGs for these reasons.

4.7 Conclusions

This Chapter has compared H-ATLAS sub-mm detected ETGs to HeViCS (Virgo Cluster) sub-mm detected ETGs. This was a strongly motivated study, as multiple *Herschel* works have revealed different levels of dust in different samples of ETGs (Skibba et al. 2011; Smith et al. 2011; Rowlands et al. 2012; di Serego Alighieri et al. 2013; Chapter 3. It has been unclear thus far whether these differences are simply due to different sample statistics and/or selection effects, or whether they are real differences which are a result of the different samples observing different types of ETGs.

Two samples were selected for this study: the A13 H-ATLAS sample of 220 ETGs described in Chapter 3, and 33 ETGs from the HeViCS S13 sample. With the aid of consistent calculations for nearest neighbour density, and MAGPHYS

panchromatic SED fitting to multi-wavelength data, we were able to objectively quantify the true differences in the properties of these ETGs. These are summarised here below.

(i) Nearest neighbour environment densities revealed true differences in the type of environment in which these ETGs reside. H-ATLAS ETGs are in isolated environments, spanning $\lesssim$0.1-10 galaxies Mpc^{-2}, whereas HeViCS ETGs are dominated by the cluster environment ($\sim$25-500 galaxies Mpc^{-2}). These results are also true for undetected ETGs in each sample, with only a trace overlap in density between samples observed at $\sim$20-100 galaxies Mpc^{-2}. An interesting feature of these results is that sub-mm detected ETGs in H-ATLAS reside in sparser environments than undetected ETGs, whereas the opposite effect is observed in HeViCS: the sub-mm detected ETGs are found in the densest regions; note that this is only a marginal effect.

(ii) ModBB fits from A13 and S13 reveal different ranges of dust-to-stellar mass ratio, with H-ATLAS ETGs demonstrating higher M_d/M_* at fixed stellar mass. In order to make the fits completely consistent between the samples, we refit the panchromatic SED using MAGPHYS. This provides access to a host of properties calculated as probability distribution functions, including stellar mass, dust mass, cold dust temperature, specific star formation rate and galaxy age.

(iii) MAGPHYS results indicate that it is difficult to accurately constrain the cold dust temperature but similar results for dust mass can still be derived even based on this inconsistency.

(iv) MAGPHYS stellar masses are lower than those produced by Zibetti et al. (2009) (HeViCS) and the GAMA team (H-ATLAS). Although it is unclear why this is, both sets of stellar masses indicate that H-ATLAS ETGs are

more massive on average than HeViCS ETGs.

(v) Correlations are found between dust mass and stellar mass for both H-ATLAS ($r_{\rm p}$=0.42) and HeViCS ($r_{\rm p}$=0.58) ETGs. Additionally strong anti-correlations are found between dust-to-stellar mass ratio and stellar mass, although the trend is shifted upwards (to higher normalised dust mass) for H-ATLAS. Investigating dust-to-stellar mass ratio as a function of nearest neighbour density reveals another anti-correlation between the two properties, where both H-ATLAS and HeViCS ETGs sit on the same trendline. This is an indicator that levels of dust mass are strongly affected by their environments.

(vi) Examinations of the sSFR reveal that dust mass is indicative of ongoing star formation in these galaxies, but is not directly related, as evidenced by different trends in specific dust mass and sSFR with stellar mass. It appears that there is very little (if any) ongoing star formation in the HeViCS ETGs, but quite the opposite is true for a large proportion of the H-ATLAS sample, with the highest sSFRs on par with that of our Milky Way galaxy.

(vii) sSFRs are plotted for H-ATLAS ETGs as a function of lookback time (and redshift). By splitting the sample into massive ($\geq 10^{10.5}\,{\rm M}_{\odot}$) and non-massive ETGs, we reveal differences of $\sim$1.5 dex on average in sSFR between the two subsets. The massive ETGs have similar sSFRs to the HeViCS ETGs.

(viii) No difference is found in the time of last starburst between the samples.

These overall results can now be used to answer the question posed at the beginning of this Chapter: are H-ATLAS ETGs random examples of strange ETGs, or are they rather younger versions of what can be thought of as 'normal' ETGs? The parametric evidence presented here certainly indicates the latter, where H-ATLAS ETGs are the younger, star-forming, dusty versions of HeViCS ETGs,

which have evolved at a faster rate influenced by the dense environment which they occupy. It is possible that environment has a strong effect on the speed at which ETGs evolve - otherwise these two extremely different ETG samples would not be found in such different environments. The additional effect of both samples of ETGs displaying the same trend of dust-to-stellar mass ratio as a function of environment further strengthens this argument.

There is currently ongoing work with ATLAS^{3D}, where they are observing resolved CO distributions of Virgo ETGs (Davis et al. 2013a; Alatalo et al. 2013), revealing mostly disk-like structures for the gas. Currently the dust distributions of H-ATLAS ETGs are unknown, which makes it difficult to compare with the Virgo ETGs on similar spatial scales. However, it may be possible in the future to observe dust with high spatial resolution in emission using ALMA, and to observe dust in absorption using HST (by unsharp-masking optical images). In Chapter 5 below, we will describe our method of estimating the dust distributions within a pilot sample of H-ATLAS ETGs, and will compare them to a small sample of Virgo ETGs with resolved CO distributions.

Chapter 5

Dust Distributions and Extents in Early-Type Galaxies

From the ashes a fire shall be woken,
a light from the shadows shall spring.

J.R.R. Tolkien, The Fellowship of the Ring

5.1 Introduction

It has been shown throughout this thesis that sub-mm detected GAMA/H-ATLAS ETGs are not the passive, 'red and dead' objects that ETGs are usually thought to be. It has been well established that these ETGs in fact have high dust levels, as well as some significant ongoing star formation (see Chapters 3 and 4). However, it is still currently unclear where these large quantities of dust are originating from, what mechanisms are heating the dust to emission and whether the dust is situated in disky structures as seen in spirals, or within the same spheroidal component as

the stellar distribution.

Dust in ETGs is thought to reside in a mainly cold, diffuse component (e.g. Goudfrooij & de Jong 1995); additionally cool dust has also been detected in some ETGs which may be associated with photo-dissociation regions (PDRs; Knapp et al. 1989). Some ETGs are known to host massive AGN (see review by Ferrarese & Ford 2005); however, as discussed in Chapter 3, ETGs with AGN and LINER signatures are excluded, and the diffuse and PDR (or clumpy) components alone are considered. Due to the lack of resolved dust lanes and structure in optical and NIR imaging, ETGs are thought to be optically thin in a global sense (e.g. Takagi et al. 2000), although some evidence of small, optically thick clouds has been found in ∼50% of a nearby, small sample of ETGs (van Dokkum & Franx 1995). Such studies have suggested that ETGs could contain a structured and fairly well-mixed interstellar medium (ISM). However, in order to understand the processes governing the distribution and heating of the dust, it is important to identify which component of the ISM the dust is interacting with.

There is strong evidence for the bulk of cold gas and dust in ETGs being settled in a cold, rotationally supported disk within the galactic plane (Buson et al. 1993; Henkel & Wiklind 1997; Young 2002; Young et al. 2011; Davis et al. 2013a) and hence decoupled from the overall structure of the stellar population; in fact Del Burgo et al. (2008) were able to ascertain that a dust disk of 7-8 kpc radius is present from 160 μm emission in the shell elliptical NGC 5982. However, such studies tend to focus on nearby ellipticals in dense environments such as the Virgo Cluster - it is currently difficult to resolve the structure of dust and gas in ellipticals that are farther away. It is possible that such disk-like structures are atypical for elliptical galaxies; alternative scenarios may include the diffuse dust being distributed throughout the spheroidal 'bulge' component and therefore more closely associated with the stellar population itself.

A fuller understanding of ETG dust geometry needs to be developed as there is a link between the distribution itself and the manner in which the dust grains are heated to emission. In spiral galaxies the stellar radiation field is responsible for the heating of the dust. However hot (10^{6-7} K) X-ray emitting halos have been linked to a large number of elliptical galaxies (e.g. Forman et al. 1979; O'Sullivan et al. 2001; Young 2002), particularly in older, more relaxed ellipticals (Sansom et al. 2006); collisions with the free ions and electrons in this component can result in the dust grains being heated to emission (Dwek & Scalo 1980; Sparks et al. 1989; Popescu et al. 2000b). These interactions between the plasma and diffuse dust can also lead to the dust grains being destroyed via sputtering over a timescale of $\sim 10^7$ years (Barlow 1978a; Draine & Salpeter 1979b; Popescu et al. 2000b). It is therefore of interest to determine whether this collisional heating or standard radiation field heating is the dominant mechanism in our ETGs.

We also consider the strong links between the dust distribution and the source of the dust itself. To this end, we postulate three scenarios that will be considered within this Chapter, connecting the origin, distribution and heating mechanism for diffuse dust in ETGs. The first of these is the concept that the dust grain population has an external origin: this may be from re-accretion of dust expelled during a major merger phase, or through gas and dust accretion from the intergalactic medium (Naab et al. 2009), or from galaxy interactions (see review by Goudfrooij 1999). Once the dust has been accreted, it settles into a rotationally-supported disk over $\sim 10^7$ years (Tohline et al. 1982; Steiman-Cameron & Durisen 1987), where it is heated by the young and/or old stellar population.

The second scenario also results in this disk-like distribution of the dust, but the grains originate within the galaxy itself via mass loss from old stars (Goudfrooij & de Jong 1995) and then settles into a disk over a certain timescale. Such a model requires the dust to not be completely destroyed via supernova shocks, astration,

or any interaction with a hot ISM (Shull 1977; Barlow 1978a,b,c).

The final scenario has the dust originating in the same way as the second, but in this case the ETG contains a massive X-ray corona which coincides with the dust distribution. In this case, the dust distribution will not settle into a disk, but will retain the overall structure of the stellar population throughout the spheroid. For this to be true, collisional heating between electrons and the dust grains must dominate to result in the FIR emission being seen. It is necessary to assume here that sputtering has not destroyed all the dust grains, or that dust is being regenerated at a rate faster than the sputtering timescale (50 Myr to 1 Gyr; Jones & Nuth 2011).

In order to explore each of these scenarios for ETGs which are not resolvable at FIR/sub-mm wavelengths (outside of the very nearby Universe), we have created a method that combines radiative transfer (RT) models and *Herschel* data to constrain both their dust distributions and heating mechanisms, as well as possibly whether the dust has an external or internal origin. This Chapter introduces this method and shows results for dust in assumed disk-like distributions. The data utilised in this Chapter are described in Section 5.2, and the two samples of ETGs created for testing are described in Section 5.3. A prescription for RT models and SED fitting is detailed in Section 5.4. The methodology we have formulated to compare optically thin simulations with the sample ETGs is provided in Section 5.5, with the results for an optically thin solution with purely optical heating described in Section 5.5.3 and with both UV+optical heating described in Section 5.6. Finally, conclusions are given in Section 5.7.

5.2 Data

This work aims to compare the radiation field energy density of a theoretical model with that of a real galaxy. In order to do this, infrared and sub-mm data

are required to calculate the dust emission and thereby the energy density of the radiation field heating this dust within the galaxy. Additionally, optical/NIR data are required to constrain the modelled energies to those of the galaxy itself. This section describes the sources of these data.

5.2.1 Data Sources

This project utilises a small portion of the GAMA I data, with our samples extracted from the sub-mm detected ETG sample in Chapter 3. The required data for this project include the GAMA photometry in optical/NIR/MIR wavebands (Hill et al. 2011 and Cluver et al. 2014[1]), as well as full Sérsic profile fitting to extract Sérsic indices and effective radii for the galaxies (see Section 2.3.3). Ancillary optical/NIR/MIR data are also required for close-by ETGs - these data are not available within the GAMA database, which focusses on galaxies at redshifts greater than 0.01. Therefore for the control ETGs (described in detail in Section 5.3.1), photometry is from the SDSS and 2MASS surveys, all of which is available from the NASA/IPAC Extragalactic Database (NED, and references therein).

Where available the long-waveband data are taken from the *Herschel*-ATLAS collaboration. This is only available for the GAMA galaxies, and therefore additional *Herschel* photometry for the control sample of nearby galaxies is taken from the literature, and the sources are fully described in Section 5.3.1.

5.3 Samples of Early-Type Galaxies

The objective of these tests is to improve our understanding of the spatial distribution of dust grains in ETGs. To achieve this we need a series of test samples,

[1]Note that the WISE MIR fluxes have been corrected for stellar emission using a blackbody extrapolation approach.

both in the very nearby Universe with spatially resolved ETGs (described below for a selection of Virgo Cluster ETGs) and in the local Universe with a selection of H-ATLAS/GAMA ETGs.

5.3.1 Virgo Control ETG Sample

The method utilised in this work aims to constrain dust extents in ETGs that are unresolved at sub-mm wavelengths, and requires multiple assumptions to work. Based on this knowledge, we chose to create a control sample of nearby ETGs with resolved dust distributions and CO maps. We selected these ETGs from within the *Herschel* Reference Survey (HRS; Davies et al. 2010; D10 from here), and ensured that these ETGs were also included in the ATLAS^{3D} catalogue (Cappellari et al. 2011a). This gives access to *Herschel* data from the former and CO gas mapping from the latter survey (Davis et al. 2013a; Alatalo et al. 2013).

The three galaxies selected for this control sample are massive lenticulars with resolved CO maps showing a disk-like distribution. Under the assumption that the dust maps the cold gas, these three galaxies are demonstrating the dust structures being assumed for the unresolved cases. Davis et al. (2013a) have published resolved CO extents for these three galaxies: in an ideal world the results from this testing will match these extents.

In addition to the requirement for *Herschel* and CO data, a full suite of optical and NIR imaging and light decompositions are needed to perform this study. These three galaxies also have these data available, which are summarised in Table 5.1. Note that the morphological classifications shown in this table were taken from the Third Reference Catalogue of Bright Galaxies (de Vaucouleurs et al. 1991).

Property	**NGC 4526**	**NGC 4459**	**NGC 4435**	**Reference**
Classification	S0	S0	S0	C11
Distance (Mpc)	17.0	17.0	17.0	D10
Sérsic index (n_r)	2.6	1.3	1.8	MD11
g (mag)	11.12	11.56	11.921	NED
r (mag)	10.67	11.10	11.13	NED
i (mag)	10.45	10.40	10.70	NED
J (mag)	7.45	8.10	8.42	NED
K (mag)	6.47	7.15	7.23	NED
$r_{\mathrm{eff},g}$ (arcsec)	60.55	39.86	36.50	MD11
$r_{\mathrm{eff},r}$ (arcsec)	56.09	29.78	33.61	MD11
$r_{\mathrm{eff},i}$ (arcsec)	56.44	30.04	33.83	MD11
$r_{\mathrm{eff},H}$ (arcsec)	51.74	30.35	35.81	MD11
W4 (Jy)	0.29	0.11	0.07	IRSA
100 (Jy)	17.33	5.20	4.77	D10
160 (Jy)	17.59	4.26	4.31	D10
250 (Jy)	7.90	1.63	1.87	D10
350 (Jy)	3.02	0.61	0.68	D10
500 (Jy)	0.96	0.19	0.21	D10

[1] http://ned.ipac.caltech.edu/

[2] http://irsa.ipac.caltech.edu/index.html

Table 5.1: The properties of four lenticular galaxies forming the control sample of this work. Classifications come from Cappellari et al. (2011a), distance data come from Davies et al. (2010) and structural properties are taken from McDonald et al. (2011). *gri* apparent magnitudes come from SDSS and JK apparent magnitudes from 2MASS. W4 is the 22 μm WISE band magnitude; 100 and 160 μm are PACS fluxes; 250, 350 and 500 μm are SPIRE fluxes. Uncertainties on these values are discussed in the main text. NED - NASA/IPAC Extragalactic Database; C11 - Cappellari et al. (2011a); D10 - Davies et al. (2010); MD11 - McDonald et al. (2011) - Virgo galaxy bulge-disk decompositions; IRSA - NASA/IPAC Infrared Science Archive - WISE all-sky survey extended sources.

5.3.2 GAMA ETG Sample

This study's main aim is to constrain dust distributions and extents within elliptical galaxies whose dust is unresolved both in emission and absorption. As with the Virgo control sample, these galaxies need to have a full suite of panchromatic data to test, as well as early-type morphologies. As our main sample of ETGs, four galaxies from the sub-mm detected sample in Chapter 3 have been selected. This sample has been chosen in particular because it contains all the required data, available from the GAMA and H-ATLAS surveys, and because results from Chapter 3 indicate these ETGs have blue colours, high dust masses and reside in sparse environments.

The four galaxies from the *SubS* were selected based on having mid-infrared data, 5σ detections in *Herschel* 250 and 350 μm bands, and 3σ detections in the other *Herschel* bands. Only those galaxies with elliptical classifications were included in this sample. Additionally, none of these four has an AGN classification according to the BPT diagram in Chapter 3. Full information for the data belonging to these four galaxies are given in Table 5.2.

These selection criteria are likely to bias any results from this study towards dusty, star-forming ellipticals. However, this is a test study and as such requires the best possible data in order to constrain the models and fitting routines. Therefore this bias should be accepted for now, and possibly re-considered when extending the study to a large range of ETGs.

5.4 Modelling technique for the optically thin cases

As mentioned in Section 5.1, little is known about the distribution of dust and heating mechanisms of this dust in ETGs. Because of this, no self-consistent

Property	**47500**	**298980**	**106410**	**619121**
Classification	E	E	E	E
Redshift	0.026	0.027	0.055	0.052
Distance (Mpc)	113.974	118.565	246.554	233.036
Sérsic index (n_r)	0.7327	2.6598	0.9035	1.467
g (mag)	16.33	16.02	17.20	17.00
r (mag)	15.93	15.44	16.78	16.59
i (mag)	15.71	15.11	16.48	16.28
J (mag)	15.54	14.67	16.09	15.95
K (mag)	15.51	14.71	16.17	15.75
$\mathrm{r_{eff},}_g$ (arcsec)	2.87	3.79	1.30	1.57
$\mathrm{r_{eff},}_r$ (arcsec)	2.91	4.06	1.38	1.67
$\mathrm{r_{eff},}_i$ (arcsec)	2.95	3.80	1.39	1.66
$\mathrm{r_{eff},}_J$ (arcsec)	2.63	2.84	1.33	1.57
$\mathrm{r_{eff},}_K$ (arcsec)	2.69	2.35	1.30	1.64
W4 (Jy)	0.008	0.024	0.006	0.012
100 (Jy)	0.259	0.626	0.112	0.211
160 (Jy)	0.301	0.520	0.163	0.270
250 (Jy)	0.129	0.288	0.063	0.133
350 (Jy)	0.073	0.130	0.039	0.061
500 (Jy)	0.032	0.040	0.017	0.017

Table 5.2: The properties of four elliptical galaxies forming the main sample of this work. Classifications come from Kelvin et al. (2014), redshift and distance data come from the GAMA database. Sérsic indices, apparent magnitudes and effective radii come from the GAMA single Sérsic profiles described in Kelvin et al. (2012). W4 fluxes are the 22 μm WISE data from the GAMA-matched catalogue and the FIR/sub-mm fluxes are taken from the H-ATLAS GAMA-matched catalogue.

model for the attenuation of stellar light and its re-radiation in the infrared of ETGs yet exists. Although RT models now have the capability to predict the UV/optical/FIR/sub-mm SED of more complex systems like spiral galaxies (see Popescu et al. 2011 for a library of models), we are still not at the stage where we can build similar models for the smoother and simpler geometries associated with ETGs. One reason for this difference in modelling capabilities is the obvious difference in the prominence of the dust distribution. Spiral galaxies exhibit prominent dust lanes, as seen in the edge-on view of these systems. In particular in the optical bands, where the stellar components above the plane can be seen through more optically thin lines of sight, the vertical distributions of stars and dust in spiral galaxies can be derived unambiguously. Modelling the optical images of edge-on spiral galaxies with RT models resulted in the determination of the main geometrical components of spiral galaxies, as well as of the relative scale-lengths and heights between stellar emissivity and dust (Xilouris et al. 1998, 1999). In ETGs the ellipsoidal shape of these systems together with the relative paucity of strong dust lanes makes a similar approach less certain. Traditionally early-type galaxies were therefore modelled as very optically thin systems, with any diffuse dust distributed in an ellipsoidal component, spatially correlated with the stellar distribution (Silva et al. 1998). Furthermore, in elliptical galaxies there is a potential extra source of dust heating, through collisions with energetic electrons and protons from the hot ISM, as modelled by Tsai & Mathews (1995).

In the process of building a self-consistent model for the panchromatic SED of ETGs, a first step is to gain knowledge about the distribution of dust in these systems, and how this dust may be heated. We therefore first propose a scenario in which dust resides in disk situated in the equatorial plane of the ellipsoidal stellar distribution. The assumed dust disk has a very small scale-height, of 90 pc, of the order of that of the molecular layer in the Milky Way, and the same

as the second dust disk introduced by Popescu et al. (2000a), and adopted in the library of models from Popescu et al. (2011). We also assume that this dust disk is optically thin, and we first test the hypothesis that this dust is heated by the old stellar populations from the ellipsoidal component. To this end we search for a consistent solution in two variables: the scale-length of the dust disk and the central face-on dust opacity. We use a combination of RT models for the fitting approach, to account for the dust and PAH emission SEDs.

To test this scenario we use a combination of RT models for the calculation of the radiation fields in the optical bands and a template fitting approach to account for the dust and PAH emission SEDs.

5.4.1 Radiative Transfer Models

The models used in this analysis are created using the RT model of Popescu et al. (2011), adapted for the geometry of elliptical galaxies. This uses a modified version of the ray-tracing code of Kylafis & Bahcall (1987) and a Milky Way type dust model, with dust efficiencies and size distributions from Weingartner & Draine (2001) and Draine & Li (2007), with a dust composition including silicates, graphites and PAHs.

We produced a suite of simulations consisting of spheroidal stellar distributions calculated as deprojected Sérsic profiles (Popescu & Tuffs 2013) for the intrinsic volume stellar emissivity, with a range of Sérsic indices covering the whole parameter space observed in galaxies (n=1, 2, 4 and 8), and a very thin (small scale height) dust disk centred in the plane of the spheroid. The simulations were derived for four values of central face-on B-band optical depth $\tau_B^{\rm f}$=(0.1, 0.3, 0.5 and 1.0). The simulations are modelled in five standard optical/NIR bands B, V, I, J and K (corresponding to central wavelengths: 4430 Å, 5640 Å, 8090 Å, 12590 Å and 22000 Å).

Following the method of Popescu et al. (2011), all simulations have been performed for a fixed galaxy size and luminosity, since the results of these calculations can then be scaled to any observed size and luminosity using the formalism from Popescu et al. (2011) (see also Popescu & Tuffs 2013). The scaling with luminosity relies on the fact that the direct stellar light is an additive quantity, and therefore the radiation fields in the UV and optical are additive quantities. Thus, we consider our fixed size to be the reference disk size from Popescu et al. (2011), $h_{s,ref}^{disk}$=5670 pc. Then, the effective radius $R_{\rm eff}$ of the modelled spheroidal stellar component is taken to be equal to $h_{s,ref}^{disk}$, and the dust scalelength is considered to be again equal to $h_{s,ref}^{disk}$. We note here that in an optically thin case the solutions for the radiation fields do not depend on the exact extent of the dust disk, therefore our choice of a dust disk extending throughout the midplane of the spheroidal stellar component is arbitrary. The extent of the dust disk will be derived as an output of our model. The simulations are performed for some unit luminosities, as defined in Table E.2 of Popescu et al. (2011) for the old stellar populations in the disk.

5.4.2 Mid-Infrared to Sub-mm SED Fits

The galaxy dust and PAH emission SED fitting code used for this work is fully described in Natale et al. (2010); N10 from here. In brief the code fits a library of MIR/FIR/sub-mm SED templates calculated using the formalism of Fischera & Dopita (2008) for a large range of interstellar radiation fields for which both the intensity and the optical/UV colour is allowed to vary. In addition to this diffusely emitting component, the code also incorporates a clumpy component associated with star-forming regions. Although the infrared SEDs are not calculated for the exact solutions of the radiation fields provided by the RT calculations, this template fitting approach is still superior to the modBB fits. Firstly the templates are

derived by making explicit calculations for the emission arising from stochastically heated dust grains which are not in equilibrium with the radiation fields, an effect that cannot be accounted for by modBB fits. Secondly, the templates take into account the variation in both strength and colour of the radiation fields, which, when combined with the solutions for the RT calculation, provide an alternative approach to self-consistent modelling. Thus the method proposed here can be used to gain information on the geometry of the problem, which cannot be addressed by a simple fit with a modBB function. Thirdly, the model used here takes into account the main morphological components in the infrared emission: the diffuse and clumpy component.

The diffuse dust emission component from N10 is calculated based on a Milky Way type dust model[2]. These templates include a full calculation of the stochastic heating of dust grains and PAH molecules based on the method of Guhathakurta & Draine (1989). The radiation fields are taken to have the spectral shape of the local interstellar radiation field, as derived by Mathis et al. (1983), with the possibility to adjust the optical/UV colour:

$$\mathrm{U} = \chi_{\mathrm{UV}} \times (\chi_{\mathrm{col}} \times \omega_i) \times \text{Planck Function}_i, \tag{5.1}$$

where i refers to the different components (given by Planck functions) of the local interstellar radiation field (as per Mathis et al. (1983)) representing the contribution from different stellar populations, and ω_i is a dilution factor which differs for each of these components.

Thus the radiation fields are varied based on two linear parameters: a dimensionless factor χ_{UV} (which scales the whole UV to optical SED) and a dimensionless factor χ_{col} (which scales only the optical part of the Mathis et al. (1983) spectrum with respect to the UV SED; see Appendix B.2 of N10). These linear factors are

[2]The full set of model parameters can be found in Table 2 of Fischera & Dopita (2008).

described in N10, but differ from the original implementation to the extent that the range for each radiation field parameter has been extended, thus expanding the size of the grid of diffuse dust emission templates. It should be noted here that there exists a degeneracy between the colour of the radiation fields as given by $\chi_{\rm col}$ and the relative abundance of PAH and solid dust grains. This degeneracy affects the ratio of PAH emission at 8 μm to FIR emission (see N10 §B.2 for further details).

The dust emission SED from the star forming regions - the clumpy component - is described in the model of N10 by a template SED, adopted from Popescu et al. (2011).

The SED fitting code therefore has four free parameters: $\chi_{\rm UV}$ giving the amplitude of the radiation fields, $\chi_{\rm col}$ giving the optical/UV colour of the radiation fields, the amplitude of the clumpy component SED template, and the dust mass $M_{\rm d}$ (which gives the overall scaling of the dust emission and the luminosity of each component (diffuse and clumpy)). This method does not output traditional average dust temperatures for the galaxy, as the output total spectrum of the dust emission code is determined by the probability distribution of the dust temperature. However, for the sake of comparison with modBB fits in the literature, each diffuse dust template fit outputs an associated dust temperature of a modBB fit with dust emissivity index β=2.0.

5.5 Testing the optically thin scenario

This section describes how the data are modelled to test the scenario that dust is distributed in an optically thin disk heated by the spheroidal stellar component. In particular we aim to determine the extent of the dust disk, should the result of this analysis give a physically plausible solution. In brief, the MIR/FIR/sub-mm data are fitted with the dust and PAH emission SED templates, allowing the average

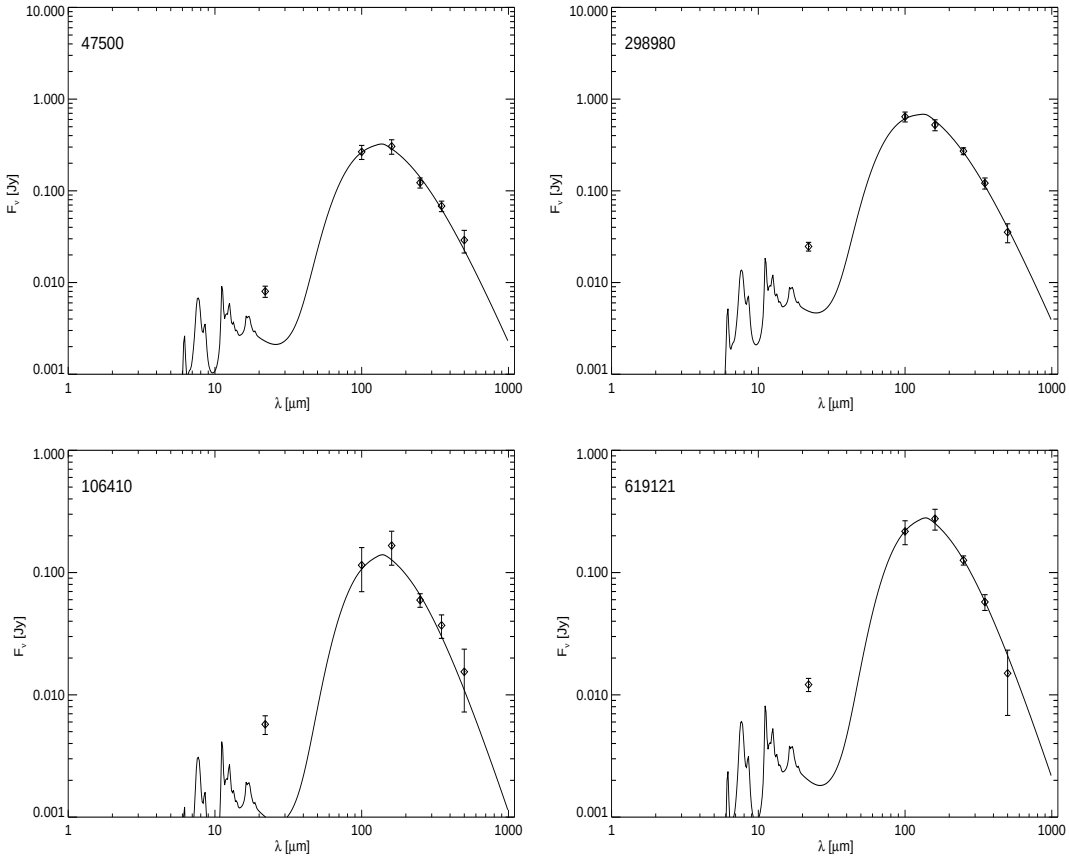

Figure 5.1: SED fits to the four GAMA galaxies, for the optically thin scenario with dust heated only by optical photons from the old stellar population in the spheroidal component. Plotted data points include WISE W4 22 μm, PACS 100 and 160 μm, and SPIRE 250, 350 and 500 μm. The WISE W3 12 μm data point is shown here, but is not included in the model fit.

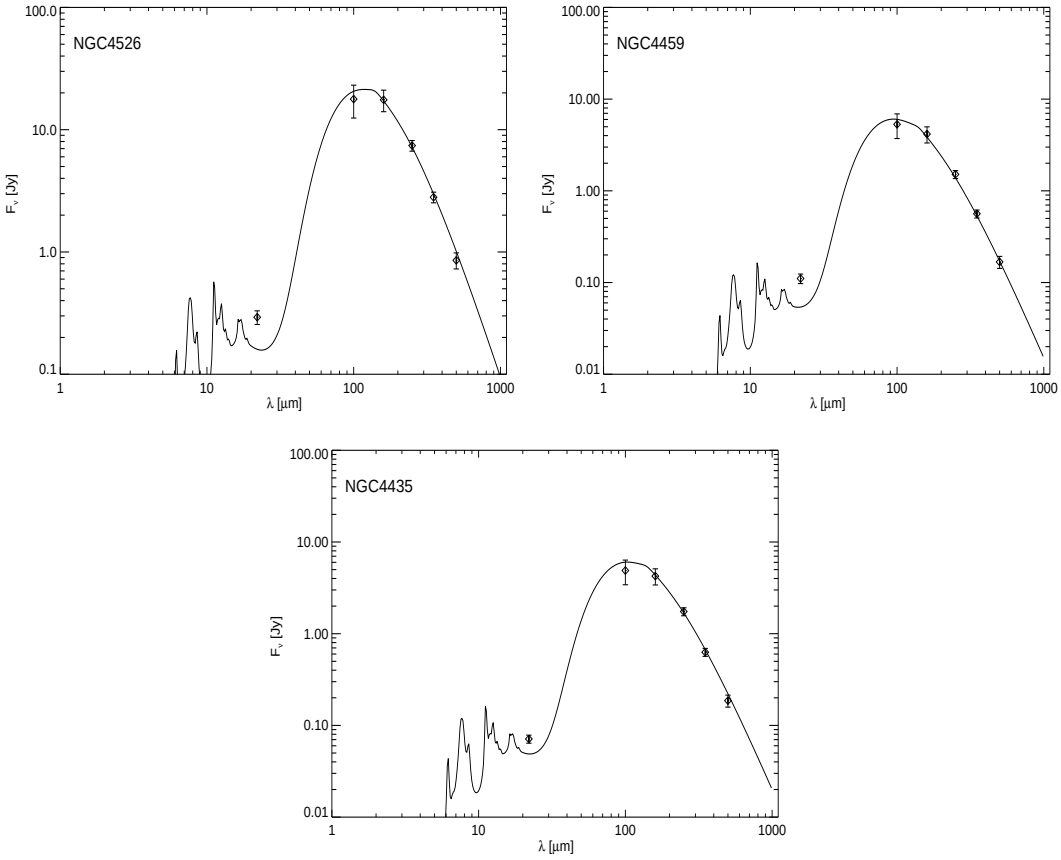

Figure 5.2: SED fits to the three Virgo Cluster galaxies, for the optically thin scenario with dust heated only by optical photons from the old stellar population in the spheroidal component. Plotted data points include WISE W4 22 μm, PACS 100 and 160 μm, and SPIRE 250, 350 and 500 μm. The WISE W3 12 μm data point is shown here, but is not included in the model fit.

radiation fields heating the dust to be determined. On the other hand, the RT models give solutions for the radiation fields at different galactocentric radii in the plane of the dust disk. Assuming the dust disk is optically thin, the solutions for the radiation fields will not depend on the exact extent of the dust disk considered in the simulations. Therefore, comparison of the solutions obtained from radiative transfer models with the average solution obtained from the dust emission fitting routine may give us information of the radius at which both methods provide a similar solution. This radius can then be taken as the effective radius out to which most of the dust is heated, or, in other words, the typical extent of the dust disk in the modelled galaxies.

5.5.1 SED template fits

Mid-infrared to sub-mm SEDs (see Section 5.4.2) are fit to the data in each of the samples described in Sections 5.3.1 and 5.3.2. Since here we are testing the hypothesis that dust is heated only by the radiation coming from the old stars in the spheroidal component, these fits are done with a diffuse dust emission template, heated only by optical emission[3]. Eq. 5.1 describing the radiation fields heating the dust becomes:

$$U_{\rm opt} = (\chi_{\rm col} \times \omega_i) \times \text{Planck Function}_i. \tag{5.2}$$

The free parameter of the fit in this case is $\chi_{\rm col}$, giving the amplitude of the radiation fields.

The result of these fits are shown in Figs. 5.1 and 5.2 for the GAMA and Virgo sample respectively. Here only the 100 μm and longer data points were used, since,

[3]Here we neglect the contribution to the dust heating coming from the UV photons emitted by the old stellar populations (UV upturn, X-ray background sources, SNIa). However this emission will be considered in the second scenario tested in this Chapter.

in this case, emission at 22μm could potentially be affected by other sources of emission than considered in our model (see below). The fits to the data points in both figures indicate a good match. However, the 22 μm point, the one that was excluded from the fit, is systematically underpredicted. For the GAMA galaxies the underprediction is quite large, at the level of 79% on average. However, for the Virgo galaxies the underprediction is relatively small, only at a level of 36%. The excess emission seen at 22 μm may indicate an additional source of heating coming from the old stellar populations, not included in our model fits. Indeed, circumstellar dust around asymptotic giant branch stars heated locally by the host stars could potentially contribute to the emission seen at 22 μm. Such emission has already been invoked to explain mid-infrared emission in the haloes or bulges of galaxies (Burgdorf et al. 2007; Simmat et al. 2010). Thus, at least qualitatively, this scenario could give a reasonable explanation for the observed SEDs, should we be able to find a consistent solution for the dust opacity and scale-length of the dust disk.

Before looking into the existence of such a solution, we describe the output parameters of the fits and list them in Table 5.3. This includes the free parameter $\chi_{\rm col}$ (ranging from 0.1-100), the dust temperature and dust mass of the ETGs, as well as the infrared luminosity (1-1000 μm range) powered by the diffuse optical radiation fields ($L_{\rm diffuse}$). The first two quantities are of importance for the sake of comparison with previous studies of these galaxies. Table 5.4 shows the parameters calculated using single modBBs, and the corresponding parameters extracted from Davies et al. (2012) for the Virgo ellipticals and from Chapter 3 for the GAMA ellipticals. The dust temperatures for both sets of ETGs are shown to correspond nicely with literature values within the uncertainties. The dust masses for the Virgo ellipticals are also very similar. The dust masses for the GAMA galaxies calculated in Chapter 3 are expected to be smaller than those calculated here by

	Free Parameters			*Other Parameters*	
Galaxy	$\chi_{\rm col}$	$\mathbf{M_d}$ ($\times 10^6\,\mathbf{M_\odot}$)	$\mathbf{T_d}$ **(K)**	$\mathbf{\log_{10}(L_{diffuse})}$ **(ergs s^{-1})**	$\chi^2_{\mathbf{min}}$ **(ergs s^{-1})**
Virgo ETGs					
NGC 4526	18.0±10.3	9.55±1.81	25.21±1.65	43.33±42.13	2.312
NGC 4459	44.0±17.5	1.30±0.38	28.32±1.46	42.87±42.20	1.316
NGC 4435	25.0 ±10.0	1.81±0.34	26.79±0.80	42.82±41.62	2.765
GAMA ETGs					
47500	6.0±2.3	13.34±3.34	22.04±0.82	43.13±42.15	2.443
298980	9.5±4.0	23.40±4.43	23.11±0.45	43.51±42.29	1.414
106410	4.5±6.5	32.69±13.73	21.69±1.86	43.45±42.79	2.249
619121	5.0±2.8	52.03±16.10	21.98±1.06	43.70±42.82	0.751

Table 5.3: Results from the SED fits to the FIR PACS and sub-mm SPIRE data, assuming dust is heated only by the diffuse optical radiation fields. Columns show the galaxy name, followed by fit outputs described in the main text.

Galaxy	$\mathbf{T_{d,lit}}$ **(K)**	$\mathbf{T_{d,SED}}$ **(K)**	$\mathbf{M_{d,lit}}$ $(\times 10^6\,\mathbf{M_\odot})$	$\mathbf{M_{d,SED}}$ $(\times 10^6\,\mathbf{M_\odot})$
NGC 4526	24.5±1.50	25.21±1.65	10.23±0.07	9.55±1.81
NGC 4459	27.2±2.00	28.32±1.46	1.66±0.08	1.30±0.38
NGC 4435	25.9±1.70	26.79±0.80	2.09±0.08	1.81±0.34
47500	22.17±1.09	22.04±0.82	4.07±0.54	13.34±3.34
298980	23.62±1.02	23.11±0.45	8.13±0.78	23.40±4.43
106410	23.50±1.81	21.69±1.86	7.08±0.95	32.69±13.73
619121	22.55±1.19	21.98±1.06	15.49±1.45	52.03±16.10

Table 5.4: Comparison of dust temperature and dust mass results from modBB fits from Davies et al. (2010) for the Virgo ETGs and from Chapter 3 for the GAMA ETGs with those calculated using our purely optical template fits.

an average factor of ∼0.35, due to our taking into account both redshift and k-correction in the Chapter 3 calculations. Indeed, this is exactly what is seen in the comparison.

The resultant energy densities, as derived from the fit, are calculated at multiple wavelengths, and are then interpolated and integrated over 2500-23850 Å to get a total energy density in ergs pc^{-3}. This energy density is hence calculated for all the test galaxies in the study. These results are given below:

NGC 4526: $\mathrm{U_{rad,gal}} = 2.2718782{\times}10^{44}\,\mathrm{ergs\,pc^{-3}}$

NGC 4459: $\mathrm{U_{rad,gal}} = 5.0297666{\times}10^{44}\,\mathrm{ergs\,pc^{-3}}$

NGC 4435: $\mathrm{U_{rad,gal}} = 3.3750335{\times}10^{44}\,\mathrm{ergs\,pc^{-3}}$

47500 : $\mathrm{U_{rad,gal}} = 7.2746060{\times}10^{43}\,\mathrm{ergs\,pc^{-3}}$

298980: $\mathrm{U_{rad,gal}} = 1.1135650{\times}10^{44}\,\mathrm{ergs\,pc^{-3}}$

106410: $\mathrm{U_{rad,gal}} = 5.6198729{\times}10^{43}\,\mathrm{ergs\,pc^{-3}}$

619121: $\mathrm{U_{rad,gal}} = 6.1714506{\times}10^{43}\,\mathrm{ergs\,pc^{-3}}$

5.5.2 Radiation Field Energy Density calculation from the RT models

As mentioned before, the energy densities calculated with the RT models are derived for each radial position in the plane of the dust disk, for a fixed size and luminosity, and for a range of Sérsic indices and dust opacities, within the optically thin limit. A typical profile of radiation fields is shown in Fig. 5.3 for a model galaxy with Sérsic index 4 and $\tau_B^{\mathrm{f}} = 0.1$. Note the cuspy central region of the profile, which is due to the de Vaucouleurs distribution of the stellar emissivity in the ellipsoidal component. As described in Popescu & Tuffs (2013), radiation fields originating from stellar components with cuspy Sérsic distributions (e.g. bulges with high Sérsic index) are dominated by the functional form of the stellar emissivity rather than by opacity effects, even for high optical depths of any embedded dust disk. At low Sérsic index, the distribution tends towards an exponential disk, and therefore the radiation field profile will be influenced by both the distribution of stellar emissivity and the dust disk.

The model radiation fields are scaled to the actual size of the observed galaxy using Eq. 3 from Popescu & Tuffs (2013), adapted for the specific case of early-type galaxies:

$$U_{\mathrm{rad,scaled},\lambda} = U_{\mathrm{rad,model},\lambda} \times \left(\frac{L_{\mathrm{gal},\lambda}/R^2_{\mathrm{eff,gal},\lambda}}{L_{\mathrm{model},\lambda}/R^2_{\mathrm{eff,model},\lambda}} \right), \tag{5.3}$$

where $L_{\mathrm{model},\lambda}$ and $L_{\mathrm{gal},\lambda}$ are the luminosity densities of the model and the observed galaxies, and $R_{\mathrm{eff,model}}$ and $R_{\mathrm{eff,gal},\lambda}$ are the effective radii of the model and observed

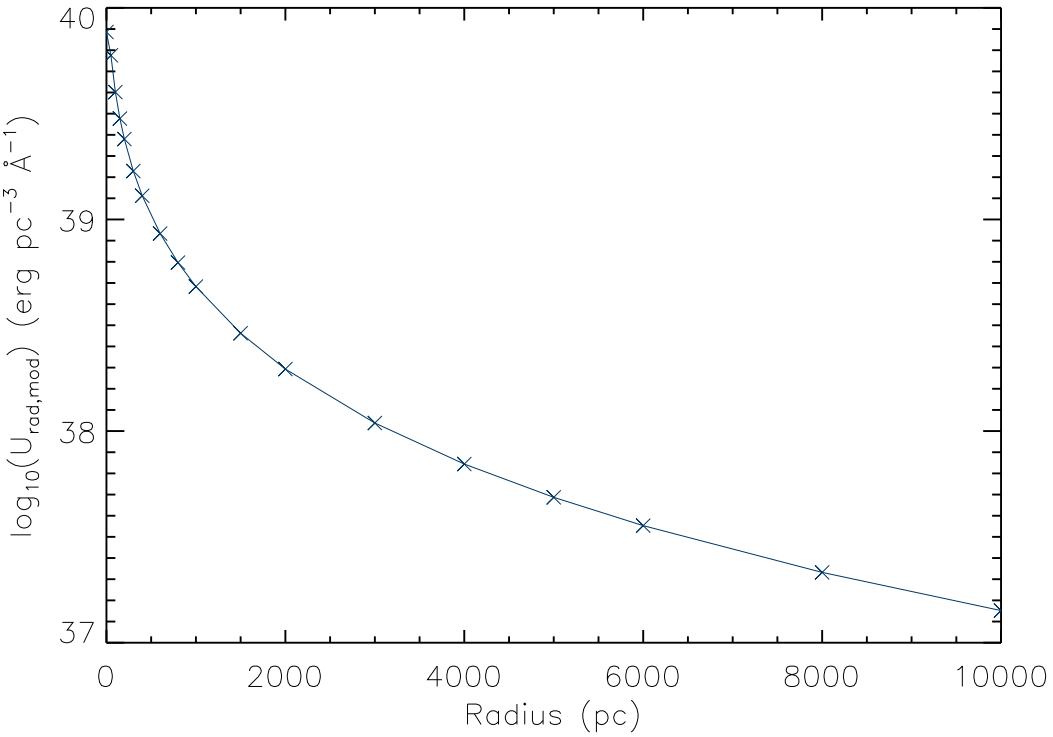

Figure 5.3: The variation of energy density with radius in the plane of the dust disk, for a model galaxy with Sérsic index of four and $\tau_B^{\rm f} = 0.1$, in the B-band. The crosses are the values at the radii output by the model and the line is the corresponding Sérsic model.

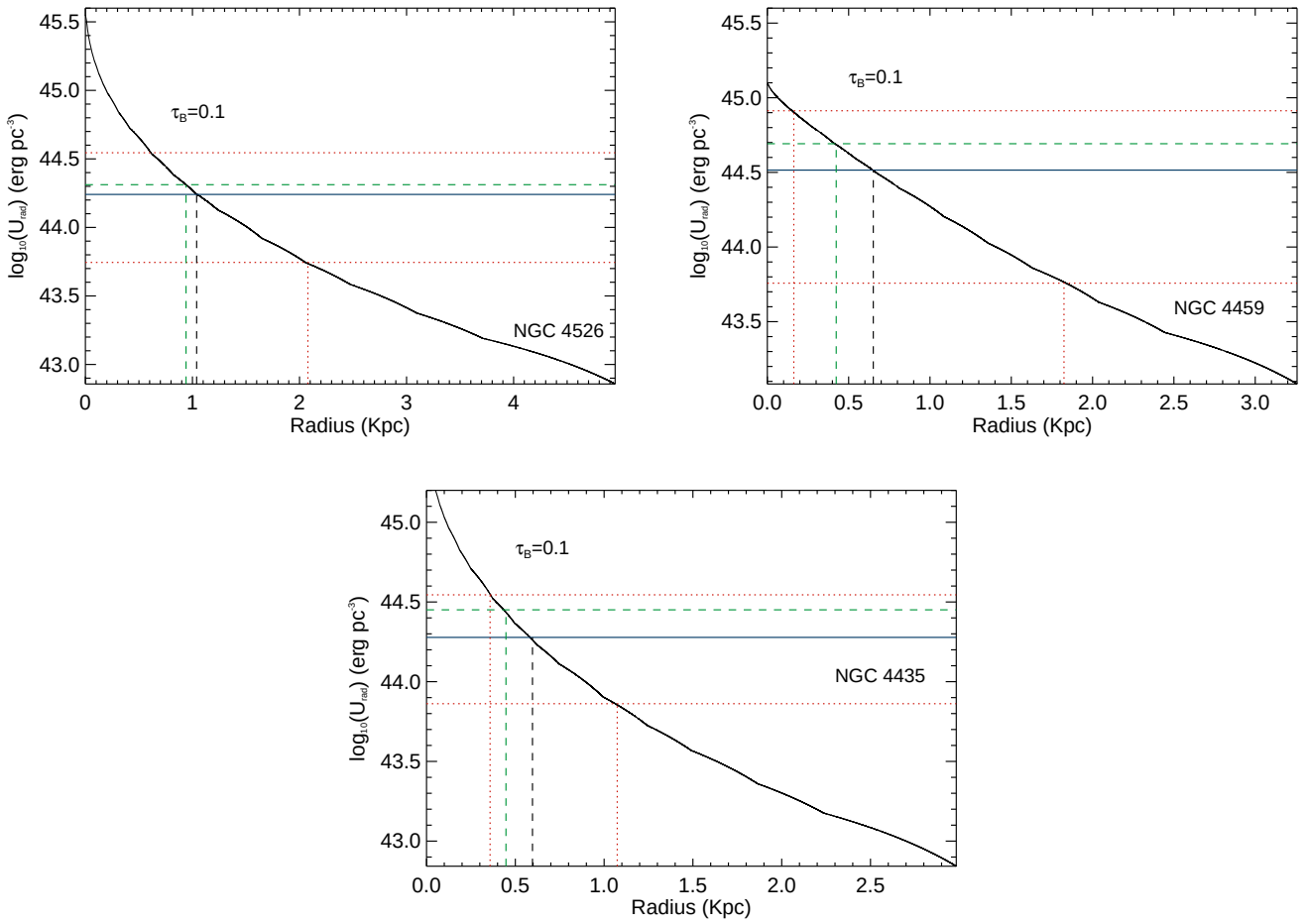

Figure 5.4: The scaled model energy density $U_{rad,mod}$ radial profiles are shown for the Virgo control sample. Green dashed vertical lines show the radius where $U_{rad,mod}$ intersects with the estimated galaxy energy density $U_{rad,gal}$ (shown as a green dashed horizontal line) for the optical only solution. The black dashed line and blue solid line show equivalent results for the UV+optical solution, with upper and lower limits represented by red dotted lines. These plots are all for an input model opacity τ_B^f=0.1.

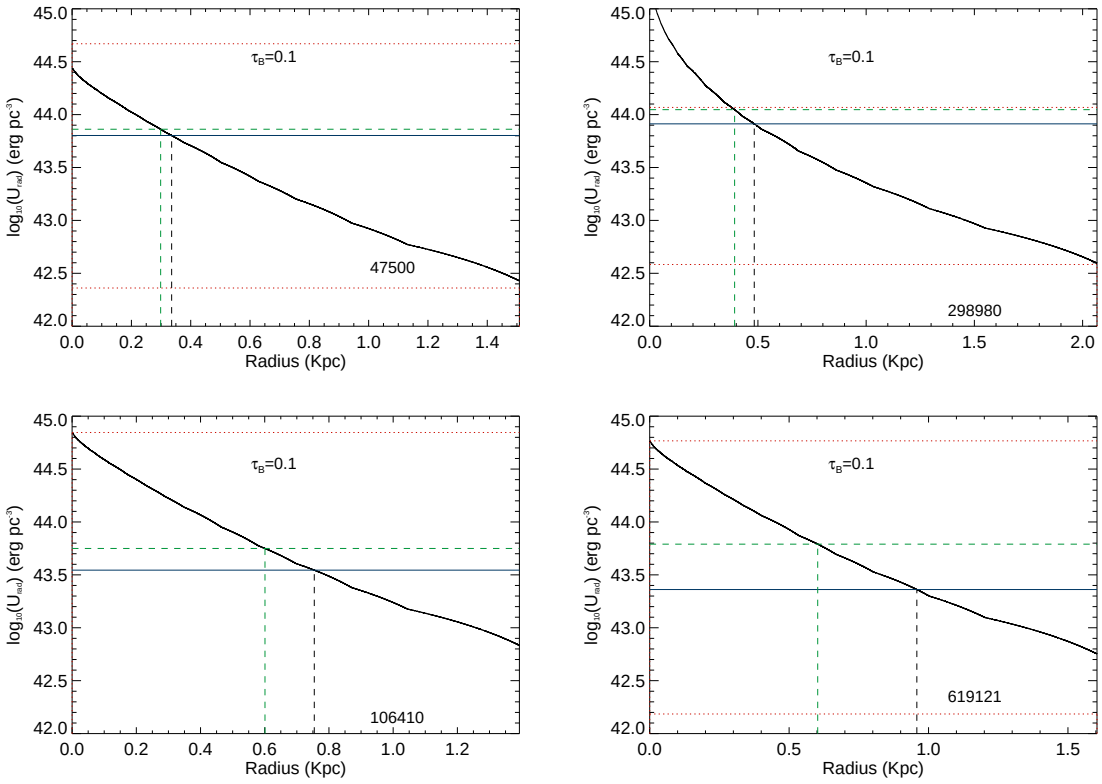

Figure 5.5: The scaled model energy density $U_{rad,mod}$ radial profiles are shown for the GAMA main sample. Green dashed vertical lines show the radius where $U_{rad,mod}$ intersects with the estimated galaxy energy density $U_{rad,gal}$ (shown as a green dashed horizontal line) for the optical only solution. The black dashed line and blue solid line show equivalent results for the UV+optical solution, with upper and lower limits represented by red dotted lines. These plots are all for an input model opacity τ_B^f=0.1.

galaxies. Here the model luminosities (L_{model}) and energy densities in the plane of the galaxy ($U_{rad,model}$) are interpolated to the same wavebands (denoted as λ for an arbitrary waveband) as the galaxy luminosity ($L_{gal,\lambda}$). Therefore model wavebands of $BVIJK$ are interpolated to $griJK$ bands. As previously described, the range of model luminosities are the unit luminosities from Table E.2 of Popescu et al. (2011).

The scaling is completed for each of these wavebands, and a total, scaled energy density ($U_{rad,scaled}$) is calculated by interpolating and integrating over the entire wavelength range. At this stage the scaled model energy densities obtained from the RT calculations can be compared to the energy density obtained from the FIR/sub-mm SED fits, to locate the radius where they overlap. This is shown for the $\tau_B^{\rm f}$ =0.1 models in Figs. 5.4 and 5.5 for the Virgo and GAMA galaxies respectively. Observe the green, dashed line, which represents the galaxy's radiation field energy density. The point at which this intersects with the modelled profile is the solution for the dust disk's radius.

5.5.3 Finding a Consistent Solution

The main assumption for this method to work is that the galaxy is optically thin in optical/NIR wavebands. This is a necessary assumption as otherwise the radiation fields calculated at each position would depend on the exact extent of the dust disk. To test if this is the case for the galaxies modelled here, we perform a consistency check by deriving the dust opacity obtained under the assumption that all the dust mass derived from the SED modelling fit is distributed within the derived radius of the dust disk. This output optical depth is calculated as

$$\tau_B^{\rm out} = \frac{M_{\rm d}\kappa_B}{\pi(Q_{\rm mod} \times R_{\rm eff,gal,}{}_B)^2}, \tag{5.4}$$

where κ_B is the B-band extinction coefficient (expressed in units of $\mathrm{pc^2\,M_\odot^{-1}}$).

The appropriate solution for Q_{mod} (defined as the ratio of the calculated dust radius to the effective radius of the modelled stellar spheroidal component) is when $\tau_B^{out} = \tau_B^{f}$: when $\tau_B^{out} \leq 1$, the system is optically thin as assumed and the solution is unique; when $\tau_B^{out} \gg 1$ then the system is optically thick and the solution is inconsistent.

Table 5.5: The results from matching modelled energy densities with calculated galaxy radiation field energy densities. The first column shows the galaxy name, followed by the results for the purely optical solutions: these results are the fraction of the galaxies effective radius taken up by the dust disk (Q), the radius of the dust disk, and the consistency check output τ_B^{out}. The final three columns are the same parameters for the UV+optical solution. Each level of the table shows the results for the models of different input optical depth τ_B^{f}.

	Optical Solution			*UV+Optical Solution*		
Galaxy	**Q**	$\mathbf{R_{gal}}$ **(pc)**	τ_B^{out}	**Q**	$\mathbf{R_{gal}}$ **(pc)**	τ_B^{out}
τ_B^{f}=0.1						
NGC 4526	0.19	940.18	1.163	$0.21\pm^{0.21}_{0.09}$	$1039.15\pm^{1039.15}_{445.35}$	0.897
NGC 4459	0.13	423.47	0.352	$0.20\pm^{0.36}_{0.15}$	$651.49\pm^{1172.69}_{488.62}$	0.148
NGC 4435	0.15	447.43	0.374	$0.20\pm^{0.16}_{0.08}$	$596.58\pm^{477.26}_{238.63}$	0.208
47500	0.20	298.55	2.857	$0.22\pm^{0.78}_{0.22}$	$335.75\pm^{1172.68}_{335.69}$	1.577
298980	0.19	392.29	1.499	$0.23\pm^{0.77}_{0.05}$	$483.06\pm^{1583.49}_{104.36}$	1.185
106410	0.43	600.72	0.774	$0.54\pm^{0.46}_{0.54}$	$754.32\pm^{638.90}_{754.26}$	0.491
619121	0.38	602.57	1.623	$0.60\pm^{0.40}_{0.60}$	$958.10\pm^{646.09}_{958.04}$	0.642

Continued on next page

	Optical Solution			*UV+Optical Solution*		
Galaxy	**Q**	$\mathbf{R_{gal}}$ **(pc)**	$\tau_{\mathbf{B}}^{\mathbf{out}}$	**Q**	$\mathbf{R_{gal}}$ **(pc)**	$\tau_{\mathbf{B}}^{\mathbf{out}}$
$\tau_B^{\rm f}$=0.3						
NGC 4526	0.19	940.18	1.218	$0.21\ \pm^{0.20}_{0.09}$	$1039.15\pm^{989.66}_{445.35}$	0.938
NGC 4459	0.12	390.90	0.378	$0.19\ \pm^{0.37}_{0.15}$	$618.92\ \pm^{1205.26}_{488.62}$	0.155
NGC 4435	0.14	417.60	0.397	$0.19\ \pm^{0.16}_{0.07}$	$566.75\ \pm^{477.26}_{208.80}$	0.219
47500	0.19	284.78	3.091	$0.21\ \pm^{0.79}_{0.21}$	$320.28\ \pm^{1188.14}_{320.22}$	1.692
298980	0.18	377.14	1.647	$0.23\ \pm^{0.77}_{0.05}$	$466.44\pm^{1600.11}_{103.76}$	1.302
106410	0.42	583.52	0.820	$0.53\ \pm^{0.47}_{0.53}$	$736.67\pm^{656.56}_{736.61}$	0.515
619121	0.38	586.14	1.715	$0.59\ \pm^{0.41}_{0.59}$	$942.59\ \pm^{661.60}_{942.53}$	0.663
$\tau_B^{\rm f}$=0.5						
NGC 4526	0.18	890.70	1.273	$0.20\pm^{0.21}_{0.08}$	$989.66\ \pm^{1039.15}_{395.87}$	0.969
NGC 4459	0.12	390.90	0.403	$0.19\pm^{0.36}_{0.15}$	$618.92\pm^{1172.69}_{488.62}$	0.161
NGC 4435	0.14	417.60	0.421	$0.19\pm^{0.15}_{0.07}$	$566.75\pm^{447.432}_{208.80}$	0.229
47500	0.18	272.15	3.330	$0.20\ \pm^{0.79}_{0.20}$	$308.29\ \pm^{1200.13}_{308.23}$	1.803
298980	0.18	363.36	1.804	$0.22\pm^{0.78}_{0.05}$	$451.81\pm^{1608.81}_{103.51}$	1.406
106410	0.41	573.37	0.8494	$0.52\pm^{0.48}_{0.52}$	$722.22\pm^{671.00}_{722.16}$	0.535
619121	0.36	572.17	1.800	$0.58\pm^{0.42}_{0.58}$	$929.90\pm^{674.29}_{929.84}$	0.681

Continued on next page

	Optical Solution			*UV+Optical Solution*		
Galaxy	**Q**	$\mathbf{R_{gal}}$ **(pc)**	$\tau_{\mathbf{B}}^{\mathbf{out}}$	**Q**	$\mathbf{R_{gal}}$ **(pc)**	$\tau_{\mathbf{B}}^{\mathbf{out}}$
$\tau_B^{\rm f}$=1.0						
NGC 4526	0.17	841.21	1.412	$0.20\pm^{0.20}_{0.09}$	$989.66\pm^{989.66}_{445.35}$	1.047
NGC 4459	0.11	358.32	0.474	$0.18\ \pm^{0.36}_{0.15}$	$586.34\pm^{1172.69}_{488.62}$	0.180
NGC 4435	0.13	387.77	0.483	$0.18\pm^{0.15}_{0.07}$	$536.92\pm^{447.43}_{208.80}$	0.256
47500	0.16	244.305	3.865	$0.19\ \pm^{0.81}_{0.19}$	$282.77\pm^{1225.66}_{282.71}$	2.056
298980	0.16	337.281	2.238	$0.20\pm^{0.78}_{0.05}$	$423.04\ \pm^{1617.15}_{96.18}$	1.671
106410	0.40	554.043	0.910	$0.49\pm^{0.50}_{0.50}$	$694.17\pm^{699.05}_{694.12}$	0.579
619121	0.34	541.479	2.010	$0.56\pm^{0.44}_{0.56}$	$904.23\pm^{699.96}_{904.17}$	0.721

The results of our search for a consistent solution are summarised in Table 5.5. One can see that for the Virgo galaxies one obtains consistent solutions in two out of three cases. We find that, under the proposed scenario (optical heating only), NGC 4459 and NGC 4435 have $\tau_B^{\rm f} = 0.3 - 0.5$[4], and a dust disk with fractional radius Q (calculated here as $\rm R_{match}/R_{\it eff}$ of the observed galaxy) Q=0.12 and 0.14 for NGC 4459 and NGC 4435 respectively. For the GAMA galaxies we find a consistent solution in only one case (106410), and this is for a $\tau_B^f = 1.0$. Since this is marginally optically thin, and since the excess emission at 22μm that would be needed to originate from circumstellar dust is quite large, we believe that this is an unlikely solution for this galaxy.

[4]We note that due to the discrete sampling of the RT models in $\tau_B^{\rm f}$, we give the solution for $\tau_B^{\rm f}$ either as a range of values, or, when $\tau_B^{\rm out}$ is close to a sampling value, the latter is adopted as the solution.

At this point we have found that two Virgo galaxies could be modelled as having dust residing in an optically thin disk heated predominantly by the old stellar population, while the rest of our galaxies need a different explanation for their observed properties. We now need to check if observables at other wavelengths are also consistent with our findings. Firstly we check UV to optical colour. Yi et al. (2005) and Kaviraj et al. (2007b) showed that NUV-r colour can be associated with stellar populations age. Both of these papers find that galaxies with old stellar populations and no residual star formation lie exclusively above (NUV-r) > 5.5 (Kaviraj et al. 2007b) and 4.7 (Yi et al. 2005). Based on photometry in NED, the NUV-r colours for the Virgo galaxies are:

NGC 4526 : (NUV-r) = 4.55
NGC 4459: (NUV-r) = 4.39
NGC 4435: (NUV-r)=4.8.

For the GAMA galaxies, the colours are derived from GAMA data in Chapter 3:

47500: (NUV-r) = 2.65
298980: (NUV-r) = 3.31
106410: (NUV-r) = 2.52
619121: (NUV-r) = 2.69.

Based on these results, it seems likely that GAMA galaxies have ongoing star formation, whilst Virgo galaxies contain intermediate-to-old age stellar populations. This is consistent with the findings of our modelling.

With this in mind we also recall that the Virgo galaxies have resolved CO maps. The presence of molecular material indicates that star formation still occurs in

these galaxies. However, as long as the level of star formation is low, as indicated by the NUV-r colours, our solution is still a valid one. Davis et al. (2013b) report the following ratios of CO extent to galaxy effective radius (equivalent to our Q parameter for dust) for these three control ETGs:

NGC 4526: R_{CO}/R_{eff}=0.13

NGC 4459: R_{CO}/R_{eff}=0.19

NGC 4435: R_{CO}/R_{eff}=0.11.

Comparing these ratios with Q derived in our modelling for the Virgo galaxies indicates the CO and dust disk extents match relatively well.

We conclude that two of the Virgo galaxies can be modelled with an optically thin dust disk solution, where the dust heating is provided by the diffuse radiation fields originating from the spheroidal component, with a small excess contribution at 22 μm coming from circumstellar dust. For the GAMA galaxies such a scenario does not seem to provide a good match to the observed data.

5.6 An Optically Thin Solution with additional heating from a young stellar population

The scenario we tested thus far is that the ETGs have little or no star formation, and therefore there is no UV contribution to dust heating and subsequent emission due to a young stellar population. Here we consider the same optically thin scenario, but we allow for an additional contribution from UV photons to the heating of the dust. In addition we also allow for a contribution of UV photons coming from the old stellar populations. The SED fitting routine is now given in terms of both χ_{UV} and χ_{col} (see Eq. 5.1) as free parameters for the diffuse radiation fields, with their ranges suitably reduced to between 0.1 and 10.0 to complement each

other. Since there are now two free parameters describing these fields, it is necessary for further uncertainty calculations to find the values of $\chi_{\rm UV}$ and $\chi_{\rm col}$ whose combination give the minimum and maximum value which still allows a good fit to the data. This is also incorporated within the SED fitting code.

The presence of a younger stellar population in a model also introduces the presence of star formation regions, in which surrounding dust is much more efficiently heated by the UV emission from these new stars. To account for this, the clumpy component template is also considered in the SED fit, as described in Section 5.4.2. Caution is required in including this template, as star formation regions in ellipticals, if present, may have different properties than those of spirals, and therefore than what is considered in the model. This template accounts for the MIR emission produced by grains in equilibrium temperature with the high radiation fields from the massive stars inside the clouds, and is strongly constrained by the 22 μm emission. We thus include the 22 μm flux in these fits. The fitting is now carried out using this new recipe, and shown in Figs. 5.6 and 5.7 for GAMA and Virgo samples respectively.

Fig. 5.7 shows that the Virgo ETGs have fits dominated by the diffuse component. The GAMA ETGs in Fig. 5.6 show different results, with the fits dominated by the diffuse component in the FIR/sub-mm region, but with the clumpy component dominating the emission in the MIR. The predominance of the clumpy component at shorter wavelength is most likely due to the high amplitude of the 22 μm WISE point. Essentially, the fits follow the trends already seen in the fits with optical heating only. Thus far, the GAMA galaxies could not be fitted with an optical solution only, due to the significant emission at 22 μm, which is difficult to reconciliate with a circumstellar dust origin. Thus, the excess emission is, in the new scenario, fitted by the clumpy component template. For two of the Virgo galaxies an optical heating solution was found to give consistent results if we allow

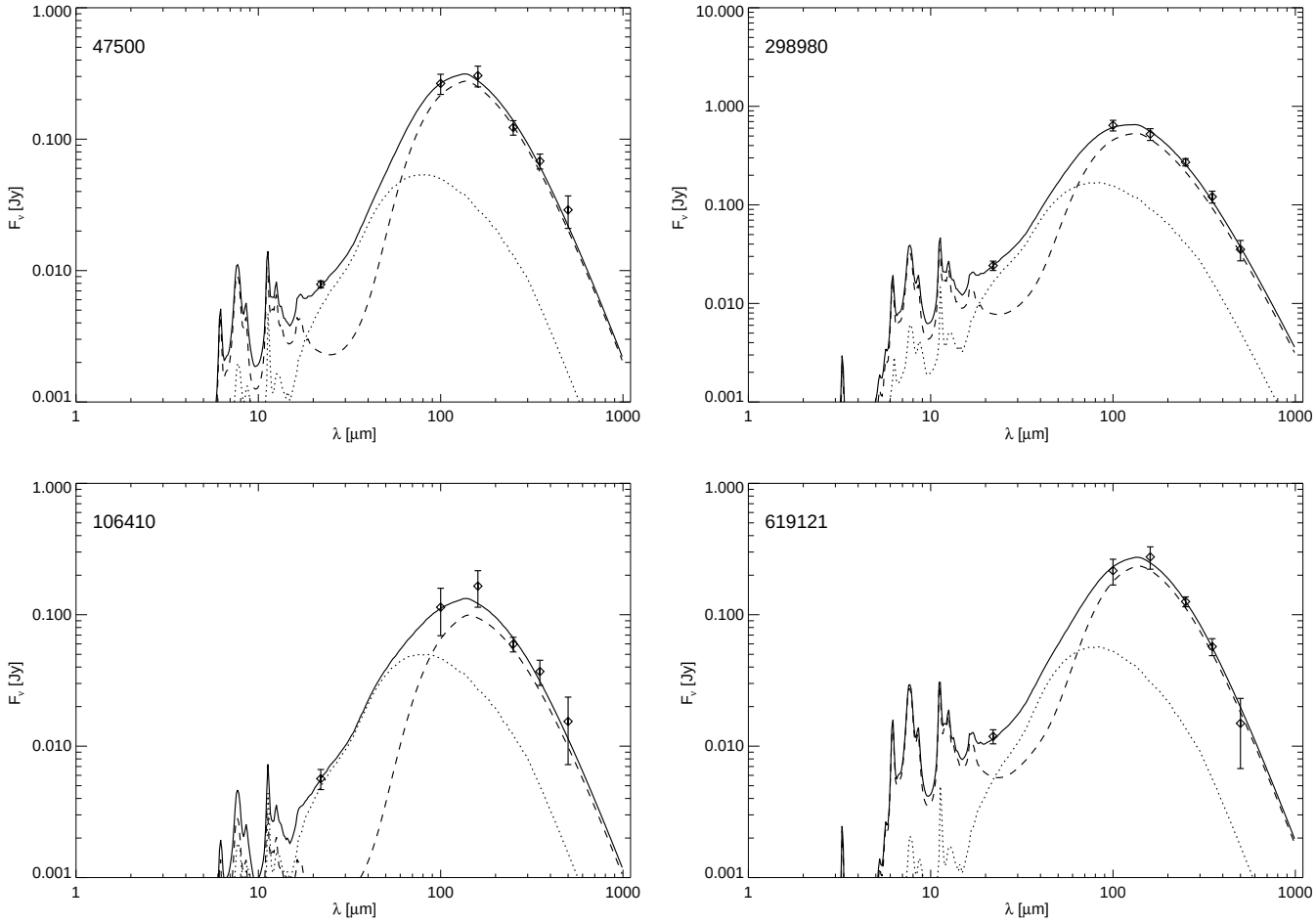

Figure 5.6: Diffuse (dashed lines) plus clumpy component (dotted lines) SED fits to the four GAMA test case galaxies. The combined fits are shown as the solid lines. Plotted data points include WISE W4 22 μm, PACS 100 and 160 μm, and SPIRE 250, 350 and 500 μm.

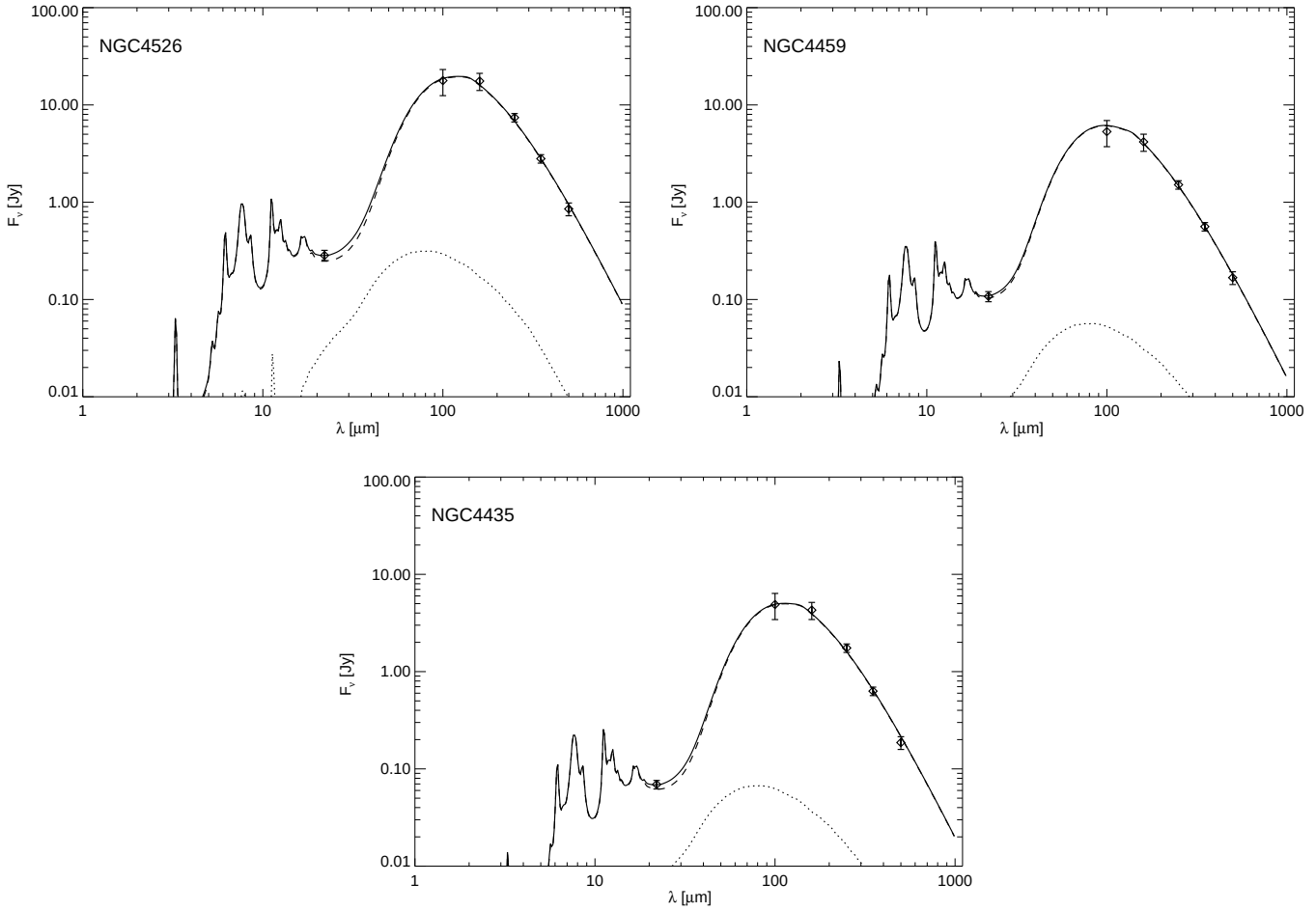

Figure 5.7: Diffuse (dashed lines) plus clumpy component (dotted lines) SED fits to the three Virgo control test case galaxies. The combined fits are shown as the solid lines. Plotted data points include WISE W4 22 μm, PACS 100 and 160 μm, and SPIRE 250, 350 and 500 μm.

for a small contribution from circumstellar dust. In the new scenario the small excess emission can then be fitted by the additional contribution of the UV heating in the diffuse component, with no significant contribution from localised dust in star forming clouds.

Output values of $\chi_{\rm UV}$ and $\chi_{\rm col}$ are given in Table 5.6, together with upper and lower limits and further fitting results. Given these limits on the two free parameters, it is also possible to calculate upper and lower limits on the energy density for the ETGs. These results are all shown in Table 5.7. We note here that previous predictions for the purely optical solution provide an upper limit for the energy densities, with the new values being lower than the previous by a factor of 1.5. Note also that there is little difference in the output values for dust grain temperature and mass compared with the purely optical fits; this implies that the diffuse component fit is also very similar to the fit from purely optical heating.

Following the same procedure as in Section 5.5.3, the energy densities calculated using SED outputs are compared to the energy densities calculated from the RT models as a function of radius. These comparisons are shown in the same figures where we tested the pure optical heating scenario (Figs. 5.4 and 5.5), overplotted as black dashed lines and blue solid lines, with upper and lower limits plotted as red dashed lines. As before, only the most optically thin case ($\tau_B^{\rm f}$=0.1) is shown. The results are given in the right columns of Table 5.5.

One can see that consistent solutions can be found for all three of the Virgo Cluster galaxies and two of the GAMA galaxies. For the Virgo Cluster galaxies NGC 4459 and NGC 4435, we find a dust extent of $Q \sim 0.2$ of $R_{\rm eff}$, slightly larger than in the previous scenario, and a dust opacity slightly lower, at around $\tau_B^{\rm f}$=0.1-0.3. The third Virgo Cluster galaxy, NGC 4526, is a marginally optically thin solution, with $\tau_B^{\rm f}$=1 and $Q \sim$0.2.

The GAMA galaxies modelled by an optically thin solution are 106410 and

	Free Parameters								*Other Parameters*		
Galaxy	$\chi_{\mathbf{col}}$	$\chi^{\mathbf{min}}_{\mathbf{col}}$	$\chi^{\mathbf{max}}_{\mathbf{col}}$	$\chi_{\mathbf{UV}}$	$\chi^{\mathbf{min}}_{\mathbf{UV}}$	$\chi^{\mathbf{max}}_{\mathbf{UV}}$	$\mathbf{M_d}$	$\mathbf{log_{10}(L_{clumpy})}$	$\mathbf{T_d}$	$\mathbf{log_{10}(L_{diffuse})}$	$\chi^2_{\mathbf{min}}$
							($\times 10^6\,\mathbf{M_\odot}$)	(**ergs s^{-1}**)	**(K)**	(**ergs s^{-1}**)	
Virgo ETGs											
NGC 4526	7.5	5.0	10.0	1.95	0.9	3.0	8.91±2.24	42.20±42.06	25.02±1.34	43.37±42.70	1.420
NGC 4459	6.0	2.0	10.0	4.5	2.0	7.0	1.35±0.03	41.83±41.73	27.91±1.63	42.87±42.21	0.642
NGC 4435	8.0	6.0	10.0	2.0	1.0	3.0	1.82±0.35	41.38±41.05	25.76±0.59	42.79±41.72	2.108
GAMA ETGs											
47500	9.0	0.1	10.0	0.6	0.3	4.0	12.88±3.98	42.54±42.50	21.24±1.24	43.15±42.67	2.607
298980	9.0	0.1	10.0	0.8	0.5	7.0	19.50±4.90	43.15±43.05	22.74±1.14	43.55±43.13	0.968
106410	10.0	0.1	10.0	0.3	0.1	6.0	42.66±25.70	43.22±43.12	19.85±3.35	43.45±43.27	2.276
619121	0.1	0.1	10.0	3.0	0.2	5.0	45.71±14.13	43.52±43.19	20.86±1.55	43.69±43.34	0.808

Table 5.6: Results from diffuse plus clumpy component template fits to the FIR PACS, sub-mm SPIRE and 22 μm WISE points for all the test cases. These fits assume both UV and optical contribution to the heating. Columns show the galaxy name, followed by fit outputs described in the main text.

Galaxy	$\mathbf{U_{rad,gal}}$ **(ergs pc^{-3})**	$\mathbf{U_{rad,gal,min}}$ **(ergs pc^{-3})**	$\mathbf{U_{rad,gal,max}}$ **(ergs pc^{-3})**
NGC 4526	1.7412212×10^{44}	5.5543054×10^{43}	3.5061683×10^{44}
NGC 4459	3.2735727×10^{44}	5.7239688×10^{43}	8.1810593×10^{44}
NGC 4435	1.8961834×10^{44}	7.2746060×10^{43}	3.5061683×10^{44}
47500	6.3504435×10^{43}	2.2979675×10^{42}	4.6748910×10^{44}
298980	8.1798902×10^{43}	3.8299457×10^{42}	1.1687228×10^{44}
106410	3.5061684×10^{43}	7.6598915×10^{41}	7.0123365×10^{44}
619121	2.2979674×10^{43}	1.5319783×10^{42}	5.8436138×10^{44}

Table 5.7: Calculated energy densities ($U_{rad,gal}$) for the Virgo and GAMA ETGs, as well as the lower ($U_{rad,gal,min}$) and upper limits ($U_{rad,gal,max}$).

619121, for which we find a dust extent of $Q \sim 0.5$ and a dust opacity of $\tau_B^{\rm f}$=0.5. For the rest of the galaxies no consistent solution can be found for the optically thin cases.

We therefore find that two of the Virgo Cluster galaxies can be equally accounted for by an optically thin model with diffuse dust emission heated solely by optical photons from the spheroidal component plus an additional contribution from circumstellar dust, or by an optically thin model with diffuse dust emission heated by both optical and UV photons, and with a very low rate of star formation. Qualitatively the two scenarios are very similar. The third Virgo Cluster galaxy can be accounted for by a marginally optically thin solution with diffuse dust heated by both optical and UV photons. For two of the GAMA galaxies we can fit an optically thin solution only if substantial contribution from star formation is allowed.

5.7 Conclusions

We have developed a method for estimating the extent of a dust disk in an ETG without obtaining spatially resolved imaging of the dust itself. This method requires a set of RT models, designed to emulate a spheroidal stellar distribution, which are calculated as deprojected Sérsic profiles for the intrinsic volume stellar emissivity with a range of Sérsic indices and for four values of central face-on B-band opacity. For a galaxy of Sérsic index n, an appropriate model is scaled to the UV and optical luminosities and effective radii of the galaxy itself. This allows the calculation of a UV+optical energy density ($U_{rad,mod}$) for the model as a function of radius.

SEDs are then fit to the same galaxy's FIR/sub-mm data, using the code of Natale et al. (2010). This model outputs a set of parameters which define the amplitude of the radiation curve of the galaxy's long-wavelength SED. These parameters can then be used to calculate the average radiation field energy density ($U_{rad,gal}$) of the galaxy itself. The radius at which $U_{rad,gal}$=$U_{rad,mod}$ is taken as the extent of the dust disk in the galaxy.

Seven galaxies are tested using this method. Three galaxies are taken from within the Virgo Cluster - they are our control cases, chosen due to the previously published CO gas disk extents. Four galaxies are from the *SubS*, described in Chapter 3; these form the main sample.

Two variations of the test described above were carried out, using different assumptions for the stellar population heating the dust, but with the same assumption that the diffuse dust distribution is optically thin. This led to the following results:

> Two of the three Virgo ETGs can be modelled as having dust residing in an optically thin disk heated predominantly by the old stellar population in the spheroidal component, with a small excess contribution at 22 μm coming

from circumstellar dust. Alternatively the dust could be heated by diffuse UV and optical radiation fields, and with a very low star formation rate. In both cases, very similar results are found for the extent of the dust disk: $0.12 \lesssim Q \lesssim 0.2$ for both NGC 4459 and NGC 4435. These values are all similar to their published CO extents (Davis et al. 2013b). The third Virgo Cluster galaxy can be accounted for by a marginally optically thin solution with diffuse dust heated by both optical and UV photons.

An optically thin solution can be fit to the GAMA ETGs only if substantial contribution to the dust heating from star formation is allowed. Furthermore, only two of the four GAMA ETGs are found to have optically thin solutions under this condition. These two ETGs are found to have dust extents of $Q \sim 0.5$ for 106410 and $Q \sim 0.6$ for 619121; these extents are a factor of three larger than those found for the Virgo ETGs. It could be argued that these GAMA ETGs may be misclassified LTGs, which might explain why these results are so different to those of the control sample. However, given that LTGs are optically thick, this solution would not give consistent results if the test cases were in fact LTGs. Additionally, the three ETGs in this GAMA sample were specifically chosen because they were classified as ellipticals (not lenticulars), thereby reducing the likelihood of misclassification.

Two of the GAMA ETGs could not be modelled as having an optically thin solution. Although an optically thick solution is not shown in this thesis, it will be addressed in future work in Agius et al. (in prep).

Chapter 6

ETGs: an uncertain future

Don't adventures ever have an end? I suppose not.
Someone else always has to carry on the story.

J.R.R. Tolkien, The Fellowship of the Ring

6.1 Predictions for Future Work

Future work in this field relies on increased reliability in the classification of different early-type morphologies. The separation of elliptical from lenticular and early-type spirals (Sa) with full confidence will allow separate studies to be carried out that accurately define the dust properties associated with each morphology. The differences exhibited in properties such as dust-to-stellar mass ratio and (NUV-r) colour in Chapter 3 indicate one of two possibilities: either these results are true and ellipticals tend towards bimodal distributions in these parameter spaces whereas lenticulars have normal distributions, or the galaxies have not all been classified correctly and these results are just a product of these misclassifications.

There are several ways in which classifications can be improved to the point

where full distinction between ETGs can be made. These include the following:

(a) Improved resolution and sensitivity in optical imaging (perhaps with VST or Hubble).

(b) The identification of a proxy that unequivocally separates out every galaxy type, ensuring total completeness and no contamination. To this end, the proxy cannot be related to the activity or quiescence of galaxies.

(c) Using a combination of multi-wavelength data to characterise the properties of galaxies, particularly the separation of different components (work with MegaMorph is aiming for this).

(d) Galaxy Zoo is using a statistical classification approach, which with better imaging can be used to improve classification of galaxies up to higher redshift.

All of these possibilities may become viable in the near future.

The work in this thesis has shown that ETGs are not necessarily associated with the properties they were once thought to be. Some ETGs have been shown to present characteristics which are more similar to those of LTGs than their other counterparts. This means that in the future the definitions of early-type and late-type, as well as the overall Hubble scheme, may become redundant, and galaxies may be classified based on their intrinsic properties, rather than their morphological properties. This has already been suggested by (for example) Cappellari et al. (2011b), wherein galaxies are separated according to their rotation speeds. Further possibilities may involve classifying galaxies based on their position within a defined evolutionary sequence.

Comparisons of ETGs shown in this thesis have focussed on two different samples: dusty ETGs in dense environments in the very nearby Universe (i.e. the Virgo

Cluster), and even dustier ETGs in sparse environments at redshifts of ∼0.03. Differences in the properties of these two different samples have been identified, yet there are some strong gaps in our knowledge which need to be filled in the future.

The first gap which needs to be considered is what properties are exhibited by ETGs with FIR luminosities equivalent to those of Virgo ETGs, also in the very nearby Universe ($\lesssim 32$ Mpc), but in sparse environments. Would they fit in as extensions of the GAMA ETGs, due to the influence of environment? Or would they host similar properties to the Virgo ETGs, which would indicate that environment is not necessarily a dominant factor in the evolution of ETGs? This could be investigated in one of the following ways: either data that have already been collected for such galaxies could be used: ideally *Herschel* or other FIR fluxes need to be available for such targets. If these data do not exist, possibly targeted FIR studies of nearby massive ETGs could be run, using instruments such as the JCMT[1] or SPICA[2]. Follow-up optical, UV and MIR observations would also be required to carry out studies such as those in this thesis.

A second gap in the work done in this thesis is due to the lack of dwarf galaxies included in the samples. The dwarf galaxy (DG) population has been studied extensively within the confines of the Virgo Cluster; the seminal work by Binggeli et al. (1985) found ∼1000 dwarf galaxies within the ∼2000 Virgo Cluster members[3]. These DGs were further sub-divided by their respective morphologies: ∼90% were found to be dwarf ellipticals (dE), and the remainder were classified as either dwarf Irregulars (dIrr) or blue compact dwarfs (BCD).

The presence of such a large population of dE galaxies is of great importance to the study of galactic formation and evolution. There are multiple theories as

[1]James Clerk Maxwell Telescope: http://www.jach.hawaii.edu/JCMT/observing/facility.html.

[2]Space Infrared Telescope for Cosmology and Astrophysics (Goicoechea & Nakagawa 2011).

[3]The Coma Cluster has been shown to host a similar dwarf-to-giant ratio (Secker & Harris 1996).

to the origin of such galaxies: giant ellipticals form via a series of galaxy interactions (major and minor mergers) and similarly it is probable that dEs formed via a combination of ram-pressure stripping and galaxy harassment from dwarf late-type spirals (dS) and dIrrs (Gunn & Gott 1972; Moore et al. 1998). More controversially, BCDs have been suggested as gas-rich, star-forming progenitors of the dE population (Bothun et al. 1986; Drinkwater et al. 1996). However, differences in the intrinsic properties of giant and dwarf ellipticals (e.g. Boselli et al. 2005[4]), and even between sub-classes of dwarf ellipticals (e.g. Paudel et al. 2010[5]) indicate that the evolution of these dEs may be affected by other forces.

Although the H-ATLAS survey has mainly focussed on giant galaxies, nearby galaxies studied by the HRS and HeViCS consortia provide multiple opportunities to study diffuse dust emission properties of optically-selected DG samples. Such work has indicated dEs in Virgo have absolute dust masses of order $\sim 10^5\,M_\odot$ and temperatures $\sim 20\,K$, with dust-to-gas ratios within 10^{-3}-10^{-2} (de Looze et al. 2010; Grossi et al. 2010). However, it is likely that the DG population in dense environments suffers the same consequences as the massive ETG population in the same environment. In order to quantitatively state whether DGs in sparse environments are similar to their cluster counterparts or not, high resolution data for nearby DGs outside of the cluster environment is required. Furthermore, if we could accurately classify a sample of DGs extending out to redshift $z \sim 0.06$, a comparison with the properties of the GAMA/H-ATLAS ETGs could be made. FIR fluxes are once again required for such galaxies, which may currently not exist because of the H-ATLAS tendency for preferentially detecting more massive galaxies. A key motivation for such a study is to discover whether early-type DGs fit into the correlations found for the GAMA/H-ATLAS ETGs, or whether they

[4]UV colour-luminosity anti-correlation for giant early-type galaxies becomes a correlation for dwarfs.

[5]Paudel et al. (2010) find a bimodality in the ages of bright and faint dEs.

exhibit completely different correlations. This may provide insight into the role dEs play in galactic formation and evolution.

The GAMA/H-ATLAS samples shown in this thesis currently suffer from a lack of follow-up data; this is a consequence of their redshift. For example, there is no kinematic information available for any of these galaxies, which prevents a comparison with ATLAS^{3D} ETGs in the nearby Universe. The increasing popularity of integral field spectrographs (IFS) means that future kinematic studies with these galaxies may become a possibility. The AAT has recently acquired an IFS called SAMI (Croom et al. 2012) that will allow spatially-resolved spectroscopy for a large number of targets. If the GAMA team are able to get time with SAMI, the GAMA/H-ATLAS sample used in this thesis may also acquire additional data.

The presence of large quantities of dust in our ETGs implies at least similar quantities of molecular gas. Knowledge of the spatial extent of any molecular gas disks in these ETGs will allow us to look for signatures of merging in the gas, and by inference, dust morphology. Additionally, it will give us the ability to compare the dust disk extents calculated in Chapter 5 for the GAMA galaxies with imaging, as was done for the control Virgo sample. Such information will make it possible to better determine the origin of the dust and gas in these ETGs; an internal origin will be implied by a relaxed distribution aligned with the stars, whereas an external origin may be indicated by an irregular, offset or patchy dust distribution. We have used these arguments in a proposal recently submitted to ALMA[6] in order to acquire 12CO(2-1) line maps for ten galaxies in the GAMA/H-ATLAS sample. It is hoped that future proposals to map the full sample with ALMA will be successful.

The large quantities of dust that have been shown to reside in some ETGs

[6]The Atacama Large Millemetre Array: http://www.almaobservatory.org/

now need to be accounted for in cosmological simulations. The Millennium Simulation Project (Lemson & Virgo Consortium 2006) is one of the largest N-body simulations of ΛCDM run to date, with more than 10^{10} particles used to trace the evolution of matter within a cubic region of the Universe over 600 Mpc on each side. This simulation in particular has been used to study the evolution of elliptical galaxies at low redshift (e.g. De Lucia et al. 2006b), and by examining how simulated star formation histories, ages and metallicities of ellipticals vary with environment and stellar mass, has corroborated observational results that suggest downsizing. However, it is currently impossible to compare observational results of dusty ETGs with cosmological simulations, because dust (and often gas) is not accounted for in such models.

6.2 Concluding Remarks

Diffuse dust in early-type galaxies has been explored throughout this thesis in both a statistical sense and for some individual galaxies. The primary motivation for this study was the need to understand where this dust originates; although we cannot say that we have fully succeeded in constraining the origin of dust in ETGs, the work itself has led to some interesting conclusions about the galaxies this dust resides in.

Typical properties associated with the general ETG population were first assessed in Chapter 1, where intrinsic colour, shape and profile parameters were of particular interest. These were linked to the identification of proxies for morphology, which are meant to be utilised as a substitution for direct visual classification of morphology. This search for a morphological proxy that readily separates early- from late-type galaxies necessitated the study run in Chapter 2, where a trio of proxies: colour, concentration index and Sérsic index were examined in the hopes of using one to create an uncontaminated and complete sample of ETGs.

These proxies were tested out on three visually classified samples of galaxies (KS14, NA10 and GZ1). The need to be so rigorous with this testing was driven by the subjectivity of visual classifications themselves. Each of these samples had their own merits: KS14 contained the most (4,110) galaxies and was classified by three 'professional' classifiers, but these classifications were marred by not using spiral structure to differentiate between ETGs and LTGs. The GZ1 sample was also driven by good statistics: the sample had ∼2000 galaxies, extended up to a redshift range of z ∼0.1 and classifications were driven by citizen volunteers, resulting in multiple classifications per galaxy. The negative aspect of this sample is the reduced quality of classifications at certain redshifts and the lack of experience of the classifiers themselves. The final NA10 sample contains the smallest number of galaxies (∼350) with a similar redshift range to GZ1 - here the detailed classifications are done by a single 'professional' eyeballer. Overlapping samples exhibit some consistency between their classifications, where KS14 and NA10 samples agree on 65% of their ETG classifications, although there is only a 27% agreement between KS14 and GZ1.

Following a thorough investigation of the completeness and reliability of each proxy on each of these samples, it was concluded that it is not possible to use a morphological proxy to select ETGs with ≥80% reliability. Selecting ETGs based on red colour results in ≳35% contamination from LTGs, and samples selected using either concentration or Sérsic index still have contaminations of at least 30%. Therefore the decision was made to abandon the use of a morphological proxy for further work in this thesis, and instead adopt visual classifications of galaxies at low redshift.

The eyeballed sample created by Kelvin et al. (2014) from a set of GAMA galaxies with redshift range $0.013 \leq z \leq 0.06$ and magnitude limit $M_r \leq -17.4$ mag was chosen to form the samples used in this study. All galaxies classified as

elliptical or lenticular by at least two of the three classifiers were picked, and additional criteria were included to remove any galaxies whose classification may be uncertain. ETGs with emission lines were then examined on the BPT diagram and those galaxies with AGN signatures were removed. Counterparts to H-ATLAS data were then separated from non-counterparts to form two samples: *SubS* - 220 sub-mm detected ETGs, and *OptS* - 551 non-detected ETGs. This leads to detected numbers of ETGs of ∼29%, of which 33% are ellipticals.

The panchromatic properties of these sub-mm detected ETGs were then compared with those of the control sample to discover that, in an average sense, distributions of concentration and Sérsic index were lower, implying these galaxies are less centrally concentrated. This result may also be related to the discovery that dust tends to lower values of these properties (Pastrav et al. 2013). Additionally, the dusty ETGs were shown to be bluer in both UV-optical and optical colour and to have more extended effective radii. Their optical luminosities reveal they are brighter on average than the undetected ETGs, although this effect is dominated by the lower luminosity ETGs. Their environments were found to be sparser than those inhabited by non-detected ETGs; these combined results all hint towards the *SubS* containing a population of ETGs distinct from those in the *OptS*.

Modified Planck functions were fit to the PACS and SPIRE data for 188 ($\geq 3\sigma$ at 350 μm) of these *SubS* galaxies in order to estimate temperatures and masses of the cold dust occupying their interstellar media. Dust mass was shown to range from 8.1×10^5 to $3.5\times10^8\,M_\odot$, with a range of rest-frame temperatures from 9-30 K. These parameters are only marginally lower than those calculated for spiral galaxies, and are also consistent with results from previous *Herschel* ETG studies (e.g. Rowlands et al. 2012).

Strong trends were found between normalised dust mass and stellar mass for *SubS* ETGs, and these were strengthened by finding that ETGs with the bluest

NUV-r colour are the least massive, have the highest dust-to-stellar mass ratios and lowest Sérsic indices. These results are indicative of downsizing, or at least show that ellipticals may be grouped into two sets: faint, blue, low mass, relatively dusty ellipticals and bright, red, massive ellipticals with lower dust-to-stellar mass ratio. This led to the conclusion that two different populations of ellipticals, or at least two different age ranges, are being studied.

These results provided the incentive for our next study: a comparison of sub-mm detected ETGs from the *SubS* with sub-mm detected ETGs from local surveys in the Virgo Cluster. We chose to compare with a HeViCS sample (di Serego Alighieri et al. 2013) due to the statistically significant number of ETGs available here. Both samples had nearest neighbour densities calculated for their galaxies in a consistent manner, which showed that H-ATLAS ETGs occupy much sparser environments than HeViCS ETGs. The modBB fits to each set of galaxies were made consistent to the same model, and an examination of the dust masses revealed that H-ATLAS ETGs have higher dust-to-stellar mass ratios on average than HeViCS ETGs.

Panchromatic SEDs were fit to the UV-sub-mm data using the MAGPHYS energy balance code. This provided a range of parameters calculated based on likelihood probability distributions. Dust masses and temperatures were consequently re-examined to find that it is difficult to accurately constrain the cold dust temperature, but dust mass does not vary strongly between fitting routines.

Correlations were found between dust and stellar mass for the two samples, and a strong anti-correlation was detected between dust-to-stellar mass ratio overall; this was found to be a function of environment.

Specific star formation rates were also examined for these samples, revealing very little ongoing star formation in HeViCS ETGs. However H-ATLAS ETGs on average tend to have high sSFRs. By splitting H-ATLAS ETGs into massive and

non-massive subsets, it was found that the former exhibit a similar mean sSFR as the HeViCS ETGs, whereas the non-massive subset have a factor of $\sim$1.5 dex higher mean sSFR. It should be noted that it is unlikely that galactic evolution can be seen over such a small redshift range; nevertheless these results do indicate different properties for different ETG stellar masses. Further checks were carried out by comparing formation timescales of the two main samples, revealing that HeViCS ETGs formed longer ago than H-ATLAS ETGs. All of these results are consistent with downsizing, whereby H-ATLAS ETGs formed later on, or at least have more extended star formation histories than HeViCS ETGs.

The final Chapter of this thesis gives an account of the study carried out with smaller samples of ETGs: three Virgo lenticulars which form the control sample, and four H-ATLAS/GAMA ellipticals which form the main sample. The aim of this experiment was to investigate the dust distribution within these galaxies, under the assumption that the diffuse dust is optically thin. Estimates of the radiation field energy density were made based on SED fits to the FIR and sub-mm data. Different assumptions were made here to calculate energy densities based on the dust being heated by different mechanisms: in the first case dust is heated only by the old stellar population, with some excess MIR emission caused by circumstellar dust around horizontal branch stars. In the second instance, the dust is heated both by an old and young stellar population, with some ongoing star formation causing the MIR excess.

Optical energy densities as a function of galactic radius are also estimated for these galaxies by the deconvolution of RT models with input Sérsic index and optical depth. These modelled energy densities are scaled to the galaxies themselves, allowing the matching of optical and long-wavelength energy densities. This allowed estimates for the extent of a dust disk to be made.

Based on these tests, the following conclusions were made. Consistent solutions

for two of the three Virgo galaxies were found, indicating that their dust heating is well described as being dominated by the old stellar population, but excess heating may be dominated either by asymptotic giant branch stars or low levels of star formation. The GAMA ETGs were not well described as having the old stellar population heating the dust, but two of the four galaxies have consistent solutions found for a dust disk (with extents of 0.5-0.6 of galactic effective radius) being heated by both young and intermediate age stellar populations.

Further work is currently being undertaken in this area to consider whether the GAMA ETGs in particular can be modelled with an optically thick solution (Agius et al. in prep). However, the study undertaken here has been considered successful for $\gtrsim$0.5 of the ETGs tested, with realistic dust extents found for these galaxies. Additionally, the dust extents for the Virgo ETGs are similar to the CO disk extents reported by Davis et al. (2013b).

The results from this thesis have provided evidence that dusty ETGs are not as rare as previously considered, and in fact have particular structural properties that differ from the classical view of ETGs. Our results are not the first of this kind, but statistically reinforce those from several simultaneous studies being carried out on ETGs in the nearby Universe (see ETG studies with ATLAS^{3D}, KINGFISH, Galaxy Zoo and many others). In particular, observational results for these dusty ETGs agree with current theories of galactic evolution: that dissipative minor merging (e.g. Kaviraj et al. 2009) is likely to be the primary mechanism advancing the formation of dusty early-type galaxies.

Bibliography

Abazajian, K. N., Adelman-McCarthy, J. K., Agüeros, M. A., et al. 2009, *Astrophys. J. Supple.*, 182, 543

Abraham, R. G., Valdes, F., Yee, H. K. C., & van den Bergh, S. 1994, *Astrophys. J.*, 432, 75

Abraham, R. G., van den Bergh, S., Glazebrook, K., et al. 1996, *Astrophys. J. Supple.*, 107, 1

Agius, N. K., di Serego Alighieri, S., Viaene, S., Baes, M., & Sansom, A. E. in prep

Agius, N. K., Sansom, A. E., Popescu, C. C., et al. 2013, *Mon. Not. Roy. Astron. Soc.*, 431, 1929

Alatalo, K., Davis, T. A., Bureau, M., et al. 2013, *Mon. Not. Roy. Astron. Soc.*, 432, 1796

Amblard, A., Cooray, A., Serra, P., et al. 2010, *Astron. Astrophys.*, 518, L9

Amblard, A., Riguccini, L., Temi, P., et al. 2014, *Astrophys. J.*, 783, 135

Aragón-Salamanca, A., Bedregal, A. G., & Merrifield, M. R. 2006, *Astron. Astrophys.*, 458, 101

Auld, R., Bianchi, S., Smith, M. W. L., et al. 2013, *Mon. Not. Roy. Astron. Soc.*, 428, 1880

Baade, W. & Gaposchkin, C. H. P. 1963, Evolution of stars and galaxies.

Baes, M., Fritz, J., Gadotti, D. A., et al. 2010, *Astron. Astrophys.*, 518, L39

Baggett, W. E., Baggett, S. M., & Anderson, K. S. J. 1998, *Astron. J.*, 116, 1626

Baldry, I., Driver, S. P., Robotham, A., et al. in prep

Baldry, I. K., Balogh, M. L., Bower, R., Glazebrook, K., & Nichol, R. C. 2004, in American Institute of Physics Conference Series, Vol. 743, The New Cosmology: Conference on Strings and Cosmology, ed. R. E. Allen, D. V. Nanopoulos, & C. N. Pope, 106–119

Baldry, I. K., Robotham, A. S. G., Hill, D. T., et al. 2010, *Mon. Not. Roy. Astron. Soc.*, 404, 86

Baldwin, J. A., Phillips, M. M., & Terlevich, R. 1981, *Pub. Astron. Soc. Pac.*, 93, 5

Balogh, M., Eke, V., Miller, C., et al. 2004, *Mon. Not. Roy. Astron. Soc.*, 348, 1355

Balogh, M. L., Navarro, J. F., & Morris, S. L. 2000, *Astrophys. J.*, 540, 113

Barlow, M. J. 1978a, *Mon. Not. Roy. Astron. Soc.*, 183, 397

Barlow, M. J. 1978b, *Mon. Not. Roy. Astron. Soc.*, 183, 417

Barlow, M. J. 1978c, *Mon. Not. Roy. Astron. Soc.*, 183, 367

Baum, W. A. 1959, *Pub. Astron. Soc. Pac.*, 71, 106

Bayet, E., Bureau, M., Davis, T. A., et al. 2013, *Mon. Not. Roy. Astron. Soc.*, 432, 1742

Becker, R. H., White, R. L., & Helfand, D. J. 1994, in *Astronomical Society of the Pacific Conference Series*, Vol. 61, Astronomical Data Analysis Software and Systems III, ed. D. R. Crabtree, R. J. Hanisch, & J. Barnes, 165

Bell, E. F., McIntosh, D. H., Katz, N., & Weinberg, M. D. 2003, *Astrophys. J. Supple.*, 149, 289

Bell, E. F., Wolf, C., Meisenheimer, K., et al. 2004, *Astrophys. J.*, 608, 752

Bender, R., Doebereiner, S., & Moellenhoff, C. 1987, *Astron. Astrophys.*, 177, L53

Bender, R., Saglia, R. P., & Gerhard, O. E. 1994, *Mon. Not. Roy. Astron. Soc.*, 269, 785

Bender, R., Surma, P., Doebereiner, S., Moellenhoff, C., & Madejsky, R. 1989, *Astron. Astrophys.*, 217, 35

Bernardi, M., Meert, A., Sheth, R. K., et al. 2013, *Mon. Not. Roy. Astron. Soc.*

Bernardi, M., Shankar, F., Hyde, J. B., et al. 2010, *Mon. Not. Roy. Astron. Soc.*, 404, 2087

Bianchi, S. 2013, *Astron. Astrophys.*, 552, A89

Bianchi, S., Ferrara, A., Davies, J. I., & Alton, P. B. 2000, *Mon. Not. Roy. Astron. Soc.*, 311, 601

Binggeli, B., Popescu, C. C., & Tammann, G. A. 1993, *Astron. Astrophys. Suppl.*, 98, 275

Binggeli, B., Sandage, A., & Tammann, G. A. 1985, *Astron. J.*, 90, 1681

Binney, J. 1976, *Mon. Not. Roy. Astron. Soc.*, 177, 19

Blain, A. W., Barnard, V. E., & Chapman, S. C. 2003, *Mon. Not. Roy. Astron. Soc.*, 338, 733

Blanton, M. R., Dalcanton, J., Eisenstein, D., et al. 2001, *Astron. J.*, 121, 2358

Blanton, M. R., Eisenstein, D., Hogg, D. W., Schlegel, D. J., & Brinkmann, J. 2005, *Astrophys. J.*, 629, 143

Blanton, M. R., Hogg, D. W., Bahcall, N. A., et al. 2003, *Astrophys. J.*, 594, 186

Blanton, M. R. & Roweis, S. 2007, *Astron. J.*, 133, 734

Boroson, B., Kim, D.-W., & Fabbiano, G. 2011, *Astrophys. J.*, 729, 12

Boselli, A. 2012, in SF2A-2012: Proceedings of the Annual meeting of the French Society of Astronomy and Astrophysics, ed. S. Boissier, P. de Laverny, N. Nardetto, R. Samadi, D. Valls-Gabaud, & H. Wozniak, 435–441

Boselli, A., Boissier, S., Heinis, S., et al. 2011, *Astron. Astrophys.*, 528, A107

Boselli, A., Ciesla, L., Buat, V., et al. 2010a, *Astron. Astrophys.*, 518, L61

Boselli, A., Cortese, L., Deharveng, J. M., et al. 2005, *Astrophys. J. Letters*, 629, L29

Boselli, A., Eales, S., Cortese, L., et al. 2010b, *Pub. Astron. Soc. Pac.*, 122, 261

Boselli, A. & Gavazzi, G. 2006, *Pub. Astron. Soc. Pac.*, 118, 517

Bothun, G. D., Mould, J. R., Caldwell, N., & MacGillivray, H. T. 1986, *Astron. J.*, 92, 1007

Boulanger, F. & Perault, M. 1988, *Astrophys. J.*, 330, 964

Bourne, N., Maddox, S. J., Dunne, L., et al. 2012, *Mon. Not. Roy. Astron. Soc.*, 421, 3027

Bower, R. G., Lucey, J. R., & Ellis, R. S. 1992, *Mon. Not. Roy. Astron. Soc.*, 254, 601

Bregman, J. N., Hogg, D. E., & Roberts, M. S. 1992, *Astrophys. J.*, 387, 484

Bregman, J. N., Snider, B. A., Grego, L., & Cox, C. V. 1998, *Astrophys. J.*, 499, 670

Bressan, A., Chiosi, C., & Fagotto, F. 1994, *Astrophys. J. Supple.*, 94, 63

Brinchmann, J., Charlot, S., White, S. D. M., et al. 2004, *Mon. Not. Roy. Astron. Soc.*, 351, 1151

Brough, S., Croom, S., Sharp, R., et al. 2013, *Mon. Not. Roy. Astron. Soc.*, 435, 2903

Bruzual, G. & Charlot, S. 2003, *Mon. Not. Roy. Astron. Soc.*, 344, 1000

Burgdorf, M., Ashby, M. L. N., & Williams, R. 2007, *Astrophys. J.*, 668, 918

Buson, L. M., Sadler, E. M., Zeilinger, W. W., et al. 1993, *Astron. Astrophys.*, 280, 409

Butcher, H. & Oemler, Jr., A. 1984, *Astrophys. J.*, 285, 426

Byrd, G. & Valtonen, M. 1990, *Astrophys. J.*, 350, 89

Caldwell, N., Rose, J. A., Sharples, R. M., Ellis, R. S., & Bower, R. G. 1993, *Astron. J.*, 106, 473

Cappellari, M., Emsellem, E., Krajnović, D., et al. 2011a, *Mon. Not. Roy. Astron. Soc.*, 413, 813

Cappellari, M., Emsellem, E., Krajnović, D., et al. 2011b, *Mon. Not. Roy. Astron. Soc.*, 416, 1680

Cassata, P., Guzzo, L., Franceschini, A., et al. 2007, *Astrophys. J. Supple.*, 172, 270

Chabrier, G. 2003, *Pub. Astron. Soc. Pac.*, 115, 763

Charlot, S. & Fall, S. M. 2000, *Astrophys. J.*, 539, 718

Choi, Y.-Y., Park, C., & Vogeley, M. S. 2007, *Astrophys. J.*, 658, 884

Clemens, M. S., Jones, A. P., Bressan, A., et al. 2010, *Astron. Astrophys.*, 518, L50

Cluver, M. E., Jarrett, T. H., Hopkins, A. M., et al. 2014, *Astrophys. J.*, 782, 90

Combes, F., Young, L. M., & Bureau, M. 2007, *Mon. Not. Roy. Astron. Soc.*, 377, 1795

Conselice, C. J. 2006, *Mon. Not. Roy. Astron. Soc.*, 373, 1389

Conselice, C. J., Blackburne, J. A., & Papovich, C. 2005, *Astrophys. J.*, 620, 564

Cooper, M. C., Newman, J. A., Coil, A. L., et al. 2007, *Mon. Not. Roy. Astron. Soc.*, 376, 1445

Cortese, L., Bendo, G. J., Boselli, A., et al. 2010a, *Astron. Astrophys.*, 518, L63

Cortese, L., Boissier, S., Boselli, A., et al. 2012a, *Astron. Astrophys.*, 544, A101

Cortese, L., Ciesla, L., Boselli, A., et al. 2012b, *Astron. Astrophys.*, 540, A52

Cortese, L., Davies, J. I., Pohlen, M., et al. 2010b, *Astron. Astrophys.*, 518, L49

Cowie, L. L., Songaila, A., Hu, E. M., & Cohen, J. G. 1996, *Astron. J.*, 112, 839

Croom, S. M., Lawrence, J. S., Bland-Hawthorn, J., et al. 2012, *Mon. Not. Roy. Astron. Soc.*, 421, 872

da Cunha, E., Charlot, S., & Elbaz, D. 2008, *Mon. Not. Roy. Astron. Soc.*, 388, 1595

Dale, D. A., Aniano, G., Engelbracht, C. W., et al. 2012, *Astrophys. J.*, 745, 95

Dariush, A., Cortese, L., Eales, S., et al. 2011, *Mon. Not. Roy. Astron. Soc.*, 418, 64

Davies, J. I., Baes, M., Bendo, G. J., et al. 2010, *Astron. Astrophys.*, 518, L48

Davies, J. I., Bianchi, S., Baes, M., et al. 2014, *Mon. Not. Roy. Astron. Soc.*, 438, 1922

Davies, J. I., Bianchi, S., Cortese, L., et al. 2012, *Mon. Not. Roy. Astron. Soc.*, 419, 3505

Davies, R. L., Efstathiou, G., Fall, S. M., Illingworth, G., & Schechter, P. L. 1983, *Astrophys. J.*, 266, 41

Davis, T. A., Alatalo, K., Bureau, M., et al. 2013a, *Mon. Not. Roy. Astron. Soc.*, 429, 534

Davis, T. A., Alatalo, K., Bureau, M., et al. 2013b, *Mon. Not. Roy. Astron. Soc.*, 429, 534

de Jong, T., Klein, U., Wielebinski, R., & Wunderlich, E. 1985, *Astron. Astrophys.*, 147, L6

de Looze, I., Baes, M., Zibetti, S., et al. 2010, *Astron. Astrophys.*, 518, L54

De Lucia, G., Springel, V., White, S. D. M., Croton, D., & Kauffmann, G. 2006a, *Mon. Not. Roy. Astron. Soc.*, 366, 499

De Lucia, G., Springel, V., White, S. D. M., Croton, D., & Kauffmann, G. 2006b, *Mon. Not. Roy. Astron. Soc.*, 366, 499

de Vaucouleurs, G. 1961a, *Astrophys. J. Supple.*, 5, 233

de Vaucouleurs, G. 1961b, *Astrophys. J. Supple.*, 6, 213

de Vaucouleurs, G. 1963, *Astrophys. J. Supple.*, 8, 31

de Vaucouleurs, G., de Vaucouleurs, A., Corwin, Jr., H. G., et al. 1991, Third Reference Catalogue of Bright Galaxies. Volume I: Explanations and references. Volume II: Data for galaxies between 0^h and 12^h. Volume III: Data for galaxies between 12^h and 24^h.

Del Burgo, C., Carter, D., & Sikkema, G. 2008, *Astron. Astrophys.*, 477, 105

Di Matteo, P., Pipino, A., Lehnert, M. D., Combes, F., & Semelin, B. 2009, *Astron. Astrophys.*, 499, 427

di Serego Alighieri, S. 2013, in IAU Symposium, Vol. 295, IAU Symposium, ed. D. Thomas, A. Pasquali, & I. Ferreras, 332–335

di Serego Alighieri, S., Bianchi, S., Pappalardo, C., et al. 2013, *Astron. Astrophys.*, 552, A8

di Serego Alighieri, S., Gavazzi, G., Giovanardi, C., et al. 2007, *Astron. Astrophys.*, 474, 851

D'Onofrio, M., Valentinuzzi, T., Fasano, G., et al. 2011, *Astrophys. J. Letters*, 727, L6

Draine, B. T. & Li, A. 2007, *Astrophys. J.*, 657, 810

Draine, B. T. & Salpeter, E. E. 1979a, *Astrophys. J.*, 231, 77

Draine, B. T. & Salpeter, E. E. 1979b, *Astrophys. J.*, 231, 77

Dressler, A. 1980, *Astrophys. J.*, 236, 351

Dressler, A., Oemler, Jr., A., Couch, W. J., et al. 1997, *Astrophys. J.*, 490, 577

Drinkwater, M. J., Currie, M. J., Young, C. K., Hardy, E., & Yearsley, J. M. 1996, *Mon. Not. Roy. Astron. Soc.*, 279, 595

Driver, S. P., Allen, P. D., Graham, A. W., et al. 2006, *Mon. Not. Roy. Astron. Soc.*, 368, 414

Driver, S. P., Hill, D. T., Kelvin, L. S., et al. 2011, *Mon. Not. Roy. Astron. Soc.*, 413, 971

Driver, S. P., Norberg, P., Baldry, I. K., et al. 2009, *Astronomy and Geophysics*, 50, 12

Driver, S. P., Popescu, C. C., Tuffs, R. J., et al. 2007, *Mon. Not. Roy. Astron. Soc.*, 379, 1022

Drory, N., Bender, R., Feulner, G., et al. 2004, *Astrophys. J.*, 608, 742

Dunne, L., Eales, S., Edmunds, M., et al. 2000, *Mon. Not. Roy. Astron. Soc.*, 315, 115

Dunne, L. & Eales, S. A. 2001, *Mon. Not. Roy. Astron. Soc.*, 327, 697

Dunne, L., Gomez, H. L., da Cunha, E., et al. 2011, *Mon. Not. Roy. Astron. Soc.*, 417, 1510

Dwek, E. 1986, *Astrophys. J.*, 302, 363

Dwek, E. 1998, *Astrophys. J.*, 501, 643

Dwek, E. & Scalo, J. M. 1980, *Astrophys. J.*, 239, 193

Dye, S., Dunne, L., Eales, S., et al. 2010, *Astron. Astrophys.*, 518, L10

Eales, S., Dunne, L., Clements, D., et al. 2010, *Pub. Astron. Soc. Pac.*, 122, 499

Ellis, S. C. & O'Sullivan, E. 2006, *Mon. Not. Roy. Astron. Soc.*, 367, 627

Elmegreen, B. G., Elmegreen, D. M., & Hirst, A. C. 2004, *Astrophys. J.*, 612, 191

Emsellem, E., Cappellari, M., Krajnović, D., et al. 2011, *Mon. Not. Roy. Astron. Soc.*, 414, 888

Emsellem, E., Cappellari, M., Krajnović, D., et al. 2007, *Mon. Not. Roy. Astron. Soc.*, 379, 401

Faber, S. M. 1973, *Astrophys. J.*, 179, 731

Faber, S. M. & Jackson, R. E. 1976, *Astrophys. J.*, 204, 668

Farouki, R. & Shapiro, S. L. 1981, *Astrophys. J.*, 243, 32

Ferrarese, L., Côté, P., Cuillandre, J.-C., et al. 2012, *Astrophys. J. Supple.*, 200, 4

Ferrarese, L. & Ford, H. 2005, *Space Sci. Rev.*, 116, 523

Ferreras, I., Charlot, S., & Silk, J. 1999, *Astrophys. J.*, 521, 81

Firmani, C., Avila-Reese, V., & Rodríguez-Puebla, A. 2010, *Mon. Not. Roy. Astron. Soc.*, 404, 1100

Fischera, J. & Dopita, M. A. 2008, *Astrophys. J. Supple.*, 176, 164

Fisher, D. B. & Drory, N. 2008, *Astron. J.*, 136, 773

Forman, W., Schwarz, J., Jones, C., Liller, W., & Fabian, A. C. 1979, *Astrophys. J. Letters*, 234, L27

Foster, C., Hopkins, A. M., Gunawardhana, M., et al. 2012, *Astron. Astrophys.*, 547, A79

Franx, M. & Illingworth, G. 1990, *Astrophys. J. Letters*, 359, L41

Franzetti, P., Scodeggio, M., Garilli, B., et al. 2007, *Astron. Astrophys.*, 465, 711

Galametz, M., Albrecht, M., Kennicutt, R., et al. 2011, in SF2A-2011: Proceedings of the Annual meeting of the French Society of Astronomy and Astrophysics, ed. G. Alecian, K. Belkacem, R. Samadi, & D. Valls-Gabaud, 119–123

Gallagher, III, J. S. 1972, *Astron. J.*, 77, 568

Gallazzi, A., Charlot, S., Brinchmann, J., & White, S. D. M. 2006, *Mon. Not. Roy. Astron. Soc.*, 370, 1106

Gavazzi, G., Boselli, A., Donati, A., Franzetti, P., & Scodeggio, M. 2003, *Astron. Astrophys.*, 400, 451

Gillett, F. C., Forrest, W. J., Merrill, K. M., Soifer, B. T., & Capps, R. W. 1975a, *Astrophys. J.*, 200, 609

Gillett, F. C., Kleinmann, D. E., Wright, E. L., & Capps, R. W. 1975b, *Astrophys. J. Letters*, 198, L65

Gladders, M. D., Lopez-Cruz, O., Yee, H. K. C., & Kodama, T. 1998, *Astrophys. J.*, 501, 571

Gnedin, O. Y. 2003, *Astrophys. J.*, 589, 752

Goicoechea, J. R. & Nakagawa, T. 2011, in EAS Publications Series, Vol. 52, EAS Publications Series, ed. M. Röllig, R. Simon, V. Ossenkopf, & J. Stutzki, 253–258

Gomez, H. L., Baes, M., Cortese, L., et al. 2010, *Astron. Astrophys.*, 518, L45

Gómez, P. L., Nichol, R. C., Miller, C. J., et al. 2003, *Astrophys. J.*, 584, 210

González-Nuevo, J., Lapi, A., Fleuren, S., et al. 2012, *Astrophys. J.*, 749, 65

Goudfrooij, P. 1999, in *Astronomical Society of the Pacific Conference Series*, Vol. 163, Star Formation in Early Type Galaxies, ed. P. Carral & J. Cepa, 55

Goudfrooij, P. & de Jong, T. 1995, *Astron. Astrophys.*, 298, 784

Goudfrooij, P., de Jong, T., Hansen, L., & Norgaard-Nielsen, H. U. 1994, *Mon. Not. Roy. Astron. Soc.*, 271, 833

Greggio, L. & Renzini, A. 1990, *Astrophys. J.*, 364, 35

Griffin, M. J., Abergel, A., Abreu, A., et al. 2010, *Astron. Astrophys.*, 518, L3

Grootes, M. W., Tuffs, R. J., Popescu, C. C., et al. 2013, *Astrophys. J.*, 766, 59

Grossi, M., Hunt, L. K., Madden, S., et al. 2010, *Astron. Astrophys.*, 518, L52

Guhathakurta, P. & Draine, B. T. 1989, *Astrophys. J.*, 345, 230

Gunn, J. E. & Gott, III, J. R. 1972, *Astrophys. J.*, 176, 1

Gutermuth, R. A., Megeath, S. T., Pipher, J. L., et al. 2005, *Astrophys. J.*, 632, 397

Haines, C. P., Gargiulo, A., & Merluzzi, P. 2008, *Mon. Not. Roy. Astron. Soc.*, 385, 1201

Hauser, M. G. & Dwek, E. 2001, *Ann. Rev. Astron, Astrophys.*, 39, 249

Häußler, B., Bamford, S. P., Vika, M., et al. 2013, *Mon. Not. Roy. Astron. Soc.*, 430, 330

Helou, G., Soifer, B. T., & Rowan-Robinson, M. 1985, *Astrophys. J. Letters*, 298, L7

Henkel, C. & Wiklind, T. 1997, *Space Sci. Rev.*, 81, 1

Hill, D. T., Kelvin, L. S., Driver, S. P., et al. 2011, *Mon. Not. Roy. Astron. Soc.*, 412, 765

Hogg, D. W. 1999, ArXiv Astrophysics e-prints

Holmberg, E. 1958, Meddelanden fran Lunds Astronomiska Observatorium Serie II, 136, 1

Hopkins, A. M., Driver, S. P., Brough, S., et al. 2013, *Mon. Not. Roy. Astron. Soc.*, 430, 2047

Hopkins, P. F., Cox, T. J., Younger, J. D., & Hernquist, L. 2009, *Astrophys. J.*, 691, 1168

Horch, E., Demarque, P., & Pinsonneault, M. 1992, *Astrophys. J. Letters*, 388, L53

Hubble, E. P. 1936, Realm of the Nebulae

Huertas-Company, M., Aguerri, J. A. L., Bernardi, M., Mei, S., & Sánchez Almeida, J. 2011, *Astron. Astrophys.*, 525, A157+

Huertas-Company, M., Mei, S., Shankar, F., et al. 2013, *Mon. Not. Roy. Astron. Soc.*, 428, 1715

Ibar, E., Ivison, R. J., Cava, A., et al. 2010, *Mon. Not. Roy. Astron. Soc.*, 409, 38

Illingworth, G. 1977, *Astrophys. J. Letters*, 218, L43

Issa, M. R., MacLaren, I., & Wolfendale, A. W. 1990, *Astron. Astrophys.*, 236, 237

Jaffe, W., Meisenheimer, K., Röttgering, H. J. A., et al. 2004, *Nature*, 429, 47

Jones, A. P. & Nuth, J. A. 2011, *Astron. Astrophys.*, 530, A44

Jones, A. P., Tielens, A. G. G. M., & Hollenbach, D. J. 1996, *Astrophys. J.*, 469, 740

Jones, A. P., Tielens, A. G. G. M., Hollenbach, D. J., & McKee, C. F. 1994, *Astrophys. J.*, 433, 797

Kauffmann, G., Heckman, T. M., Tremonti, C., et al. 2003a, *Mon. Not. Roy. Astron. Soc.*, 346, 1055

Kauffmann, G., Heckman, T. M., White, S. D. M., et al. 2003b, *Mon. Not. Roy. Astron. Soc.*, 341, 54

Kauffmann, G., White, S. D. M., Heckman, T. M., et al. 2004, *Mon. Not. Roy. Astron. Soc.*, 353, 713

Kaviraj, S. 2008, Modern Physics Letters A, 23, 153

Kaviraj, S. 2010, *Mon. Not. Roy. Astron. Soc.*, 406, 382

Kaviraj, S., Peirani, S., Khochfar, S., Silk, J., & Kay, S. 2009, *Mon. Not. Roy. Astron. Soc.*, 394, 1713

Kaviraj, S., Rey, S.-C., Rich, R. M., Yoon, S.-J., & Yi, S. K. 2007a, *Mon. Not. Roy. Astron. Soc.*, 381, L74

Kaviraj, S., Rowlands, K., Alpaslan, M., et al. 2013, *Mon. Not. Roy. Astron. Soc.*, 435, 1463

Kaviraj, S., Schawinski, K., Devriendt, J. E. G., et al. 2007b, *Astrophys. J. Supple.*, 173, 619

Kaviraj, S., Tan, K.-M., Ellis, R. S., & Silk, J. 2011, *Mon. Not. Roy. Astron. Soc.*, 411, 2148

Kaviraj, S., Ting, Y.-S., Bureau, M., et al. 2012, *Mon. Not. Roy. Astron. Soc.*, 423, 49

Kawata, D. & Gibson, B. K. 2003, *Mon. Not. Roy. Astron. Soc.*, 340, 908

Kelm, B., Focardi, P., & Sorrentino, G. 2005, *Astron. Astrophys.*, 442, 117

Kelvin, L. S., Driver, S. P., Robotham, A. S. G., et al. 2014, *Mon. Not. Roy. Astron. Soc.*, 439, 1245

Kelvin, L. S., Driver, S. P., Robotham, A. S. G., et al. 2012, *Mon. Not. Roy. Astron. Soc.*, 421, 1007

Kewley, L. J., Heisler, C. A., Dopita, M. A., & Lumsden, S. 2001, *Astrophys. J. Supple.*, 132, 37

Kim, D.-W., Fabbiano, G., & Trinchieri, G. 1992, *Astrophys. J.*, 393, 134

Klein, U., Wielebinski, R., & Morsi, H. W. 1988, *Astron. Astrophys.*, 190, 41

Knapp, G. R. 1999, in *Astronomical Society of the Pacific Conference Series*, Vol. 163, Star Formation in Early Type Galaxies, ed. P. Carral & J. Cepa, 119

Knapp, G. R., Guhathakurta, P., Kim, D.-W., & Jura, M. A. 1989, *Astrophys. J. Supple.*, 70, 329

Kobayashi, C. 2004, *Mon. Not. Roy. Astron. Soc.*, 347, 740

Kobulnicky, H. A. & Kewley, L. J. 2004, *Astrophys. J.*, 617, 240

Kodama, T. & Arimoto, N. 1997, *Astron. Astrophys.*, 320, 41

Kodama, T., Arimoto, N., Barger, A. J., & Arag'on-Salamanca, A. 1998, *Astron. Astrophys.*, 334, 99

Kodama, T., Bower, R. G., & Bell, E. F. 1999, *Mon. Not. Roy. Astron. Soc.*, 306, 561

Kodama, T., Smail, I., Nakata, F., Okamura, S., & Bower, R. G. 2001, *Astrophys. J. Letters*, 562, L9

Kodama, T., Yamada, T., Akiyama, M., et al. 2004, *Mon. Not. Roy. Astron. Soc.*, 350, 1005

Kormendy, J. & Bender, R. 1996, *Astrophys. J. Letters*, 464, L119

Kormendy, J. & Bender, R. 2012, *Astrophys. J. Supple.*, 198, 2

Kormendy, J. & Djorgovski, S. 1989, *Ann. Rev. Astron, Astrophys.*, 27, 235

Kormendy, J., Fisher, D. B., Cornell, M. E., & Bender, R. 2009, *Astrophys. J. Supple.*, 182, 216

Kraft, R. P., Forman, W. R., Jones, C., et al. 2011, *Astrophys. J.*, 727, 41

Krajnović, D., Emsellem, E., Cappellari, M., et al. 2011, *Mon. Not. Roy. Astron. Soc.*, 414, 2923

Kuchinski, L. E., Terndrup, D. M., Gordon, K. D., & Witt, A. N. 1998, *Astron. J.*, 115, 1438

Kuntschner, H. 2000, *Mon. Not. Roy. Astron. Soc.*, 315, 184

Kuntschner, H., Emsellem, E., Bacon, R., et al. 2010, *Mon. Not. Roy. Astron. Soc.*, 408, 97

Kylafis, N. D. & Bahcall, J. N. 1987, *Astrophys. J.*, 317, 637

Lackner, C. N. & Gunn, J. E. 2012, *Mon. Not. Roy. Astron. Soc.*, 421, 2277

Larson, R. B. 1974, *Mon. Not. Roy. Astron. Soc.*, 166, 585

Lee, G.-H., Park, C., Lee, M. G., & Choi, Y.-Y. 2012, *Astrophys. J.*, 745, 125

Leeuw, L. L., Sansom, A. E., Robson, E. I., Haas, M., & Kuno, N. 2004, *Astrophys. J.*, 612, 837

Lemson, G. & Virgo Consortium, t. 2006, ArXiv Astrophysics e-prints

Lintott, C., Schawinski, K., Bamford, S., et al. 2011, *Mon. Not. Roy. Astron. Soc.*, 410, 166

Lintott, C. J., Schawinski, K., Slosar, A., et al. 2008, *Mon. Not. Roy. Astron. Soc.*, 389, 1179

Lotz, J. M., Primack, J., & Madau, P. 2004, *Astron. J.*, 128, 163

Lucero, D. M., Young, L. M., & van Gorkom, J. H. 2005, *Astron. J.*, 129, 647

MacArthur, L. A., Courteau, S., & Holtzman, J. A. 2003, *Astrophys. J.*, 582, 689

Macchetto, F., Pastoriza, M., Caon, N., et al. 1996, *Astron. Astrophys. Suppl.*, 120, 463

Madden, S. C., Galliano, F., Jones, A. P., & Sauvage, M. 2006, *Astron. Astrophys.*, 446, 877

Martin, D. C., Fanson, J., Schiminovich, D., et al. 2005, *Astrophys. J. Letters*, 619, L1

Mateus, A., Sodré, L., Cid Fernandes, R., et al. 2006, *Mon. Not. Roy. Astron. Soc.*, 370, 721

Mathis, J. S., Mezger, P. G., & Panagia, N. 1983, *Astron. Astrophys.*, 128, 212

McDonald, M., Courteau, S., Tully, R. B., & Roediger, J. 2011, *Mon. Not. Roy. Astron. Soc.*, 414, 2055

Mei, S., Blakeslee, J. P., Côté, P., et al. 2007, *Astrophys. J.*, 655, 144

Merrill, K. M. & Stein, W. A. 1976, *Pub. Astron. Soc. Pac.*, 88, 285

Moore, B., Katz, N., Lake, G., Dressler, A., & Oemler, A. 1996, *Nature*, 379, 613

Moore, B., Lake, G., & Katz, N. 1998, *Astrophys. J.*, 495, 139

Morgan, W. W. 1958, *Pub. Astron. Soc. Pac.*, 70, 364

Morganti, R., de Zeeuw, P. T., Oosterloo, T. A., et al. 2006, *Mon. Not. Roy. Astron. Soc.*, 371, 157

Mortlock, A., Conselice, C. J., Hartley, W. G., et al. 2013, *Mon. Not. Roy. Astron. Soc.*, 433, 1185

Moss, C. & Whittle, M. 1993, *Astrophys. J. Letters*, 407, L17

Mould, J. R., Huchra, J. P., Freedman, W. L., et al. 2000, *Astrophys. J.*, 529, 786

Mulchaey, J. S. & Jeltema, T. E. 2010, *Astrophys. J. Letters*, 715, L1

Murakami, I. & Babul, A. 1999, *Mon. Not. Roy. Astron. Soc.*, 309, 161

Naab, T., Burkert, A., & Hernquist, L. 1999, *Astrophys. J. Letters*, 523, L133

Naab, T., Jesseit, R., & Burkert, A. 2006, *Mon. Not. Roy. Astron. Soc.*, 372, 839

Naab, T., Johansson, P. H., & Ostriker, J. P. 2009, *Astrophys. J. Letters*, 699, L178

Naim, A., Ratnatunga, K. U., & Griffiths, R. E. 1997, *Astrophys. J. Supple.*, 111, 357

Nair, P. B. & Abraham, R. G. 2010, *Astrophys. J. Supple.*, 186, 427

Natale, G., Tuffs, R. J., Xu, C. K., et al. 2010, *Astrophys. J.*, 725, 955

Negrello, M., Hopwood, R., De Zotti, G., et al. 2010, Science, 330, 800

Nishi, R. & Tashiro, M. 2000, *Astrophys. J.*, 537, 50

Obreja, A., Domínguez-Tenreiro, R., Brook, C., et al. 2013, *Astrophys. J.*, 763, 26

Odewahn, S. C., Windhorst, R. A., Driver, S. P., & Keel, W. C. 1996, *Astrophys. J. Letters*, 472, L13

Oemler, Jr., A. 1974, *Astrophys. J.*, 194, 1

Oke, J. B. & Gunn, J. E. 1983, *Astrophys. J.*, 266, 713

Oohama, N., Okamura, S., Fukugita, M., Yasuda, N., & Nakamura, O. 2009, *Astrophys. J.*, 705, 245

Oosterloo, T., Morganti, R., & Sadler, E. 1999, *Pub. Astron. Soc. Australia*, 16, 28

O'Sullivan, E., Forbes, D. A., & Ponman, T. J. 2001, *Mon. Not. Roy. Astron. Soc.*, 328, 461

Parkin, T. J., Wilson, C. D., Foyle, K., et al. 2012, *Mon. Not. Roy. Astron. Soc.*, 422, 2291

Pascale, E., Auld, R., Dariush, A., et al. 2011, *Mon. Not. Roy. Astron. Soc.*, 415, 911

Pastrav, B. A., Popescu, C. C., Tuffs, R. J., & Sansom, A. E. 2013, *Astron. Astrophys.*, 553, A80

Paudel, S., Lisker, T., Kuntschner, H., Grebel, E. K., & Glatt, K. 2010, *Mon. Not. Roy. Astron. Soc.*, 405, 800

Peletier, R. F., Davies, R. L., Illingworth, G. D., Davis, L. E., & Cawson, M. 1990, *Astron. J.*, 100, 1091

Peng, C. Y., Ho, L. C., Impey, C. D., & Rix, H. 2002, *Astron. J.*, 124, 266

Peng, C. Y., Ho, L. C., Impey, C. D., & Rix, H.-W. 2010, *Astron. J.*, 139, 2097

Phillips, M. M., Jenkins, C. R., Dopita, M. A., Sadler, E. M., & Binette, L. 1986, *Astron. J.*, 91, 1062

Pimbblet, K. A., Smail, I., Kodama, T., et al. 2002, *Mon. Not. Roy. Astron. Soc.*, 331, 333

Pipino, A., D'Ercole, A., & Matteucci, F. 2008, *Astron. Astrophys.*, 484, 679

Poglitsch, A., Waelkens, C., Geis, N., et al. 2010, *Astron. Astrophys.*, 518, L2

Pope, A., Scott, D., Dickinson, M., et al. 2006, *Mon. Not. Roy. Astron. Soc.*, 370, 1185

Popescu, C. C., Misiriotis, A., Kylafis, N. D., Tuffs, R. J., & Fischera, J. 2000a, *Astron. Astrophys.*, 362, 138

Popescu, C. C. & Tuffs, R. J. 2013, *Mon. Not. Roy. Astron. Soc.*, 436, 1302

Popescu, C. C., Tuffs, R. J., Dopita, M. A., et al. 2011, *Astron. Astrophys.*, 527, A109

Popescu, C. C., Tuffs, R. J., Fischera, J., & Völk, H. 2000b, *Astron. Astrophys.*, 354, 480

Postman, M., Franx, M., Cross, N. J. G., et al. 2005, *Astrophys. J.*, 623, 721

Postman, M. & Geller, M. J. 1984, *Astrophys. J.*, 281, 95

Press, W. 1992, Numerical recipes in FORTRAN: the art of scientific computing, FORTRAN Numerical Recipes (Cambridge University Press)

Prieto, M., Eliche-Moral, M. C., Balcells, M., et al. 2013, *Mon. Not. Roy. Astron. Soc.*, 428, 999

Proctor, R. N. & Sansom, A. E. 2002, *Mon. Not. Roy. Astron. Soc.*, 333, 517

Rigby, E. E., Maddox, S. J., Dunne, L., et al. 2011, *Mon. Not. Roy. Astron. Soc.*, 415, 2336

Roberts, M. S. & Haynes, M. P. 1994, *Ann. Rev. Astron, Astrophys.*, 32, 115

Robotham, A. S. G., Liske, J., Driver, S. P., et al. 2013, *Mon. Not. Roy. Astron. Soc.*, 431, 167

Robotham, A. S. G., Norberg, P., Driver, S. P., et al. 2011, *Mon. Not. Roy. Astron. Soc.*, 416, 2640

Roche, P. F. & Aitken, D. K. 1984, *Mon. Not. Roy. Astron. Soc.*, 208, 481

Roche, P. F., Aitken, D. K., Smith, C. H., & Ward, M. J. 1991, *Mon. Not. Roy. Astron. Soc.*, 248, 606

Rowlands, K., Dunne, L., Maddox, S., et al. 2012, *Mon. Not. Roy. Astron. Soc.*, 419, 2545

Sadler, E. M. & Gerhard, O. E. 1985, *Mon. Not. Roy. Astron. Soc.*, 214, 177

Salim, S. & Rich, R. M. 2010, *Astrophys. J. Letters*, 714, L290

Salim, S., Rich, R. M., Charlot, S., et al. 2007, *Astrophys. J. Supple.*, 173, 267

Sandage, A. 1961, The Hubble atlas of galaxies

Sandage, A. 1972, *Astrophys. J.*, 176, 21

Sandage, A. & Bedke, J. 1994, The Carnegie Atlas of Galaxies. Volumes I, II.

Sansom, A. E., O'Sullivan, E., Forbes, D. A., Proctor, R. N., & Davis, D. S. 2006, *Mon. Not. Roy. Astron. Soc.*, 370, 1541

Sarzi, M., Falcón-Barroso, J., Davies, R. L., et al. 2006, *Mon. Not. Roy. Astron. Soc.*, 366, 1151

Saunders, W., Bridges, T., Gillingham, P., et al. 2004, in Society of Photo-Optical Instrumentation Engineers (SPIE) Conference Series, Vol. 5492, Society of Photo-Optical Instrumentation Engineers (SPIE) Conference Series, ed. A. F. M. Moorwood & M. Iye, 389–400

Savage, B. D. 1975, *Astrophys. J.*, 199, 92

Savoy, J., Welch, G. A., & Fich, M. 2009, *Astrophys. J.*, 706, 21

Schade, D., Lilly, S. J., Crampton, D., et al. 1999, *Astrophys. J.*, 525, 31

Schlegel, D. J., Finkbeiner, D. P., & Davis, M. 1998, *Astrophys. J.*, 500, 525

Secker, J. & Harris, W. E. 1996, *Astrophys. J.*, 469, 623

Seibert, M., Wyder, T., Neill, J., et al. 2012, in American Astronomical Society Meeting Abstracts, Vol. 219, American Astronomical Society Meeting Abstracts 219, 340.01

Sellgren, K. 1984, *Astrophys. J.*, 277, 623

Serjeant, S., Bertoldi, F., Blain, A. W., et al. 2010, *Astron. Astrophys.*, 518, L7

Serra, P., Oosterloo, T., Morganti, R., et al. 2012, *Mon. Not. Roy. Astron. Soc.*, 422, 1835

Sérsic, J. L. 1963, Boletin de la Asociacion Argentina de Astronomia La Plata Argentina, 6, 41

Shankar, F., Marulli, F., Bernardi, M., et al. 2013, *Mon. Not. Roy. Astron. Soc.*, 428, 109

Shao, Z., Xiao, Q., Shen, S., et al. 2007, *Astrophys. J.*, 659, 1159

Shapiro, K. L., Falcón-Barroso, J., van de Ven, G., et al. 2010, *Mon. Not. Roy. Astron. Soc.*, 402, 2140

Sharp, R., Saunders, W., Smith, G., et al. 2006, in Society of Photo-Optical Instrumentation Engineers (SPIE) Conference Series, Vol. 6269, Society of Photo-Optical Instrumentation Engineers (SPIE) Conference Series

Shull, J. M. 1977, *Astrophys. J.*, 216, 414

Siebenmorgen, R., Kruegel, E., & Mathis, J. S. 1992, *Astron. Astrophys.*, 266, 501

Silva, L., Granato, G. L., Bressan, A., & Danese, L. 1998, *Astrophys. J.*, 509, 103

Simmat, E., Tuffs, R. J., & Popescu, C. C. 2010, in American Institute of Physics Conference Series, Vol. 1240, American Institute of Physics Conference Series, ed. V. P. Debattista & C. C. Popescu, 87–88

Simmons, B. D. & Urry, C. M. 2008, *Astrophys. J.*, 683, 644

Skibba, R. A., Engelbracht, C. W., Dale, D., et al. 2011, *Astrophys. J.*, 738, 89

Smith, D. J. B., Dunne, L., Maddox, S. J., et al. 2011, *Mon. Not. Roy. Astron. Soc.*, 416, 857

Smith, G., Brzeski, J., Miziarski, S., et al. 2004, in Society of Photo-Optical Instrumentation Engineers (SPIE) Conference Series, Vol. 5495, Society of Photo-Optical Instrumentation Engineers (SPIE) Conference Series, ed. J. Antebi & D. Lemke, 348–359

Smith, M. W. L., Gomez, H. L., Eales, S. A., et al. 2012, *Astrophys. J.*, 748, 123

Somerville, R. S., Hopkins, P. F., Cox, T. J., Robertson, B. E., & Hernquist, L. 2008, *Mon. Not. Roy. Astron. Soc.*, 391, 481

Somerville, R. S. & Primack, J. R. 1999, *Mon. Not. Roy. Astron. Soc.*, 310, 1087

Sparks, W. B., Macchetto, F., & Golombek, D. 1989, *Astrophys. J.*, 345, 153

Spolaor, M., Proctor, R. N., Forbes, D. A., & Couch, W. J. 2009, *Astrophys. J. Letters*, 691, L138

Stanford, S. A., Eisenhardt, P. R., & Dickinson, M. 1998, *Astrophys. J.*, 492, 461

Stebbins, J. & Whitford, A. E. 1952, *Astrophys. J.*, 115, 284

Stecher, T. P. 1965, *Astrophys. J.*, 142, 1683

Stecher, T. P. & Donn, B. 1965, *Astrophys. J.*, 142, 1681

Steiman-Cameron, T. Y. & Durisen, R. H. 1987, in IAU Symposium, Vol. 127, Structure and Dynamics of Elliptical Galaxies, ed. P. T. de Zeeuw & S. D. Tremaine, 403

Steinmetz, M. & Navarro, J. F. 2002, *New Astron.*, 7, 155

Strateva, I., Ivezić, Ž., Knapp, G. R., et al. 2001, *Astron. J.*, 122, 1861

Strauss, M. A., Weinberg, D. H., Lupton, R. H., et al. 2002, *Astron. J.*, 124, 1810

Takagi, T., Vansevicius, V., & Arimoto, N. 2000, Institute of Space and Astronautical Science Report, 14, 155

Takeda, H., Nulsen, P. E. J., & Fabian, A. C. 1984, *Mon. Not. Roy. Astron. Soc.*, 208, 261

Tanaka, M., Kodama, T., Arimoto, N., et al. 2005, *Mon. Not. Roy. Astron. Soc.*, 362, 268

Taylor, E. N., Hopkins, A. M., Baldry, I. K., et al. 2011, *Mon. Not. Roy. Astron. Soc.*, 418, 1587

Temi, P., Brighenti, F., & Mathews, W. G. 2007, *Astrophys. J.*, 660, 1215

Temi, P., Brighenti, F., & Mathews, W. G. 2009a, *Astrophys. J.*, 695, 1

Temi, P., Brighenti, F., & Mathews, W. G. 2009b, *Astrophys. J.*, 707, 890

Terlevich, A. I., Kuntschner, H., Bower, R. G., Caldwell, N., & Sharples, R. M. 1999, *Mon. Not. Roy. Astron. Soc.*, 310, 445

Thomas, D., Maraston, C., Bender, R., & Mendes de Oliveira, C. 2005, *Astrophys. J.*, 621, 673

Tohline, J. E., Simonson, G. F., & Caldwell, N. 1982, *Astrophys. J.*, 252, 92

Tonnesen, S. & Bryan, G. L. 2009, *Astrophys. J.*, 694, 789

Toomre, A. & Toomre, J. 1972, *Astrophys. J.*, 178, 623

Trager, S. C. 2004, Origin and Evolution of the Elements, 388

Trager, S. C., Faber, S. M., Worthey, G., & González, J. J. 2000, *Astron. J.*, 119, 1645

Tsai, J. C. & Mathews, W. G. 1995, *Astrophys. J.*, 448, 84

Tuffs, R. J., Popescu, C. C., Völk, H. J., Kylafis, N. D., & Dopita, M. A. 2004, *Astron. Astrophys.*, 419, 821

van den Bergh, S. 1976, *Astrophys. J.*, 206, 883

van den Bergh, S. 2009, *Astrophys. J.*, 702, 1502

van Dokkum, P. G. & Franx, M. 1995, *Astron. J.*, 110, 2027

van Gorkom, J. & Schiminovich, D. 1997, in *Astronomical Society of the Pacific Conference Series*, Vol. 116, The Nature of Elliptical Galaxies; 2nd Stromlo Symposium, ed. M. Arnaboldi, G. S. Da Costa, & P. Saha, 310

Vazdekis, A., Kuntschner, H., Davies, R. L., et al. 2001, *Astrophys. J. Letters*, 551, L127

Vika, M., Bamford, S. P., Häußler, B., et al. 2013, *Mon. Not. Roy. Astron. Soc.*, 435, 623

Visvanathan, N. & Sandage, A. 1977, *Astrophys. J.*, 216, 214

Vulcani, B., Bamford, S. P., Häußler, B., et al. 2014, ArXiv e-prints

Walcher, C. J., Lamareille, F., Vergani, D., et al. 2008, *Astron. Astrophys.*, 491, 713

Weingartner, J. C. & Draine, B. T. 2001, *Astrophys. J.*, 548, 296

White, S. D. M. 1980, *Mon. Not. Roy. Astron. Soc.*, 191, 1P

Whittet, D. C. B. 1992, Dust in the Galactic Environment (Institute of Physics Graduate Series in Astronomy)

Wijesinghe, D. B., Hopkins, A. M., Brough, S., et al. 2012, *Mon. Not. Roy. Astron. Soc.*, 423, 3679

Willett, K. W., Lintott, C. J., Bamford, S. P., et al. 2013, *Mon. Not. Roy. Astron. Soc.*, 435, 2835

Worthey, G. 1998, *Pub. Astron. Soc. Pac.*, 110, 888

Worthey, G., Faber, S. M., & Gonzalez, J. J. 1992, *Astrophys. J.*, 398, 69

Worthey, G., Faber, S. M., Gonzalez, J. J., & Burstein, D. 1994, *Astrophys. J. Supple.*, 94, 687

Wyder, T. K., Martin, D. C., Schiminovich, D., et al. 2007, *Astrophys. J. Supple.*, 173, 293

Xilouris, E. M., Alton, P. B., Davies, J. I., et al. 1998, *Astron. Astrophys.*, 331, 894

Xilouris, E. M., Byun, Y. I., Kylafis, N. D., Paleologou, E. V., & Papamastorakis, J. 1999, *Astron. Astrophys.*, 344, 868

Yan, R., Newman, J. A., Faber, S. M., et al. 2006, *Astrophys. J.*, 648, 281

Yi, S. K., Yoon, S.-J., Kaviraj, S., et al. 2005, *Astrophys. J. Letters*, 619, L111

Young, L. M. 2002, *Astron. J.*, 124, 788

Young, L. M., Bureau, M., Davis, T. A., et al. 2011, *Mon. Not. Roy. Astron. Soc.*, 414, 940

Zibetti, S., Charlot, S., & Rix, H.-W. 2009, *Mon. Not. Roy. Astron. Soc.*, 400, 1181

Appendix A

Data from Chapter 3

This Appendix shows the main parameters of GAMA galaxies making up the *SubS* and *OptS*; these samples are created in Chapter 3 and are used throughout the rest of this thesis as the main sub-mm detected, optically selected sample of ETGs (*SubS*) and the control sample of undetected ETGs (*OptS*). Table A.1 shows the following properties for the *SubS*: GAMA CATAID, Right Ascension and Declination in J2000 coordinates, spectroscopic redshift, AB apparent GALEX NUV and SDSS r band magnitude, absolute r band magnitude, SPIRE 250μm flux, stellar mass, concentration index, Sérsic index, effective radius, and optical colour.

Table A.3 provides further information on the sub-mm properties of the *SubS*. The five PACS and SPIRE fluxes are given for the 187 ETGs fit with modified Planck functions, as are the resultant cold dust temperatures, dust temperature errors, dust masses and errors, and χ^2 results for the fit.

Table A.1: An example of the *SubS* dataset: including GAMA CATAID, J2000 Right Ascension and Declination and spectroscopic redshift. NUV apparent magnitude is taken from the GALEX Main Data table (note that not all galaxies have NUV detections), r band apparent magnitude is the aperture matched SDSS Petrosian magnitude. Absolute r band magnitudes are rest-frame magnitudes calculated as described in Taylor et al. (in prep). SPIRE 250μm fluxes are taken from the Herschel-GAMA matched data. Stellar mass is also calculated as described in Taylor et al. (in prep). Concentration and Sérsic index calculations are described in the main text in Chapter 3. Effective radius of the galaxy is taken from the SIGMA catalogue, and converted to kpc as described in the text in Chapter 3. Optical colours are calculated as described in Taylor et al. (in prep). Note that absolute magnitudes and colours are all K-corrected. The full dataset is shown in the enclosed CD.

CATAID	RA (degrees)	DEC (degrees)	z_{spec}	m_{NUV} (mag)	m_r (mag)	M_r (mag)	$F_{250\mu m}$ (Jy)	$\log_{10}(M_*)$ ($M_\odot$)	C_r	n_r	R_{eff} (Kpc)	M_{u-r} (mag)
7839	179.6154	0.7179	0.0475	20.56	14.64	-22.16	0.0564	11.06	2.98	4.24	6.48	2.49
14812	212.9300	0.7201	0.0247	18.16	14.99	-20.28	0.2226	9.98	1.67	1.53	2.49	1.56

Continued on next page

CATAID	RA	DEC	z_{spec}	m_{NUV}	m_r	M_r	$F_{250\mu m}$	$\log_{10}(M_*)$	C_r	n_r	R_{eff}	M_{u-r}
16026	217.5345	0.7035	0.0538	20.32	16.56	-20.42	0.1422	10.21	2.46	1.19	2.22	1.83
16242	218.1343	0.7715	0.0341	25.52	15.14	-21.03	0.1018	10.54	2.38	3.14	5.08	2.16
16792	220.1397	0.6370	0.0501	18.99	15.75	-21.13	0.1296	10.43	2.46	1.87	4.50	1.80
16926	220.9427	0.7179	0.0504	21.30	16.41	-20.47	0.0466	10.30	2.49	1.45	2.43	2.26
16993	221.3283	0.6629	0.0583	-99.00	16.73	-20.40	0.0433	9.84	2.55	1.58	1.81	1.32
22834	179.2375	1.1159	0.0393	19.23	15.21	-21.09	0.5019	10.36	2.26	1.34	4.04	1.69
23498	181.8772	1.1473	0.0492	19.14	16.93	-19.88	0.0417	9.77	2.45	1.50	1.60	1.51
23565	182.2069	1.1918	0.0371	19.08	15.53	-20.75	0.0915	10.39	2.33	2.53	3.43	2.02
28738	213.1505	1.0579	0.0463	19.20	16.20	-20.44	0.1349	10.03	2.49	1.23	2.33	1.57
30911	177.3756	-1.0865	0.0192	18.62	13.13	-21.72	0.0732	11.01	3.28	3.52	3.09	2.66
36880	211.8419	-1.0964	0.0551	20.11	15.36	-21.74	0.1031	10.75	2.37	2.13	6.73	2.31
39145	175.4361	-0.6880	0.0501	17.71	15.80	-21.05	0.2159	10.15	2.23	1.08	1.96	1.35
39671	177.9132	-0.6545	0.0405	20.54	17.48	-18.95	0.0434	9.56	2.53	3.63	0.98	1.75
40164	180.0178	-0.7596	0.0471	18.73	15.50	-21.21	0.0669	10.48	2.75	2.33	2.84	1.65
41144	184.4704	-0.6572	0.0296	-99.00	14.58	-21.12	0.6332	10.37	2.23	1.34	4.07	1.66
41302	185.3986	-0.7029	0.0399	-99.00	17.15	-19.19	0.1161	9.75	2.26	0.82	2.04	1.90

Table A.2: An example of the *OptS* dataset: including GAMA CATAID, J2000 Right Ascension and Declination and spectroscopic redshift. NUV apparent magnitude is taken from the GALEX Main Data table (note that not all galaxies have NUV detections), r band apparent magnitude is the aperture matched SDSS Petrosian magnitude. Absolute r band magnitudes are rest-frame magnitudes calculated as described in Taylor et al. (in prep). Stellar mass is also calculated as described in Taylor et al. (in prep). Concentration and Sérsic index calculations are described in the main text in Chapter 3. Effective radius of the galaxy is taken from the SIGMA catalogue, and converted to kpc as described in the text in Chapter 3. Optical colours are calculated as described in Taylor et al. (in prep). Note that absolute magnitudes and colours are all K-corrected. The full dataset is shown in the enclosed CD.

CATAID	RA (degrees)	DEC (degrees)	z_{spec}	m_{NUV} (mag)	m_r (mag)	M_r (mag)	$\log_{10}(M_*)$ ($M_\odot$)	C_r	n_r	R_{eff} (Kpc)	M_{u-r} (mag)
492487	216.9002	-1.4109	0.0552	22.29	17.49	-19.72	9.95	2.55	2.62	1.29	2.19
271610	175.0572	1.3765	0.0407	21.74	18.27	-18.23	9.40	2.55	2.60	0.98	1.95
381157	131.6530	1.8110	0.0523	22.89	16.60	-20.51	10.38	2.83	3.76	1.25	2.48

Continued on next page

CATAID	RA	DEC	z_{spec}	m_{NUV}	m_r	M_r	$\log_{10}(M_*)$	C_r	n_r	R_{eff}	M_{u-r}
375599	129.9289	1.4268	0.0501	22.93	17.47	-19.59	9.93	2.63	2.59	1.20	2.14
215052	132.6634	0.4602	0.0525	-999.00	17.85	-19.27	9.80	2.66	2.95	1.26	2.21
53810	175.1328	-0.2496	0.0468	20.86	17.99	-18.75	9.38	2.09	1.02	1.13	1.59
377710	138.6471	1.5627	0.0553	21.68	17.36	-19.84	10.04	2.93	3.82	1.35	2.23
514022	214.0467	-1.2685	0.0503	21.39	16.61	-20.38	10.15	2.68	3.30	1.23	2.00
91999	214.5090	0.4842	0.0528	22.21	16.40	-20.65	10.41	2.70	2.56	1.29	2.42
422830	132.5551	2.6821	0.0593	20.67	17.46	-19.89	10.10	2.56	2.64	1.45	2.22
348009	139.8936	2.2438	0.0566	22.23	17.43	-19.79	9.90	2.60	2.33	1.39	2.34
508936	219.0553	-1.4700	0.0564	22.79	17.85	-19.33	9.55	2.27	1.04	1.39	1.52
78712	218.3370	0.0136	0.0568	20.29	17.96	-19.31	9.78	2.65	2.69	1.40	1.92
77610	213.8997	0.0375	0.0534	22.33	17.64	-19.45	9.80	2.22	1.11	1.33	2.09
508594	217.5675	-1.5736	0.0555	-99.00	17.82	-19.39	9.59	2.53	1.43	1.39	1.46
271948	177.1559	1.3357	0.0469	20.95	17.09	-19.73	9.93	2.57	2.53	1.19	2.39
92000	214.5074	0.4831	0.0527	23.18	17.92	-19.64	9.93	2.18	2.71	1.33	2.23
422812	132.5046	2.6544	0.0599	22.60	16.78	-20.59	10.34	2.63	2.95	1.50	2.43
522105	132.4807	2.8741	0.0595	19.74	17.75	-19.53	9.82	2.76	2.33	1.49	1.89

Table A.3: An example of resultant parameters from modified blackbody fitting (described in Chapter 3). First column shows GAMA CATAID, followed by PACS 100 and 160μm fluxes, and SPIRE 250, 350 and 500μm fluxes (all in units of Jansky). Best fit cold dust temperatures and associated errors are shown in columns 7 and 8 in units of Kelvin. Columns 9 and 10 show dust mass and error derived from the best fit dust temperature, in units of solar masses. The final column shows the χ^2 value associated with the fit. The full dataset is shown in the enclosed CD.

CATAID	$F_{100\mu m}$ (Jy)	$F_{160\mu m}$ (Jy)	$F_{250\mu m}$ (Jy)	$F_{350\mu m}$ (Jy)	$F_{500\mu m}$ (Jy)	T_d (K)	ΔT_d (K)	$\log_{10}(M_d)$ ($M_\odot$)	$\Delta\log_{10}(M_d)$ ($M_\odot$)	χ^2_{min}
14812	0.308	0.365	0.223	0.109	0.035	20.50	0.87	6.90	5.85	2.6174
16026	0.322	0.305	0.142	0.050	0.015	25.25	1.09	7.10	6.05	1.8909
16242	0.172	0.255	0.102	0.044	0.008	23.17	1.45	6.68	5.91	3.2798
16792	0.150	0.192	0.130	0.069	0.029	19.92	1.31	7.30	6.43	2.4590
16926	0.120	0.130	0.047	0.029	0.017	25.37	2.30	6.56	5.74	5.5844
22834	1.218	0.969	0.502	0.198	0.074	24.90	0.94	7.41	6.33	3.7673
23498	0.096	0.058	0.042	0.029	0.011	19.32	4.29	6.84	6.10	3.1385